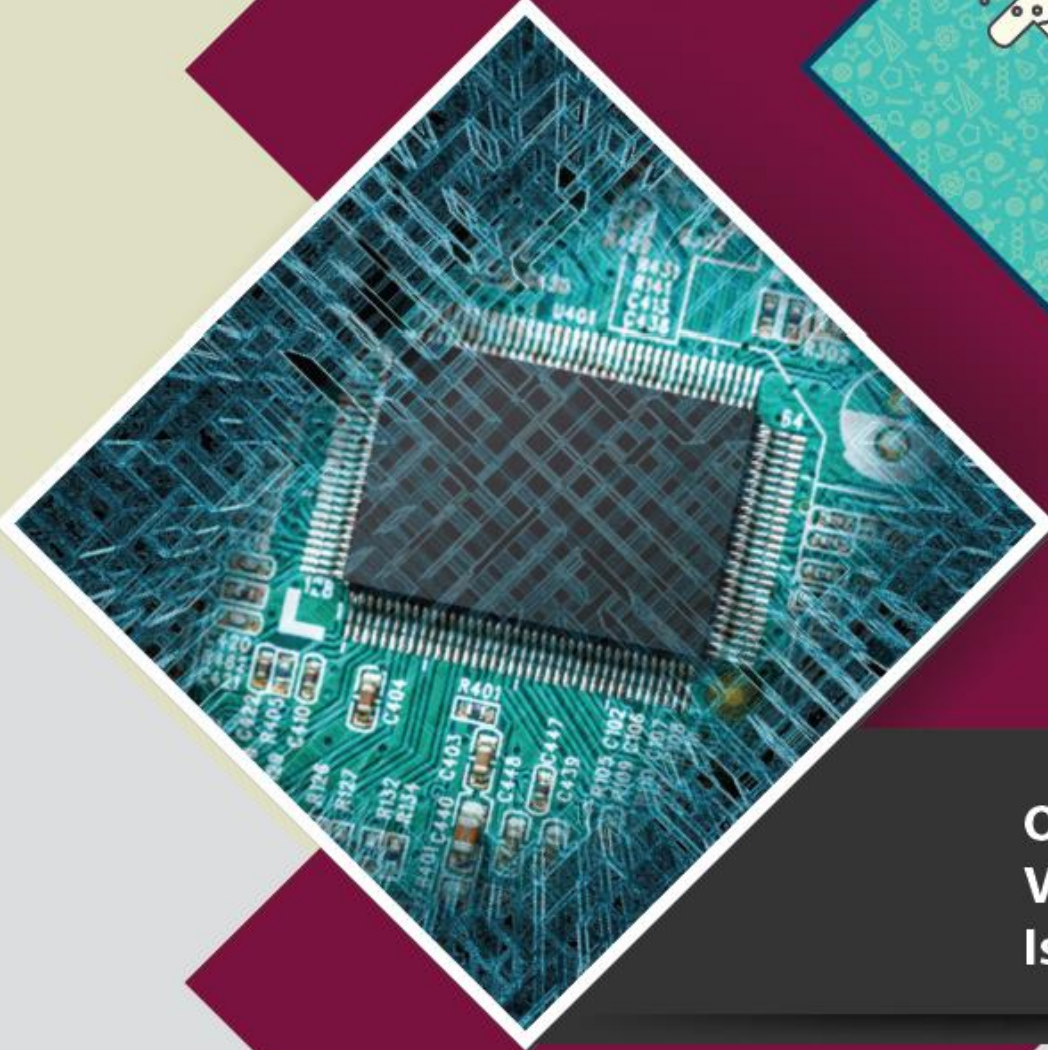


e-ISSN: 2822-2881



FUJECE

Firat University Journal of Experimental and Computational Engineering



October: 2024
Volume: 3
Issue: 3



<https://dergipark.org.tr/tr/pub/fujece>

Owner

On Behalf of Firat University

Rector

Prof. Dr. Fahrettin GÖKTAŞ

Editor-in-Chief

Prof. Dr. Mehmet YILMAZ, Firat University, Türkiye

Vice Editor-in-Chief

Prof. Dr. Ebru AKPINAR, Firat University, Türkiye

Prof. Dr. Ragıp İNCE, Firat University, Türkiye

Prof. Dr. Mete Onur KAMAN, Firat University, Türkiye

Assoc. Prof. Dr. Erkut YALÇIN, Firat University, Türkiye

Editorial Advisory Board

Prof. Dr. Yakup DEMİR, Firat University, Türkiye

Prof. Dr. Levent TAŞÇI, Firat University, Türkiye

Prof. Dr. Abdussamet ARSLAN, Gazi University, Türkiye

Prof. Dr. Ahmet ŞAŞMAZ, Firat University, Türkiye

Prof. Dr. Abdulkadir Cuneyt AYDIN, Atatürk University, Türkiye

Prof. Dr. Fatih CETİŞLİ, Pamukkale University, Türkiye

Prof. Dr. Bilal ALATAŞ, Firat University, Türkiye

Prof. Dr. Erhan AKIN, Firat University, Türkiye

Prof. Dr. Erkan KÖSE, Nuh Naci Yazgan University, Türkiye

Prof. Dr. Filiz KAR, Firat University, Türkiye

Prof. Dr. Hasan SOFUOĞLU, Karadeniz Technical University, Türkiye

Prof. Dr. Özge Kaya HANAY, Firat University, Türkiye

Prof. Dr. Yusuf AYVAZ, Yıldız Technical University, Türkiye

Prof. Dr. M. Şaban TANYILDIZI, Firat University, Türkiye

Doç. Dr. Tacettin GEÇKİL, İnönü University, Türkiye

Doç. Dr. José NORAMBUENA-CONTRERAS, Bio Bio University, Chile

Res. Assist. Dr. Ulaş Baran BALOĞLU, University of Bristol, England

Editorial Board

Prof. Dr. Mehmet YILMAZ (Editor-in-Chief)	Civil Engineering
Prof. Dr. Ebru AKPINAR (Vice Editor-in-Chief)	Mechanical Engineering
Prof. Dr. Ragıp İNCE (Vice Editor-in-Chief)	Civil Engineering
Prof. Dr. Mete Onur KAMAN (Vice Editor-in-Chief)	Mechanical Engineering
Assoc. Prof. Dr. Erkut YALÇIN (Vice Editor-in-Chief)	Civil Engineering
Prof. Dr. Ali TOPAL	Civil Engineering
Prof. Dr. Ali YAZICI	Software Engineering
Prof. Dr. Ayşe Vildan BEŞE	Chemical Engineering
Prof. Dr. Bilge Hilal CADIRCI EFELİ	Bioengineering
Prof. Dr. Kadir TURAN	Mechanical Engineering
Prof. Dr. H. Soner ALTUNDOĞAN	Bioengineering
Prof. Dr. Mehmet Deniz TURAN	Metallurgy and Materials Engineering
Prof. Dr. Mustafa YANALAK	Geodesy and Photog. Engineering
Prof. Dr. Nuno MENDES	Mechanical Engineering
Prof. Dr. Rashid NADIROV	Chemical
Prof. Dr. Serdar Ethem HAMAMCI	Electrical-Electronics Engineering
Prof. Dr. Selçuk ALEMDAĞ	Geological Engineering
Prof. Dr. Mehmet KARAKÖSE	Computer Engineering
Prof. Dr. Alvaro Garcia HERNANDEZ	Civil Engineering
Prof. Dr. Ömür GÖKKUŞ	Environmental Engineering
Assoc. Prof. Dr. Fatih DEMİR	Software Engineering
Lecturer Batuhan SELVİ (Language Editor)	English Language Teaching
Mustafa Gani GENÇER (Language Editor)	English Language Teaching
Res. Assist. Dr. Özge Erdoğan YAMAÇ (Secretariat)	Civil Engineering
Res. Assist. Beyza Furtana YALÇIN (Pub. Coordinators)	Civil Engineering
Ahmet BAL (Layout Editor)	Social Studies Education

Composition

Ahmet BAL

Correspondence Address

Firat University Faculty of Engineering Journal of Experimental and Computational Engineering Publishing

Coordinatorship

23119 Elazığ/TÜRKİYE

E-mail: fujece@firat.edu.tr

Web page: <http://fujece.firat.edu.tr/>

Firat University Journal of Experimental and Computational Engineering a peer-reviewed journal.

CONTENTS

Attention Based Energy Demand Forecasting in Smart Grid Environments (Research Article) Akıllı Şebeke Ortamlarında Dikkat Tabanlı Enerji Talep Tahmini (Araştırma Makalesi) Yunus Emre İŞIKDEMİR, Fuat AKAL	227
An Experimental Study on the Compressibility of Clays Reinforced with Basalt Fiber (Research Article) Bazalt Fiber ile Takviye Edilen Killerin Sıkıştırılabilirliği Üzerine Deneysel Bir Çalışma (Araştırma Makalesi) Yasemin Aslan TOPÇUOĞLU, Zülfü GÜROCAK	241
Detection of Road Damages Using Machine Learning Methods with Data Collected from Various Geographies: A Study on Türkiye (Research Article) Geliştirilmiş Öğretme-Öğrenme Tabanlı Optimizasyon Algoritmaları Kullanılarak Konsol İstinat Duvarı Tasarımının Optimizasyonu (Araştırma Makalesi) Ahmet Cihangir KAVCI, Ömer Faruk CANSIZ	255
Evaluation of the Biomechanical Properties of Endodontic Files with Different Taper Angles Using Finite Element Analysis (Research Article) Farklı Taper Açılarında Sahip Endodontik Eğelerin Biyomekanik Özelliklerinin Sonlu Elemanlar Analiziyle Değerlendirilmesi (Araştırma Makalesi) Mehmet ESKİBAĞLAR, Serkan ERDEM	271
Mn and Ti Co-doping of LiNiO ₂ to Improve Performance (Research Article) LiNiO ₂ 'nin Performans Geliştirmesi İçin Mn ve Ti Eş Katkısı (Araştırma Makalesi) Erdinç ÖZ, Jeff DAHN	280
Simulation of the Collapse Mechanism of a Minaret under the Effect of Strong Wind (Research Article) Kuvvetli Rüzgar Etkisindeki Minarenin Göçme Mekanizmasının Simülasyonu (Araştırma Makalesi) Taha Yasin ALTIOK, Ali DEMİR	292
Investigation of Phosphate Removal from Aqueous Solutions Using Zinc Extraction Waste (Research Article) Çinko Ekstraksiyon Atığı Kullanılarak Sulu Çözeltilerden Fosfat Gideriminin Araştırılması (Araştırma Makalesi) Feride Naime TÜRK	313
Development of a Production Process for Biomass-Based Activated Carbon via Hydrothermal Carbonization Method (Research Article) Hidrotermal Karbonizasyon Yöntemiyle Biyokütle Bazlı Aktif Karbon Üretim Prosesinin Geliştirilmesi (Araştırma Makalesi) Nida KATI, Ferhat UÇAR	326
An Application of DC Motor Modelled Classical Sliding Mode Control with Moving Sliding Surface to Rotary Inverted Pendulum System (Research Article) Hareketli Kayma Yüzeyle DC Motor Modelli Klasik Kayan Kipli Kontrolün Dönel Ters Sarkaç Sistemine Uygulanması (Araştırma Makalesi) Muhammet AYDIN, Oğuz YAKUT	337

Effect of Ground Diatomite on Early Strength of Self-Compacting Mortars (Research Article)

Öğütülmüş Diyatomitin Kendiliğinden Yerleşen Harçların Erken Dayanımına Etkisi (Araştırma Makalesi)

Büşra KARABULUT, Merve Şahin YÖN, Mehmet KARATAŞ

350

An Artificial Intelligence-Based Hybrid Approach to Detect the Type of Buried Objects with Broad Frequency Band Antenna Systems (Research Article)

Geniş Frekans Bantlı Anten Sistemleriyle Gömülü Nesnelerin Türünün Tespitinde Yapay Zeka Tabanlı Hibrit Bir Yaklaşım (Araştırma Makalesi)

Ebru EFEOĞLU

362



Akıllı Şebeke Ortamlarında Dikkat Tabanlı Enerji Talep Tahmini

Yunus Emre ISIKDEMİR^{1*} , Fuat AKAL² 

¹Computer Engineering Department, Graduate School of Science & Engineering, Hacettepe University, Ankara, Türkiye.

²Computer Engineering Department, Hacettepe University, Ankara, Türkiye.

¹yeisikdemir@gmail.com, ²akal@hacettepe.edu.tr

Geliş Tarihi: 21.01.2024
Kabul Tarihi: 02.04.2024

Düzeltilme Tarihi: 10.03.2024

doi: 10.62520/fujece.1423120
Araştırma Makalesi

Alıntı: Y.E. İşıkdemir ve F. Akal, "Akıllı şebeke ortamlarında dikkat tabanlı enerji talep tahmini", Fırat Üni. Deny. ve Hes. Müh. Derg., vol. 3, no 3, pp. 227-240, Ekim 2024.

Öz

Akıllı şebeke, modern enerji peyzajının kritik bir unsuru olup, artan enerji taleplerini karşılamak için güvenilir, verimli ve sürdürülebilir bir yol sağlamaktadır. Bununla birlikte, akıllı şebeke teknolojisi tarafından üretilen büyük miktardaki veri, gelişmiş veri işleme ve analiz tekniklerinin geliştirilmesini gerektirmektedir. Bu makalede, akıllı şebeke uygulamalarında zaman serisi tahmininde kullanılmak üzere, dilatasyonlu konvolüsyon ve dikkat mekanizmalarını birleştiren bir dikkat tabanlı zaman serisi iş akışı öneriyoruz. Bu akış, dilatasyonlu konvolüsyonları kullanarak zaman serisi verilerinden zamansal özellikler çıkarır ve dikkat mekanizmalarını kullanarak gizli durumlardaki önemli zaman noktalarını vurgular. Deneysel değerlendirmeler sonucunda, enerji talebi tahmininde, yaygın olarak kullanılan derin öğrenme tabanlı yöntemlere göre %8'e kadar daha iyi bir performans gösterdiği gözlemlendi. Bu kazancı diğer modellerin aldığı eğitim süresinin yalnızca 1/3'ü kadar bir sürede elde edilmiştir. Ayrıca, tamamen farklı bir alanda %42'lik bir kazanç elde edilmiştir ve akışın diğer alanlara uyarlanabileceği gösterilmiştir. Bu çalışma, araştırmacılara akıllı şebeke uygulamaları için daha doğru ve verimli tahmin modelleri geliştirmelerine yardımcı olabilir, ayrıca enerji sistemlerinin sürdürülebilir yönetimi ve akıllı şebeke operasyonlarının optimizasyonu için yapay zeka ve dikkat tabanlı tahmin tekniklerinin potansiyeli hakkında değerli bilgiler sunabilir.

Anahtar kelimeler: Akıllı şebeke, Zaman serisi tahmini, Attention mekanizması, Dönüştürücüler, Enerji talebi tahmini

*Yazılan yazar

İntihal Kontrol: Evet – Turnitin
Şikayet: fujece@firat.edu.tr

Telif Hakkı ve Lisans: Dergide yayın yapan yazarlar, CC BY-NC 4.0 kapsamında lisanslanan çalışmalarının telif hakkını saklı tutar.



Attention Based Energy Demand Forecasting in Smart Grid Environments

Yunus Emre ISIKDEMIR ^{1*} , Fuat AKAL ² 

¹Computer Engineering Department, Graduate School of Science & Engineering, Hacettepe University, Ankara, Türkiye.

²Computer Engineering Department, Hacettepe University, Ankara, Türkiye.

¹yeisikdemir@gmail.com, ²akal@hacettepe.edu.tr

Received: 21.01.2024

Accepted: 02.04.2024

Revision: 10.03.2024

doi: 10.62520/fujece.1423120

Research Article

Citation: Y.E. Işıkdemir and F. Akal, "Attention based energy demand forecasting in smart grid environments", *Firat Univ. Jour. of Exper. and Comp. Eng.*, vol. 3, no 3, pp. 227-240, October 2024.

Abstract

The smart grid is a crucial aspect of the modern energy landscape, providing a reliable, efficient, and sustainable way of meeting the growing energy demands. However, the vast amounts of data generated by smart grid technology necessitate the development of advanced data processing and analysis techniques. In this paper, we propose an attention-based time series workflow that combines dilated convolution and attention mechanisms for time series forecasting in smart grid applications. This workflow extracts temporal features from time series data using dilated convolutions and emphasizes significant temporal points in the hidden states using attention mechanisms. Experimental evaluations showed up to an 8% better performance for energy demand forecasting compared to commonly used deep learning-based methods. Our workflow achieved this gain by requiring 1/3 of the training time other models took. We also improved performance by 42% in various domains, demonstrating the adaptability of our approach across different areas. This study may assist researchers in constructing accurate forecasting models for smart grid environments. Furthermore, it highlights that the attention-based approach can be employed to promote sustainable energy and optimize smart grid environments.

Keywords: Smart grid, Time series forecasting, Attention, Transformers, Energy demand forecasting

*Corresponding author

Plagiarism Checks: Yes – Turnitin

Complaints: fujece@firat.edu.tr

Copyright & License: Authors publishing with the journal retain the copyright to their work licensed under the CC BY-NC 4.0

1. Introduction

A smart grid is a modern electrical power grid that includes advanced technologies such as digital communication, automation, and monitoring [1]. It is an effective and environmentally friendly power distribution system created to address increasing energy needs while keeping the environmental impact to a minimum level [2]. A smart grid can adaptively control the flow of electricity based on immediate shifts in demand and supply. The use of smart grids helps humanity for energy management, reduced costs, increased energy efficiency and more sustainable future. It helps incorporate renewable energy into the grid and allows energy to flow both ways between consumers and the grid [3,4].

Time series based energy demand forecasting plays an important role in smart grids [5]. Since precise energy demand forecasting may allow to optimize energy distribution, reduce energy waste and efficient energy management. In this way, companies supply energy based on expected demand and help to avoid energy shortages using the results of this forecasting. [6-8].

Deep learning is a type of machine learning that utilizes artificial neural networks to identify complex patterns in large data sets. It mimics the activation of the human brain and neurons using multiple nodes. Each of these nodes has weights to learn from the data and extract useful information [9]. With the use of Internet of Things (IoT) devices and sensors in the smart grid, large amounts of data are generated and necessitating the use of deep learning algorithms. The use of these algorithms enables the analysis of large data sets, such as energy consumption. This allows for the estimation of possible future consumption and optimization of the energy supply.

An attention mechanism, that has become quite popular recently and achieved successful results, is a concept of modeling the relationship between two sequences. It allows to focus specific part of the input sequence and produce specific output. In this study, this mechanism is used to capture dependencies between different time steps for accurately forecasting energy demand. Moreover, this mechanism may also help to make the model more interpretable by identifying the key factors that influence the output [10].

The Encoder Decoder Long Short Term Memory architecture, also known as Seq2Seq, is a commonly employed framework for sequence modeling [11]. The model uses two neural networks which are the encoder and decoder. The encoder learns to extract features and represent the data in a latent vector form. The decoder learns to reconstruct the output sequence. However, the bottleneck issue limits efficient transmission of information in this architecture because there is a single connection between the encoder and the decoder [12]. This study used an attention mechanism to mitigate the bottleneck issue in this framework. This was achieved by establishing multiple connections from the encoder to the decoder. The connections prioritize the most important time steps. By doing so, the attention mechanism may facilitate the efficient transmission of information and improve the overall performance of the model.

The subsequent sections of this paper are structured as follows: related works which focus on relevant literature; methodology which provides a detailed research design, data collection and analysis procedures; experimental results which include the findings of the statistical analyses; and conclusion which summarizes the main findings of the study.

2. Related Works

With the use of smart grid technology becoming more and more common, there is a lot of data that needs advanced analysis techniques. Making accurate predictions about the future based on time series data is really important for smart grid operations. Since it helps us understand how people use energy and allows us to manage energy systems more efficiently. Therefore, many researchers conduct experiments to create good models for estimating the future trends in energy demand. In this section, we will provide an overview of the current state of forecasting methods in smart grids.

Chujai and colleagues [13] used the Autoregressive Moving Average (ARMA) and Autoregressive Integrated Moving Average (ARIMA) models to predict how much power individual households would use each day, week, and quarter. The study found that the ARIMA model worked best for forecasting power usage on a monthly and quarterly basis. On the other hand, the ARMA model was found to be more effective for shorter time periods, like predicting daily and weekly power consumption. These results are significant for managing energy consumption because they offer guidance on the best methods for predicting power usage based on different timeframes.

In their study, Cascone et al. [14] suggested a two step method for predicting household energy usage. They used a mix of Convolutional Neural Network and Long Short-Term Memory (CNN-LSTM) architecture. In the first step, they applied an LSTM model to estimate the total active power generated over a 500-hour period. For the second step, they employed a combination of convolutional neural network features and LSTM for a weekly energy consumption forecast. The outcomes of the study were positive, showing potential benefits for predicting power consumption.

Seliverstova et al. [15] highlight that electricity consumption forecasting can be divided into four types based on the timeframe, namely ultra-short-term, short-term, medium-term, and long-term. The study employed various algorithms, including ARIMA, Group Method of Data Handling (GMDH), LSTM, and seq2seq. After conducting experiments, it was found that GMDH performed the best among the tested methods.

Tae-Young Kim and Sung-Bae Cho [16] employed CNN-LSTM hybrid deep learning approach for forecasting power consumption in their study. CNN layer was utilized to simplify the complexity of the spatial information and extract the most important features for forecasting. LSTM layer was applied to model the sequential relationship. Deep Neural Network was utilized to interpret the results and generate the forecasted value. They achieved highly accurate power consumption forecasts.

Shi and Wang [17] proposed a combination of landmark based spectral clustering (LSC) and deep learning techniques to cluster and forecast the power consumption dataset. The dataset was transformed into a matrix, and missing values were imputed. The data samples were then divided into three distinct clusters based on their periodicity and regularity using LSC.

Keskin et. al. [18] introduced an approach that utilizes a hierarchical architecture of LSTM (HLSTM). The proposed method is tested on real life crime, electric power consumption, and financial data sets. Results show that the HLSTM improves modeling of distant temporal interactions compared to traditional LSTM architecture.

Oh and Lee [19] used dense sampling method to capture more information from the input data. The proposed method samples data from both the time and window axes, resulting in a larger training dataset and other benefits such as model-agnosticism and easier window selection.

3. Methodology

In this study, we propose a time series workflow that is capable of capturing both long range and short range relationship of the data, shown in Figure 1. The workflow consists of data understanding and analysis, dilated convolution operation for temporal feature extraction, LSTM with attention for learning sequential correlation, and forecasting steps. The analysis step involves downsampling the dataset [20], into daily intervals and imputing missing values using spline interpolation. Temporal features are then extracted using dilated convolution and fed to LSTM layers. To prevent bottleneck, hidden states of all LSTM layers are used instead of a single connection of LSTM layers. The attention layer is then used to focus on the most important parts of the series to map output using an encoder-decoder LSTM architecture. The information is concatenated and the final prediction is performed. This workflow offers a comprehensive approach to time series forecasting that effectively incorporates multiple techniques and processes to improve the accuracy and reliability of predictions.

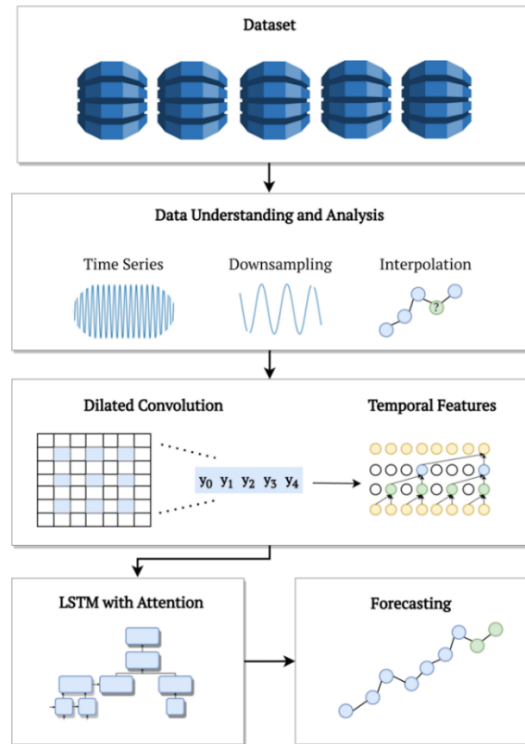


Figure 1. Workflow of the proposed methodology

The primary objective of this study is to determine the effectiveness of the proposed workflow for a forecasting model, which can accurately predict future energy consumption patterns. This accuracy will enable proper planning and management of electricity distribution, thereby contributing to the efficient and sustainable use of energy resources. To further validate our approach we conducted our experiments on two other time series datasets and one of them was from a different domain. The subsequent subsections will provide comprehensive details on the aforementioned steps.

3.1. Dataset

The Hourly Energy Demand Generation and Weather Dataset is a collection of hourly measurements of electricity generation, demand, and weather conditions. The dataset consists of observations from 2015 to 2018. Each row represents the measurement for each hour of the day. As our primary dataset, we used it to analyze the relationship between energy demand and weather patterns, which is crucial for predicting future energy consumption and ensuring the stability of the smart grid. The dataset includes a wide range of weather variables such as temperature, wind speed, and precipitation, as well as energy demand and generation data from various sources such as solar, wind, and fossil fuel power plants. In the context of this study, the variable of interest is the total load, which represents the actual electrical demand. The aim of this research, however, is to develop benchmark models for comparing the effectiveness of our proposed approach to other existing models in predicting the total load variable, which is crucial in various fields including energy management, weather forecasting, and infrastructure planning. Therefore, we considered two other datasets to further validate our approach.

First, the Individual Household Electric Power Consumption Dataset provides information on the electricity consumption of a single household for four years, from December 2006 to November 2010. It includes data points for power consumption within the household collected every minute. The dataset contains 2,075,259 records. The features include the date and time of each measurement and the active and reactive power consumed by the household.

Second, the Airline Passengers Dataset is a famous and frequently used dataset for time series forecasting. It consists of monthly information from 1949 to 1960 about how many people flew on airplanes during those years. In this particular dataset, passenger counts range from 104 to 622, exhibiting a standard deviation of 119. The mean passenger count is 280. The airline passengers dataset is commonly studied to compare diverse deep learning model for time series analysis. The airline passengers dataset is valuable for several reasons, including its historical significance, which provides a significant amount of data for analysis and forecasting, and its relevance to practical applications. Time series analysis researches frequently use this dataset to assess and compare various models and algorithms for time series forecasting. We picked this known dataset to show that our approach works in other domains.

3.2. Data Understanding and Analysis

Our research objective is to make daily forecasts at a time, which require data at daily interval. Due to the dataset's inherent challenges, such as missing values and high-frequency intervals between measurements, certain steps must be taken to preprocess the data before it can be used for forecasting. Therefore, the dataset was preprocessed to ensure that only relevant data was used for modeling. Data downsampling involves decreasing the time or frequency of a dataset that is beneficial when the original data is collected more frequently than intended for analysis. In our study, we reduced the minutely data to daily intervals to better align with our research goals. This not only simplifies the analysis and modeling processes but also meets our research objectives more effectively. The downsampling process can be summarized as:

Let $X = \{x_0, x_1, \dots, x_n\}$ a time series data with n observations taken at a minute-level frequency, such that x_i represents the data value at time i . Let $T = \{t_0, t_1, \dots, t_n\}$ the corresponding time stamps, where t_i is the time stamp of the i th observation. To downsample the data from minute-level frequency to daily frequency, it can be computed the daily average of the observations for each day shown in equations 1 and 2.

$$\mathbf{X} = \{\mathbf{y}_0, \mathbf{y}_1, \dots, \mathbf{y}_n\} \tag{1}$$

where n is the number of days covered by the time series, and \mathbf{y}_i is the average value of the observations for the i th day. The mathematical formula for computing \mathbf{y}_i is:

$$\mathbf{y}_i = \frac{1}{M} \sum_j^M (x_j) \tag{2}$$

where M is the number of observations on the i th day, and $\sum_j^M (x_j)$ represents the sum of the observations on the i th day.

Spline interpolation is widely used interpolation method that is used for imputing missing values in this study. This method works by creating a smooth curve using a set of mathematical expressions called polynomials [21]. The method's application can be particularly advantageous in analyzing time series data, especially in contexts like energy demand prediction. This is because missing values in such data can be attributed to various factors, and a strictly linear trend is not always observed. Spline interpolation is advantageous over other imputation methods because it produces a smooth curve that captures the underlying trend in the data, while also preserving the pattern of the original data. In addition, spline interpolation is less sensitive to outliers than other imputation methods [22] which makes it a more robust approach for handling missing values. The mathematical representation of the cubic spline interpolation formula can be expressed by equations 3-7.

$$S_i(x) = a_i + b_i(x - x_i) + c_i(x - x_i)^2 + d_i(x - x_i)^3 \tag{3}$$

$$a_i = f_i \tag{4}$$

$$b_i = \frac{(f_{i+1} - f_i)}{h_i} - \frac{h_i}{3} (2c_i + c_{i+1}) \quad (5)$$

$$c_i = \frac{(f_{i+1} - f_i)}{h_i} - \frac{h_i}{3} (2b_i + b_{i+1}) \quad (6)$$

$$d_i = \frac{(b_{i+1} - b_i)}{3h_i} \quad (7)$$

where $S_i(x)$ represents the cubic spline function for the i -th interval, which is defined by the coefficients a_i , b_i , c_i , and d_i . The coefficient a_i represents the value of the function at the i -th data point denoted by f_i . The coefficient b_i and c_i represents the slope and curvature of the function at the i -th data point respectively. The rate of change of curvature is represented by the coefficient d_i .

3.3. Dilated Convolution for Efficient Feature Extraction

LSTM [23] is used as a part of our architecture. LSTM is a type of recurrent neural network (RNN) that is designed to analyze and process sequential relationships in data. LSTM networks can be particularly useful in cases where data has long term dependencies and timing is critical such as natural language processing or speech recognition tasks. The distinguishing feature of LSTMs is their adeptness at discriminative memory or discard previous input values based on the present input and past memory state. This is accomplished through gates that regulate the flow of information in and out of the memory cell. These cells are connected to three gates that have specific functions: input gate, forget gate, and output gate expressed by equations 8-13.

$$f_t = \sigma(W_f \cdot [h_{t-1}, x_t] + b_f) \quad (8)$$

$$i_t = \sigma(W_i \cdot [h_{t-1}, x_t] + b_i) \quad (9)$$

$$\tilde{C}_t = \tanh(W_C \cdot [h_{t-1}, x_t] + b_C) \quad (10)$$

$$C_t = f_t * C_{t-1} + i_t * \tilde{C}_t \quad (11)$$

$$o_t = \sigma(W_o \cdot [h_{t-1}, x_t] + b_o) \quad (12)$$

$$h_t = o_t * \tanh(C_t) \quad (13)$$

where, the forget gate, represented by f_t , determines which information is retained in the cell state, while the input gate, i_t , controls which new input values are added to it. The candidate values for the cell state are denoted by \tilde{C}_t , and the new cell state value, C_t , is a combination of the forget gate and input gate. The output gate, o_t , determines which part of the cell state is activated using the hyperbolic tangent function, and h_t is the output generated from the cell state value and the output gate decision. By utilizing this mechanism, LSTMs can discover and represent intricate patterns and dependencies in sequential data, making them a potent tool for various applications in artificial intelligence and machine learning.

Dilated convolution [24] is a special type of convolution operation that creates gaps between the kernel elements during the convolution process. In this way, a larger receptive field for the network is achieved without an increase in parameters, as shown in Figure 2.

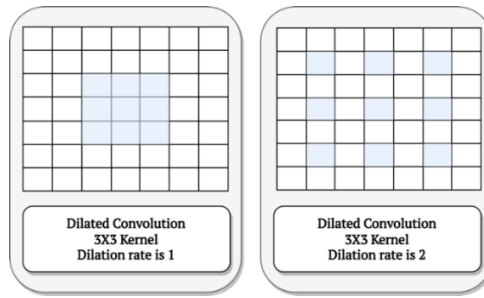


Figure 2. Dilated convolution

In this study, we used dilated convolution for extracting features for LSTM layers. In the context of using dilated convolution with LSTM based neural networks, multiple dilated convolutional layers can be stacked on top of an LSTM layer to extract hierarchical features from time series data shown in Figure 3.

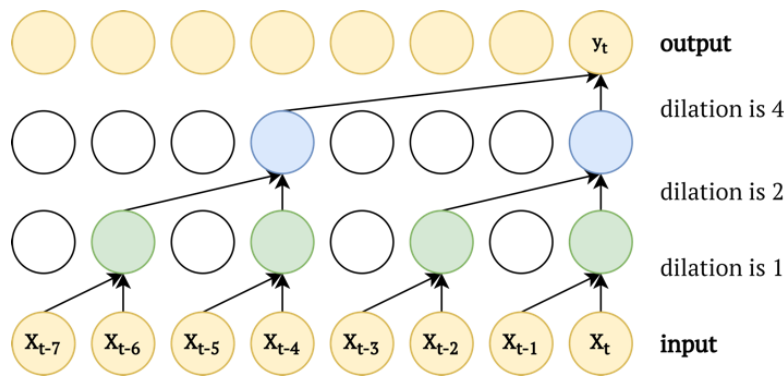


Figure 3. Temporal features

This method can be helpful for understanding connections that persist for a long time in the information, and it can also recognize specific characteristics at various levels. By combining dilated convolutional layers with an LSTM layer, the model can understand intricate patterns and relationships in the data without losing information [25]. It also reduces the risk of overfitting and limiting the number of parameters needed.

3.4. Attention for Preventing Bottleneck

In the analysis of time series data using deep learning models, attention [26] is a technique that lets the model highlight important parts of the data as it processes them. This is achieved by using an additional layer that learns how to weight different parts of the time series based on their relevance. By focusing on the most informative parts of the data, attention mechanisms can improve the model's performance on tasks such as prediction and classification. In this study, we used an attention mechanism to prevent a single connection bottleneck from encoder-decoder LSTM.

Classical Encoder-Decoder LSTM [27] architecture uses a single connection for passing information from encoder to decoder as shown in Figure 4.

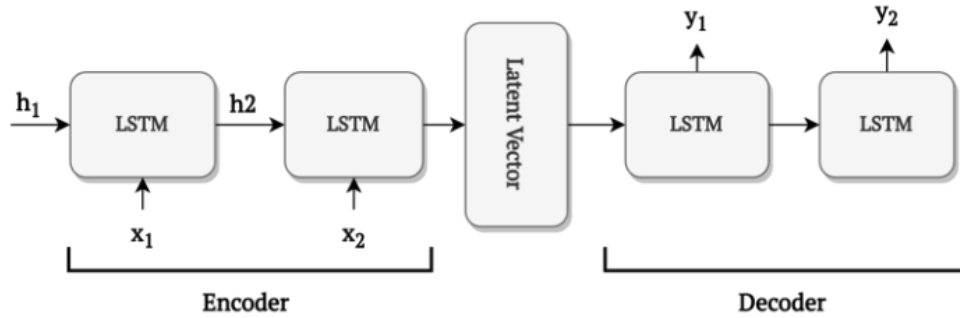


Figure 4. Encoder-decoder LSTM

The utilization of the most common approach with a single connection from the encoder LSTM to the decoder LSTM in a sequence to sequence model can potentially result in a bottleneck for the flow of information between the two network components. This limits the ability of the model to effectively capture the underlying temporal dependencies in the input sequence. To alleviate the issue of information bottleneck caused by a single connection from the encoder LSTM to the decoder LSTM, an attention mechanism was employed for each of the LSTM components which help to improve the information flow by carefully considering and combining the hidden information from the encoder. It does this by giving more importance to the parts that are most relevant to the current decoding step, as illustrated in Figure 5.

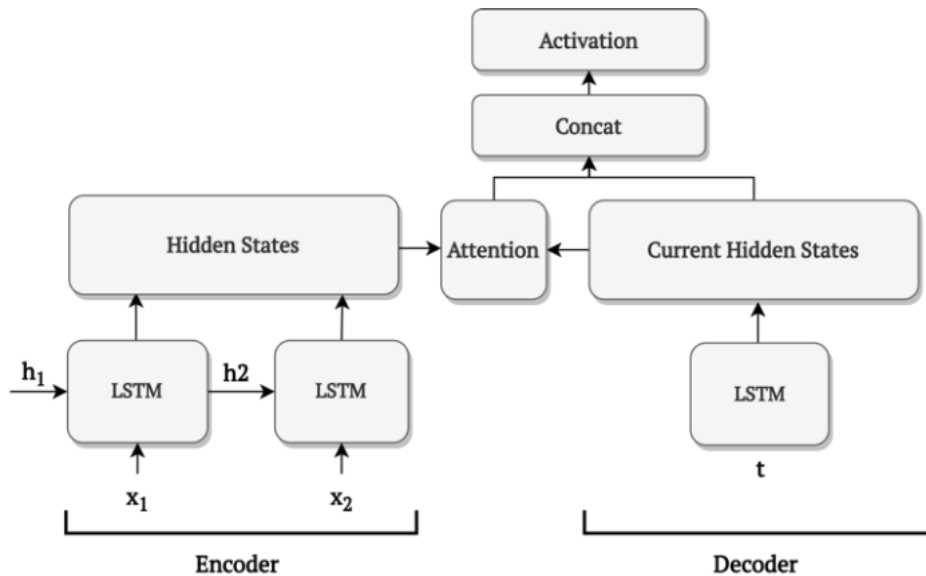


Figure 5. Encoder-decoder LSTM with attention

In time series analysis, the attention mechanism helps deep learning models focus on different parts of the time series data. This may help enhance the modeling of temporal dependencies. The subsequent section of this study will provide a detailed discussion of the experimental results.

4. Experimental Evaluations

In this section, experimental evaluations will be conducted. Specifically, the proposed end-to-end workflow will be evaluated and compared against commonly used deep learning architectures for time series forecasting. This comparative analysis will enable a comprehensive assessment of the effectiveness and efficiency of the proposed approach in addressing the challenges associated with accurate forecasting of both short-term and long-term relationships in time series. The results of this

comparison will provide valuable insights into the potential benefits and limitations of the proposed workflow and its ability to outperform existing state-of-the-art techniques in time series forecasting.

4.1. Experimental Setup

Hardware has an important place in training neural networks. The well configured scalable systems helps for efficient training with reducing training time. In this study, the experimental setup consisted of a GIGABYTE GeForce GTX1070 graphics processing unit, 16GB of 3000Mhz DDR4 Dual Kit random access memory, and an INTEL Core i5 8400 2.8GHz 9MB cache 6-core central processing unit. In this study, we used the Adam optimizer, RMSE, and ReLU activation function for our deep learning models. Adam optimizer is a widely employed optimization algorithm in the deep learning approach for updating weights. RMSE is a standard measure for evaluating how well a model performs by calculating the difference between predicted and actual outputs. ReLU is a widely-used activation function in deep learning known for its efficiency and its ability to address the vanishing gradient problem [28].

4.2. Performance Evaluation On Hourly Energy Demand Generation and Weather Dataset

The “Hourly Energy Demand Generation Dataset” is used as a benchmark dataset to evaluate and compare our proposed workflow with other widely used deep learning architectures. To facilitate forecasting of the power consumption for the following day at each time step, the data is transformed into a daily frequency and a window size of 7 is utilized to observe each day in a week. The outcomes of the experiments are detailed in Table 1, which illustrates the performance of the models across varying epochs while maintaining a fixed cell size of 50 to prevent excessive model complexity.

Table 1. Univariate forecasting performance evaluation for hourly energy demand generation and weather dataset

Algorithm	RMSE 100 Epochs	RMSE 200 Epochs	RMSE 300 Epochs
Vanilla LSTM	2837.759	2801.604	2786.482
Stacked LSTM	2731.751	2761.259	2756.587
Bidirectional LSTM	2748.272	2720.271	2723.574
CNN-LSTM	2890.369	2823.410	2809.712
Encoder-Decoder LSTM	2865.107	2840.697	2828.476
Proposed Workflow	2591.870	2596.983	2593.754

Based on the experimental results, our proposed workflow demonstrates a performance improvement ranging roughly from 5% to 11% compared to other deep learning models for the energy demand forecasting task. This improvement in performance can be attributed to the workflow's ability to effectively capture both short-term and long-term dependencies present in the time series data. This feature allows the model to more accurately capture the intricate patterns and relationships that exist within the time series data. Figure 6 visually presents the comparison results, aiding in a better understanding of the obtained outcomes. Also note that, the proposed workflow requires less training time as compared to the others.

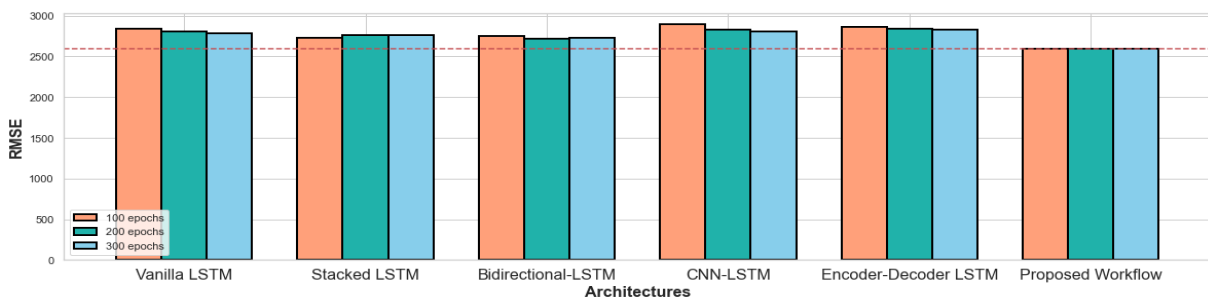


Figure 6. Encoder-decoder LSTM with attention

4.3. Performance Evaluation On Individual Household Electric Power Consumption Dataset

An individual household electric power consumption dataset is used as an another validation dataset. The objective of this task is to forecast power consumption by the household. The data is downsampled into daily frequency and the window size is selected as 7 to observe each day in a week to forecast next day in each time step. The findings are presented in Table 2. It presents the performance of the models for different epochs, while keeping the cell size fixed at 50, to avoid over-complicating the models.

Table 2. Univariate Forecasting Performance Evaluation For Individual Household Electric Power Consumption Dataset

Algorithm	RMSE 100 Epochs	RMSE 200 Epochs	RMSE 300 Epochs
Vanilla LSTM	385.547	397.571	398.474
Stacked LSTM	393.241	401.987	401.889
Bidirectional LSTM	401.517	403.587	402.481
CNN-LSTM	382.674	428.458	432.175
Encoder-Decoder LSTM	375.674	383.487	387.985
Proposed Workflow	366.781	378.284	389.425

Drawing upon the outcomes of the experiments, our proposed workflow demonstrates a performance improvement ranging from 2.4% to 9% compared to other deep learning models for the task of energy demand forecasting. Although the results seem to converge for the encoder-decoder LSTM and the proposed workflow after 300 epochs, the workflow managed to achieve better performance in earlier epochs. That is, the training time is reduced to 1/3, which is an important aspect in training deep learning models. This is because the workflow is designed to capture both the short-term and long-term dependencies of the time series data. It uses an encoder to extract features with dilated convolution from the input time series, the sequential correlation is learned by the LSTM architecture, the most important points of the hidden states are emphasized by the attention layer, and the decoder generates future time steps by mapping to the target time step. This allows the model to effectively capture the complex patterns and relationships in the time series data.

4.4. Performance Evaluation On Airline Passengers Dataset

In order to ensure that the results obtained from a given data analysis workflow can be generalized and applied to other domains, it is important to validate the workflow using widely accepted benchmark datasets. In this study, we used the airline passengers dataset as a benchmark dataset to validate the proposed workflow for time series analysis. The airline passengers dataset is a well-known and widely used benchmark dataset that has been used in many studies for comparing different time series analysis methods. By using this dataset to validate our workflow, we are able to demonstrate that our proposed method is competitive with other architectures that have been previously applied to this dataset. Table 3 displays the quantitative assessment of the performance in terms of root mean squared error based on different numbers of epochs.

Table 3. Univariate forecasting performance evaluation for airline passengers dataset

Algorithm	RMSE 100 Epochs	RMSE 200 Epochs	RMSE 300 Epochs
Vanilla LSTM	42.388	38.891	45.283
Stacked LSTM	44.477	44.941	46.307
Bidirectional LSTM	39.660	33.424	35.964
CNN-LSTM	58.529	51.606	46.432
Encoder-Decoder LSTM	37.819	41.692	44.946
Proposed Workflow	28.717	31.773	33.987

Considering results of our experiments, it appears that the proposed workflow outperforms commonly used deep learning architectures in terms of root mean squared error. The performance improvement is achieved with a range from 27% to 68%. This suggests that the proposed workflow may provide a more

effective approach for modeling the underlying structure of the data, particularly in capturing patterns over time and accounting for dependencies between different time steps or observations. In addition, we observed that increasing the epoch value beyond 200 tended to result in overfitting. This highlights the importance of carefully selecting hyperparameters in deep learning models to avoid overfitting and ensure generalizability.

4.5. Overall Performance Evaluation

The preceding sections entail an evaluation of the performance of the proposed attention-based workflow in comparison to other commonly used deep learning architectures for time series forecasting on each dataset separately. The aim of this section is to provide a comprehensive summary of the obtained results, which are exhibited in Figure 7, serving as a benchmark and facilitating a lucid depiction of the achieved outcomes. Benchmarks 1, 2, and 3 denote the performance evaluation of the hourly energy demand generation and weather dataset, individual household electric power consumption dataset, and airline passengers dataset respectively. The RMSE values in Table 1 and Table 2 are relatively high compared to Table 3 due to the larger sensor measurements. Conversely, Table 3 illustrates the deviation of passenger numbers from actual values, which are smaller in magnitude.

There are two major findings. First, our proposed workflow performs better for all three benchmarks. The average gains in performance are 8%, 5.5%, and 42% for benchmarks 1, 2, and 3, respectively. Second, our approach provides results independent of the dataset used. For instance, Bidirectional-LSTM works better on Benchmark 1 than Benchmark 3 while the situation is reversed for Encoder-Decoder-LSTM. While our approach did not exhibit a substantial improvement for some cases, e.g., Proposed Workflow vs. Encoder-Decoder LSTM in Benchmark 3, we showcased its adaptability to different domains, making it scalable and flexible. This underscores its potential utility in diverse industries and domains.

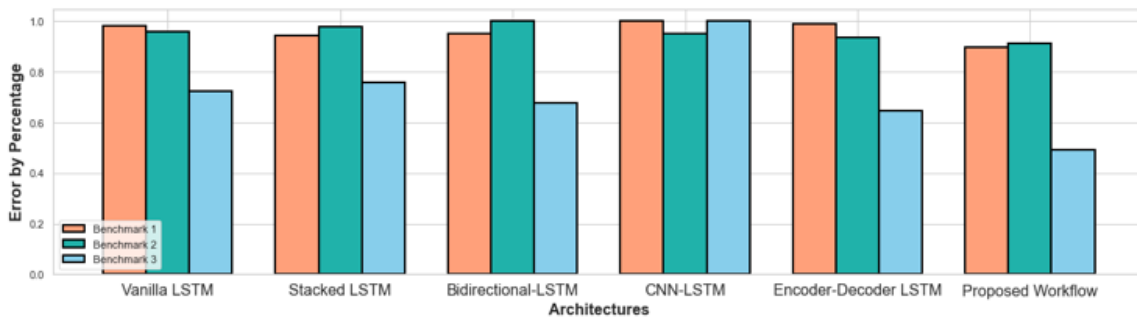


Figure 7. Encoder-decoder LSTM with attention

5. Conclusion

This study highlights the significance of accurate energy demand forecasting in the context of efficient electricity distribution management in smart grids. To this end, we collected and preprocessed a time series dataset of electricity consumption that is primarily associated with smart grid environments. In this research paper, we propose an attention-based time series workflow that integrates dilated convolution and attention mechanisms for time series forecasting in smart grid applications. The workflow employs dilated convolution to extract temporal features from the time series data and attention mechanism to selectively emphasize the significant temporal points in the hidden states. We subsequently evaluated several deep learning-based time series forecasting models and compared them with our proposed workflow. The experimental findings demonstrate that the proposed workflow shows promising results in smart grid domains and can achieve these results in a lower number of epochs, providing a shorter training time. Additionally, we tested our proposed workflow on a dataset from a different domain, i.e., the airline passenger dataset for forecasting customer numbers. The results indicate that the proposed workflow can be adaptable to different domains. Despite several challenges

that require future research attention, such as the scarcity of data and the necessity to optimize the model architecture and hyperparameters for varying datasets and forecasting horizons, this study contributes to the burgeoning literature on energy demand forecasting and establishes the groundwork for further research on deep learning-based techniques for smart grid applications.

6. Author Contribution Statement

Author 1 contributed to the writing of the original draft, methodology, visualization and experiments. Author 2, conceptualized the study and was involved in writing, reviewing and editing.

7. Ethics Committee Approval and Conflict of Interest

“There is no conflict of interest with any person/institution in the prepared article”

8. References

- [1] V. Kulkarni, S. K. Sahoo, S. B. Thanikanti, S. Velpula, and D. I. Rathod, "Power systems automation, communication, and information technologies for smart grid: A technical aspects review," *TELKOMNIKA (Telecommunication Computing Electronics and Control)*, vol. 19, no. 3, pp. 1017-1029, 2021.
- [2] A. H. Bagdadee, M. Aurangzeb, S. Ali, and L. Zhang, "Energy management for the industrial sector in smart grid system," *Ener. Repor.*, vol. 6, pp. 1432-1442, 2020.
- [3] M. S. Hossain, N. A. Madloul, N. A. Rahim, J. Selvaraj, A. K. Pandey, and A. F. Khan, "Role of smart grid in renewable energy: An overview," *Ren. and Sust. Ener. Rev.*, vol. 60, pp. 1168-1184, 2016.
- [4] S. Raghavendra, S. Neelakandan, M. Prakash, B. T. Geetha, S. M. R. Asha, and M. K. Roberts, "Artificial humming bird with data science enabled stability prediction model for smart grids," *Sust. Comp.: Infor. and Syst.*, vol. 36, p. 100821, 2022.
- [5] D. F. Costa Silva, A. R. Galvão Filho, R. V. Carvalho, F. de Souza L. Ribeiro, and C. J. Coelho, "Water flow forecasting based on river tributaries using long short-term memory ensemble model," *Ener.*, vol. 14, no. 22, pp. 7707, 2021.
- [6] Z. Chen, F. Xiao, F. Guo, and J. Yan, "Interpretable machine learning for building energy management: A state-of-the-art review," *Adv. in Appl. Ener.*, vol. 100123, 2023.
- [7] S. Dong, P. Wang, and K. Abbas, "A survey on deep learning and its applications," *Comp. Scie. Rev.*, vol. 40, p. 100379, 2021.
- [8] Y. Xu and L. Zhao, "Inception-LSTM Human Motion Recognition with Channel Attention Mechanism," *Comput. and Math. Meth. in Med.*, 2022.
- [9] J. Shi and Z. Wang, "A hybrid forecast model for household electric power by fusing landmark-based spectral clustering and deep learning," *Sust.*, vol. 14, no. 15, pp. 9255, 2022.
- [10] M. M. Keskin, F. İrim, O. Karaahmetoğlu, and E. Kaya, "Time series prediction with hierarchical recurrent model," *Sig., Ima. and Vid. Proce.*, vol. 17, no. 5, pp. 2121-2127, 2023.
- [11] I. S. Oh and J. S. Lee, "Dense sampling of time series for forecasting," *IEEE Acc.*, vol. 10, pp. 75571-75580, 2022.
- [12] G. Hebrail and A. Berard, "UCI machine learning repository: Individual household electric power consumption dataset," *EDF R&D*, vol. 30, no. 08, 2012.
- [13] G. Garnero and D. Godone, "Comparisons between different interpolation techniques," *The International Archives of the Photogr., Remote Sens. and Spatial Infor. Scien.*, vol. 40, pp. 139-144, 2014.
- [14] D. Garcia, "Robust smoothing of gridded data in one and higher dimensions with missing values," *Comp. Stat. & Data Analy.*, vol. 54, no. 4, pp. 1167-1178, 2010.
- [15] S. Hochreiter and J. Schmidhuber, "Long short-term memory," *Neural Comp.*, vol. 9, no. 8, pp. 1735-1780, 1997.

- [16] F. Yu and V. Koltun, "Multi-scale context aggregation by dilated convolutions," arXiv preprint arXiv:1511.07122, 2015.
- [17] R. Xi, M. Hou, M. Fu, H. Qu, and D. Liu, "Deep dilated convolution on multimodality time series for human activity recognition," in 2018 International Joint Conference on Neural Networks (IJCNN), pp. 1-8, July 2018.
- [18] A. Vaswani, N. Shazeer, N. Parmar, J. Uszkoreit, L. Jones, A. N. Gomez, and I. Polosukhin, "Attention is all you need," in Adv. in Neural Infor. Proce. Syst., vol. 30, 2017.
- [19] I. Sutskever, O. Vinyals, and Q. V. Le, "Sequence to sequence learning with neural networks," in Adv. in Neural Infor. Proce. Syst., vol. 27, 2014.
- [20] M. S. Ko, K. Lee, J. K. Kim, C. W. Hong, Z. Y. Dong, and K. Hur, "Deep concatenated residual network with bidirectional LSTM for one-hour-ahead wind power forecasting," IEEE Transac. on Sustain. Ener., vol. 12, no. 2, pp. 1321-1335, 2020.
- [21] A. V. Seliverstova, D. A. Pavlova, S. A. Tonoyan, and Y. E. Gapanyuk, "The time series forecasting of the company's electric power consumption," in Advances in Neural Computation, Machine Learning, and Cognitive Research II: Selected Papers from the XX International Conference on Neuroinformatics, October 8-12, 2018, Moscow, Russia, pp. 210-215, Springer International Publishing, 2019.
- [22] A. Shobol, M. H. Ali, M. Wadi, and M. R. TüR, "Overview of big data in smart grid," in Proc. 8th Intl. Conf. Renew. Energy Res. Appl. (ICRERA), pp. 1022-1025, 2019.
- [23] D. C. Sekhar, P. R. Rao, R. Kiranmayi, "Large Scale Predictive Analytics based Real-Time Energy Management and Enhance Power Quality in Smart Grid," in Proceedings of the 2022 IEEE 7th International Conference for Convergence in Technology (I2CT), Apr. 1-5, pp. 1-5, 2022.
- [24] F. Yu and V. Koltun, "Multi-scale context aggregation by dilated convolutions," arXiv preprint arXiv:1511.07122, 2015.
- [25] R. Xi, M. Hou, M. Fu, H. Qu, and D. Liu, "Deep dilated convolution on multimodality time series for human activity recognition," in 2018 International Joint Conference on Neural Networks (IJCNN), pp. 1-8, July 2018.
- [26] A. Vaswani, N. Shazeer, N. Parmar, J. Uszkoreit, L. Jones, A. N. Gomez, and I. Polosukhin, "Attention is all you need," in Adv. in Neural Inform. Proce. Syst., vol. 30, 2017.
- [27] I. Sutskever, O. Vinyals, and Q. V. Le, "Sequence to sequence learning with neural networks," in Adv. in Neural Infor. Proce. Syst., vol. 27, 2014.
- [28] M. S. Ko, K. Lee, J. K. Kim, C. W. Hong, Z. Y. Dong, and K. Hur, "Deep concatenated residual network with bidirectional LSTM for one-hour-ahead wind power forecasting," IEEE Transac. on Sustain. Ener., vol. 12, no. 2, pp. 1321-1335, 2020.



Bazalt Fiber ile Takviye Edilen Killerin Sıkıştırılabilirliği Üzerine Deneysel Bir Çalışma

Yasemin ASLAN TOPÇUOĞLU^{1*} , Zülfü GÜROCAK² 

^{1,2}Jeoloji Mühendisliği Bölümü, Mühendislik Fakültesi, Fırat Üniversitesi, Elazığ, Türkiye.

^{1*} yaslan@firat.edu.tr, ² zgurocak@firat.edu.tr

Geliş Tarihi: 15.02.2024
Kabul Tarihi: 14.04.2024

Düzeltilme Tarihi: 24.03.2024

doi: 10.62520/fujece.1436305
Araştırma Makalesi

Alıntı: Y. Aslan Topçuoğlu ve Z. Gürocağ, "Bazalt fiber ile takviye edilen killerin sıkıştırılabilirliği üzerine deneysel bir çalışma", Fırat Üni. Deny. ve Hes. Müh. Derg., vol. 3, no 3, pp. 241-254, Ekim 2024.

Öz

Geleneksel zemin iyileştirme yöntemlerine alternatif olarak ortaya çıkan ve farklı türdeki fiberler kullanılarak yapılan zemin güçlendirme çalışmalarında bazalt fiber kullanımı oldukça yaygın hale gelmiştir. Hammaddesi bazalt kayası olan bazalt fiber, yüksek dayanımlı, ekonomik, çevre dostu, doğal ve bol miktarda bulunması gibi özelliklerinden dolayı zemin güçlendirme çalışmalarında tercih edilmektedir. Bu çalışmada bazalt fiber takviyesinin yüksek plastisiteli bentonit kilinin sıkıştırılabilirliğine olan etkileri incelenmiştir. Bentonit kiline 24 mm uzunluğunda ve %0.5 ile %5.0 arasında farklı oranlarda bazalt fiber takviyesi yapılmış ve bu karışımlarda standard proktor deneyleri gerçekleştirilmiştir. Deneysel çalışmalar ile maksimum kuru yoğunluk (γ_{dmax}) ve optimum su içeriği (ω_{opt}) değerleri belirlenmiş ve bazalt fiber takviyesinin bu parametrelere olan etkileri değerlendirilmiştir. Deney sonuçlarına göre, %2.5 bazalt fiber takviye oranına kadar γ_{dmax} değerleri artmakta iken, ω_{opt} değerleri ise azalmıştır. Bazalt fiber oranının %2.5'dan daha fazla olduğu örneklerde ise γ_{dmax} değerleri azalmış, ω_{opt} değerleri ise artış göstermiştir. Elde edilen sonuçlar, bentonitin en iyi sıkıştırılabildiği bazalt fiber oranının %2.5 olduğunu ve bu orandan daha büyük oranlardaki bazalt fiber takviyesinin sıkıştırılabilirliği olumsuz yönde etkilediğini göstermiştir.

Anahtar kelimeler: Bazalt fiber, Bentonit kili, Güçlendirme, Sıkıştırılabilirlik

*Yazışılan yazar

İntihal Kontrol: Evet – Turnitin

Şikayet: fujece@firat.edu.tr

Telif Hakkı ve Lisans: Dergide yayın yapan yazarlar, CC BY-NC 4.0 kapsamında lisanslanan çalışmalarının telif hakkını saklı tutar.



An Experimental Study on the Compressibility of Clays Reinforced with Basalt Fiber

Yasemin ASLAN TOPÇUOĞLU^{1*} , Zülfü GÜROCAK² 

^{1,2}Department of Geological Engineering, Faculty of Engineering, Firat University, Elazığ, Türkiye.

^{1*}yaslan@firat.edu.tr, ²zgurocak@firat.edu.tr

Received: 15.02.2024

Accepted: 14.04.2024

Revision: 24.03.2024

doi: 10.62520/fujece.1436305

Research Article

Citation: Y. Aslan Topçuoğlu and Z. Gürocak, "An experimental study on the compressibility of clays reinforced with basalt fiber", *Firat Univ. Jour. of Exper. and Comp. Eng.*, vol. 3, no 3, pp. 241-254, October 2024.

Abstract

The use of basalt fiber has become quite common in soil reinforcement works, which emerged as an alternative to traditional soil improvement methods and are carried out using different types of fibers. Basalt fiber, whose raw material is basalt rock, is preferred in soil reinforcement works due to its features such as high strength, economical, environmentally friendly, natural and abundant. In this study, the effects of basalt fiber reinforcement on the compressibility of high plasticity bentonite clay were examined. Bentonite clay was reinforced with 24 mm long basalt fiber at different rates between 0.5% and 5.0%, and standard proctor tests were carried out on these mixtures. With experimental studies, maximum dry density (γ_{dmax}) and optimum water content (ω_{opt}) values were determined and the effects of basalt fiber reinforcement on these parameters were evaluated. According to the test results, while γ_{dmax} values increased up to 2.5% basalt fiber reinforcement ratio, ω_{opt} values decreased. In samples with basalt fiber ratio greater than 2.5%, γ_{dmax} values decreased and ω_{opt} values increased. The results obtained showed that the basalt fiber ratio at which bentonite can be compressed best is 2.5%, and basalt fiber reinforcement at rates greater than this ratio negatively affects the compressibility.

Keywords: Basalt fiber, Bentonite clay, Reinforcement, Compressibility

*Corresponding author

Plagiarism Checks: Yes – Turnitin

Complaints: fujece@firat.edu.tr

Copyright & License: Authors publishing with the journal retain the copyright to their work licensed under the CC BY-NC 4.0

1. Introduction

In engineering studies, when soil properties do not have the desired values, there are many methods used to improve these properties, and these methods vary depending on the type of project. While methods such as compaction, stone columns, drainage and pre-loading are mostly used in improvement works on soil foundation, chemical stabilization is the most preferred method in filled soils. However, in recent years, the use of fiber as an alternative to chemical stabilization has become widespread. The use of fibers, which have been used in many engineering fields for many years, is still very new in geotechnical studies.

Fibers, defined by Ekinçioğlu [1] as naturally occurring or artificially produced materials with higher strength and elasticity modulus than the material from which they are obtained, contain fewer structural errors than large mass structures because they are produced with a thin diameter. For this reason, the fiber form of the same material has superior mechanical properties [2]. Another type of artificial fibers, which are of many types such as glass, polyester, acrylic and carbon, and which are increasingly used today, is basalt fiber (BF). Its raw material is basalt rock, which is very common in volcanic areas. BFs, which are preferred due to their easy access and durability, attract attention due to their features such as being more economical and ecological, being naturally and abundantly found in nature, as well as having high strength and chemical resistance. The use of BFs in concrete production is older than its use in soil reinforcement works. Although there are many studies on the effects of BF on concrete, studies on the use of BF in different lengths and ratios in soil reinforcement studies, especially in different soil types, are not sufficient and new research is needed on this subject. Many of the studies on the use of BF in soil reinforcement studies aimed to determine the most effective BF length and ratio [3-13]. However, there are almost no studies investigating the effect of fibers on the compressibility of soils.

In the study conducted by Sabat [14] on this subject, polypropylene fiber was added to the soil stabilized with rice husk powder and lime and the change in soil properties was examined. The researcher revealed that the polypropylene fiber ratio decreased γ_{dmax} and increased the ω_{opt} value. Kulkarni and Patil [15] carried out a series of experiments using different proportions of slag and glass fibers of 6 mm and 12 mm length. It was determined that γ_{dmax} and California Bearing Rate (CBR) value for aqueous conditions increased as a result of mixing optimum proportions of slag and varying proportions of 6 mm and 12 mm glass fiber with the soil. According to the results of the research, 12 mm length fiber reinforcement showed better performance than 6 mm length fiber reinforcement. In his study, Baruah [16] added 10 mm length glass fiber to the soil at different rates (0.5, 1.0 and 1.5% by weight) and as a result of experimental studies, it was determined that the ω_{opt} and unconfined compressive strength values increased and the γ_{dmax} value decreased with the increasing fiber ratio. Balagoudra et al. [17] it was determined that the ω_{opt} value of the soil reinforced with 0.25%, 0.50, 0.75, 1.00% polypropylene fiber and 4% lime decreased until the 0.75% fiber ratio, and then the ω_{opt} value increased. Researchers stated that the γ_{dmax} value increased up to 0.75% fiber content and then decreased.

In their study, Aravalli et al. [18] used 12 mm long BF in the ratios of 0.15% and 0.25% as reinforcement in the soil and examined the changes in the index properties of the soil. Researchers found that as the BF ratio increases, the ω_{opt} value decreases and the γ_{dmax} value increases. In the research, it was stated that the high tensile strength of the fiber caused the fiber to elongate, and this elongation in the fiber caused the void ratio to decrease, the γ_{dmax} value to increase and the ω_{opt} value to decrease. Ayininuola & Balogun [19] used glass fiber as reinforcement in two different substrates at rates of 0.4, 0.8, 1.2, 1.6, 2.0, 2.5 and 3.0% by weight. According to the results of experimental studies, it was stated that γ_{dmax} and CBR values increased in both soils with the glass fiber additive. Pandit et al. [10] in their study where they used 12 mm long BF as reinforcement at 2, 4, 6 and 8% by weight, they determined that the γ_{dmax} value of samples with 4% BF reinforcement increased by 9.56% compared to the unreinforced soil, and the ω_{opt} value decreased by 41%. While the ω_{opt} value decreases up to 4% fiber content, γ_{dmax} increases. If the fiber ratio exceeds 4%, the ω_{opt} value increases and the γ_{dmax} value decreases.

According to the results of the study by Kale et al. [20], which used BF reinforcement at 1.5%, 3.0%, 4.5% and 6.0% in 12 mm, 18 mm and 24 mm lengths, the γ_{dmax} value of the soil increases up to 3% BF

ratio, while the ω_{opt} value decreases. Kehinde et al. [21] determined that γ_{dmax} values increased with increasing glass fiber ratio in two different soils and reached the maximum value at 0.6% fiber ratio. However, the researchers stated that γ_{dmax} values decreased when more fiber was used, and stated that the change in ω_{opt} value with fiber content is complex and difficult to interpret. They stated that the reason for this may be the swelling of the glass fiber as a result of the high degree of interaction of the glass fiber with water and the increase in volume, thus decreasing the density. In general, the researchers determined that glass fiber reinforcement affects the compression properties and an optimal fiber ratio should be determined for γ_{dmax} , and if this optimal ratio is exceeded, the density decreases due to fiber swelling.

In his study where Chaudhary [22] used BF as reinforcement at different rates (3, 6, 9, 12 and 15%), he stated that ω_{opt} values were not affected much by the BF ratio, but some increase was due to the moisture absorption feature of the fiber. In the study, it was stated that there was a slight decrease in γ_{dmax} values as the BF ratio increased. In the study conducted by Kambale and Rakkaraddi [23], glass, basalt and polypropylene fiber were used in varying amounts (0.5, 1 and 2%) on different soils. Especially with the increase of BF ratio, γ_{dmax} value first increased and then decreased. ω_{opt} values showed different changes, increasing and decreasing, depending on the increase in fiber ratio for different soil types. Al-Kaream et al. [24] used 0.5, 1.0 and 1.5% polypropylene fiber as reinforcement in clay soil. As a result of the research, it was determined that 1% polypropylene fiber reinforcement reduced the compressibility of the soil, and the specific gravity and γ_{dmax} values decreased with the increase in fiber ratio. At the same time, it was stated that the optimum water content values increased continuously with the increase in the polypropylene fiber ratio. Hamirani and Kumar [25] preferred polypropylene fiber as a reinforcement material in the soil at rates of 0.5, 1.0, 1.5 and 2.0% by dry weight. Researchers have determined that as the fiber ratio increases, the γ_{dmax} value decreases and the ω_{opt} value increases. Data obtained from studies conducted with fiber reinforcement in the literature are given in the Table 1.

In the studies summarized above, different fiber types were used on different soil types. In each study, different fiber ratios were determined and the effect of fiber reinforcement on soil properties was demonstrated. However, studies examining the effect of BF reinforcement on soil compressibility are quite limited. Therefore, it is important to examine the effects of BF reinforcement on the compressibility of clayey soils. When the literature is examined, 12 mm basalt fiber [10, 18] and mostly low plasticity clay [20, 22, 23] were used in the studies. However, in this study, 24 mm long BF and bentonite clay with very high plasticity (PI = 466%) were used and in this respect it differs from the literature. In this study, compaction experiments were carried out on samples prepared by adding 24 mm long BF to bentonite at rates of 0.5, 1.0, 1.5, 2.0, 2.5, 3.0, 3.5, 4.0, 4.5 and 5.0% by dry weight, and the effects of BF ratio on the compaction parameters of bentonite (γ_{dmax} and ω_{opt}) were examined.

Table 1. Fiber reinforcement and its effects on the soil in the literature

Researcher Researchers/	Soil type	Additive/Reinforcement type and rate	Fiber length (mm)	Effect on the soil
Sabat [14]	CH	RHA: 5, 10, 15, 20% L:1, 2, 3, 4, 5% PF: 0.5, 1, 1.5, 2%	12	With fiber reinforcement, γ_{dmax} decreased and ω_{opt} increased
Kulkarni and Patil [15]	CH	BFS: 5, 10, 15, 20, 25, 30% GF: 0.25, 0.50, 0.75, 1.00, 1.25%	6, 12	γ_{dmax} increased with fiber reinforcement
Baruah [16]	CL	GF: 0.5, 1.0, 1.5%	10	With increased fiber ratio, ω_{opt} increased and γ_{dmax} decreased
Balagoudra et al. [17]	C	PF: 0.25, 0.50, 0.75, 1% L: 4%	12	ω_{opt} decreased up to 0.75% fiber ratio and increased with increasing fiber content, γ_{dmax} increased up to 0.75% fiber ratio and decreased with increasing fiber content
Aravalli et al. [18]	CH	BF: 0.15, 0.20, 0.25%	12	As the fiber ratio increased, ω_{opt} decreased and γ_{dmax} increased.
Ayininuola and Balogun [19]	CL ML	GF: 0.4, 0.8, 1.2, 1.6, 2.0, 2.5, 3.0%	25	γ_{dmax} increased in both soils with fiber reinforcement
Pandit et al. [10]	CH	BF: 2, 4, 6, 8%	12	As the fiber ratio increased, ω_{opt} decreased and γ_{dmax} increased. As the fiber ratio increased from 4% to 8%, ω_{opt} increased and γ_{dmax} decreased.
Kale et al. [20]	C	BF: 1.5, 3.0, 4.5, 6.0%	12, 18, 24	Up to 3% fiber content, γ_{dmax} increased and ω_{opt} decreased
Kehinde et al. [21]	CL ML	GF: 0.5, 1, 1.5%	25	γ_{dmax} increased up to 0.6% fiber content and decreased with increasing fiber content. The change in ω_{opt} value with fiber addition is complex
Chaudhary [22]	CH	BF: 3, 6, 9, 12, 15%	13	ω_{opt} does not change much with fiber reinforcement, γ_{dmax} decreased as the fiber ratio increased.
Kambale and Rakkaraddi [23]	SC MH-OH CH	GF, BF, PF: 0.5, 1, 2%	12	As the basalt fiber ratio increased, the γ_{dmax} , first increased and then decreased. ω_{opt} showed different changes, increased and decreased depending on the increase in fiber ratio.
Al-Kaream et al. [24]	CL	PF: 0.5, 1, 1.5%	12	As the fiber ratio increased, γ_{dmax} decreased and ω_{opt} increased continuously.
Hamirani and Kumar [25]	C	PF: 0.5, 1, 1.5, 2%	-	As the fiber ratio increased, γ_{dmax} decreased and ω_{opt} increased
This Study	CH	BF: 0.5, 1, 1.5, 2, 2.5, 3, 3.5, 4, 4.5, 5%	24	γ_{dmax} increased up to 2.5% BF ratio, decreased with increasing fiber content, ω_{opt} decreased up to 2.5% BF ratio, increases with increasing fiber content

RHA: Rice Husk Ash, L: Lime, PF: Polypropylene Fiber, BFS: Blast Furnace Slag, GF: Glass Fiber; BF: Basalt Fiber, C: Clay
ML: Low plasticity silt, CL: Low plasticity clay, CH: High plasticity clay, SC: Clay sand, OH: High plasticity organic clays and silts,
MH: High plasticity inorganic silts and clayey silts

2. Material

2.1. Properties of bentonite clay and basalt fiber

Bentonite is a clay used in many different areas such as mining, industry, agriculture and engineering. It is formed as a result of the chemical decomposition of volcanic ash, tuff and lava, which predominantly contain montmorillonite and are rich in aluminum and magnesium. Na - bentonite, which has three different types of bentonites: Ca-bentonite, Na - bentonite and Na - Ca-bentonite, has a high swelling capacity. The general chemical formula of bentonite is; $(\text{Na}, \text{Ca}) (\text{Al}, \text{Mg})_6 (\text{Si}_4\text{O}_{10})_3 (\text{OH})_6 n\text{H}_2\text{O}$ [26]. In this study, the chemical and engineering properties of bentonite clay (Figure 1) obtained from the Tokat - Reşadiye clay quarry were determined by Aslan Topçuoğlu [27] and presented in Table 2.

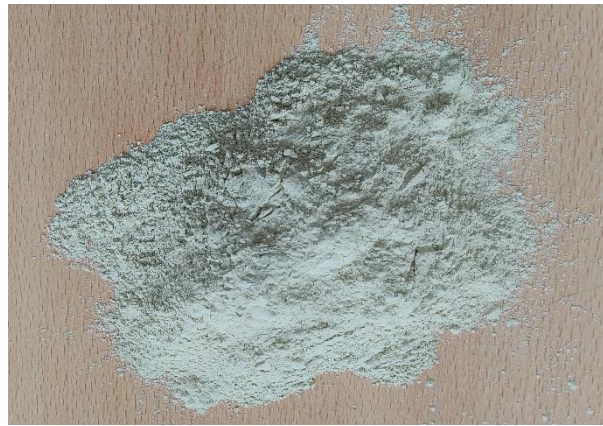


Figure 1. Bentonite clay used in the study

Table 2. Chemical and geotechnical properties of the clay used in the study [27]

Main Oxides (%)	Value
SiO ₂	62.50
Al ₂ O ₃	17.60
Fe ₂ O ₃	3.63
CaO	2.86
Na ₂ O	2.58
K ₂ O	0.92
TiO ₂	0.32
SO ₃	0.076
Cr ₂ O ₃	<0.01
Loss on ignition	6.60
Bentonite Type	Na - Bentonite
Liquid Limit (LL, %)	507
Plastic Limit (PL, %)	41
Plasticity Index (PI, %)	466
Soil Class (USCS)	CH

The raw material of BF used as reinforcement material in this study was basalt and this rock was an important natural building material that has been used throughout human history. Basalt, which is a dark-colored, fine-grained rock type formed by the cooling of lava erupted as a result of volcanism, melts when heated like hard, dense, thermo-plastic materials [28]. Basalt which is the raw material of BF, is an important raw material due to its wide distribution in volcanic regions and easy accessibility. Basalt rock is melted into fibers by centrifugal blowing at temperatures above 1500°C to form fibers with a diameter of 7 - 13 µm and a length of 60 - 100 mm [29]. BFs attract attention due to their high strength and corrosion resistance, resistance to high temperatures and easy processing. BF has low

density, is cheaper than carbon fiber and has higher strength than glass fiber [30]. With these properties, BF is used in many areas such as construction, automotive and electronics. The BF used in this study has a length of 24 mm (Figure 2) and physical and mechanical properties are given in Table 3.



Figure 2. BF used in the study

Table 3. Mechanical and physical properties of BF used in the study

Feature	Value
Length fiber (mm)	24
Diameter of monofilament (μm)	$15 \pm 1,5$
Humidity, Max (%)	2
Modulus of elasticity (GPa)	90
Tensile strength (MPa)	3000
Thermal conductivity (W/mK)	0.031- 0.038
Elongation at break (%)	3.5
Density (gr/cm^3)	2.63

2.2. Method

2.2.1. Sample preparation and experimental studies

Bentonite clay (BC) obtained from Tokat – Reşadiye (Turkey) clay quarry was dried in an oven at 105 °C for 24 hours and BF purchased from a commercial company was separated with the help of a compressor (Figure 3a). Then 0.5, 1.0, 1.5, 2.0, 2.5, 3.0, 3.5, 4.0, 4.5 and 5.0% by weight BF was added to bentonite and mixed by hand and mixer for 10 minutes to prepare mixture samples (Figure 3b). Standard proctor tests were performed on each mixture and the ω_{opt} and γ_{dmax} values of the unreinforced and BF reinforced samples were determined. Table 4 shows the BC and BF ratios of the mixtures prepared for the standard proctor tests.



Figure 3. Separated BF used in the study (a) and preparation of mixtures (b)

Table 4. BC and BF ratios used in proctor experiments

Sample Number	BC (%)	BF (%)
BC	100	0.0
BC + 0.5% BF	99.5	0.5
BC + 1.0% BF	99.0	1.0
BC + 1.5% BF	98.5	1.5
BC + 2.0% BF	98.0	2.0
BC + 2.5% BF	97.5	2.5
BC + 3.0% BF	97.0	3.0
BC + 3.5% BF	96.5	3.5
BC + 4.0% BF	96.0	4.0
BC + 4.5% BF	95.5	4.5
BC + 5.0% BF	95.0	5.0

BC: Bentonite Clay, BF: Basalt fiber

2.2.2. Standard proctor experiments

The standard proctor test is performed to determine the compressibility properties of soils at different water contents and the compaction parameters ω_{opt} and γ_{dmax} . The test is carried out by compressing the soil into the mold in three layers under a load of 2.5 kg, which is allowed to free fall from a height of 30.5 cm. In this study, a total of 55 standard proctor tests were performed on both unreinforced bentonite and 10 mixtures reinforced with BF according to ASTM D698-12e2 [31] standard (Figure 4a, b). The experiments were carried out at the Rock-Soil Mechanics Laboratory, Department of Geological Engineering, Firat University and the results of the standard proctor tests are presented in Table 5. γ - ω curves of all samples are shown in Figure 5.

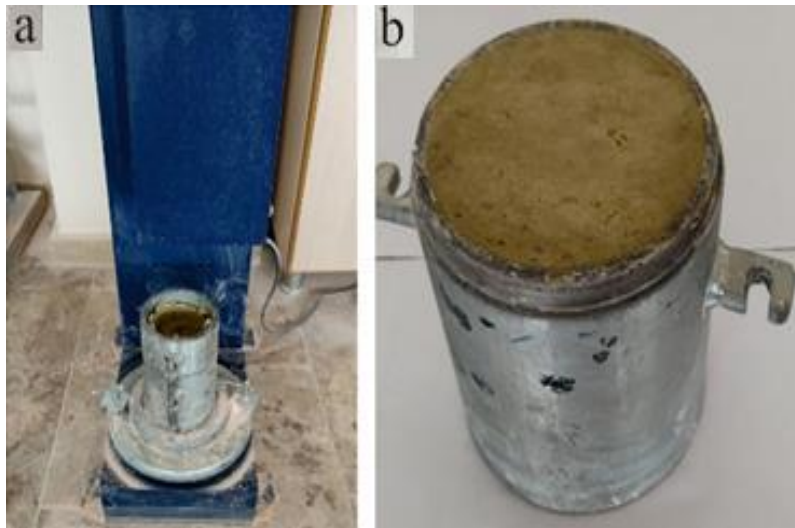


Figure 4. Compressing the sample in the proctor mold (a) and compressed sample (b)

Table 5. γ_{dmax} and ω_{opt} values of unreinforced and reinforced clay samples

Sample	γ_{dmax} (kN/m ³)	ω_{opt} (%)
BC	12.36	38.50
BC + 0.5% BF	12.51	38.40
BC + 1.0% BF	12.60	38.32
BC + 1.5% BF	12.71	38.10
BC + 2.0% BF	12.84	37.50
BC + 2.5% BF	12.91	37.00
BC + 3.0% BF	12.78	37.10
BC + 3.5% BF	12.61	37.25
BC + 4.0% BF	12.48	38.12
BC + 4.5% BF	12.22	38.85
BC + 5.0% BF	11.90	39.00

BC: Bentonite clay, BF: Basalt fiber

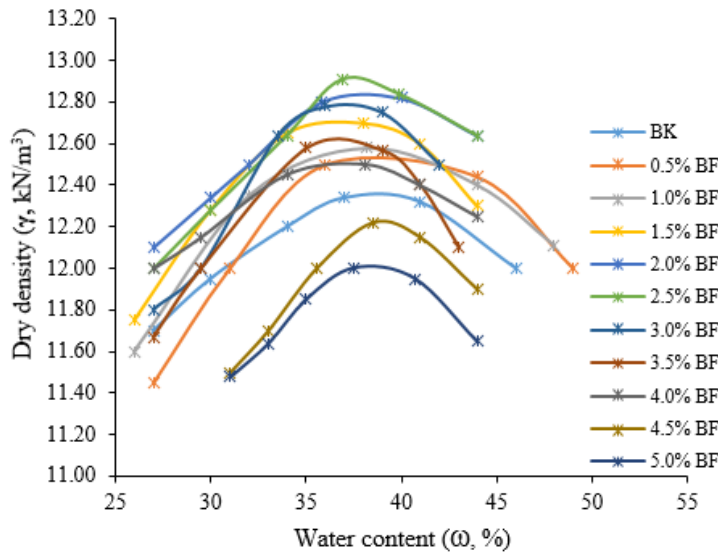


Figure 5. γ - ω curves of all samples

3. Findings and Discussion

According to the results obtained in the experimental studies, the γ_{dmax} value of unreinforced bentonite was 12.36 kN/m³ and the ω_{opt} value was 38.50%. The γ_{dmax} values of BF reinforced mixtures vary between 11.90 - 12.91 kN/m³. There was an increase in γ_{dmax} values up to 2.5% BF ratio and γ_{dmax} value reached 12.91 kN/m³ in the BC + 2.5% BF sample. However, as the BF ratio exceeded 2.5%, γ_{dmax} values started to decrease and γ_{dmax} value decreased to 11.90 kN/m³ in the BC + 5.0% BF sample. This value was even lower than the γ_{dmax} value of unreinforced bentonite (Figure 6). The ω_{opt} values of BF reinforced samples ranged between 37.00% and 39.00%. The minimum ω_{opt} value was determined in the BC + 2.5% BF sample and the maximum ω_{opt} value was found in the BC + 5.0% BF sample. Depending on the increase in BF ratio, it was observed that the ω_{opt} values first decreased until 2.5% BF ratio and then increased with increasing fiber ratio (Figure 7).

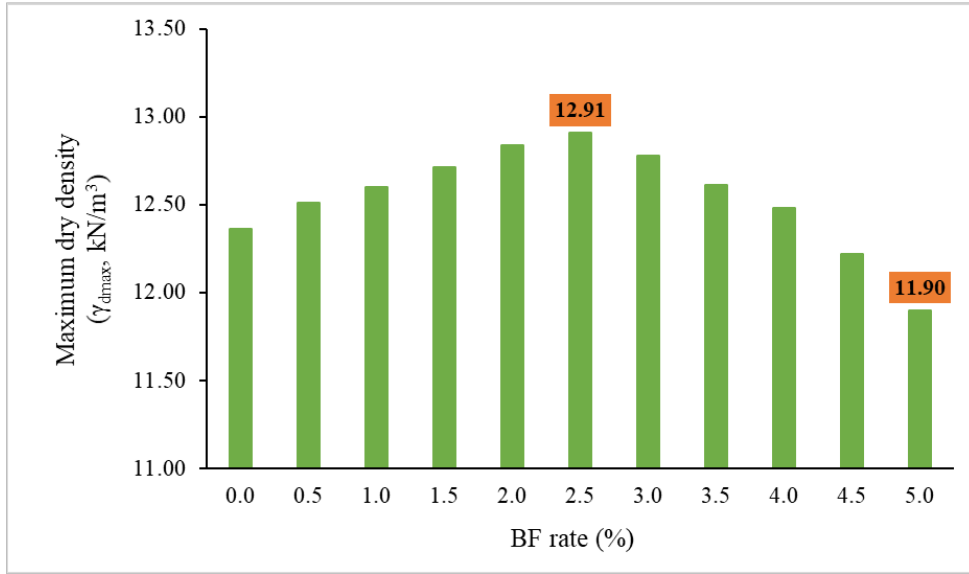


Figure 6. BF ratio - γ_{dmax} change graph

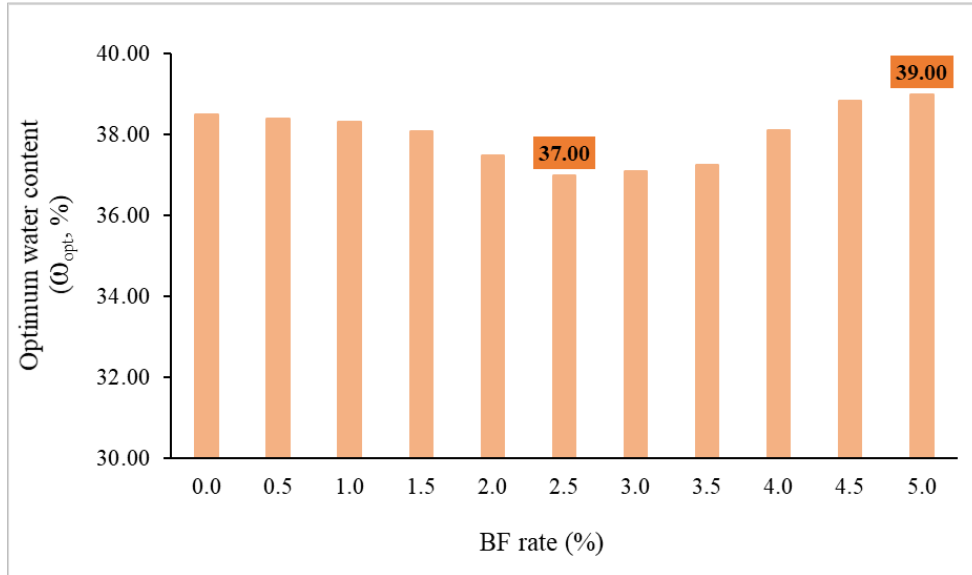


Figure 7. BF ratio - ω_{opt} change graph

When the rates of change in the γ_{dmax} values of the reinforced clay samples compared to the unreinforced clay sample (Table 6), it was determined that the rate of increase in the γ_{dmax} value of the sample reinforced with 2.5% BF was 4.45%, the rate of increase in the γ_{dmax} values decreased with the increase in the BF ratio, and even in the BC + 4.5% BF and the BC + 5.0% BF samples, there was a decrease of 1.13% and 3.72% (Table 6, Figure 8).

Table 6. % γ_{dmax} and % ω_{opt} changes of reinforced samples compared to unreinforced clay

Sample Number	γ_{dmax} (% change)	ω_{opt} (% change)
BC	-	-
BC + 0.5% BF	1.21	-0.26
BC + 1.0% BF	1.94	-0.47
BC + 1.5% BF	2.83	-1.04
BC + 2.0% BF	3.88	-2.60
BC + 2.5% BF	4.45	-3.90
BC + 3.0% BF	3.40	-3.64
BC + 3.5% BF	2.02	-3.25
BC + 4.0% BF	0.97	-0.99
BC + 4.5% BF	-1.13	0.91
BC + 5.0% BF	-3.72	1.30

BC: Bentonite clay, BF: Basalt fiber
 (-) shows decreasing values

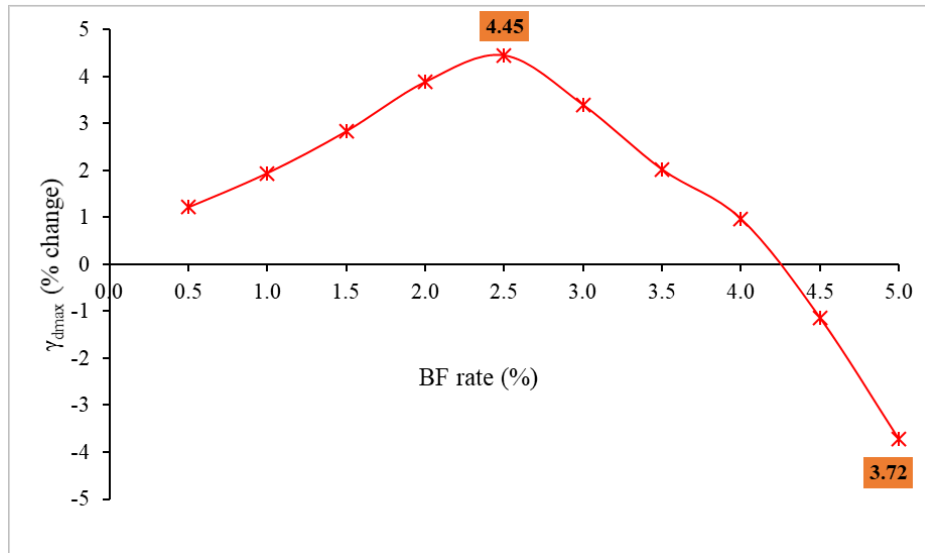


Figure 8. BF ratio - % γ_{dmax} change graph

When the rates of change in the ω_{opt} values of BF reinforced samples were examined (Table 6); a decrease rate of approximately 4% was observed in the the BC + 2.5% BF sample. This rate of decrease depending on the BF additive ratio gradually decreased with the increase in BF ratio, and there was a small increase of 0.91% and 1.30% in BC + 4.5% BF and BC + 5.0% BF samples (Table 6, Figure 9).

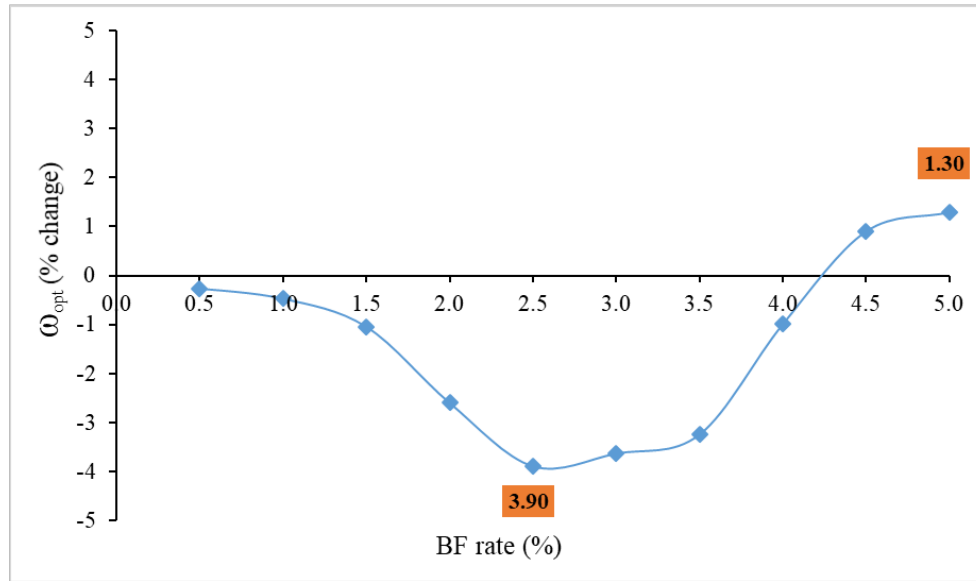


Figure 9. BF ratio - % ω_{opt} change graph

The results obtained from this study were compared with the results in the literature and the results were found to be compatible. In studies conducted by various researchers such as [10, 17-21] it was stated that γ_{dmax} values increase and ω_{opt} values decrease as the fiber ratio increases for different soil and fiber types. Especially in some studies [17, 21], it was specified that the γ_{dmax} value increases up to a certain fiber ratio, that was, up to a peak value, and decreases with further increasing fiber ratio. In the same studies, it was indicated that ω_{opt} values decrease up to a peak fiber ratio and increase with increasing fiber ratio. Aravalli et al. [18] attributed the increase in γ_{dmax} value and decrease in ω_{opt} value to the elongation of the fiber due to the high tensile strength of the fiber and this elongation causes a decrease in the void ratio. The increase in ω_{opt} value with increasing fiber ratio was associated with the water absorption feature of the fiber by Chaudhary [22]. On the other hand, Kehinde et al. [21] stated that due to the high chemical interaction of glass fiber with water at increasing fiber ratios, excess fiber swells and causes volume increase, thus decreasing the density. Ayininuola and Balogun [19], on the other hand, stated that the fiber contribution contributes to holding the soil particles together and thus the bond force between the soil particles develops, arguing that the increase in γ_{dmax} values up to a certain BF ratio was related to this bond force. Considering the information in the literature, it can be said that when the fiber ratio was very high, light fibers replace heavy fibers, thus γ_{dmax} decreases, and ω_{opt} value increases due to the water absorption feature of the fiber. Consistent with the literature, in this study, if more than 2.5% BF was used, ω_{opt} values increased due to the water absorption feature of the fiber. Since the fiber additive contributes to holding the soil particles together, if a low amount of fiber was used, these forces will be very weak and γ_{dmax} values decrease. Additionally, if the optimum fiber ratio was more than 2.5%, the fiber will not be distributed homogeneously in the soil and γ_{dmax} values will decrease as fiber clusters/clumps will occur. As a matter of fact, in this study, there was a decrease in γ_{dmax} values after 2.5% BF rate. This can be explained by the fact that the fibers increase in volume by absorbing high amounts of water, the fibers replace the heavier soil grains, and the increasing fiber ratio in the soil matrix creates resistance to compression. Thus, compressibility becomes difficult. When the results of this study investigating the effect of BF reinforcement on the compressibility of bentonite clay were evaluated on the basis of the literature, it can be said that up to a certain BF ratio, γ_{dmax} values increase and the soil gains a better compressibility due to the increased integration between the fibers and the soil grains and the improved bond forces.

4. Conclusions

In this study, the effects of BF reinforcement on the compressibility of bentonite were investigated. The γ_{dmax} value of unreinforced bentonite is 12.36 kN/m³ and the ω_{opt} value is 38.50%. With BF reinforcement of bentonite, γ_{dmax} values increased and reached 12.91 kN/m³ in the BC + 2.5% BF sample. However, γ_{dmax} values decreased at BF ratios above 2.5%. Depending on the increase in BF ratio, ω_{opt} values decreased up to 2.5% BF reinforcement ratio, and ω_{opt} values increased with BF ratio exceeding 2.5%. With the BF reinforcement used at different rates in bentonite, which is a clay with a length of 24 mm and very high plasticity, 2.5% BF was determined as the optimum value. Thus, it can be said that the BF reinforcement ratio where the best compressibility for bentonite occurs is 2.5% and the compressibility of the soil decreases after this BF ratio. Significant increases in soil strength occur by reinforcing at the optimum fiber ratio determined in current studies. This situation has been clearly stated in similar studies [3 - 7, 11 - 13]. When the optimum BF ratio is used, the ground becomes more durable and less deformable. The results obtained from this study showed that when BF reinforced soils are used as backfill, not only the effect of BF reinforcement on strength but also its effect on compressibility should be considered when determining the BF reinforcement ratio.

5. Author Contribution Statement

There is no conflict of interest with any person/institution in the prepared article. YAT and ZG prepared the study concept and design, performed the experiments, and analysed and interpreted the data.

6. Ethics Committee Approval and Conflict of Interest

There is no need for an ethics committee approval in the prepared article. There is no conflict of interest with any person/institution in the prepared article

7. References

- [1] Ö. Ekincioglu, "Mechanical behavior of cement based composites reinforced with hybrid fibres-an optimum design", Istanbul Technical University Institute of Science and Technology, 2003.
- [2] D. Asi, "Cam elyaf katkılı kompozit malzemelerin aşınma performansının incelenmesi", Yüksek Lisans Tezi, Afyon Kocatepe Üniversitesi Fen Bilimleri Enstitüsü, Afyon, 2008.
- [3] L. Gao, G. Hu, N. Xu, J. Fu, C. Xiang and C. Yang, "Experimental study on unconfined compressive strength of basalt fiber reinforced clay soil", *Adva. in Mat. Scie. and Engin.*, pp. 1-8, 2015.
- [4] C.P. Ndepete and S. Sert, "Use of basalt fibers for soil improvement", *Acta Phys. Polon.*, vol. 130, no. 1, pp. 355-356, 2016.
- [5] T. Özdemir, G.E. Polat, O. Azdeniz, A. Boz and A. Sezer, "Bazalt fiber ve kireç ile güçlendirilmiş kil zeminin dayanım özellikleri", 2016.
- [6] W. Yixian, G. Panpan, S. Shengbiao, Y. Haiping and Y. Binxiang, "Study on strength influence mechanism of fiber-reinforced expansive soil using jute", *Geotech. and Geol. Engin.*, vol. 34, pp. 1079-1088, 2016.
- [7] P.G. Gisymol and K. Ramya, "A study on the effect of basalt fiber in organic soil", *IOSR Jour. of Mech. and Civil Eng. (IOSR-JMCE)*, vol. 14, no. 4, pp. 13-17, 2017.
- [8] A. Boz, A. Sezer, T. Özdemir, G.E. Hızal and O. Azdeniz Dolmacı, "Mechanical properties of lime-treated clay reinforced with different types of randomly distributed fibers", *Arab. Jour. of Geosc.*, vol. 11, no. 6, pp. 122, 2018.
- [9] A. Kenan and A. Özocak, "Effect of basalt fiber addition on shear strength of silty soils", *International Symposium on Natural Hazards and Disaster Management*, pp. 918-924, 2018.
- [10] V.M. Pandit, C. Rohit, K. Tushar, C. Ayushi, G. Bhushan and C. Deepali, "Study of basalt fiber on compaction characteristics of black cotton soil", *6th International Conference on Recent Trends in Engineering & Technology (ICRTET)*, pp. 850-853, 2018.

- [11] A. Sungur, M.F. Yazıcı and S.N. Keskin, “Experimental research on the engineering properties of basalt fiber reinforced clayey soil”, *Europ. Jour. of Sc. and Techn. Spec. Issue*, vol. 28, pp. 895-899, 2021.
- [12] Z. Gürocak and Y. Aslan Topçuoğlu, “The effect of basalt fiber use on the unconfined compressive strength of low plasticity clay”, **Gümüşhane Uni. Jour. of Sci.e and Techno.*, vol. 13, no. 3, pp. 688-701, 2023.
- [13] Y. Aslan Topçuoğlu and Z. Gürocak, “Determination of the optimum basalt fiber ratio for maximum strength in sodium bentonite clay reinforcement”, *Dicle Uni. Jour. of Eng.*, vol. 14, no. 3, pp. 479-487, 2023.
- [14] A.K. Sabat, “Effect of polypropylene fiber on engineering properties of rice husk ash-lime stabilised expansive soil”, **EJGE**, vol. 17, 2012.
- [15] V.R. Kulkarni and G.K. Patil, “Experimental study of stabilization of BC soil by using slag and glass fibers”, **Jour. of Civil Eng. and Envir. Tech.*, vol. 1, no. 2, pp. 107-112, 2014.
- [16] H. Baruah, “Effect of glass fiber on red soil”, *Intern. Jour. of Adv. Techn. in Eng. and Sci.*, vol. 3, no. 1, pp. 217-223, 2015.
- [17] R.S. Balagoudra, V. Krishna, H.S. Yaligar, T. Jayasurya and G.C. Shwetha, “Soil stabilization using lime and polypropylene fiber material”, *Intern. Jour. of Eng. Sci.e and Comp.*, vol. 7, no. 5, 2017.
- [18] A.B. Aravalli, A.M. Hulagabali, C.H. Solanki and G.R. Dodagoudar, “Enhancement of index and engineering properties of expansive soil using chopped basalt fibers”, 2017.
- [19] G.M. Ayininuola and L.O. Balogun, “Investigation of glass fiber potential in soil stabilization”, **Internat. Jour. of Eng. and Adv. Techn.*, vol. 7, no. 5, 2018.
- [20] R.Y. Kale, N.D. Dahake, S.M. Sahu, G.A. Gawande, P.J. Wailker, V.R. Patekar and C.R. Pawar, “Soil stabilization by using basalt fibers”, *Intern. Jour. of Sci. Res.& Eng. Tren.*, vol. 6, no. 3, pp. 1931-1935, 2020.
- [21] A.S. Kehinde, I.E. Igbokwe, J.E. Okon and B.E. Koku-Ojumu, “Geotechnical properties of lateritic soil stabilized with glass fiber”, *Intern. Jour. of Eng. Res. & Tech.*, vol. 9, no. 9, pp. 1078-1081, 2020.
- [22] R. Chaudhary, “Enhancing the properties of soil by stabilization technique using basalt fiber”, *Civil Engineering Department, Delhi Technological University*, 2021.
- [23] N. Kambale and P.G. Rakkaraddi, “Comparative study of soil stabilization with addition of glass, basalt and polypropylene fibres”, *Internat. Jour. of Creat. Res. Thoug. (IJCRT)**, vol. 10, no. 9, pp. b674-b681, 2022.
- [24] K.W.A. Al-Kaream, M.Y. Fattah and M.K. Hameedi, “Compressibility and strength development of soft soil by polypropylene fiber”, *Internat. Jour. of GEOMATE*, vol. 22, no. 93, pp. 91-97, 2022.
- [25] S.N. Hamirani and A. Kumar, “Effects of polypropylene fibers on soil reinforcement”, *Intern. Res. Jour. of Moder. in Eng. Tech. and Sci.*, vol. 4, no. 12, 2022.
- [26] MTA-Maden Tetkik Arama, **https://www.mta.gov.tr/v3.0/sayfalar/bilgi-merkezi/maden-serisi/img/kaolen.pdf**, 2023.
- [27] Y. A. Topçuoğlu, “The effect of different additive materials on the engineering properties of soils”, *PhD Thesis, Firat University, Elazığ, Türkiye*, 2020.
- [28] H. Jamshaid and R. Mishra, “A green material from rock: basalt fiber-a review”, *The Jour. of the Textile Instit.*, vol. 107, no. 7, pp. 923-937, 2015.
- [29] T. Czigany, J. Vad and K. Poloskei, “Basalt fiber as a reinforcement of polymer composites”, *Period. Polyt. of Mech. Eng.*, vol. 49, pp. 3-14, 2005.
- [30] K. Singha, “A short review on basalt fiber”, **Intern. Jour. of Text. Sci.*, vol. 1, no. 4, pp. 19-28, 2012.
- [31] ASTM D698-12e2, “Standard test methods for laboratory compaction characteristics of soil using standard effort”, *ASTM International, West Conshohocken, PA*, 2012.



Farklı Coğrafyalardan Elde Edilen Verilerle Yol Hasarlarının Makine Öğrenmesi Yöntemleri Kullanılarak Tespiti: Türkiye Üzerine Bir İnceleme

Ahmet Cihangir KAVCI^{1*} , Ömer Faruk CANSIZ² 

^{1,2}İnşaat Mühendisliği Bölümü, Mühendislik ve Doğa Bilimleri Fakültesi, İskenderun Teknik Üniversitesi, Hatay, Türkiye.
¹acihangirkvc@gmail.com, ²ofaruk.cansiz@iste.edu.tr

Geliş Tarihi: 17.01.2024
Kabul Tarihi: 24.04.2024

Düzeltilme Tarihi: 12.03.2024

doi: 10.62520/fujece.1421398
Araştırma Makalesi

Alıntı: A.C. Kavcı, Ö. F. Cansız, "Farklı coğrafyalardan elde edilen verilerle yol hasarlarının makine öğrenmesi yöntemleri kullanılarak tespiti: Türkiye üzerine bir inceleme", Fırat Üni. Deny. ve Hes. Müh. Derg., vol. 3, no 3, pp. 255-270, Ekim 2024.

Öz

Karayolu hasarı, özellikle sürücülerin konforunu ve güvenliğini ciddi şekilde etkilemektedir. Yollardaki hasarların tespiti, sadece ulaşım güvenliği açısından değil, aynı zamanda maliyet açısından da büyük önem taşımaktadır. Yol hasarlarının tespiti, erken müdahale ve onarımı sağlamak açısından kritik öneme sahiptir. Bu çalışmada, YOLO (You Only Look Once) v8 algoritmasının yol hasar tespit performansı, Çekya-Türkiye, Hindistan-Türkiye, ABD-Türkiye ve Japonya-Türkiye dahil olmak üzere farklı coğrafyalardan elde edilen veri setleri kullanılarak değerlendirildi. Bulgular, algoritmanın hasar tespit konusundaki yeteneklerini ve belirli hasar türlerini ayırt etmede karşılaştığı zorlukları ortaya koydu. Türkiye veri setinin oluşturulması için Hatay ilindeki yolların görüntüleri kaydedildi. Bu görüntüler, Microsoft'un VoTT uygulaması kullanılarak etiketlendi. Geliştirilen modeller arasında karşılaştırmalar ve değerlendirmeler yapıldı. Bu modeller arasında en iyi sonuçları Japonya-Türkiye modeli, 0.55 mAP ve 0.54 F1 skoru ile verdi. Modellerin sonuçları, hasarın görünümünün coğrafi konuma ve yol verilerinin kalitesine göre değiştiğini gösterdi. Yerel görüntülerden ve belirsiz hasar türlerinden oluşan verilerin eğitimde önemli olduğu gözlemlendi.

Anahtar kelimeler: Yol hasar tespiti, YOLO algoritması, Makine öğrenmesi, Nesne tespiti, RDD2022

*Yazışılan yazar

İntihal Kontrol: Evet – Turnitin
Şikayet: fujece@firat.edu.tr

Telif Hakkı ve Lisans: Dergide yayın yapan yazarlar, CC BY-NC 4.0 kapsamında lisanslanan çalışmalarının telif hakkını saklı tutar.



Detection of Road Damages Using Machine Learning Methods with Data Collected from Various Geographies: A Study on Türkiye

Ahmet Cihangir KAVCI ^{1*} , Ömer Faruk CANSIZ ² 

^{1,2}Civil Engineering Department, Engineering and Natural Sciences Faculty, İskenderun Technical University, Hatay, Türkiye.

¹acihangirkvc@gmail.com, ²ofaruk.cansiz@iste.edu.tr

Received: 17.01.2024
Accepted: 24.04.2024

Revision: 12.03.2024

doi: 10.62520/fujece.1421398
Research Article

Citation: A.C. Kavcı, Ö. F. Cansız, “Detection of road damages using machine learning methods with data collected from various geographies: a study on Türkiye”, Fırat Univ. Jour.of Exper. and Comp. Eng., vol. 3, no 3, pp. 255-270, October 2024.

Abstract

Road damage seriously affects the comfort and safety of drivers. The detection of road damage is of great importance not only for transportation safety, but also in terms of cost. The detection of road damage is critical for enabling early intervention and repair. In this study, the road damage detection performance of the YOLO (You Only Look Once) v8 algorithm was evaluated using datasets obtained from different geographies, including Czechia -Türkiye, India-Türkiye, USA-Türkiye, and Japan-Türkiye. The findings revealed both the capabilities of the algorithm in damage detection and the challenges it faced in distinguishing certain types of damage. For the creation of the Türkiye dataset, images of roads in the province of Hatay were recorded. These images were labeled using Microsoft's VoTT application. Comparisons and evaluations were made among the developed models. Among these models, the Japan-Türkiye model yielded the best results with a 0.55 mAP and 0.54 F1 score. The results of the models indicated that the appearance of damage varies according to the geographical location and the quality of road data. It was observed that data consisting of local images and uncertain damage types were important in training.

Keywords: Road damage detection, YOLO algorithm, Machine learning, Object detection, RDD2022

*Corresponding author

1. Introduction

Currently, monitoring and maintenance of road infrastructure are largely conducted through physical observations. However, this method not only leads to delays in identifying damages, but is also notably time-consuming. Manual road surveillance faces challenges in keeping pace with the rapid deterioration of roads due to factors such as rising traffic density, environmental effects, and wear over time. In Türkiye, there has been a significant rise in the number of vehicles over the years due to an increasing population and per capita gross national income. In Figure 1, the red-colored histogram depicts the country's population, while the black line demonstrates the number of vehicles.

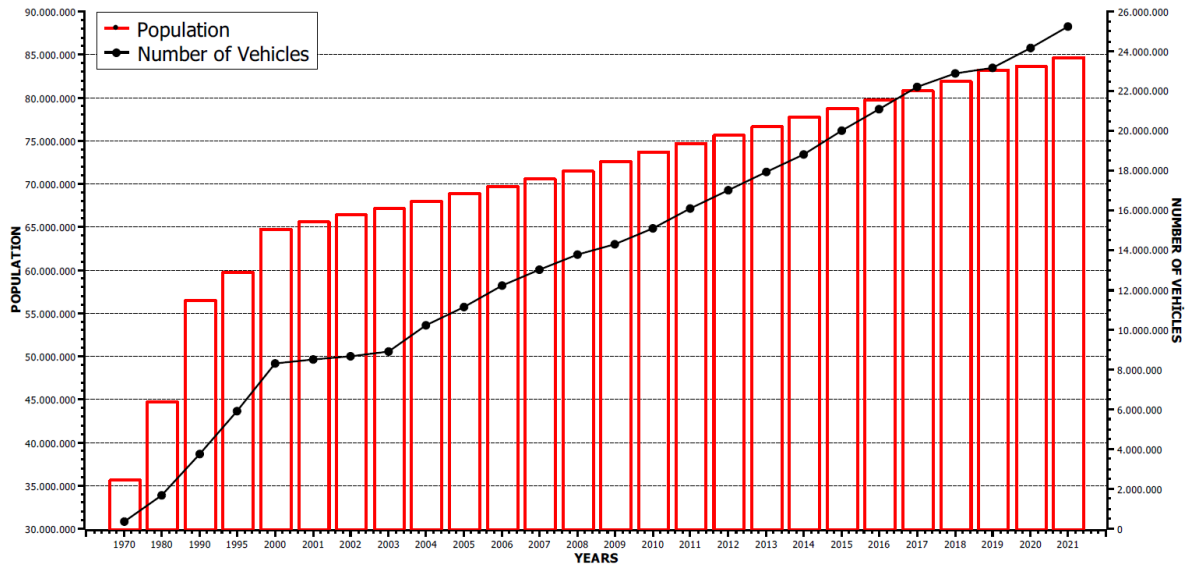


Figure 1. Distribution of population and number of vehicles in Türkiye by years [1]

Concomitant with the increase in the number of vehicles, as seen in Figure 2, road networks have undergone expansion and their quality has been enhanced. In Figure 2, the line graphs depict different types of roads; in particular, the augmentation in bituminous roads, represented by red and black, has elevated the significance of road maintenance and administration. To administer the expanding road networks, the highways within the country have been segmented into regions, and these regions further subdivided into administrative units.

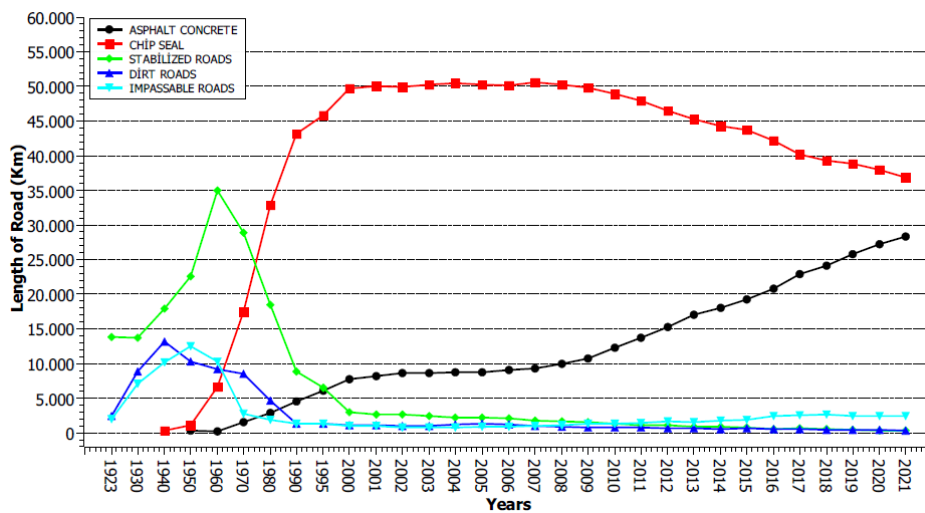
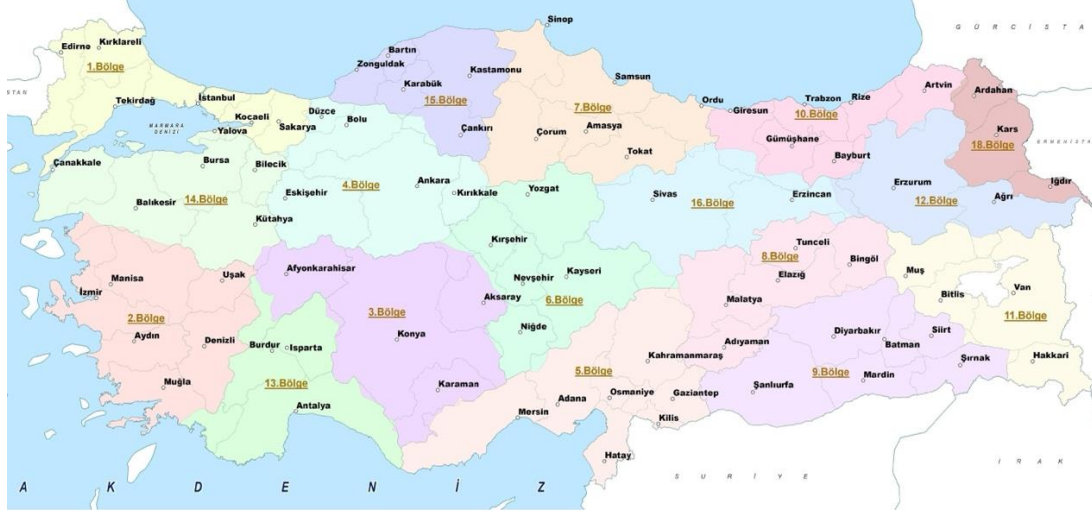
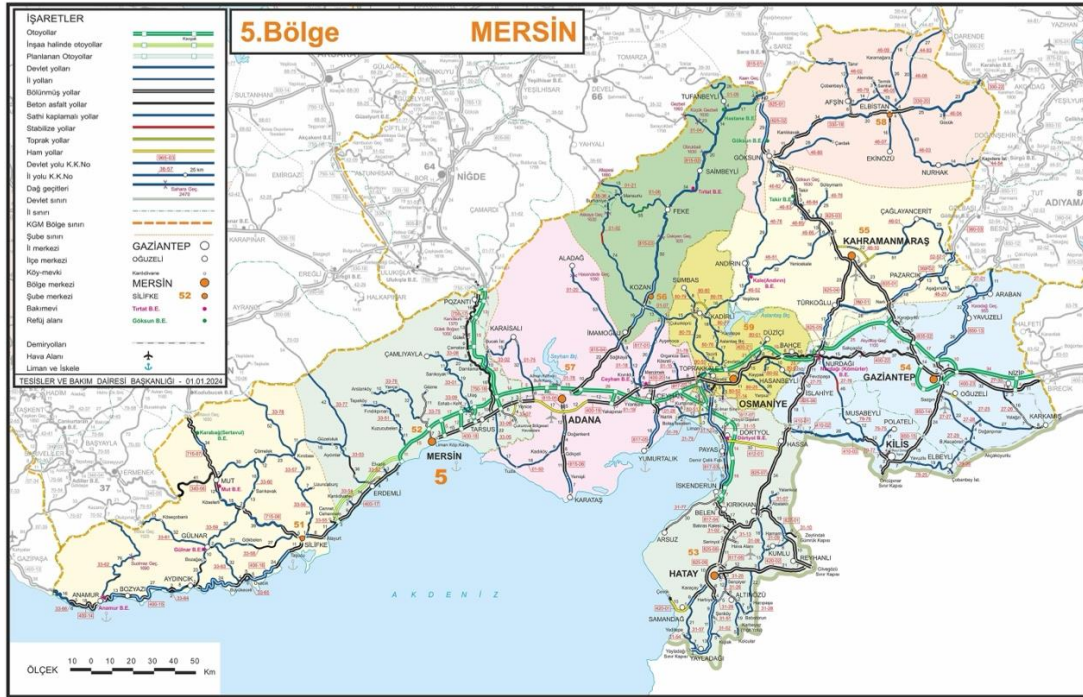


Figure 2. Lengths of road types in Türkiye by year [1]

The regional directorates and administrative divisions in Türkiye are given in Figure 3. Delays in detecting and repairing road damage not only amplify the extent of the damage but also lead to higher repair costs and constitute serious safety risks to drivers. The detection of road damage is crucial for early intervention and repair. Therefore, numerous studies are being conducted using machine learning techniques to detect, discern, and classify road damages.



a



b

Figure 3. Highways (a) regional directorates (b) branches of the 5th region [2, 3].

The literature on road damage detection has experienced significant advancements in recent years, particularly with the utilization of deep neural networks and deep learning models. Maeda et al. introduced a method for road damage detection and classification using deep neural networks with smartphone images, highlighting the importance of utilizing smartphone technology for data collection [4]. Wang et al. focused on adjusting relevant parameters of the model based on analyses of aspect ratios and sizes of damaged areas in the training dataset. As a result of this approach, they obtained an F1 score of 0.62 [5]. Additionally, Maeda et al. emphasized the lack of a uniform road damage dataset and made their experimental results and smartphone application publicly available [4]. Cao et al. conducted a comprehensive evaluation of deep

learning models for road damage detection using multiple dashcam images and highlighted the importance of increasing the diversity of image sources to improve model performance [6]. Arya et al. discussed transfer learning-based road damage detection for multiple countries and highlighted the need for effective solutions in countries struggling with road damage detection [7]. Furthermore, Arya et al. summarized the Global Road Damage Detection Challenge (GRDDC), which aimed to propose methods for automatically detecting road damages in countries like India, Japan, and the Czechia [8]. Arya et al. presented a labeled image dataset (RDD2020) for road damage detection using deep learning, providing a valuable resource for developing and testing road damage detection models [9].

Jeong and Kim explored the use of image tiling techniques to effectively use high-resolution road damage images captured in Norway in combination with other images of similar resolution. This approach was used to train twelve YOLO (You Only Look Once) v5x models for the detection of four distinct types of road damage. The study achieved an impressive average F1 score of 0.6744, demonstrating the effectiveness of the proposed methodology [10]. Wang and colleagues addressed the need for efficient road damage detection as an alternative to traditional, time-consuming manual methods. They proposed an automated, image-based approach utilizing a consensus model based on the YOLOv5 network and attention modules specifically designed for road-focused imaging. This innovative model combines ensemble learning with increased test duration to enhance detection performance. When evaluated across five test datasets in the CRDDC2022, the method attained an average F1 score of 0.65177, showcasing its potential for real-world applications [11].

Lu and colleagues presented an improved YOLOv5-based model for road condition and vehicle detection. The model aims to address the challenges related to the uneven distribution of samples and the presence of small objects in the dataset. Experimental results demonstrated that the improved model maintained real-time performance while achieving a mean average precision (mAP) of 64.5%, surpassing the original YOLOv5 model's mAP of 62% [12]. Xie and Liang explored the use of deep learning-based models, namely YOLOv5 and Nanodet, which are renowned for their high-speed detection capabilities, in the context of road damage detection. The models were trained using a dataset of 21,041 images and subsequently adapted for mobile Android devices. A comparative analysis of the models' performance revealed that the YOLOv5s model achieved a mAP of 51% on a PC [13]. Madarapu Sathvik and his team, the YOLOv7 algorithm was employed to detect potholes on road surfaces. The authors reported an F1 score of 0.51, indicating promising results for this application [14].

Overall, the literature review highlights the progress made in road damage detection through the use of deep learning models, smartphone technology, and innovative algorithms. The availability of datasets and challenges like the GRDDC have further contributed to advancements in this field, paving the way for more efficient and accurate road damage detection and classification methods.

These studies indicate that machine learning techniques are efficacious in detecting road damage. These methods can aid in early intervention, thereby reducing repair times and costs. Considering the growing number of vehicles and expansion of road networks in Türkiye, there is a demand for automatic and effective methods for road damage detection. This study will explore the application of machine learning techniques for the detection of road damage.

2. Data Set and Methodology

2.1. Dataset

The availability of a standardized road damage dataset is crucial for the development and evaluation of road damage detection systems. Maeda et al. highlighted the absence of a benchmark dataset for road damage detection, in collaboration with seven municipalities in Japan, created a dataset for road damage detection by recording images of roads spanning over 1,500 km and spending over 40 hours, thereby making them processable for analysis [4]. In the dataset, each type of damage was labeled with class tags such as 'D00', 'D10'. Figure 4 shows sample images from the RDD2018 dataset. Arya et al. introduced the RDD2020 dataset, comprising 26,336 road images with over 31,000 instances of road damage, intended for developing

deep learning-based methods for automatic detection and classification of road damage [9]. Arya et al. further expanded on the road damage dataset with RDD2022, which includes images from six countries and was released as part of the Crowd sensing-based Road Damage Detection Challenge [15].

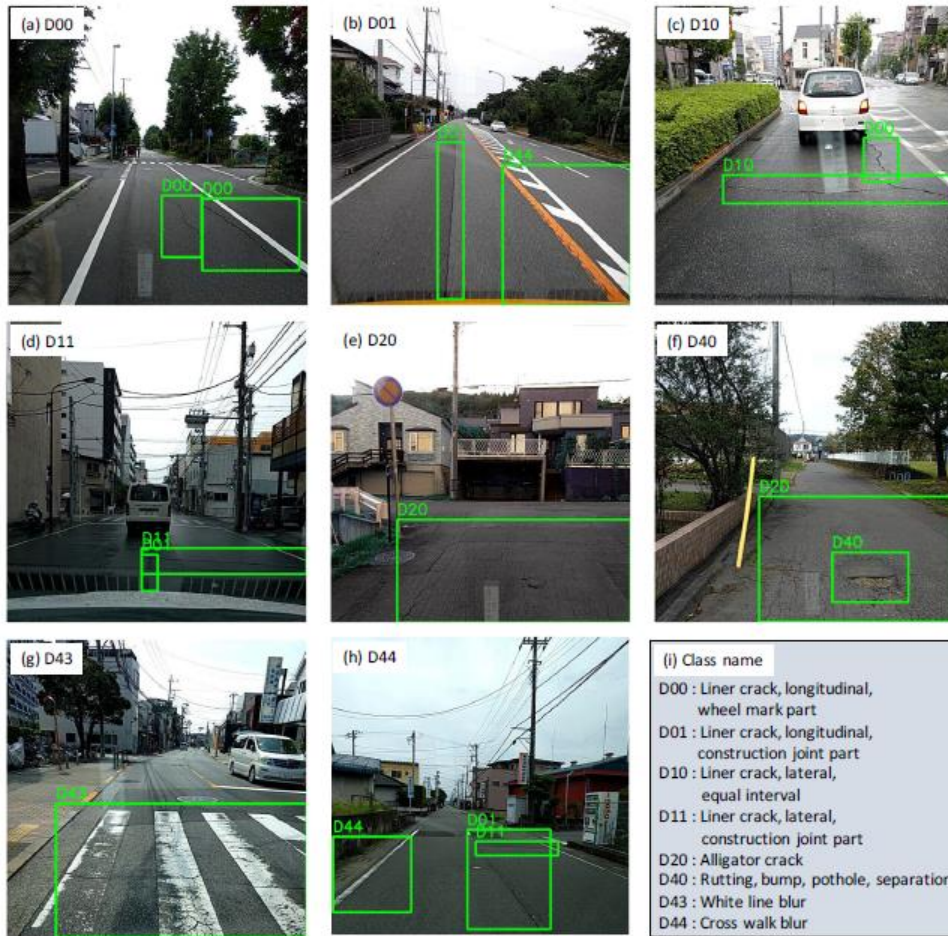


Figure 4. Damage types and sample photos in the RDD2018 dataset [4]

Within the scope of the study, addition to the RDD2022 dataset, a dataset comprising images of Hatay's highways has been created to be recognized by models employing the Convolutional Neural Networks (CNN) algorithm in Türkiye. For the creation of the dataset, the use of a 70mai Dash Cam 4K A800S camera, featuring a 140-degree field of view and a resolution of 2848 x 1600 pixels, was employed (as shown in Figure 5) [16]. To record the roads, image recording was carried out starting from the center of Iskenderun and traveling through the surrounding districts.



Figure 5. 70mai Dash Cam 4K A800S and vehicle integration

It was configured to produce an output in mp4 format every 3 minutes. The purpose of the video recording was to capture the entire road without any loss of image. The recorded images were transformed into photographs at a rate of one frame for every 50 frames. The created dataset consisted of a total of 2209 photographs with a resolution of 2848x1600. The acquired photographs were assessed by an expert in the field of transportation. Images that would technically not be worth labeling, such as blurriness, noise, or photos that did not show the road, were cleaned up. Types of damage were identified among the selected, high-quality images.

Table 1. Types and details of road damage in RDD2022 and the created dataset.

Type of Damage	Class Name
Longitudinal Liner Crack	D00
Lateral Liner Crack	D10
Alligator Crack	D20
Rutting, Bump, Pothole, Separation	D40

2.2. Method

The collected images were labeled according to the types of damage and prepared for model training using the VoTT (Visual Object Tagging Tool) toolbox [17]. The labeling process and bounding boxes are shown in Figure 6. The gathered dataset was labeled using VoTT, an open-source image labeling program. The labels of the data obtained from RDD2022 and the Hatay highways were converted from Pascal-VOC format to YOLO format, making them suitable for the YOLOv8 algorithm. Models were developed on datasets obtained from various geographies, such as Czechia-Türkiye, India-Türkiye, USA-Türkiye, and Japan-Türkiye. These models and their labeling processes are displayed in Figure 7.



Figure 6. The ultimate annotated image comprises of bounding boxes and a class label, which in this instance is denoted as D00

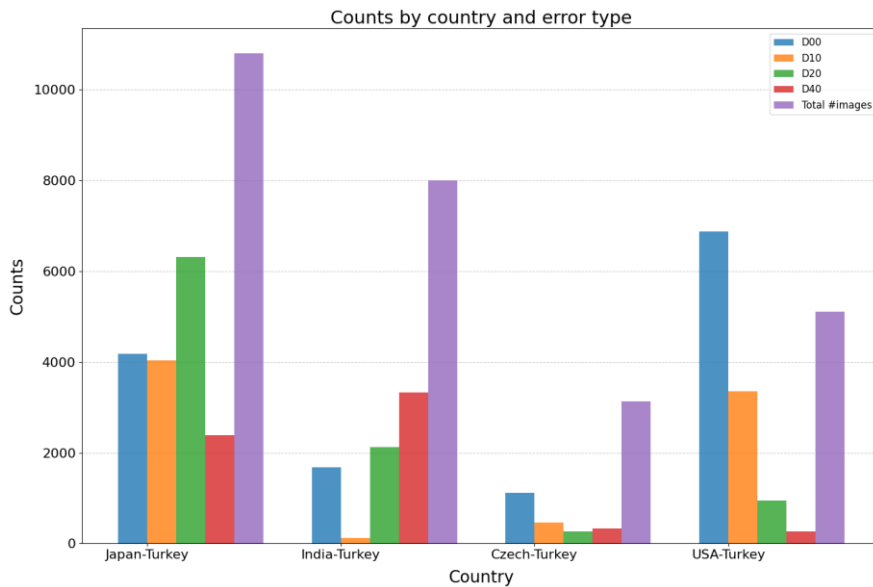


Figure 7. The content of the models and their label classes

The YOLO algorithm operates faster than other algorithms by processing the image through the neural network in a single pass. The introduction of the YOLO algorithm by Redmon and colleagues has created a fundamental change in the field by providing a faster and more efficient alternative for real-time object detection [18].

YOLOv8, the eighth iteration of the algorithm, offers faster and more accurate results compared to its previous versions [19]. Equipped with a deep learning-based structure, YOLOv8 typically operates in conjunction with convolutional neural networks. This algorithm scans the image in a single pass, determining which object each pixel belongs to. Consequently, unlike traditional methods, it integrates the steps of region detection and classification into a single process.

The structure of the YOLOv8 algorithm is illustrated in Figure 8. The sequential definition of this structure encompasses three main components: the backbone, neck, and head. The backbone, often represented by a convolutional neural network, serves the purpose of extracting noteworthy characteristics from the image at different scales. The neck component processes these extracted features, thereby augmenting the spatial and semantic information. Ultimately, the head component utilizes these enhanced features to generate predictions for the task of object detection.

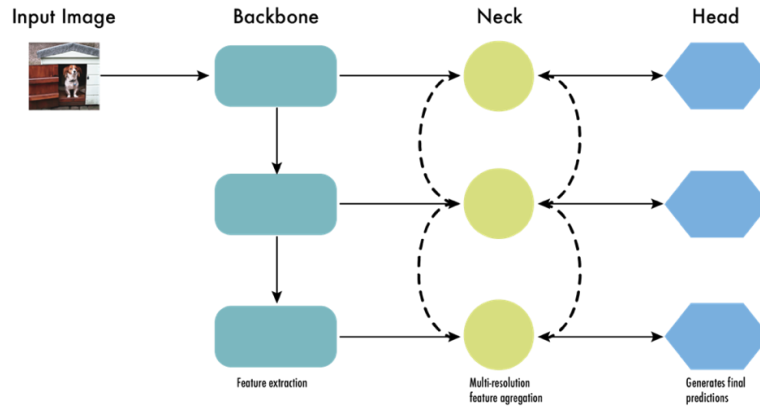


Figure 8. Structure of the YOLOv8 algorithm [20]

3. Results

3.1. Experiment Environment and Metrics

The data that has been compiled for the purpose of identifying road damage has been categorized into four main types of damage: D20, D40, D00 and D10. These were then divided into training and testing datasets. The developed models were trained and tested on Colab using an A100 graphics card [21]. This GPU features 6,912 cores, 40 GB of memory capacity, and a power of 19.49 TFLOPS. Various metrics have been examined to evaluate models with different image and label counts from different countries. The most commonly preferred metrics in object detection evaluation, such as the mAP (Mean Average Precision) and F1 score, were used. Additionally, the results of the method have been presented in a confusion matrix. The customized matrix for this study is displayed in Table 2, while the formulas for each metric are given below.

Precision is the likelihood of correctly guessing a positive instance from all predicted positive instances, and recall is the likelihood of guessing a positive instance from true positive instances. The formulas for precision and recall are shown in equations (1), (2).

$$P = \frac{TP}{TP + FP} \quad (1)$$

$$R = \frac{TP}{TP + FN} \quad (2)$$

Table 2. Confusion Matrix Explanation.

Terms	Results
True Positive (TP)	Cases where the model predicts damage and there is indeed damage.
True Negative (TN)	Cases where the model predicts no damage and there is indeed no damage.
False Positive (FP)	Cases where the model predicts damage but there is no damage.
False Negative (FN)	Cases where the model predicts no damage but there is actually damage.

In the field of object detection, Precision and Recall are interdependent metrics that are not suitable for direct assessment of the detection process. Consequently, the introduction of Average Precision (AP) serves to

characterize the precision of detection, while the F1-Score acts as a holistic measure to assess the model comprehensively. Increasing values of AP and F1-Score indicate high accuracy of the network, while mAP reflects the average accuracy in n defect categories. The mathematical formulations for AP, mAP, and F1-Score are delineated in equations (3), (4), and (5).

$$AP = \int_0^1 P(R)dR \quad (3)$$

$$mAP = \frac{1}{n} \sum_{i=1}^m AP^i \quad (4)$$

$$F1 - Score = 2 \times \frac{P \times R}{P + R} \quad (5)$$

mAP, or Mean Average Precision, serves as a measure employed to assess the efficacy of object detection systems. It represents the average accuracy of all predictions made by the system. Typically, it is calculated by taking the average of AP (Average Precision) values for different IoU (Intersection over Union) thresholds. The accuracy of the predicted bounding boxes in AP is evaluated through the utilization of IoU. IoU is a metric that represents the proportion of the intersecting area to the combined area of the actual and predicted bounding boxes, as depicted in Figure 9. It measures how closely the actual and predicted bounding boxes overlap. In this study, the IoU threshold is set at 0.5, meaning a prediction must have an IoU of at least 0.5 to be considered accurate.

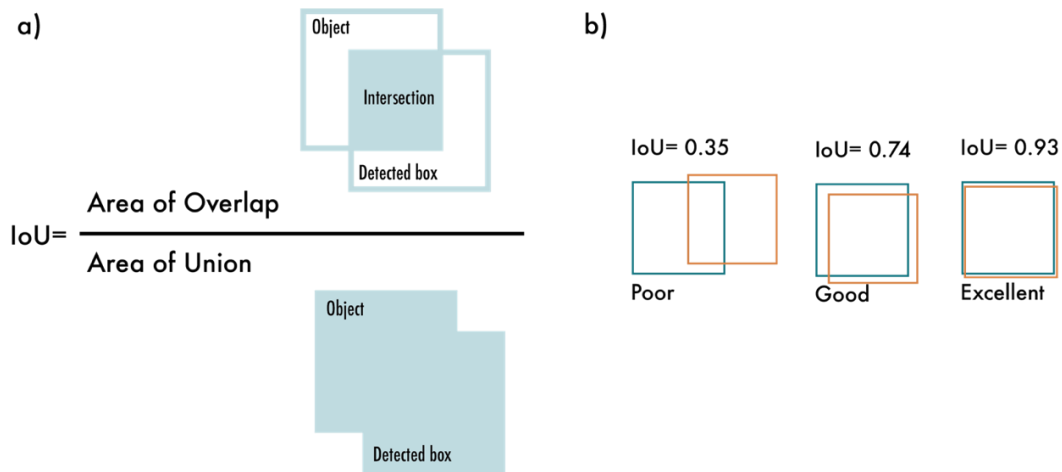


Figure 9. Intersection over Union (IoU). (a) The intersection area of two bounding boxes divided by their total area yields the IoU value; (b) three distinct IoU values for boxes placed differently are given as examples [20]

3.2. Experimental Results

In this section, we delve into the empirical outcomes obtained from the conducted experiments. The results are systematically organized and displayed in Table 3. The table encapsulates a comparative analysis of detection performance metrics across different bilateral model configurations, with a particular emphasis on the collaborative models between Türkiye and various other countries. It is noteworthy that the Japan-Türkiye model configuration stands out, exhibiting superior performance as evidenced by the quantitative measures.

Table 3. Comparison of Detection Performance of the Models

Country	F1 Score	mAP@0.5
Czechia-Türkiye	0.34	0.31
India-Türkiye	0.41	0.367
USA-Türkiye	0.51	0.52
Japan-Türkiye	0.54	0.55

Upon examining the tabulated data, it becomes apparent that the Japan-Türkiye collaboration yields the most commendable results with an F1 Score of 0.54 and an mAP@0.5 of 0.55. These figures not only surpass the other country pairs but also suggest a robust model performance in detecting the objects of interest with high accuracy and reliability.

The results from the Czechia-Türkiye pair indicate a relatively lower detection performance, with an F1 Score of 0.34 and an mAP@0.5 of 0.31. Similarly, the India-Türkiye configuration demonstrates moderate performance improvements with an F1 Score of 0.41 and an mAP@0.5 of 0.367. The USA-Türkiye model shows further enhancement in detection capabilities, achieving an F1 Score of 0.51 and an mAP@0.5 of 0.52, which is indicative of a well-tuned model that balances precision and recall effectively.

Table 4. Summary of comparison with methods in other studies using road damage detection

	F1 Score	mAP
Sathvik et al. [14]	0.51	-
Wang et al. [11]	0.65	-
Xie and Liang [13]	-	0.64
Our method (Japan-Türkiye)	0.54	0.55

Designated as Table 4, this summary ranks each method according to their F1 score and mean Average Precision (mAP) values. According to the table, the method developed by Sathvik et al. [14] has been evaluated with an F1 score of 0.51, but the mAP value has not been provided. The study by Wang et al. [11] exhibits higher performance with an F1 score of 0.65. Xie and Liang [13] are represented solely by the mAP value and have achieved a considerably high value of 0.64. Lastly, the method referred to as Our method (Japan-Türkiye) shows a balanced performance with both F1 score (0.54) and mAP (0.55) values. This comparison table serves as a useful resource for analyzing the performance of road damage detection methods developed in different countries. Notably, the method developed through collaboration between Japan and Türkiye demonstrates a balanced performance in terms of both F1 score and mAP values, indicating it as an effective alternative for road damage detection. Let's take a closer look at the graphs presented below for a more detailed analysis and evaluation of our Japan-Türkiye model.

The F1-Confidence Curve illustrates how the F1 scores of a model's predictions vary within a certain confidence range. In the curve shown in Figure 10, the horizontal axis denotes the confidence level of the model's predictions, while the vertical axis indicates the F1 score. While the D40 class has low F1 scores, the

D20 class shows higher F1 scores. The best F1 score for all classes is the value of 0.54, obtained at approximately a 0.32 confidence threshold.

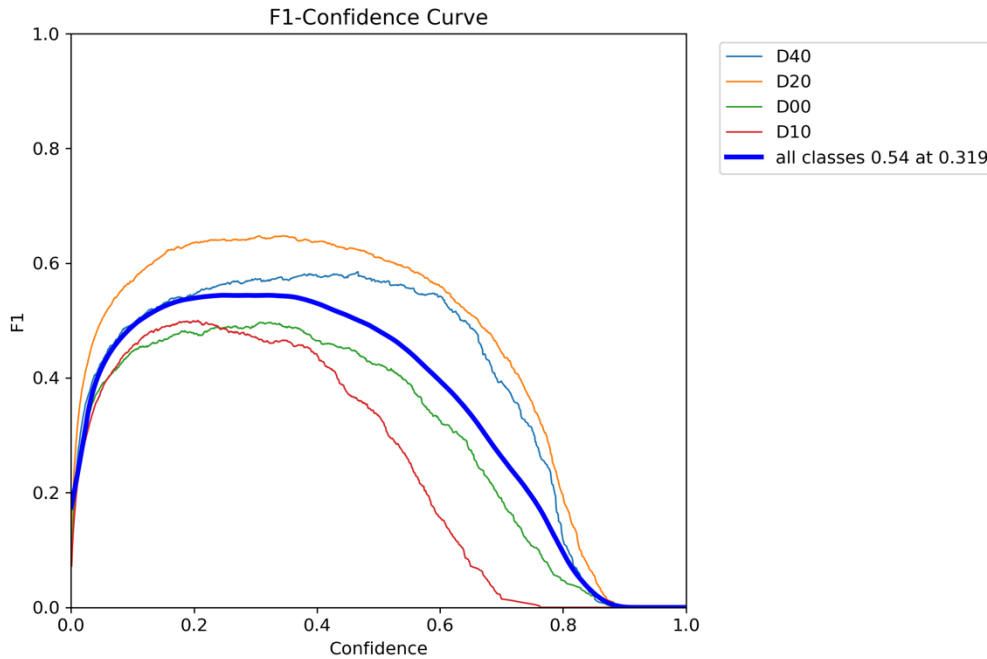


Figure 10. Japan-Türkiye F1-Confidence Curve

The Precision-Confidence Curve demonstrates the precision of a model's predictions within a certain confidence range. In the curve presented in Figure 11, the horizontal axis denotes confidence, reflecting how certain the model's predictions are, while the vertical axis indicates precision, which reflects how many of the selected items are indeed positive. The D20 class demonstrates higher precision compared to other classes, while the D40 class exhibits the lowest precision. The maximum precision for all classes is specified as 1.00 at a confidence threshold of 0.877.

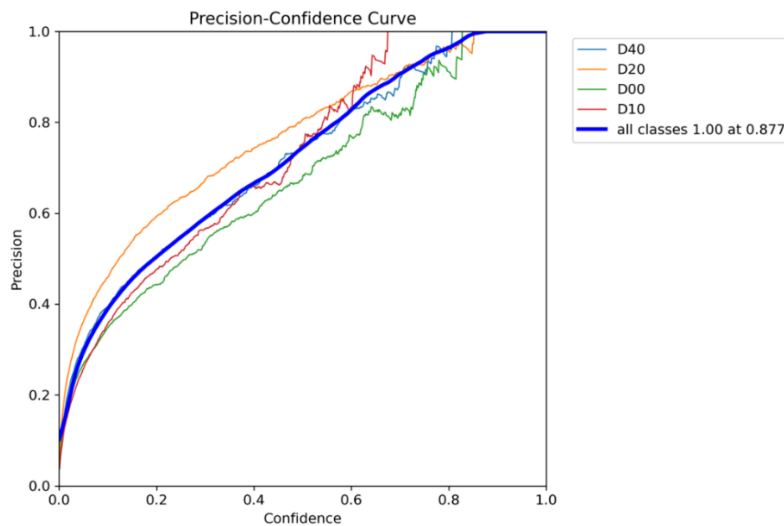


Figure 11. Japan-Türkiye Precision-Confidence Curve

The Recall-Confidence Curve illustrates how well the model detects true positives at a certain level of confidence. In the curve presented in Figure 12, the horizontal axis denotes the confidence level, while the

vertical axis indicates recall, which is the proportion of true positives that have been correctly identified. The D20 class exhibits high recall, while the D40 class shows the lowest recall. The maximum recall for all classes is shown as 0.87, but this is achieved at a 0.00 confidence threshold, which may not be practical to use.

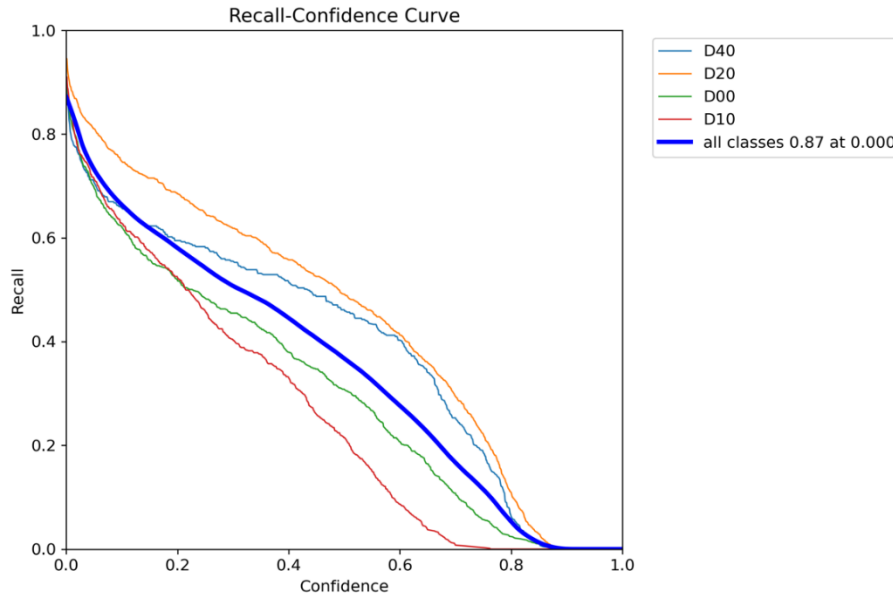


Figure 12. Japan-Türkiye Recall-Confidence Curve

The Confusion Matrix demonstrates the accurate and erroneous predictions generated by the model for every category. The normalized confusion matrix expresses these values as percentages of the total number of samples, providing a clearer indication of the model's performance. This is useful for comparing the model's performance across different classes. The normalized confusion matrix is presented in Figure 13. The high accuracy rate (0.66) of the D20 class is notable, but it seems that the D00 and D10 classes tend to be confused with the background (0.46 and 0.48, respectively).

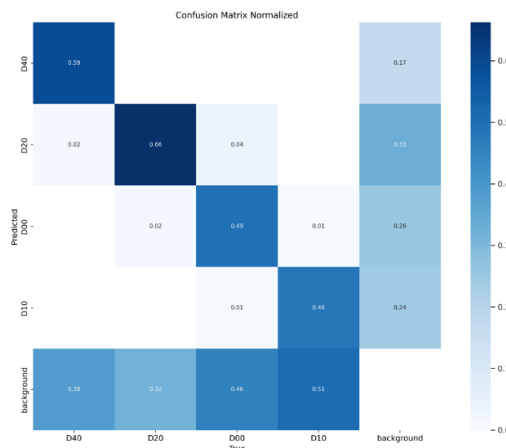


Figure 13. Japan-Türkiye Normalized confusion matrix

The Precision-Recall Curve displays the precision and recall values of the model at different threshold levels. The larger the area under the curve presented in Figure 14, the better the performance of the model. Here, the D20 class has the highest mAP@0.5 value (0.678), indicating better classification performance compared to other classes.

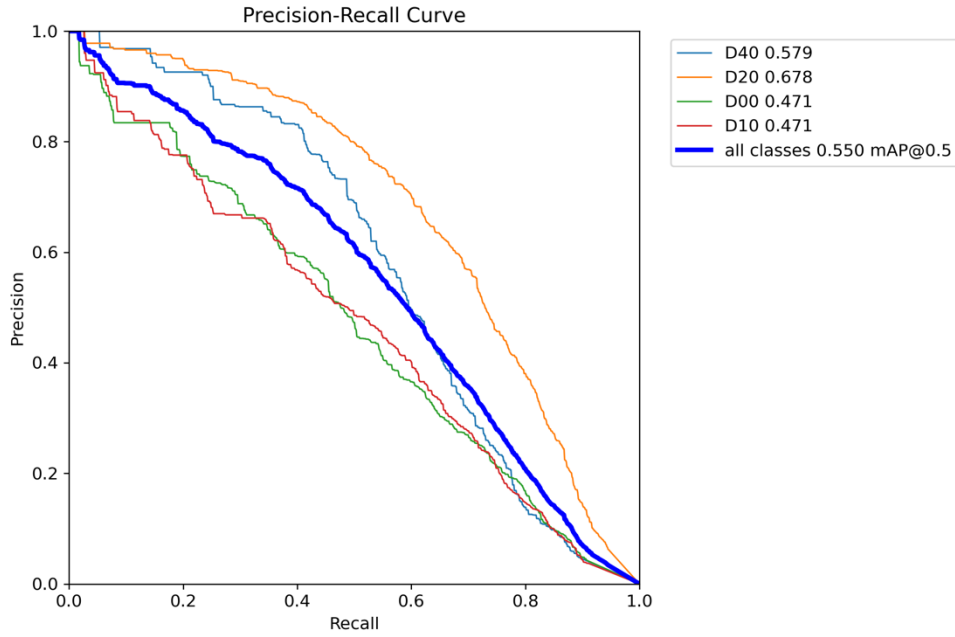


Figure 14. Japan-Türkiye Precision-Recall Curve

Figure 15 shows the curves of the metrics showing the epochs and their changes during the training of the model. A decrease in losses over time indicates that the model is learning from the data. Training losses have significantly dropped, while validation losses have decreased in a somewhat slower but steady manner. The increase in precision and recall metrics also indicates an improvement in the model's performance.

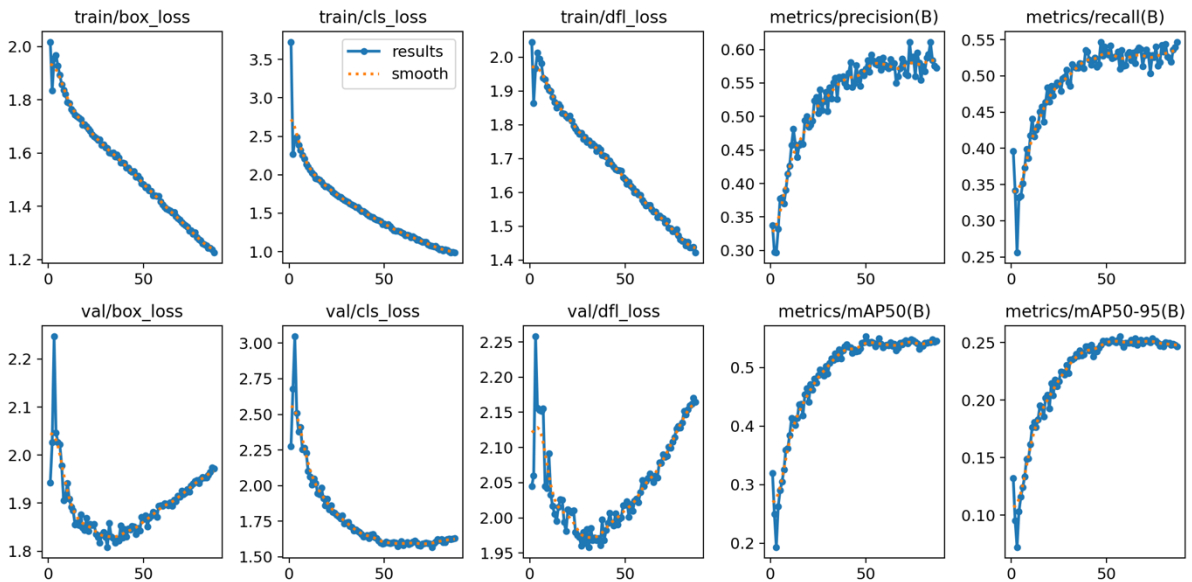


Figure 15. Japan-Türkiye model training curves

4. Conclusion

The study embarked on an exploration of road damage detection using the YOLOv8 algorithm, leveraging datasets from diverse geographical contexts, including collaborations between Türkiye and other countries such as Czechia, India, the USA, and Japan. The primary objective was to assess the algorithm's efficacy in identifying road damages, a critical concern for transportation safety and maintenance cost optimization.

The methodological approach entailed the utilization of the VoTT Image Labeling Program for object labeling and the employment of Nvidia's A100 graphics card within Google's Colab service for the training process. The evaluation of the models was predicated on their mAP and F1 scores, with a particular focus on the Japan-Türkiye model, which demonstrated superior performance.

The results of the study are succinctly summarized as follows:

- The Japan-Türkiye model emerged as the most effective, achieving an mAP of 0.55 and an F1 score of 0.54.
- Comparative analysis revealed that this model outperformed other bilateral configurations, with notable proficiency in detecting specific types of road damage such as potholes and alligator cracks.
- The study highlighted the variability in damage appearance across different geographies and underscored the importance of training models on local datasets.

However, the study is not without its limitations. The detection of certain damage types, such as longitudinal and lateral cracks, proved challenging, often resulting in misclassification. Additionally, the model exhibited a tendency towards overfitting, as evidenced by fluctuations in validation losses. These insights pave the way for future research, emphasizing the refinement of detection algorithms and the exploration of more sophisticated training methodologies to enhance model generalizability and accuracy.

Based on the findings and insights from this study, several directions for future research have been identified for the development and improvement of road damage detection methodologies. Suggested areas for future work include:

- Algorithm Enhancement: Investigating the integration of advanced machine learning algorithms and exploring the potential of deep learning architectures beyond YOLOv8. This includes the examination of newer versions of YOLO or alternative frameworks that may offer improved detection capabilities, especially for less distinct types of road damage.
- Data Augmentation and Diversification: Expanding the dataset to include a wider array of geographical locations and road conditions. This would entail the collection and labeling of road damage images from varied climates and topographies to enhance the model's generalizability and robustness across different environments.

By pursuing these directions, future research can significantly contribute to the advancement of road damage detection technologies, ultimately enhancing road safety and maintenance efficiency.

5. Acknowledgments

This investigation was conducted with the assistance of the Scientific Research Projects Coordination Office at İskenderun Technical University, within the framework of project number 2022LTP06.

6. Author Contribution Statement

In the study, Author 1 contributed to the formation of the idea, design, literature review, evaluation of the results obtained, procurement of the materials used and examination of the results; Author 2 contributed to the formation of the idea and control of the article in terms of content.

7. Ethics Committee Approval and Conflict of Interest Statement

There is no need to obtain ethics committee permission for the prepared article. There is no conflict of interest with any person/institution in the prepared article

8. References

- [1] Highway Transportation Statistics, "Karayolu Ulaşım İstatistikleri (2021)." [Online].

- Available:<https://www.kgm.gov.tr/SiteCollectionDocuments/KGMdocuments/Yayinlar/YayinPdf/KarayoluUlasimIstatistikleri2021.pdf>
- [2] K. G. M. B. İ. Dairesi, “Bölgeler — kgm.gov.tr.” [Online]. Available: <https://www.kgm.gov.tr/Sayfalar/KGM/SiteTr/Bolgeler/Bolgeler.aspx>
 - [3] K. G. M. B. İ. Dairesi, “Bolge5 — kgm.gov.tr.” [Online]. Available: <https://www.kgm.gov.tr/Sayfalar/KGM/SiteTr/Bolgeler/5Bolge/Harita.aspx>
 - [4] H. Maeda, Y. Sekimoto, T. Seto, T. Kashiyama, and H. Omata, “Road Damage Detection and Classification Using Deep Neural Networks with Smartphone Images,” *Comput.-Aided Civ. Infrast. Eng.*, vol. 33, no. 12, pp. 1127–1141, Dec. 2018.
 - [5] W. Wang, B. Wu, S. Yang, and Z. Wang, “Road Damage Detection and Classification with Faster R-CNN,” in *2018 IEEE International Conference on Big Data (Big Data)*, Seattle, WA, USA: IEEE, pp. 5220–5223, Dec. 2018.
 - [6] M.-T. Cao, Q.-V. Tran, N.-M. Nguyen, and K.-T. Chang, “Survey on performance of deep learning models for detecting road damages using multiple dashcam image resources,” *Adv. Eng. Inform.*, vol. 46, p. 101182, Oct. 2020.
 - [7] D. Arya, “Transfer Learning-based Road Damage Detection for Multiple Countries,” Aug. 2020.
 - [8] D. Arya, “Global Road Damage Detection: State-of-the-art Solutions,” Nov. 2020.
 - [9] D. Arya, H. Maeda, S. K. Ghosh, D. Toshniwal, and Y. Sekimoto, “RDD2020: An annotated image dataset for automatic road damage detection using deep learning,” *Data Brief*, vol. 36, p. 107133, May 2021.
 - [10] D. Jeong and J. Kim, “Road Damage Detection using YOLO with Image Tiling about Multi-source Images,” in *2022 IEEE International Conference on Big Data (Big Data)*, pp. 6401–6406 Dec. 2022.
 - [11] S. Wang et al., “An Ensemble Learning Approach with Multi-depth Attention Mechanism for Road Damage Detection,” in *2022 IEEE International Conference on Big Data (Big Data)*, pp. 6439–6444, Dec. 2022.
 - [12] Z. Lu, L. Ding, Z. Wang, L. Dong, and Z. Guo, “Road Condition Detection Based on Deep Learning YOLOv5 Network,” in *2023 IEEE 3rd International Conference on Electronic Technology, Communication and Information (ICETCI)*, pp. 497–501, May 2023.
 - [13] F. Xie and G. Liang, “Using Highly Accurate and Portable Deep Learning Models in Road Damage Detection and Classification,” in *2022 10th International Conference on Information Systems and Computing Technology (ISCTech)*, pp. 172–175, Dec. 2022.
 - [14] M. Sathvik, G. Saranya, and S. Karpagaselvi, “An Intelligent Convolutional Neural Network based Potholes Detection using Yolo-V7,” in *2022 International Conference on Automation, Computing and Renewable Systems (ICACRS)*, pp. 813–819, Dec. 2022.
 - [15] D. Arya, H. Maeda, S. K. Ghosh, Durga Toshniwal, and Yoshihide Sekimoto, “RDD2022: A multi-national image dataset for automatic Road Damage Detection,” Sep. 2022.
 - [16] “70mai Dash Cam 4K A800S,” dashcam.70mai.com. [Online]. Available: <https://dashcam.70mai.com/a800s/>
 - [17] “microsoft/VoTT,” GitHub. [Online]. Available: <https://github.com/Microsoft/VoTT>
 - [18] J. Redmon, S. Divvala, R. Girshick, and A. Farhadi, “You Only Look Once: Unified, Real-Time Object Detection,” in *2016 IEEE Conf. Comput. Vis. Pattern Recognit. CVPR*, June 2016.
 - [19] G. Jocher, A. Chaurasia, and J. Qiu, “YOLO by Ultralytics,” GitHub. [Online]. Available: <https://github.com/ultralytics/ultralytics>
 - [20] J. Terven, D.-M. Córdoba-Esparza, and J.-A. Romero-González, “A Comprehensive Review of YOLO Architectures in Computer Vision: From YOLOv1 to YOLOv8 and YOLO-NAS,” *Mach. Learn. Knowl. Extr.*, vol. 5, no. 4, pp. 1680–1716, Dec. 2023.
 - [21] “Google Colaboratory,” colab.research.google.com. [Online]. Available: <https://colab.research.google.com>



Farklı Taper Açıklarına Sahip Endodontik Eğelerin Biyomekanik Özelliklerinin Sonlu Elemanlar Analiziyle Değerlendirilmesi

Mehmet ESKİBAĞLAR^{1*} , Serkan ERDEM² 

¹Endodonti Anabilim Dalı, Diş Hekimliği Fakültesi, Fırat Üniversitesi, Elazığ, Türkiye.

²Makine Mühendisliği, Mühendislik Fakültesi, Fırat Üniversitesi, Elazığ, Türkiye.

¹meskibaglar@firat.edu.tr, ²serdem@firat.edu.tr

Geliş Tarihi: 20.03.2024

Kabul Tarihi: 13.05.2024

Düzelme Tarihi: 04.04.2024

doi: 10.62520/fujece.1456044

Araştırma Makalesi

Alıntı: M. Ekibağlar ve S. Erdem, "Farklı taper açıklarına sahip endodontik eğelerin biyomekanik özelliklerinin sonlu elemanlar analiziyle değerlendirilmesi", Fırat Üni. Deny. ve Hes. Müh. Derg., vol. 3, no 3, pp. 271-279, Ekim 2024.

Öz

Bu çalışma, farklı taper açıklarına sahip nikel-titanyum (Ni-Ti) döner aletlerin bükülme ve burulma sırasındaki gerilim dağılımını sonlu elemanlar analizi (SEA) kullanılarak değerlendirilmeyi amaçlamaktadır. Çalışma için 0.02, 0.04 ve 0.06 sabit taper açıklarına sahip döner alet eğeleri Solidworks yazılımı kullanılarak modellendi. Bu modeller ANSYS yazılımına aktarıldı. Eğelerin esnekliğini ve burulma sertliğini değerlendirmek için SEA yöntemi kullanılarak, ISO 3630-1 spesifikasyonuna göre testler gerçekleştirildi. Test sonuçlarına göre 0.02 taper açısına sahip eğe sistemi bükülmeye maruz kaldığında 0.04 ve 0.06 tapera sahip eğelerden daha yüksek esneklik gösterdi. Burulma direnci açısından 0.06 taper açısına sahip döner eğe, 0.02 ve 0.04 taper açısına sahip eğelerden daha yüksek burulma direnci gösterdi. Aletin geometrisi, döner eğelerin mekanik davranışını (bükülme ve burulma) etkilemektedir. Klinisyen döner eğelerdeki davranışsal farklılıkların farkında olmalı, üretici talimatlarına ek olarak klinik duruma göre uygun eğeyi kullanmalıdır.

Anahtar kelimeler: Endodontik eğe, Bükme testi, Burulma testi, Sonlu elemanlar analizi

*Yazışılan yazar

İntihal Kontrol: Evet– Turnitin

Şikayet: fujece@firat.edu.tr

Telif Hakkı ve Lisans: Dergide yayın yapan yazarlar, CC BY-NC 4.0 kapsamında lisanslanan çalışmalarının telif hakkını saklı tutar.



Evaluation of the Biomechanical Properties of Endodontic Files with Different Taper Angles Using Finite Element Analysis

Mehmet ESKIBAĞLAR^{1*} , Serkan ERDEM² 

¹Department of Endodontics, Faculty of Dentistry, Firat University, Elazığ, Türkiye.

²Department of Mechanical Engineering, Faculty of Engineering, Firat University, Elazığ, Türkiye.

¹meskibaglar@firat.edu.tr, ²serdem@firat.edu.tr

Received: 20.03.2024

Accepted: 13.05.2024

Revision: 04.04.2024

doi: 10.62520/fujece.1456044

Research Article

Citation: M. Eskibağlar ve S. Erdem, "Evaluation of the biomechanical properties of endodontic files with different taper angles using finite element analysis", *Firat Univ. Jour. of Exper. and Comp. Eng.*, vol. 3, no 3, pp. 271-279, October 2024.

Abstract

This study aims to evaluate the stress distribution of nickel-titanium (Ni-Ti) rotary tools with different conical angles during bending and torsion using finite element analysis (FEA). For the study, rotary file models with fixed taper angles of 0.02, 0.04, and 0.06 were modeled using Solidworks software. These models were transferred to ANSYS software. It was performed according to the ISO 3630-1 test specification using the FEA method to evaluate the flexibility and torsional stiffness of the files. According to the test results, the file system with a 0.02 taper angle showed higher flexibility when subjected to bending compared to the files with 0.04 and 0.06 taper angles. Regarding torsional resistance, the rotary file with a 0.06 taper angle demonstrated higher torsional resistance than the files with 0.02 and 0.04 taper angles. The geometry of the instrument affects the mechanical behavior (bending and torsional) of rotary files. Clinicians should be aware of the behavioral differences in rotary files and, in addition to following manufacturer instructions, should use the appropriate file according to the clinical situation.

Keywords: Endodontic file, Bending test, Torsional test, Finite element analysis

*Corresponding author

Plagiarism Checks: Yes – Turnitin

Complaints: fujece@firat.edu.tr

Copyright & License: Authors publishing with the journal retain the copyright to their work licensed under the CC BY-NC 4.0

1. Introduction

For a long time, Nickel-titanium (Ni-Ti) rotary file have been used for the mechanical preparation of teeth in root canal treatments [1]. Ni-Ti files exhibit superior flexibility when compared to stainless steel files. They also better preserve the anatomy of the root canal system [2]. However, during chemomechanical preparation processes, Ni-Ti files are significantly subjected to stress and strain. As a result of these stresses and strains, Ni-Ti rotary files can fracture within the root canal system [3]. Manufacturers have been modifying many features of Ni-Ti rotary files, such as design, geometry, and heat treatment, to enhance their clinical performance [4]. Currently, there are over 160 different Ni-Ti rotary file systems with various designs, kinematics, or heat treatments. Among these files, there are rotary file systems with the same apical size but with 0.02, 0.04, 0.06 taper angles [5-7].

Finite Element Analysis (FEA) is a numerical method used for evaluating the mechanical behaviors of materials used in endodontics [8]. It also allows for the simulation to be repeated without any risk by modifying the material properties as desired [9]. This makes it possible to observe the distribution of stress and strain that cannot be obtained under laboratory conditions and to monitor the mechanical behavior of the material [1, 4].

In the literature, there are many FEA studies on Ni-Ti rotary file systems [3, 4]. However, there is no study focusing solely on the variability of taper angle under ISO-3630-1 tests for a Ni-Ti rotary file. The purpose of this study is to comparatively evaluate three Ni-Ti rotary files, designed by us, with taper angles of 0.02, 0.04, 0.06 and a #30 apical size against the test limits of ISO 3630-1. The null hypothesis of this study is that files with different taper angles will produce different results against bending and torsional tests.

2. Materials and Method

The Ni-Ti endodontic rotary file models were designed to feature a commercially unavailable convex triangular and non-cutting tip design with concentric pitches, ISO #30 apical diameters, and conical angles of 0.02, 0.04, and 0.06 (**Figure1**).

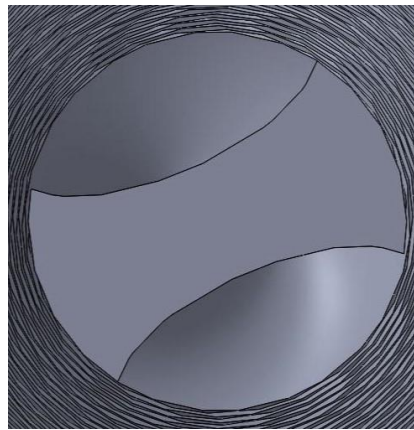


Figure1. Cross-sectional geometry of the designed Ni-Ti rotary file

These models were designed in 3D with a working length of 16 mm using Solidworks software (Dassault Systems SA, Concord, MA) and saved with a .prt extension (**Figure 2**). The resulting Ni-Ti rotary file models were then saved with a Parasolid (.x_t) extension and made ready for use in ANSYS Workbench 2019 R1 software (ANSYS, Inc., Canonsburg, PA).

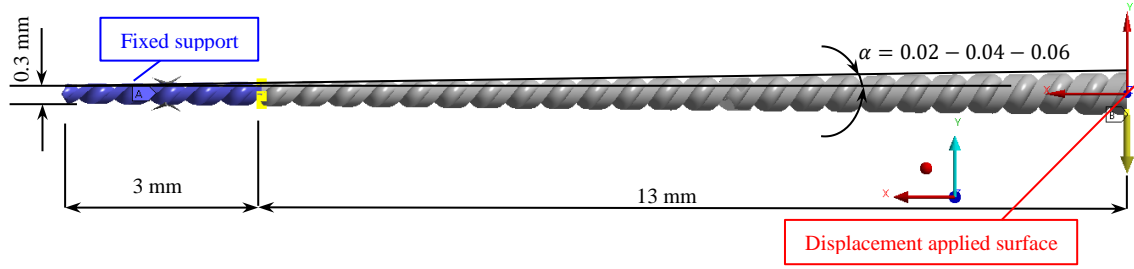


Figure 2. Ni-Ti endodontic rotary file model

For the properties of the rotary file, Ni-Ti material properties were selected in the ANSYS Workbench software. The mechanical properties used for this material are presented in Table 1 [1].

Table 1. Material properties of the Ni-Ti rotary file used in the analysis

Parameter	Description	Value
E	Young's modulus	60000 MPa
ν	Poisson ratio	0.36
K	Bulk modulus	71429 MPa
G	Shear modulus	22059 MPa
σ_S^{AS}	Starting stress value for the forward phase transformation	520 MPa
σ_f^{AS}	Final stress value for the forward phase transformation	600 MPa
σ_S^{SA}	Starting stress value for the reverse phase transformation	300 MPa
σ_f^{SA}	Final stress value for the reverse phase transformation	200 MPa
$\bar{\epsilon}_L$	Maximum residual strain	0.07 mm/mm
α	Parameter measuring the difference between material responses in tension and compression	0
E_S	Elastic modulus of the full martensite phase If 0 or undefined, the martensite and austenite phases share the same elastic modulus	60000 MPa

The created models were meshed using quadratic elements in the ANSYS Workbench software (**Figure 3**). The models with 0.02, 0.04, 0.06 taper angles contain, respectively, 3701 nodes-1083 elements, 4694 nodes-1474 elements, and 7834 nodes-2150 elements. In this software, the axes of the Ni-Ti rotary files were positioned such that their axes were along the -x axis.

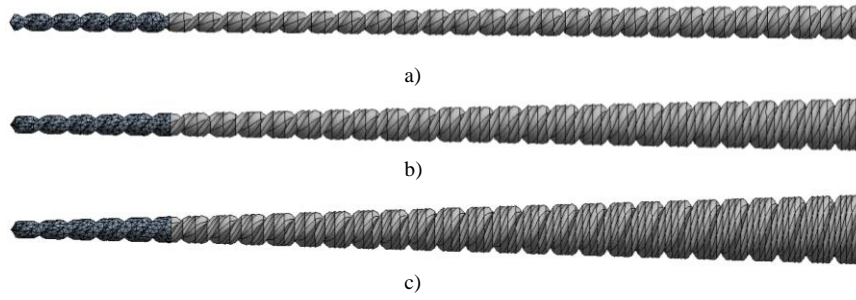


Figure 3. Mesh models created for analysis; a) $\alpha=0.02$, b) $\alpha=0.04$, c) $\alpha=0.06$

The analyses of the Ni-Ti rotary file systems were conducted in ANSYS Workbench software according to ISO 3630-1 boundary conditions [10]. The boundary conditions for the bending test were achieved by applying fixed support at the apical end of the file as indicated in Figure 1, and at the coronal end, a displacement of 13 mm along the -y axis was given to provide a bending angle of 45 degrees. To achieve fixed support condition, the model was cut and separated 3 mm away from the apex in Solidworks software. In ANSYS Workbench software, a bonded connection boundary condition was applied to enable these two parts to move as a single piece. Free boundary conditions were applied to the coronal part of the model in the -x and -z axes (**Figure 4**).

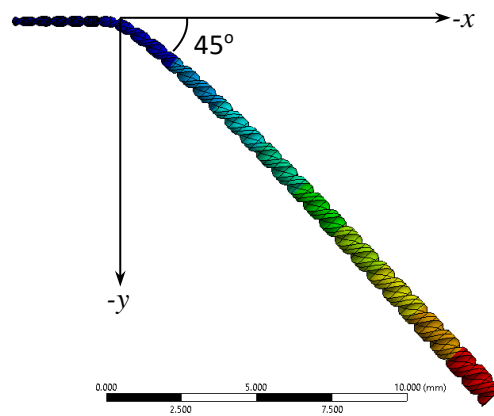


Figure 4. Application of 45-degree displacement to the Ni-Ti rotary file model in the -y axis

To observe the torsional behaviors of the created models, a boundary condition was applied as shown in **Figure 5**. Different from the bending test, a torque of 2 Nmm was applied from the coronal end of the model in the -x axis (Figure 5).

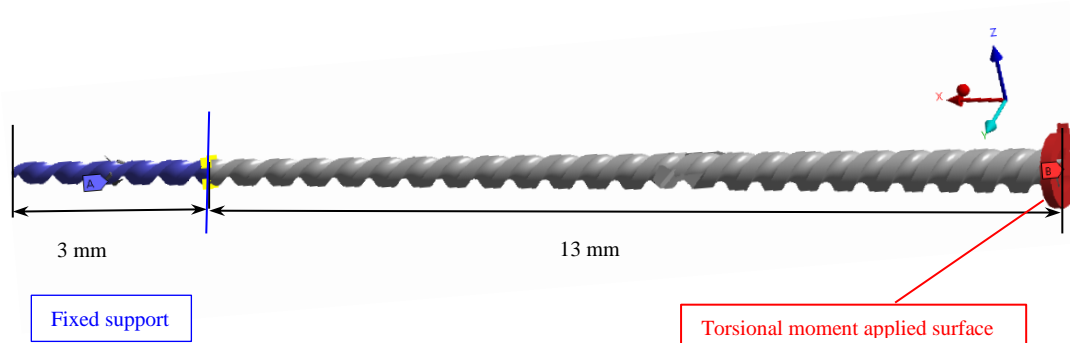


Figure 5. Application of rotational torque to the file model along the -x axis

3. Results and Discussion

3.1. Bending Test

Subjecting the file models to a 45-degree bending test showed similar behavior for each taper angle. The maximum von Mises stress value increased linearly up to about 10 degrees of bending, reaching ~700 MPa. For the taper angle $\alpha=0.02$, this continued in a nearly constant manner up to ~45 degrees of bending, while for $\alpha=0.04$, the stress increased to 1200 MPa after a bending angle of 35 degrees. However, for $\alpha=0.06$, after about 20 degrees of bending, the stress increased linearly up to 45 degrees, reaching ~2000 MPa.

As the taper angle increased, the reaction bending moment also increased. With the increase in the bending angle, the reaction bending moment required to bend the rotary files was obtained in a manner similar to Figure 5. Up to ~10 degrees of bending, the reaction bending moment for each rotary file's taper angle increased linearly, being 0.6 N.mm for $\alpha=0.02$, 1.5 N.mm for $\alpha=0.04$, and 3 Nmm for $\alpha=0.06$. After ~10 degrees of bending, the reaction bending moment continued to be constant for $\alpha=0.02$, slightly increased to ~4 N.mm for $\alpha=0.04$, and despite a decrease in the rate of increase, linearly rose to 9.5 N.mm for $\alpha=0.06$.

When the models were forced to bend at an angle of 45 degrees, the behavior of the maximum von Mises stress corresponding to the bending angle was obtained in **Figure 6**, and the reaction bending moment corresponding to the bending angle was obtained in **Figure 7**.

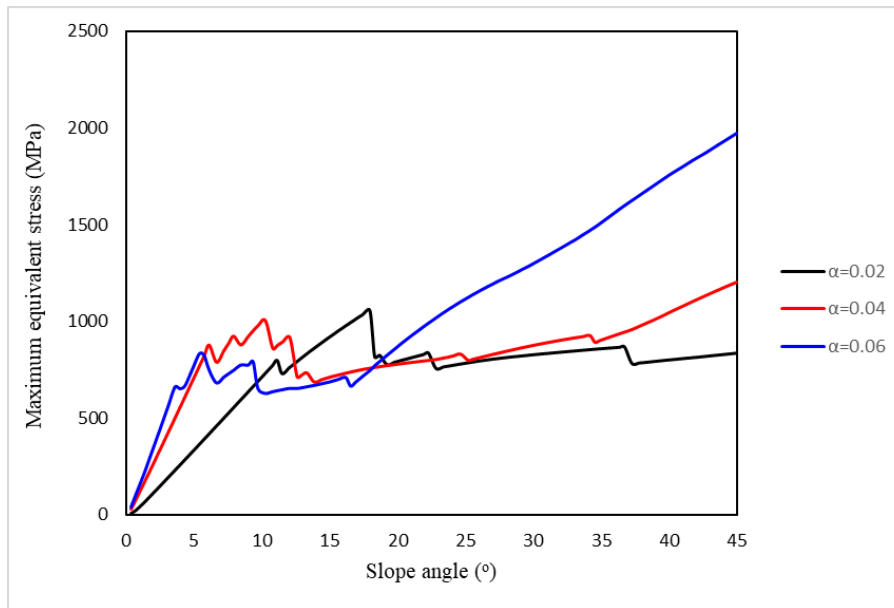


Figure 6. The effect of taper angle variation on bending angle- Maximum equivalent stress behavior

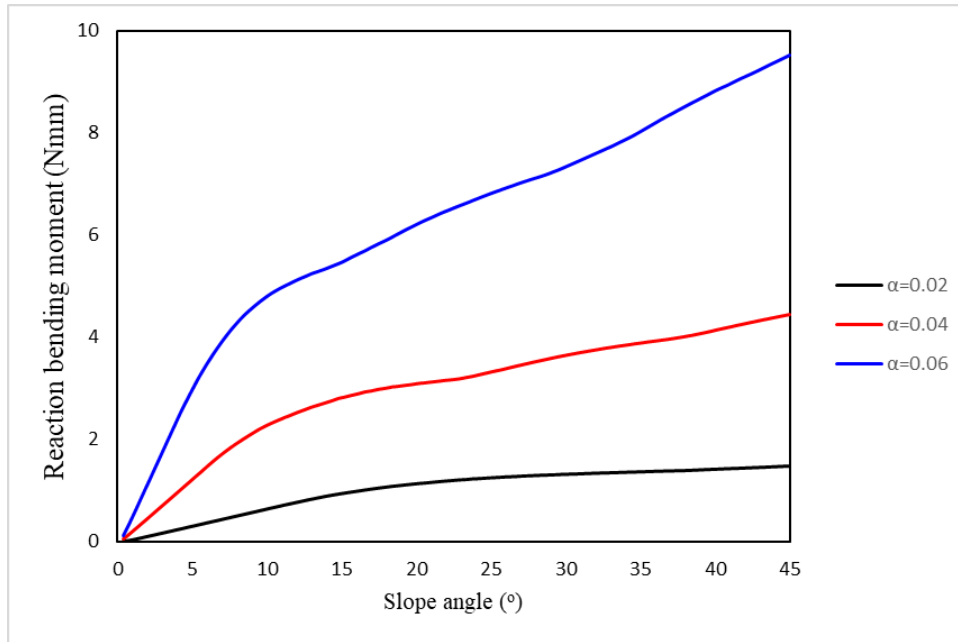


Figure 7. The effect of taper angle variation on bending angle - Reaction bending moment behavior

3.2. Torsion Test

The file models with taper angles of $\alpha=0.02$, 0.04 , 0.06 were fixed supported along a surface 3 mm from the apical end, and subsequently, a torque of 2 Nmm was applied to the surface on the coronal side. Applying a 2 Nmm moment to the Ni-Ti rotary file models showed similar behavior for each sample. As the Rotational Moment increased, the maximum equivalent stress increased linearly, found to be $\sim 400\text{ MPa}$ for $\alpha=0.06$, $\sim 700\text{ MPa}$ for $\alpha=0.04$, and $\sim 1000\text{ MPa}$ for $\alpha=0.02$. The maximum von Mises stress corresponding to the applied torque was obtained as shown in Figure 8.

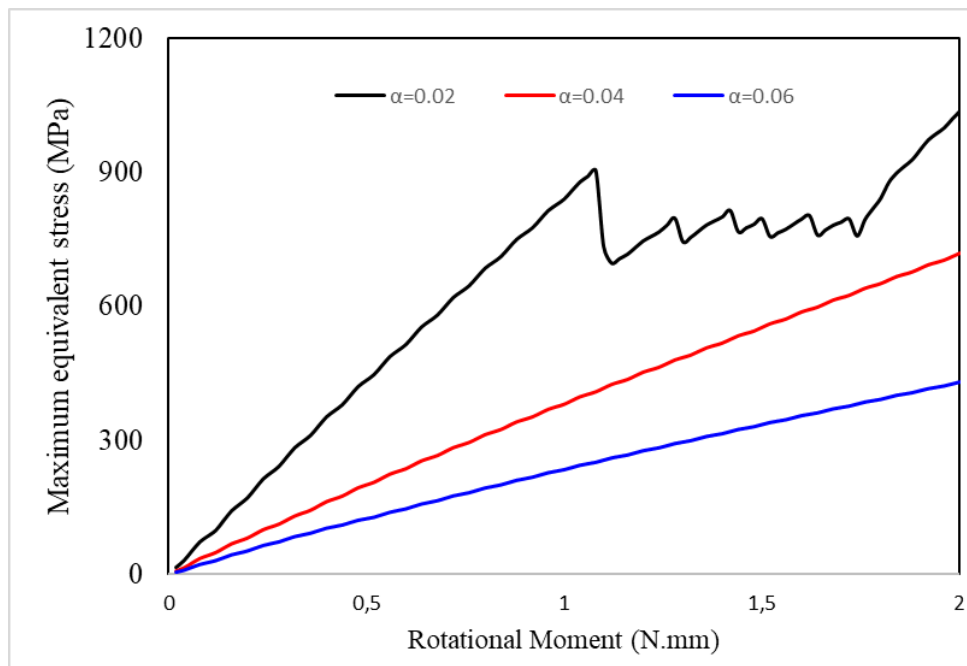


Figure 8. The effect of taper angle variation on Rotational Moment - Maximum equivalent stress behavior

In this study, the mechanical behaviors of endodontic rotary files with different taper angles during torsion and bending tests were examined using Finite Element Analysis (FEA). FEA is a numerical method capable of evaluating the mechanical behavior of an instrument, in addition to stress distribution during endodontic treatments [11-12]. FEA involves modeling a structure with loads and constraints to identify, analyze, and solve potential structural or performance issues. Moreover, FEA allows the application of different properties, such as alloy or design modifications, without causing any damage to the material. This situation enables the evaluation of the mechanical properties of rotary file systems used in endodontics by reducing time and cost [13-14]. We also used FEA in our study due to its advantages.

In superelastic material behavior, when subjected to a tensile test, the material undergoes a certain amount of deformation but recovers its shape along a different path once the force is removed [3]. Additionally, different thermomechanical treatments are applied to endodontic rotary files [15, 16]. However, the study focused on the effect of different taper angles on bending and torsional rigidity, so the ultimate differences in material properties were disregarded. This study was conducted according to ISO 3630-1 boundary conditions [4, 14, 17] and is similar to other studies evaluated with FEA. The bending and torsional properties of the files were assessed. FEA results under bending conditions show that the rotary file with a 0.02 taper angle is more flexible than those with 0.04 and 0.06 taper angles. As a result of this difference, the null hypothesis in our study was accepted. This difference can be explained by the smaller cross-sectional structure in the apical 3 mm portion of the file with a 0.02 angle. Based on these results, rotary files with lower taper angles should be used in shaping curved root canal systems. In similar clinical conditions, a file with a 0.06 taper angle would need to apply more force to the walls of the root canal to achieve the same degree of bending. This is thought to potentially cause complications such as perforations or the formation of zips in the apical region of the root canal system in teeth with curvature. However, when rotary files are placed within the root canal system, the boundary conditions can change due to varying contact points.

In the torsion test, the effect of the tool connection was simulated by fixing the instruments 3 mm from the file tip and applying a torque of 2 Nmm. According to the test results, the rotary file system with a 0.06 taper had a lower angular rotation value compared to the others. The increase in cross-section in this test reduced the stress due to an increase in the file's inertia. This also reflected in the stress behavior. In this study, the bending test was performed on the xz axis. In tests to be performed on different axes, different results can be obtained due to the pitch structure of the file. In addition the results obtained in this study are consistent with the findings of studies showing that torsional rigidity depends on the cross-sectional geometry [11, 18, 19]. Additionally, the stress levels in tools under torsion cannot be predicted solely by stiffness responses. The combination of factors such as the cross-sectional geometry of the files, their mechanical properties, the location of stress application, and the location where deformation is measured, influences the stress [2, 20].

4. Conclusion

Clinicians might prefer samples with a higher taper angle considering the stress that rotary files will be subjected to, based on their bending and torsional behavior. However, it is important to take into account that increasing the taper angle could make the movement of the file more challenging.

5. Author Contribution Statement

Mehmet Eskibağlar: Conceptualization, Methodology, Data curation, Writing-Original draft preparation;
Serkan Erdem: Visualization, Software, Validation, Investigation, Writing-Reviewing and Editing

6. Ethics Committee Approval and Conflict of Interest

The authors declare that they have no known competing financial interests or personal relationships that could have appeared to influence the work reported in this paper.

7. References

- [1] L. de Arruda Santos, J. B. López, E. B. de Las Casas, M. G. de Azevedo Bahia, and V. T. L. Buono, "Mechanical behavior of three nickel-titanium rotary files: A comparison of numerical simulation with bending and torsion tests," *Mat. Sci. and Eng.: C*, vol. 37, pp. 258-263, 2014.
- [2] H. Kim, H. Kim, C. Lee, B. Kim, J. Park, and A. Versluis, "Mechanical response of nickel–titanium instruments with different cross-sectional designs during shaping of simulated curved canals," *Internat. Endod. Jour.*, vol. 42, no. 7, pp. 593-602, 2009.
- [3] S. C. S. Martins, P. R. Garcia, A. C. D. Viana, V. T. L. Buono, and L. A. Santos, "Off-centered geometry and influence on NiTi endodontic file performance evaluated by finite element analysis," *Jour. of Mat. Eng. and Perfor.*, vol. 29, pp. 2095-2102, 2020.
- [4] P. Y. H. Chien, L. J. Walsh, and O. A. Peters, "Finite element analysis of rotary nickel-titanium endodontic instruments: a critical review of the methodology," *Europ. Jour. of Oral Sci.*, vol. 129, no. 5, p. e12802, 2021.
- [5] URL: https://bondent.eu/product_family/endo/ (Visited on Dec. 8, 2023).
- [6] URL: https://incidental.com.tr/uploads/catalogs/RubyDent_tr.pdf (Visited on Dec. 8, 2023).
- [7] URL: https://www.fkg.ch/sites/default/files/FKG_Race%20Family_Brochure_EN_WEB_202201.pdf (Visited on Dec. 8, 2023).
- [8] E. Berutti, G. Chiandussi, I. Gaviglio, and A. Ibba, "Comparative analysis of torsional and bending stresses in two mathematical models of nickel-titanium rotary instruments: ProTaper versus ProFile," *Jour. of Endod.*, vol. 29, no. 1, pp. 15-19, 2003.
- [9] O. C. Zienkiewicz, R. L. Taylor, and J. Z. Zhu, *The finite element method: its basis and fundamentals*. Elsevier, 2005.
- [10] D. R. C. Instruments—Part, "1: General requirements and test methods," Geneva, Switzerland: International Organization for Standardization, pp. 3630-1, 2008.
- [11] A. G. Ismail, M. H. A. Zaazou, M. Galal, N. O. M. Kamel, and M. A. Nassar, "Finite element analysis comparing WaveOne Gold and ProTaper Next endodontic file segments subjected to bending and torsional load," *Bull. of the Nati. Res. Cen.*, vol. 43, pp. 1-6, 2019.
- [12] N. Wakabayashi, M. Ona, T. Suzuki, and Y. Igarashi, "Nonlinear finite element analyses: advances and challenges in dental applications," *Jour. of Dent.*, vol. 36, no. 7, pp. 463-471, 2008.
- [13] A. Versluis, H.-C. Kim, W. Lee, B.-M. Kim, and C.-J. Lee, "Flexural stiffness and stresses in nickel-titanium rotary files for various pitch and cross-sectional geometries," *Jour. of Endod.*, vol. 38, no. 10, pp. 1399-1403, 2012.
- [14] N. Bonessio et al., "Validated finite element analyses of WaveOne Endodontic Instruments: a comparison between M-Wire and NiTi alloys," *Intern. Endod. Jour.*, vol. 48, no. 5, pp. 441-450, 2015.
- [15] H. S. Topçuoğlu, G. Topçuoğlu, Ö. Kafdağ, and H. Balkaya, "Effect of two different temperatures on resistance to cyclic fatigue of one Curve, EdgeFile, HyFlex CM and ProTaper next files," *Austr. Endod. Jour.*, vol. 46, no. 1, pp. 68-72, 2020.
- [16] J. N. Martins et al., "Characterization of the file-specific heat-treated ProTaper Ultimate rotary system," *Intern. Endod. Jour.*, vol. 56, no. 4, pp. 530-542, 2023.
- [17] E. C. Kökan, A. Y. Atik, Ş. Özüpek, and E. Podnos, "Structural Assessment of Endodontic Files via Finite Element Analysis," *Appl. Sci.*, vol. 13, no. 18, p. 10293, 2023.
- [18] E. Ninan and D. W. Berzins, "Torsion and bending properties of shape memory and superelastic nickel-titanium rotary instruments," *Jour. of Endod.*, vol. 39, no. 1, pp. 101-104, 2013.
- [19] R. He and J. Ni, "Design improvement and failure reduction of endodontic files through finite element analysis: application to V-Taper file designs," *Jour. of Endod.*, vol. 36, no. 9, pp. 1552-1557, 2010.
- [20] M. I. El-Anwar, S. A. Yousief, E. M. Kataia, and T. M. A. El-Wahab, "Finite element study on continuous rotating versus reciprocating nickel-titanium instruments," *Braz. Dental Jour.*, vol. 27, pp. 436-441, 2016.



LiNiO₂'nin Performans Geliştirmesi İçin Mn ve Ti Eş Katkısı

Erdoğan ÖZ^{1,2*} , Jeff DAHN³ 

¹ Fizik Bölümü, Fen Fakültesi, Atatürk Üniversitesi, Erzurum, Türkiye.

² Nanobilim ve Nanomühendislik Anabilimdalı, Fen Bilimleri Enstitüsü, Atatürk Üniversitesi, Erzurum, Türkiye.

³ Fizik ve Atmosferik Bilimler Bölümü, Dalhousie Üniversitesi, Halifax, Kanada.

^{1,2}erdinc.oz@atauni.edu.tr, ³jeff.dahn@dal.ca

Geliş Tarihi: 27.03.2024

Kabul Tarihi: 29.05.2024

Düzeltilme Tarihi: 24.05.2024

doi: 10.62520/fujece.1459826

Araştırma Makalesi

Alıntı: E. Öz ve J. Dahn, "Linio₂'nin performans geliştirmesi için mn ve ti eş katkısı", Fırat Üni. Deny. ve Hes. Müh. Derg., vol. 3, no 3, pp. 280-291, Ekim 2024.

Öz

LiNiO₂ (LNO) yüksek kapasiteye sahiptir ancak lityum-iyon pillerde pratik kullanımını sınırlayan yapısal istikrarsızlık ve kapasite azalmasından muzdariptir. Bu çalışma, bu sorunların üstesinden gelmek için bir strateji olarak LNO yapısındaki Ni bölgelerine Mn ve Ti birlikte katkılayarak LiNi_{0.95}Mn_{0.025}Ti_{0.025}O₂ (MnTi25) elde etmeyi ve fiziksel ve elektrokimyasal özelliklerini araştırmayı önermektedir. MnTi25, LNO'ya kıyasla gelişmiş yapısal kararlılık ve önemli ölçüde azaltılmış katyon karışımını ortaya çıkararak kayda değer elektrokimyasal sonuçlar vermiştir. MnTi25'in yarı hücre performansı etkileyicidir ve yerleşik %4 Mn ikameli ZoomWeMn4 standardına benzer bir kapasite sergileyerek etkili Li-iyon çıkarma ve ekleme işlemi göstermektedir. Ayrıca, grafit anoda karşı yapılan tam hücre testi, MnTi25'in ticari bir LNO bazlı malzeme ile neredeyse aynı kapasiteyi sunduğunu göstermektedir. Bu kayda değer başarı, yüksek kapasite potansiyelini korurken LNO'nun sınırlamalarını ele almada ortak katkının etkinliğini vurgulamaktadır. Bu çalışma, MnTi25'in, malzemenin yapısını Mn ve Ti birlikte katkılama yoluyla uyarlayarak yüksek performanslı lityum-iyon piller için umut verici bir katot malzemesi olabileceğini göstermektedir.

Anahtar kelimeler: Lityum-iyon bataryalar, Mn ve Ti çift katkılama, Geliştirilmiş yapısal kararlılık

*Yazışılan yazar

İntihal Kontrol: Evet– Turnitin

Şikayet: fujece@firat.edu.tr

Telif Hakkı ve Lisans: Dergide yayın yapan yazarlar, CC BY-NC 4.0 kapsamında lisanslanan çalışmalarının telif hakkını saklı tutar.



Mn and Ti Co-doping of LiNiO₂ to Improve Performance

Erdinc OZ^{1,2*} , Jeff DAHN³ 

¹Physics Department, Faculty of Science, Atatürk University, Erzurum, Türkiye.

²Nanoscience and Nanoengineering Department, Institute of Science, Atatürk University, Erzurum, Türkiye.

³Department of Physics & Atmospheric Science, Department of Chemistry, Dalhousie University, Halifax, Canada.

^{1,2}erdinc.oz@atauni.edu.tr, ³jeff.dahn@dal.ca

Received: 27.03.2024

Accepted: 29.05.2024

Revision: 24.05.2024

doi: 10.62520/fujece.1459826

Research Article

Citation: E. Oz ve J. Dahn, "Mn and Ti Co-doping of LiNiO₂ to Improve Performance", Firat Univ. Jour.of Exper. and Comp. Eng., vol. 3, no 3, pp. 280-291, October 2024.

Abstract

LiNiO₂ (LNO) has high capacity but suffers from structural instability and capacity fade, which limits its practical use in lithium-ion batteries. This study proposes co-doping LNO with Mn and Ti (MnTi25) as a strategy to overcome these issues. MnTi25 was thoroughly characterized, revealing improved structural stability and significantly reduced cation mixing compared to pristine LNO. The half-cell performance of MnTi25 is noteworthy, exhibiting a capacity similar to the established 4% Mn-substituted ZoomWeMn4 standard, demonstrating efficient Li-ion extraction and insertion. Additionally, full-cell testing against a graphite anode shows that MnTi25 delivers a capacity almost identical to a commercial LNO-based material. This promising achievement highlights the effectiveness of co-doping in addressing LNO's limitations while preserving its high-capacity potential. This study demonstrates that MnTi25 can be a promising cathode material for high-performance lithium-ion batteries by tailoring the material's structure through co-doping.

Keywords: Lithium-ion batteries, Mn and Ti dual doping, Improved structural stability

*Corresponding author

1. Introduction

Lithium-ion batteries (LIBs) reign supreme in portable electronics due to their high energy density and impressive cycle life. However, realizing their full potential for electric vehicles and grid storage demands further advancements in these aspects. In this quest, Ni-rich layered LiNiO_2 (LNO) cathodes hold immense promise, boasting a theoretical capacity surpassing 275 mAh g^{-1} [1], significantly exceeding conventional LiCoO_2 . Despite their alluring potential, practical application remains hindered by inherent drawbacks such as structural instability, voltage fade, and thermal instability, primarily stemming from Ni cation migration and oxygen loss. For example, according to the study by Yoon et al. [2], H2 - H3 phase transformations occurred in LiNiO_2 particles at 4.2 and 4.3V cut-off voltage levels, causing structural instabilities, and as a result, microcracks were observed on the particle surfaces. These cracks not only adversely affect ionic and electronic transport, causing performance losses, but also cause the electrolyte to diffuse into the particle interior, rendering the particle surface useless for redox reactions. Another situation is that when LiNiO_2 is in the state of charge (delithiation), Ni^{4+} is highly reactive and reacts with the electrolyte after Li ions leave the crystal structure. In this case, the LiNiO_2 phase usually decomposes into more stable $\text{Li}_x\text{Ni}_{1-x}\text{O}_2$ phases, O_2 and NiO [3], [4]. Different strategies such as substitution/doping of Fe [5], Al [6], and Co [7] into the crystal structure or surface coating with MgO [8], Silica [9], and AlPO_4 [10] have been tried to prevent these negative properties of NRO. However, surface coating may also increase the weight and volume of the battery, reducing its energy and power density. Surface coating may also cause interface resistance, coating cracking, or coating peeling, which may affect the cycling performance and the rate capability of the battery [11, 12].

Co-doping represents a noteworthy approach whereby two distinct atomic species within the material matrix concurrently manifest advantageous physical and electrochemical characteristics, while also offsetting each other's inherent limitations. One of the studies on co-doping LNO is on $\text{LiNi}_{0.990}\text{Al}_{0.005}\text{Ti}_{0.005}\text{O}_2$ sample synthesized by wet milling solid-state reaction method by Song et al [13]. Performance tests showed an initial capacity of 196.3 mAh/g at a current density of 0.1C and a voltage range of $2.2 - 4.4\text{V}$. On the other hand, it decreased to 113.8 mAh/g capacity after 20 cycles and showed 57.9% capacity retention. Zhou and Zheng et al. conducted another investigation on the co-doping of Mg and Al into LNO [14]. They demonstrated that the co-doping of Mg and Al inhibits the coalescence of secondary particles and facilitates Li diffusion by expanding the interlayer spacing. Based on their findings, they identified $\text{LiNi}_{0.95}\text{Al}_{0.04}\text{Mg}_{0.01}\text{O}_2$ as the optimal composition, which exhibits an initial capacity of 200.8 mAh/g and a capacity retention of 83.7% after 200 cycles at 0.5C .

Addressing these limitations has spurred extensive research into doping LNO with transition metals. Among the contenders, Mn and Ti stand out for their unique and complementary benefits: Sharing a similar ionic radius and oxidation state with Ni^{2+} , Mn^{4+} holds the potential to mitigate cation migration and stabilize the layered structure. Moreover, Mn redox contributes to the overall capacity, enhancing the theoretical energy density. For instance, Arai et al. reported 10% Mn substitution as the upper limit and obtained an initial capacity of 200 mAh/g in performance tests [15]. However, their study also highlighted the need for further optimization to address the voltage polarization observed and capacity fade after 10 cycles. Another important advantage of Mn over other dopants is its abundance and low cost [16]. Additionally, previous studies have reported that the positive effect of Mn doping on the thermal stability of LiNiO_2 cathode material is similar to that of Ti and far superior to that of Co doping [17]. With its exceptional oxygen affinity, Ti^{4+} can act as an "electronic pillar," stabilizing the Ni oxidation state and reducing voltage fade. In contrast, Ti^{4+} ions exhibit a greater preference for occupying transition metal (Mn^{4+} , Ni^{3+} , etc.) sites compared to Li^+ sites. This preference arises from the differing energetic costs associated with substituting Li^+ or transition metals with Ti^{4+} at these distinct lattice positions. The substitution of Ti^{4+} into transition metal sites leads to an expansion of the interplanar spacing and unit cell volume, which can facilitate the lithium insertion/extraction process [18]. Kim and Amine prevented the migration of Ni^{2+} ions to the Li sites by substituting Ti^{4+} for Ni sites in LiNiO_2 . This reduced the capacity loss by decreasing the cation mixing ratio [19]. Their results showed that $\text{LiNi}_{1-x}\text{Ti}_x\text{O}_2$ ($0.025 < x < 0.2$) materials had an initial capacity of 240 mAh/g and maintained high-capacity retention after 100 cycles. It is important to note that if the Ti substitution rate exceeds $x=0.25$, the Ni^{2+} ions formed for charge balancing will begin to occupy the Li sites, resulting in a

loss of capacity. Additionally, highly substituted Ti ions may settle between the layers of the crystal structure instead of occupying Ni sites, which could negatively impact both ionic and electronic diffusion.

While previous studies have explored the individual merits of Mn and Ti doping on LNO, their independent approaches may not fully address the multifaceted challenges faced by these cathodes. Recognizing this gap, this study delves into the synergistic effects of co-doping LNO with 0.25 mol Mn and 0.25 mol Ti on the cathode material's physical and electrochemical performances. By systematically characterizing the doped LNO material and evaluating its electrochemical performance, we aim to contribute to the development of high-performance Ni-rich cathodes, advancing the potential of LIBs for next-generation energy storage applications.

2. Material and Method

2.1. Material Synthesis

In the context of our experimental investigation, we synthesized the $\text{Ni}_{0.974}\text{Mn}_{0.026}(\text{OH})_2$ precursor using the co-precipitation method within a continuously stirred tank reactor (CSTR) (Brunswick Scientific/Eppendorf BioFlo 310). The principal advantages of the coprecipitation method are the simultaneous mixing of transition metals at the atomic level, the achievement of the requisite phase and crystallization at relatively mild sintering temperatures, and the retention of time [20]. Aqueous solutions of $\text{Ni}(\text{SO}_4 \cdot 6\text{H}_2\text{O})$ (98%, Alfa Aesar) and $\text{Mn}(\text{SO}_4)$ (98%, Alfa Aesar) were meticulously prepared, maintaining the specified Ni:Mn molar ratios. The Nickel and Manganese reagents were combined into a single solution (400 mL, 2 M). Subsequently, these solutions were added dropwise in a simultaneous manner, utilizing peristaltic pumps, to a stirred reaction vessel containing NH_3 solution (1 L, 1 M). To maintain a precise pH concentration (pH 11.0 and 0.5 M NH_3), we introduced a NaOH solution (98%, Alfa Aesar) (10 M) and an NH_3 solution (5 M). For 20 hours, the solutions were gradually incorporated into the reaction vessel, which was maintained at 60 °C, stirred at 900 rpm, and placed under an N_2 atmosphere. Following the reaction, the vessel was cooled to room temperature, and the resulting precipitate was meticulously filtered and rinsed four times with deionized water. Finally, the precipitate was dried overnight at 100 °C in ambient air (Figure 1a).

The process of inserting Li into the precursor crystal structure is called "lithiation". In this step, the precursor and a lithium source are physically mixed and heat-treated at high temperature. Carbonate or hydroxide compounds can be used as lithium sources. The lithiation step was carried out for $\text{Li}_2\text{CO}_3:\text{Ni}_{0.974}\text{Mn}_{0.026}(\text{OH})_2:\text{TiO}_2$ using the 1.02:0.95:0.025 ratios. In the first lithiation step, the samples were ground by hand, heat treated at 480 °C for 3 hours, and cooled to room temperature. The objective of this step is to remove carbonate from Li_2CO_3 and water from the $\text{Ni}_{0.974}\text{Mn}_{0.026}(\text{OH})_2$. Then the samples were ground again by hand for 15 minutes and then heated up at 825 °C for 20 hours in O_2 atmosphere. The purpose of the second lithiation step is to allow Li^+ , Ti^{+4} and O_2 released from the Li source to diffuse into the $\text{Ni}_{0.974}\text{Mn}_{0.026}(\text{OH})_2$ (Figure 1b).

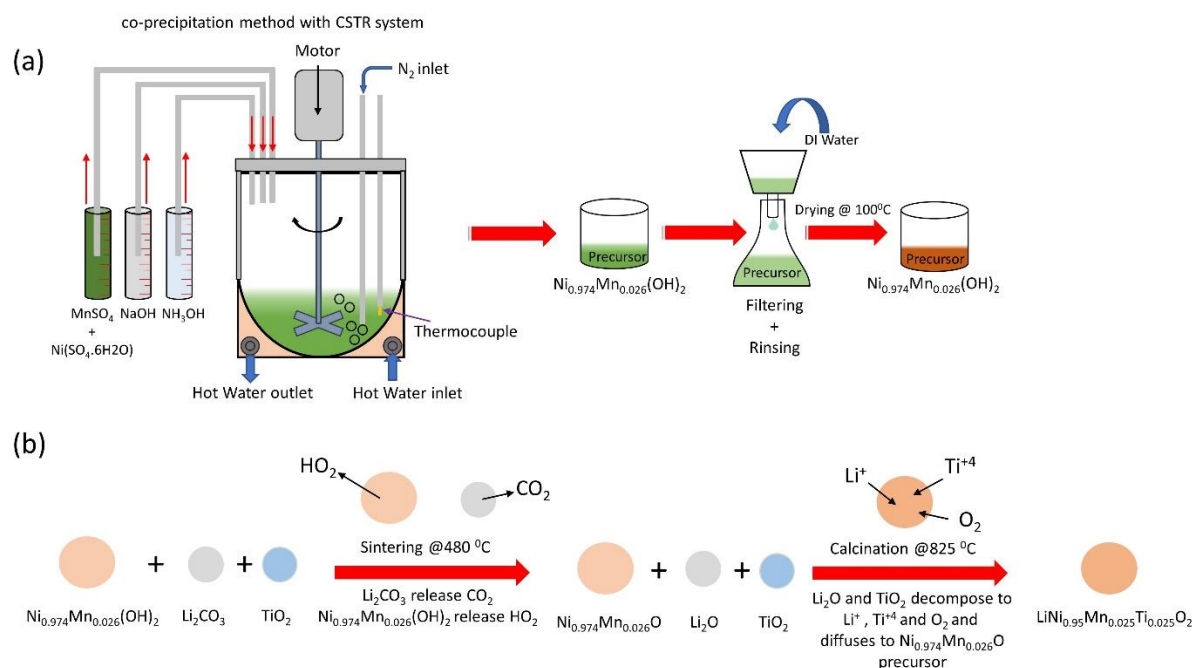


Figure 1. (a) Synthesis process of precursor by co-precipitation using CSTR. (b) Schematic representation of the lithiation step of the precursor

To compare the MnTi25 sample with a standard sample, $Ni_{0.96}Mn_{0.04}(OH)_2$ precursor was obtained from ZoomWe (Hunan ZoomWe Zhengyuan Advanced Material Trade Company, Ltd., Changsha 410000, China). To obtain $LiNi_{0.96}Mn_{0.04}O_2$ (ZoomWeMn4), the same lithiation steps as MnTi25 were applied.

2.2. Physical Characterization

X-ray diffraction (XRD) patterns were acquired using a Siemens D5 diffractometer equipped with a copper (Cu) target X-ray tube and a diffracted beam monochromator. The samples were meticulously analyzed within a scattering angle (2θ) range from 15° to 80° , with data collection intervals of 0.02° over 3 seconds. Scanning electron microscopy (SEM) imaging was conducted using a Hitachi S4700 Scanning Electron Microscope equipped with a backscattered electron detector. Before imaging, the samples were meticulously prepared by affixing the powders onto adhesive carbon tape. The resulting images were captured under an accelerating voltage of 3 kV and a current of $20 \mu A$. Particle size analyses of the samples were made with a Partica laser scattering particle size distribution analyzer (Horiba). An ICP-MS (Thermo Fisher Scientific, MA, USA) paired with an ESI SC-4DXS autosampler (Elemental Scientific, NE, USA) was used for sample elemental distribution analysis. Standard samples of the elements to be measured were prepared as 4ppm, 2ppm, and 1ppm standards.

2.3. Electrochemical Characterization

A mixture was made by Super-S carbon black (Timcal) as the active material, polyvinylidene fluoride (PVDF, Arkema, Kynar 301F) as the binder, and N-methyl-2-pyrrolidone (NMP, Sigma-Aldrich, 99.5%) as the solvent in a weight ratio of 92:4:4. The resulting slurry was coated onto aluminum foil using a $150 \mu m$ high-adjustable doctor blade and dried in a vacuum oven at $110^\circ C$. The dried electrodes were then calendared under pressure and punched into circular discs (1.25 cm diameter) with an electrode material loading of $10\text{--}12 \text{ mg.cm}^{-2}$. The discs were subsequently dried overnight in a vacuum at $110^\circ C$.

For the half-cell performances, positive electrodes were used as cathode, Li metal as anode material, and Celgard 2032 membrane as a separator with the electrolyte of 1.2 M $LiPF_6$ (BASF, 99.9%) in a mixture of

fluoroethylene carbonate (FEC) and dimethyl carbonate (DMC) was used as the electrolyte (FEC: DMC 1:4 v/v). A 2032 type coin cell battery was used for the tests and all assemblies were performed in an Ar-filled glove-box.

For full cells, the negative/positive electrode capacitance ratio should be 1.0-1.5. Outside this range, rapid capacity losses are observed in full cells. During the production of the positive electrode, the mixing ratios stated above for the half-cell were used. For slurry to be used more efficiently during coating, the total solid mixture/NMP ratio varies between 1.0 and 1.5. Graphite (Novonix) with a capacity of 3 mAh/cm² coated on copper foil was used as the negative electrode in full cells. The discs used as negative electrodes were punched to be 12.75 mm in diameter. Since the punched discs for the positive electrode have a constant radius (11.25 mm) and to provide the N/P ratio in full cells, different thicknesses were tried during the coating of the slurry on aluminum foil. 1.2 M LiPF₆ in EC: DMC 3:7 w/w were used as electrolyte. In addition, 2% FEC and 1% LFO (lithium difluorophosphate) were added to the electrolyte solution. About 10 microliters of electrolyte are used in each battery. BMF (Polypropylene Blown Micro Fiber available from 3M Company) separator was used as a membrane. Since this membrane has a thicker structure compared to Celgard, a one-piece BMF membrane disc was used in each battery.

3. Results and Discussions

Figure 2 shows the XRD patterns of the powder samples obtained after the final heat treatment. Both samples were found to be isostructural with LiNiO₂, which has a rhombohedral layered structure (R-3m)[21]. The XRD peaks of the commercial standard ZoomWeMn4 sample and the MnTi25 samples are identical, as shown in Figure 1a. The MnTi25 sample is very similar to the standard in the separation of the (018) and (110) peaks, which is indicative of good crystallization (Figure 2b). However, no impurity peak was observed in the impurity region of both samples (Figure 2c). The crystal structure and refinement parameters are shown in Table 1. The results of the calculations indicate that the *a* lattice parameter of the MnTi25 sample increased by 0.31% and the *c* parameter increased by 0.27% in comparison to the standard ZoomWeMn4 sample.

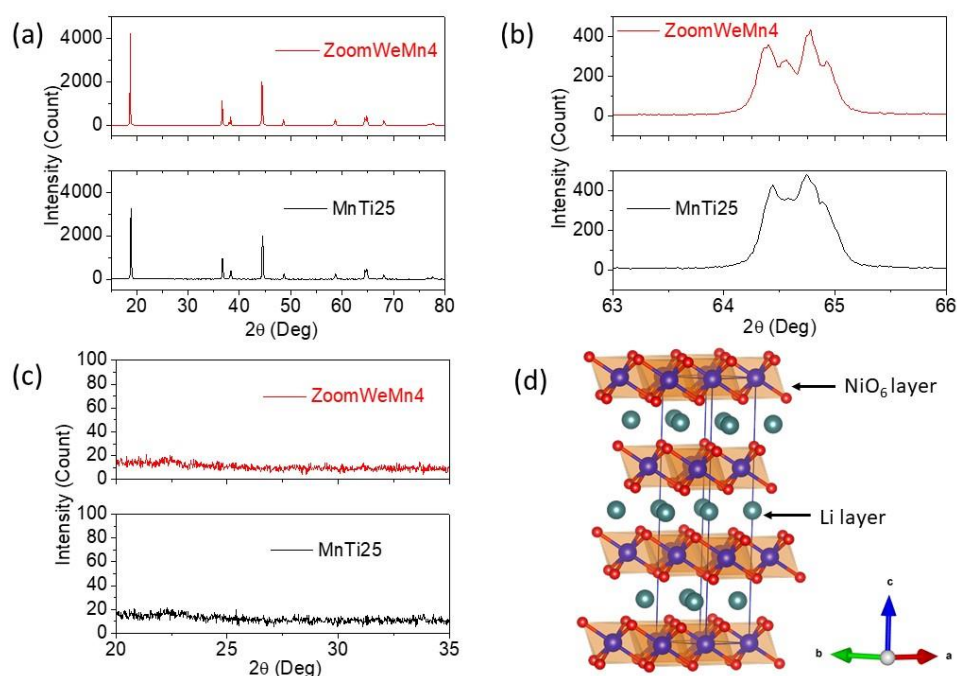


Figure 2. (a) XRD diffraction patterns of MnTi25 and ZoomWe Mn4 samples. (b) Peak splitting of (018) and (110) reflections, indicating the degree of crystallization. (c) Impurity region from 20 to 30°. (d) Layered structure of LiNiO₂ crystal, plotted using refinement results

LNO has a layered structure consisting of Li and NiO₆ layers (Figure 2d). To maintain charge neutrality, Ni³⁺ ions are inherently present within the crystal lattice. However, during the synthesis process, Ni²⁺ ions are generated and exhibit a propensity to migrate toward the Li layers—a phenomenon commonly referred to as ‘cation mixing’ (Ni_{Li}) [22]. Notably, due to the distinct ionic radii of Ni²⁺, which is larger than that of Ni³⁺ and smaller than that of Li⁺, the incorporation of Ni²⁺ within the crystal structure results in contrasting effects. Specifically, the Li plates shrink, while the Ni plates expand [23]. This negatively affects the Li diffusion into the crystal structure during charge/discharge cycles. Previous studies have reported that Mn substitution into Ni sites in LiNiO₂ predominantly results in the Mn⁴⁺ oxidation state [24]. This substitution leads to a discernible increase in *c* (three times the interslab distance) parameters, attributed to the smaller ionic radius of Mn⁴⁺ compared to Ni³⁺. On the other hand, the Ti tends to exist in LiNiO₂ as Ti⁴⁺, which is more stable than Ti³⁺, and the ionic radius of Ti⁴⁺ is larger than that of Ni³⁺ [23], Ti⁴⁺ substituting Ni sites causes an increase in the crystal structure parameters. However, an increase in the incorporation of both Ti⁴⁺ and Mn⁴⁺ leads to enhanced cation mixing within the crystal lattice, due to the induced transformation of Ni³⁺ to Ni²⁺ to maintain charge balance. Consequently, an increase in the Ni_{Li} cation mixture was observed, but *c/a*, an indicator of trigonal distortion, decreased.

Table 1. The Lattice and the Refinement parameters of the samples

Sample	Lattice parameters			Refinement parameters		
	<i>a=b</i> (Å)	<i>c</i> (Å)	<i>c/a</i>	χ^2	R _{wp}	Ni _{Li} (%)
ZoomWe Mn4	2.872	14.183	4.938	0.624	13.02	0.7
MnTi25	2.881	14.221	4.936	0.685	12.51	4.9

SEM images of the samples at different magnifications are presented in Figure 3. The Ni_{0.974}Mn_{0.026}(OH)₂ precursor, obtained through CSTR, exhibits a spherical structure (Figure 3a). The precursors are formed by the aggregation of smaller primary particles while forming the spherical structure, as seen in the figure. The overall structure of the samples is homogeneously distributed and has a similar spherical structure (Figure 3b). After the lithiation step, the MnTi25 sample maintained its spherical structure but transformed into a more rectangular shape due to the addition of Li to the primary particles (Figure 3c). The sample's particle distribution consists of spherical structures with a uniform distribution (Figure 3d).

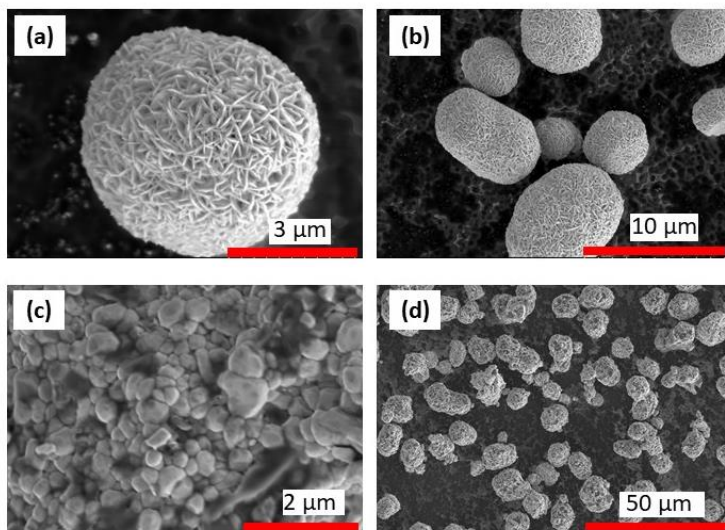


Figure 3. SEM image in different magnifications of precursors (a)-(b), and MnTi25 samples (c)-(d)

The ICP-MS measurements were used to analyze the atomic ratios of all elements in the samples. The atomic ratios of Li:Ni:Mn:Ti in standard ZoomWeMn4 and MnTi25 are 1.057:1.938:0.0417:0 and 1.073:0.945:0.0279:0.0267, respectively, which are very close to the desired stoichiometries. Figure 4 shows the average particle size distribution of the samples. The average particle size of the ZoomWeM4 material used as a commercial standard is observed to be 15 μm with a single peak, while the MnTi25 sample has approximately 10 μm (75%) and 92 μm (25%) with double peaks. This can be seen as an indication that some secondary particles agglomerate to form larger secondary particles.

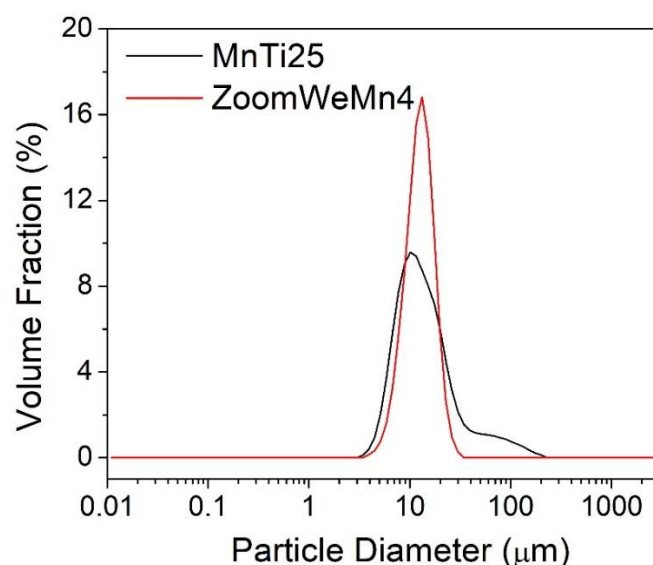


Figure 4. Particle size distribution of the standard ZoomWeMn4 and MnTi25 samples

Figure 5 shows the differential capacity as a function of voltage, half-cell cyclic, and current density performances of standard ZoomWeMn4 and MnTi25. The redox peaks observed in the dQ/dV profiles correspond to multiple phase transitions in the material (Figure 5a-b). These transitions are associated with abrupt changes in the lattice parameters, such as contraction and expansion, and the ordering of lithium ions and vacancies within the crystal structure [25]. In the cathode material composed of lithium nickel oxide (LNO), as lithium ions depart from the crystal lattice, the structural arrangement undergoes a sequence of transitions: hexagonal (H1) to monoclinic (M), followed by another transition to hexagonal (H2), and finally to hexagonal (H3) [25], [26] (Figure 5a-b). Sharp redox peaks in the dQ/dV curves typically signify abrupt and potentially harmful structural alterations. Therefore, a broad redox peak with diminished intensity, which suggests an extended phase transition, is more desirable for maintaining structural stability [27], [28]. When considering this, it is clear that the broader redox peaks of MnTi25 indicate suppression of abrupt phase transitions. Furthermore, the intensity of the redox peak that represents the $H2 \rightleftharpoons H3$ phase transition at $\sim 4.1\text{V}$, which is considered to be responsible for the loss of LNO capacity [29], [30], is reduced in MnTi25.

The long cycle and Coulombic efficiency performances of the samples are shown in Figure 5c. The MnTi25 cathode performance starts with a specific capacity of 196.6 mAh/g while the standard cathode starts with 194.4 mAh/g. After 100 cycles, the MnTi25 and standard cathode have a specific capacity of 166.7 mAh/g and 164.5 mAh/g, respectively. This result shows that MnTi25 and standard cathode materials have 84.8% and 84.6% capacity retention, respectively. On the other hand, both cathode materials consistently deliver 99% Coulombic efficiency over 100 cycles.

A comparison of the current density performance of the cathode materials at C/20, C/10, C/5, C, and 2C is presented in Figure 5d. The rate capacity graphs of both samples exhibit similar values and a consistent change trend. At a current density of C/20, the MnTi25 and ZoomWeMn4 samples demonstrated capacities of 210.18 mAh/g and 212.86 mAh/g, respectively. However, upon increasing the current density to 2C, a notable decrease in capacity was observed. Specifically, the capacities of the MnTi25 and ZoomWeMn4 samples diminished to 179.63 mAh/g and 183.50 mAh/g, respectively. This phenomenon signifies a capacity retention of 85.5% for MnTi25 and 86.2% for ZoomWeMn4 when the current density was amplified by 40. However, it's worth noting that the MnTi25 sample exhibits a very notable capacity retention. Despite the increase in current density by a factor of 40, MnTi25 manages to retain over 85.5% of its capacity. This is a significant performance characteristic, indicating the stability of MnTi25 under conditions of increased current density.

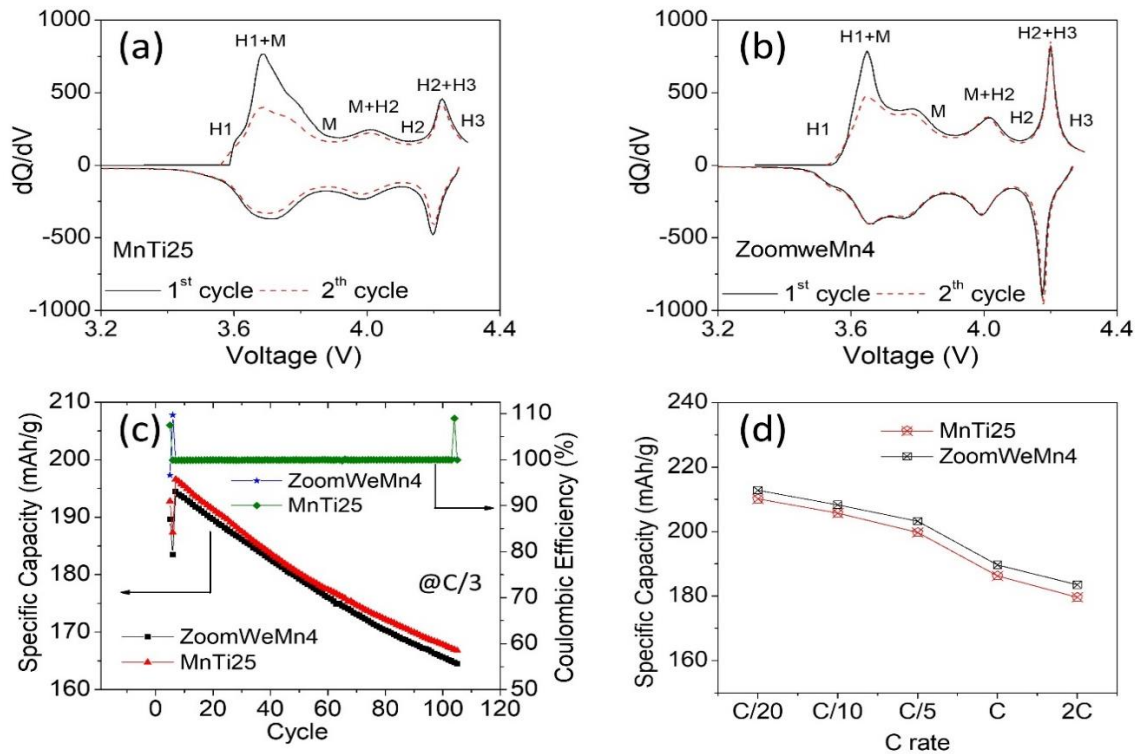


Figure 5. Capacity performance of MnTi25 and ZoomWe Mn4 samples within 3.0 - 4.3V: (a) cycling stability and Coulombic efficiency at C/3 current density for 100 cycles, (b) rate capability at various current densities, and (c) normalized capacity as a function of cycle number

Figure 6 shows the comprehensive depiction of formation cycles at C/20 and full cell performance of the samples against the graphite anode in the voltage range of 3.0-4.2 V at C/3 current density. The first two formation charge/discharge cycles of MnTi25 and ZoomWeMn4 samples at C/20 are shown in Figures 6a and b. During the initial operation of the cells, formation cycles are applied to ensure the controlled formation of the Solid Electrolyte Interphase (SEI). The loss of Li due to irreversible reactions on graphite is referred to as 'irreversible capacity loss' and is considered a loss of cell capacity. The hysteresis observed during the formation cycles at 3.0 V may indicate irreversible capacity loss. An increase in hysteresis is indicative of an increase in capacity loss between cycles. The narrow hysteresis observed in the MnTi25 sample (Figure 6a), similar to the standard sample (Figure 6b), indicates a low level of irreversible capacity loss. The performance graphs (Figure 6c) show that the MnTi25 sample starts with a capacity of 190.8 mAh/g and maintains 178.5 mAh/g over 50 cycles, demonstrating a capacity retention of 93.7%. Similarly, the ZoomWeMn4 sample begins with a capacity of 188.8 mAh/g, holds 176.5 mAh/g after the cycles, and shows a capacity retention of 93.5%.

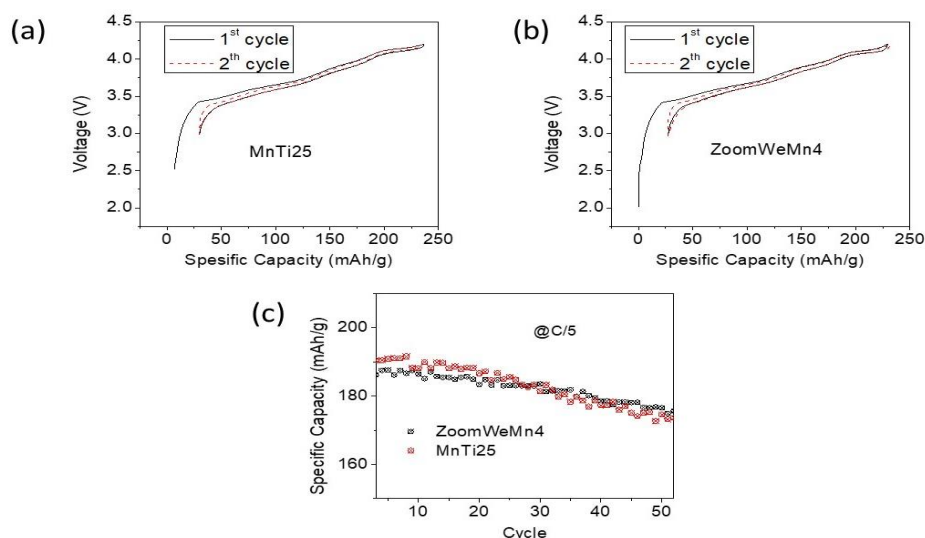


Figure 6. Initial full-cell charge/discharge curves of (a) MnTi25 and (b) ZoomWe Mn4 samples at C/20 current density within 3.0-4.2V. (c) The performance capacity of the samples for 50 cycles at a C/5 current density

The decrease in capacity performance of MnTi25 can be attributed to the increase in cation mixing: Substituting Mn^{4+} and Ti^{4+} reduces Ni^{3+} to Ni^{2+} to maintain charge balance. Li^+ ions leave the crystal structure and form vacancies during charging, and some Ni^{2+} ions can migrate from transition metal slabs into these vacancies due to their similar radii to Li^+ , and increase the cation mixing. The migration of Ni^{2+} ions into vacancies prevents Li^+ ion diffusion into slabs and migration into vacancies during discharge, resulting in capacity loss. Another factor is that Mn^{4+} and Ti^{4+} ions are electrochemically inactive and do not contribute to the redox reactions [24], [31]. However, considering both half-cell and full-cell performances, Mn and Ti co-substitution improved capacity retention. When comparing the two samples, the Mn content of MnTi25 is reduced compared to the standard sample and Ti is substituted instead. The fact that the capacity retention of the MnTi25 sample is noticeably higher in battery performance tests demonstrates that the Ti substitution makes a positive contribution to performance. This is explained by the fact that although Ti is electrochemically inactive, the Ti-O bonds are stronger than the Ni-O and Mn-O bonds and prevent degradation of the crystal structure during charging/discharging [32].

4. Conclusion

In this study, the effects of Mn and Ti co-doping on the physical and electrochemical properties of LiNiO_2 cathode material for lithium-ion batteries were investigated. It was found that Ti doping enhanced the structural stability, and cycling stability of Mn-doped LiNiO_2 while maintaining its high-capacity potential. The co-doped material, MnTi25, delivered a capacity of 190.8 mAh/g in full cells against a graphite anode, with a capacity retention of 93.7% after 50 cycles. The MnTi25 material also exhibited a remarkable rate capability, retaining over 85.5% of its capacity when the current density was increased by 40 times. These results indicate that MnTi25 can be a promising cathode material for high-performance lithium-ion batteries, by modifying the material's structure through co-doping. This study contributes to developing Ni-rich cathodes, advancing the potential of lithium-ion batteries for next-generation energy storage applications.

5. Future Works

The present study successfully demonstrates that co-doping the LNO material with Mn and Ti leads to significant improvements in its structural and electrochemical properties. These results pave the way for further exploration of the influence of varying Mn and Ti dopant ratios. Optimization of this dopant ratio represents a promising avenue for achieving superior performance characteristics. Future work will involve

the synthesis of LNO materials with a systematic variation in the Mn:Ti ratio. These materials will be carefully characterized to determine the optimal dopant ratio that maximizes the desired structural and electrochemical properties. In addition, the performance of these optimized LNO cathodes will be evaluated in various battery configurations, including different electrolytes and cell designs. This comprehensive approach will not only provide valuable insights into the structure-property relationships in Mn-Ti co-doped LNO, but will also guide the development of high-performance lithium-ion battery cathodes.

6. Acknowledgements

EO would like to thank TUBITAK for funding his research with the 2219 International Postdoctoral Research Fellowship Program for Turkish Citizens. The authors thank NSERC and Tesla Canada for the funding under the auspices of the Alliance Grants program.

7. Credit Authorship Contribution Statement

Erdinc Oz: Conceptualization, Data curation, Formal analysis, Investigation, Methodology, Validation, Visualization, writing – original draft, Writing - review & editing. Jeff Dahn: Investigation, Supervision, Review & editing.

8. Ethics Committee Approval and Conflict of Interest

The authors declare that they have no known competing financial interests or personal relationships that could have appeared to influence this work.

9. References

- [1] J. R. Dahn, U. von Sacken, and C. A. Michal, "Structure and electrochemistry of $\text{Li}_{1\pm y}\text{NiO}_2$ and a new Li_2NiO_2 phase with the Ni (OH) $_2$ structure," *Sol. State Ion*, vol. 44, no. 1–2, pp. 87–97, Dec. 1990.
- [2] C. S. Yoon, D. W. Jun, S. T. Myung, and Y. K. Sun, "Structural Stability of LiNiO_2 Cycled above 4.2 v," *ACS Ener. Lett*, vol. 2, no. 5, pp. 1150–1155, May 2017.
- [3] J. Xu et al., "Elucidation of the surface characteristics and electrochemistry of high-performance LiNiO_2 ," *Chem. Comm.*, vol. 52, no. 22, pp. 4239–4242, Mar. 2016.
- [4] J. Xu et al., "Understanding the degradation mechanism of lithium nickel oxide cathodes for Li-ion batteries," *ACS Appl Mater Inter.*, vol. 8, no. 46, pp. 31677–31683, Nov. 2016.
- [5] J. N. Reimers, E. Rossen, C. D. Jones, and J. R. Dahn, "Structure and electrochemistry of $\text{Li}_x\text{Fe}_y\text{Ni}_{1-y}\text{O}_2$," *Sol. State Ion*, vol. 61, no. 4, pp. 335–344, Jun. 1993.
- [6] T. Ohzuku, A. Ueda, and M. Kouguchi, "Synthesis and Characterization of $\text{LiAl}_{1/4}\text{Ni}_{3/4}\text{O}_2$ (R $\bar{3}m$) for Lithium-Ion (Shuttlecock) Batteries," *J. Electr. Soc*, vol. 142, no. 12, pp. 4033–4039, Dec. 1995.
- [7] A. Rougier, I. Saadoune, P. Gravereau, P. Willmann, and C. Delmas, "Effect of cobalt substitution on cationic distribution in $\text{LiNi}_{1-y}\text{Co}_y\text{O}_2$ electrode materials," *Sol. State Ion*, vol. 90, no. 1–4, pp. 83–90, Sep. 1996.
- [8] H. J. Kweon, S. J. Kim, and D. G. Park, "Modification of $\text{Li}_x\text{Ni}_{1-y}\text{Co}_y\text{O}_2$ by applying a surface coating of MgO ," *J Pow. Sour.*, vol. 88, no. 2, pp. 255–261, Jun. 2000.
- [9] H. Omanda, T. Brousse, C. Marhic, and D. M. Schleich, "Improvement of the Thermal Stability of $\text{LiNi}_{0.8}\text{Co}_{0.2}\text{O}_2$ Cathode by a SiO_x Protective Coating," *J. Electr. Soc*, vol. 151, no. 6, p. A922, May 2004.
- [10] J. Cho, T.-J. Kim, J. Kim, M. Noh, and B. Park, "Synthesis, Thermal, and Electrochemical Properties of AlPO_4 -Coated $\text{LiNi}_{0.8}\text{Co}_{0.2}\text{O}_2$ Cathode Materials for a Li-Ion Cell," *J. Electr. Soc*, vol. 151, no. 11, p. A1899, Oct. 2004.
- [11] H. Qian et al., "Surface Doping vs. Bulk Doping of Cathode Materials for Lithium-Ion Batteries: A Review," *Elect. Ener. Rev.*, vol. 5, no. 4, pp. 1–32, Nov. 2022.

- [12] T. F. Yi, X. Y. Li, H. Liu, J. Shu, Y. R. Zhu, and R. S. Zhu, "Recent developments in the doping and surface modification of LiFePO₄ as cathode material for power lithium ion battery," *Ion. (Kiel)*, vol. 18, no. 6, pp. 529–539, Jun. 2012.
- [13] M. Y. Song, C. K. Park, S. Do Yoon, H. R. Park, and D. R. Mumm, "Electrochemical properties of LiNi_{1-y}MyO₂ (M = Ni, Ga, Al and/or Ti) cathodes," *Ceram Int*, vol. 35, no. 3, pp. 1145–1150, Apr. 2009.
- [14] L. Shen et al., "Cobalt-free nickel-rich cathode materials based on Al/Mg co-doping of LiNiO₂ for lithium ion battery," *J. Coll. Inter. Sci*, vol. 638, pp. 281–290, May 2023.
- [15] H. Arai, S. Okada, Y. Sakurai, and J. Yamaki, "Electrochemical and Thermal Behavior of LiNi_{1-z}MzO₂ (M = Co, Mn, Ti)," *J. Electr. Soc*, vol. 144, no. 9, pp. 3117–3125, Sep. 1997.
- [16] L. Mu et al., "Structural and Electrochemical Impacts of Mg/Mn Dual Dopants on the LiNiO₂ Cathode in Li-Metal Batteries," *ACS Appl Mat. Inter.*, vol. 12, no. 11, pp. 12874–12882, Mar. 2020.
- [17] H. Arai, S. Okada, Y. Sakurai, and J. Yamaki, "Electrochemical and Thermal Behavior of LiNi_{1-z}MzO₂ (M = Co, Mn, Ti)," *J. Electr. Soc*, vol. 144, no. 9, pp. 3117–3125, Sep. 1997.
- [18] H. Yang et al., "Simultaneously Dual Modification of Ni-Rich Layered Oxide Cathode for High-Energy Lithium-Ion Batteries," *Adv Funct Mater*, vol. 29, no. 13, p. 1808825, Mar. 2019.
- [19] J. Kim and K. Amine, "The effect of tetravalent titanium substitution in LiNi_{1-x}TixO₂ (0.025 ≤ x ≤ 0.2) system," *Electr. Comm.*, vol. 3, no. 2, pp. 52–55, Feb. 2001.
- [20] Z. Xu et al., "Effects of precursor, synthesis time and synthesis temperature on the physical and electrochemical properties of Li(Ni_{1-x-y}CoxMny)O₂ cathode materials," *J. Pow. Sour.*, vol. 248, pp. 180–189, Feb. 2014.
- [21] T. Ohzuku, A. Ueda, and M. Nagayama, "Electrochemistry and Structural Chemistry of LiNiO₂ (R3m) for 4 Volt Secondary Lithium Cells," *J. Electr. Soc*, vol. 140, no. 7, pp. 1862–1870, Jul. 1993.
- [22] R. A. Yuwono et al., "Evaluation of LiNiO₂ with minimal cation mixing as a cathode for Li-ion batteries," *Chem.l Eng. Jour.*, vol. 456, p. 141065, Jan. 2023.
- [23] R. D. Shannon and IUCr, "Revised effective ionic radii and systematic studies of interatomic distances in halides and chalcogenides," *0567-7394*, vol. 32, no. 5, pp. 751–767, Sep. 1976.
- [24] T. Xu, F. Du, L. Wu, Z. Fan, L. Shen, and J. Zheng, "Boosting the electrochemical performance of LiNiO₂ by extra low content of Mn-doping and its mechanism," *Electr. Acta*, vol. 417, p. 140345, Jun. 2022.
- [25] W. Li, J. N. Reimers, and J. R. Dahn, "In situ x-ray diffraction and electrochemical studies of Li_{1-x}NiO₂," *Sol. State Ion*, vol. 67, no. 1–2, pp. 123–130, Dec. 1993.
- [26] H. Arai, S. Okada, Y. Sakurai, and J. I. Yamaki, "Reversibility of LiNiO₂ cathode," *Sol. State Ion*, vol. 95, no. 3–4, pp. 275–282, Mar. 1997.
- [27] C. S. Yoon et al., "Cation Ordering of Zr-Doped LiNiO₂ Cathode for Lithium-Ion Batteries," *Chem. of Mat.*, vol. 30, no. 5, pp. 1808–1814, Mar. 2018.
- [28] U. H. Kim et al., "Microstructure-Controlled Ni-Rich Cathode Material by Microscale Compositional Partition for Next-Generation Electric Vehicles," *Adv Ener. Mater*, vol. 9, no. 15, p. 1803902, Apr. 2019.
- [29] H. H. Ryu, K. J. Park, C. S. Yoon, and Y. K. Sun, "Capacity fading of ni-rich li[NixCoyMn1-x-y]O₂ (0.6 ≤ x ≤ 0.95) Cathodes for High-Energy-Density Lithium-Ion Batteries: Bulk or Surface Degradation?," *Chem. of Mat.*, vol. 30, no. 3, pp. 1155–1163, Feb. 2018.
- [30] H. H. Ryu, G. T. Park, C. S. Yoon, and Y. K. Sun, "Suppressing detrimental phase transitions via tungsten doping of LiNiO₂ cathode for next-generation lithium-ion batteries," *J. Mat. Chem A Mater*, vol. 7, no. 31, pp. 18580–18588, Aug. 2019.
- [31] Y. Yao, "The effect of electrochemically inactive Ti substituted for Ru in Li₂Ru_{1-x}TixO₃ on structure and electrochemical performance," *Jour. of Ener. Chem.*, vol. 60, pp. 222–228, Sep. 2021.
- [32] B. Zong, "Influence of Ti doping on microstructure and electrochemical performance of LiNi_{0.5}Mn_{1.5}O₄ cathode material for lithium-ion batteries," *Mater Today Commun*, vol. 24, p. 101003, Sep. 2020.



Kuvvetli Rüzgar Etkisindeki Minarenin Göçme Mekanizmasının Simülasyonu

Taha Yasin ALTIOK^{1*} , Ali DEMİR² 

^{1,2}İnşaat Mühendisliği Bölümü, Mühendislik Fakültesi, Manisa Celal Bayar Üniversitesi, Manisa, Türkiye.

¹taha.altio@cbu.edu.tr, ²ali.demir@cbu.edu.tr

Geliş Tarihi: 28.03.2024
Kabul Tarihi: 03.06.2024

Düzeltilme Tarihi: 01.05.2024

doi: 10.62520/fujece.1460766
Araştırma Makalesi

Alıntı: T. Y. Altio ve A. Demir, "Kuvvetli rüzgar etkisindeki minarenin göçme mekanizmasının simülasyonu", Fırat Üni. Deny. ve Hes. Müh. Derg., vol. 3, no 3, pp. 292-312, Ekim 2024.

Öz

Bu çalışmada, kuvvetli rüzgar etkisi altında göçen bir minarenin göçme mekanizması simüle edilerek, bu tür yapısal etkileşimlerin anlaşılması ve potansiyel riskli bölgelerin tespiti hedeflenmiştir. Rüzgar profilleri Eurocode ve Türk Standartları'na göre tanımlanmış ve Hesaplamalı Akışkanlar Dinamiği analizlerinde kullanılmıştır. Analizlerden elde edilen basınç ve emme gerilmeleri, Abaqus/Cae programında ilgili minare yüzeyine uygulanmış ve doğrusal olmayan sonlu eleman analizleri gerçekleştirilmiştir. Nümerik analizler sonucunda yer değiştirmeler, gerilmeler, plastik şekil değiştirmeler ve hasarlar elde edilmiş ve sonuçlar karşılaştırmalı olarak sunulmuştur. Her iki standartla elde edilen sonuçlar oldukça yakın olup, tepe yer değiştirmeleri İtalyan Yapı Kodu ve Eurocode 8'de belirtilen limit değerlerini aşmaktadır. Ayrıca, minarenin geçiş segmentindeki birçok ağ elemanı doğrusal olmayan sonlu eleman analizlerinde çekme gerilmeleri nedeniyle hasar görmüştür. Son olarak, minarenin göçme davranışı kullanılan yöntemlerle başarıyla simüle edilmiştir.

Anahtar kelimeler: Yığma, Göçme mekanizması, Rüzgar, Hasar analizleri, Hesaplamalı akışkanlar mekaniği

*Yazışılan yazar

İntihal Kontrol: Evet – Turnitin
Şikayet: fujece@firat.edu.tr

Telif Hakkı ve Lisans: Dergide yayın yapan yazarlar, CC BY-NC 4.0 kapsamında lisanslanan çalışmalarının telif hakkını saklı tutar.



Simulation of the Collapse Mechanism of a Minaret under the Effect of Strong Wind

Taha Yasin ALTIOK^{1*} , Ali DEMİR² 

^{1,2}Department of Civil Engineering, Faculty of Engineering, Manisa Celal Bayar University, Manisa, Türkiye.

¹taha.altiok@cbu.edu.tr, ²ali.demir@cbu.edu.tr

Received: 28.03.2024

Accepted: 03.06.2024

Revision: 01.05.2024

doi: 10.62520/fujece.1460766

Research Article

Citation: T. Y. Altıok ve A. Demir, "Simulation of the collapse mechanism of a minaret under the effect of strong wind", *Firat Univ. Jour. of Exper. and Comp. Eng.*, vol. 3, no 3, pp. 292-312, October 2024.

Abstract

In this study, the collapse mechanism of a destroyed minaret under strong wind influence was simulated to understand such structural interactions and identify potential risky regions. Wind profiles were defined according to Eurocode and Turkish Standards and were used in Computational Fluid Dynamics analyses. The pressure and suction stresses obtained with these wind analyses were applied on the minaret's surface with Abaqus and the nonlinear finite element analyses were performed. As a result of the numerical analyses, displacements, stresses, plastic strains, and damages were obtained and results were comparatively presented. The results obtained with both standards are quite close and top displacements exceed the limit value specified in the Italian Building Code and Eurocode 8. Besides, many mesh elements in the minaret's transition segment were damaged with tension stresses in nonlinear finite element analyses. Finally, the minaret's failure behaviour was successfully simulated with the used methods.

Keywords: Masonry, Failure mechanism, Wind, Damage analysis, Computational fluid mechanics

*Corresponding author

1. Introduction

The wind comprises numerous vortices of different sizes and rotational directions, transported within a prevailing air current that moves in relation to the surface of the Earth. The presence of these vortices imparts a turbulent character behaviour to the wind. The wind-induced response of structures encompasses static, stochastic, and resonant behaviors owing to turbulence and wake effects, vortex resonance, galloping, interference, divergence, and flutter. The wind loads depend on the wind strength, the topography of the terrain, and the interaction of wind and structures. Therefore, investigation of the wind effect on the structure and the relationship between the wind environment and movement is important to simulate a more realistic behaviour.

In certain regions, winds pose a greater threat to tall and slender structures like reinforced concrete (RC) or masonry minarets, RC chimneys, clock-lighting towers, silos, or turbine towers compared to earthquakes. Numerous studies in the literature have investigated these structures extensively. Chimneys may be subject to downwind gusts due to drag forces, as well as possible downwind eddy shedding. Reddy et al. [1] determined that the earthquake force exerted on the RC chimney in an area with a baseline wind velocity of 44 m/s is close to the wind load. Karaca and Türkelî [2] investigated the wind load and response of industrial RC chimneys by following the procedures of five different codes. They determined that the wind loads calculated according to the Eurocode-1 [3] are three to four times higher than the wind load values of other codes. So, they expressed that the Eurocode-1 was more reliable by determining the wind effects. They also determined that the effect of slender industrial RC chimneys on wind responses should be considered to perform a safe and economical design.

In recent times, structural engineers have placed more emphasis on investigating the performance of tall structures, considering various uncertainties for wind loads [4], [5], [6], [7], [8]. Li et al. [9] performed wind tunnel experiments to study the impact of wind on the Jin Mao Building, one of China's tallest structures, standing at 420.5 meters with 88 floors. The effectiveness of wind tunnel testing methods was verified by comparing full-scale measurements with wind tunnel test results. Additionally, an assessment of the building's performance under typhoon conditions was carried out. Merrick and Bitsuamlak [10] investigated the shape effects of wind triggering the response of tall buildings. Aly et al. [11] proposed a method to predict high-rise building responses to wind loads, which integrates lateral, crosswind, and torsional responses. Yang et al. [12] performed experiments on a high rise building model in hurricane like winds, finding that wind loads varied significantly based on the model's position relative to the center of the vortex. Heiza and Tayel [13] investigated the effects of earthquakes and winds on approximately 30 structures. They determined that the wind was more effective in tall buildings and the earthquake was more effective in low rise buildings. Kwon and Karaem [14] carried out a series of studies using 8 major regulations to develop a global standard within the scope of determining the wind effect. Ouyang and Spence [15] conducted probabilistic performance-based studies to estimate the damage to buildings exposed to extreme winds.

One of the structures most affected and damaged by the winds is the minarets. The architectural features of the minarets vary according to the construction age and material. While masonry materials demonstrate strong resistance to compressive stresses, they may encounter issues under tensile stresses. To address tensile stresses in historical minarets, masonry units (stone, brick) are interconnected both horizontally and vertically using clamps and dowels [16-17]. Most of the minarets in Turkey have been built as RC structures, recently [18]. Minarets are usually built by masters without any project [19]. After the 1999 earthquakes, it was announced that 80.9% of the 1176 mosques in Turkey didn't have a building permit [19]. Many researchers have carried out experimental and numerical studies on minarets, especially involving earthquakes [16-17], [20-33]. Observations from the studies indicated that damages were primarily concentrated in the transition segment and upper part of the minarets [31-35].

Numerical examination methods refer to various calculation and simulation techniques used for structural analysis in engineering applications. These methods are commonly employed to understand the behaviors of complex structures, evaluate their performances, and optimize design processes. Common numerical examination methods include Finite Element Method (FEM), Finite Volume Method (FVM), Finite Difference Method (FDM), Finite Time Domain Method (FTDM), and Computational Fluid Dynamics

(CFD). These methods have different advantages and disadvantages depending on the engineering problems and their applications. In the context of structural behavior problems, Finite Element Method is generally preferred, while CFD methods are preferred for fluid mechanics. Wind effects can be assessed using either wind tunnel tests or Computational Fluid Dynamics (CFD) analysis. Physical wind tunnel tests are time consuming and costly. CFD modelling, which has recently been adopted in airflow studies in buildings, offers many advantages in evaluating wind performance. While structural models can be changed quickly in CFD analysis, design changes in physical studies require a lot of effort. CFD relies on the premise of a three-dimensional, fully turbulent, and incompressible flow regime. Both internal and external flows were simulated utilizing the standard k - ϵ turbulence model, a widely accepted technique within the realm of natural ventilation investigation [36-43]. In recent years, numerous studies have been conducted to determine the wind effects on minarets. Ural et al. [44] investigated the effects of dead load, wind load, and seismic load on an 800-year-old curved historical minaret in Aksaray and provided recommendations for restoration processes. Türkeli [2] studied the impacts of wind and earthquake loads on a 61-meter-high RC minaret. They recommended utilizing time history analysis to evaluate lateral loads in the design of RC minarets, emphasizing the importance of considering cross-section modifications. [45] explored the displacement mechanisms of minarets under dead load and wind load through various numerical studies. Based on the analysis results, insights were drawn regarding the errors made during the construction of minarets. . Reşatoğlu et al. [46] investigated the behaviour of some RC minarets in Cyprus under earthquake and wind loads calculated with various codes. They tried to determine the effective lateral load in minaret design by examining wind load and distributions, principal stresses, displacements, and base shear forces. Adam et al. [47] attempted to determine the behavior of a historical masonry minaret in Egypt under its own weight, wind, and seismic loads using nonlinear finite element analyses with static and dynamic loads. Türkeli [48] studied the behaviour of a historical masonry minaret under the wind and earthquake loads. In the study, the wind was more dominant in the behaviour of the minaret. It was expressed that the main cause of the failure is the tensile and shear stress buildup on the cylindrical body and the transition segment. Pouraminian [49] examined the behavior of a historical brick minaret in Iran, with a height of 16.11 meters, against wind and seismic loads. According to the results, the minaret was found to be at a slight risk of damage under seismic loading and safe even under strong wind effects. Al-Zuhairi et al. [50] conducted finite element analyses on a historical masonry minaret, considering wind and self-weight loads. They concluded that the minaret exhibited sufficient resistance against principal stresses occurring only when both self-weight and wind load up to 120 km/h were acting together. Awad and Desouki [51] investigated the potential use of mosque minarets as solar chimneys in hot and arid regions. Through laboratory tests and CFD simulations, they concluded that traditional mosque minarets could serve as a viable and sustainable option for passive cooling in hot climates. Masonry structures are divided into three groups based on the accuracy required for modeling with FEM: Detailed Micro Modeling, Simplified Micro Modeling, and Macro Modeling. In Detailed Micro Modeling, the properties of each material constituting the structure (stone, brick, mortar, etc.), such as compressive and tensile strength, Poisson's ratio, elasticity modulus, and shear modulus, are individually inputted into the system, and separate modeling is performed. Detailed Micro Modeling provides more realistic results than other modeling methods. However, it is more time-consuming during the solution phase compared to other methods. In Simplified Micro Modeling, the region where mortar is present is neglected, and modeling is done by enlarging the dimensions of the materials constituting the masonry unit by half the size of the neglected mortar layer. Masonry units are separated from each other by interface lines, and joint interface lines are defined separately. It is assumed that cracks occur on these surfaces. In Macro Modeling, the structural element subjected to homogenization is considered as a composite material. Especially in nonlinear analyses, the increase in the number of unknowns and the stiffness matrix of large-sized systems prolong the solution time. In such cases, the homogenization technique ensures that the brick-stone and mortar, which constitute the wall structure of a masonry structure, are entered as a single material. This approach not only ensures realistic modeling and analysis of the structure but also provides significant time savings in the modeling and analysis stages.

In the current literature, research on the seismic effects on minaret-type structures is commonly conducted. However, studies regarding the influence of wind are seldom undertaken. In these studies, the surrounding structures of the wind-affected building are often being neglected, and the impact of neighboring structures on wind flow are not taken into account. This study, however, focuses on investigating the wind effects on delicate, tall, and slender structures, taking into consideration the

presence of surrounding buildings. In this context, the behaviour of a concrete minaret collapsed with a wind effect is simulated. A wind profile is created using TS 498 [52] and Eurocode-1 [3]. CFD numerical simulation analyses are performed using the wind profiles with the RWIND program [53]. In these analyses, environmental factors are considered by modelling other structures around the minaret. Nonlinear Static/General analyses are carried out by applying the wind's pressure and suction stresses on the minaret's surfaces modelled in the Abaqus/Cae [54]. Consequently, the minaret's failure mechanism is estimated by considering the displacements, stresses, and damages. Considering the results obtained, this study offers important ideas for predicting the behaviour of thin and tall structures that are fragile against dynamic effects under the influence of wind. In addition, it gives more realistic results by considering the effect of a collapsed minaret on the wind flow in the surrounding structures.

2. Wind damages of minarets

The wind is an important dynamic effect, especially for slender structures. Turkey's coastal regions have a high potential to face severe windstorms. The strong winds destroyed many minarets in the past. In 2002, during a storm, the minaret of Ebubekir Sıddık Mosque in Ankara-Kayaş collapsed, leading to the death of two individuals and injuring five others (Figure 1a) [55]. On February 27, 2002, the five minarets collapsed, and the four minarets got damaged because of a wind speed of 96 km/h in Mersin-Erdemli (Figure 1b) [56]. On February 9, 2003, another minaret collapsed due to the wind speed of 100 km/h (Figure 1c) [57]. Two 15 m high minarets of the Ulu Mosque in Kahramanmaraş collapsed in 2005 during a 60 km/h windstorm and one person got injured (Figure 1d) [58]. The stone minaret of the 22-year-old Kurtuluş Mosque collapsed due to the strong wind that occurred in Kırıkkale in 2010 (Figure 1e) [59]. In February 2015, the minaret of Şafak Mosque in İzmir collapsed during a strong windstorm with a maximum wind speed of 90 km/h (Figure 1f) [60]. In Ordu Ulubey, the longest minaret in the city with a length of 57 m collapsed due to the strong wind effect in 2016 (Figure 1g) [61]. Due to the wind in Niğde, a minaret collapsed from the transition zone in January 2021 (Figure 1h) [62]. In Aydın Nazilli, the upper part and spire of a minaret collapsed due to the wind with an average speed of 70 km/h in October 2021 (Figure 1i) [63].



Figure 1. Minarets damaged by wind, (a) Ebubekir Sıddık Mosque/Ankara-Kayaş, (b)-(c) Mersin-Erdemli, (d) Ulu Mosque/Kahramanmaraş, (e) Kurtuluş Mosque/Kırıkkale, (f) Şafak Mosque/İzmir, (g) Ordu-Ulubey, (h) Niğde, (i) Aydın/Nazilli



Figure 1. Minarets damaged by wind, (a) Ebubekir Sıddık Mosque/Ankara-Kayaş, (b)-(c) Mersin-Erdemli, (d) Ulu Mosque/Kahramanmaraş, (e) Kurtuluş Mosque/Kırkkale, (f) Şafak Mosque/İzmir, (g) Ordu-Ulubey, (h) Niğde, (i) Aydın/Nazilli (Continue)

3. General Properties of the Collapsed Minaret

3.1. Geometrical Properties

The minaret of the Industry mosque was built in Manisa in 1989. The minaret consists of a boot, transition segment, cylindrical body, two balconies, upper part, spire, and end ornament parts. (Figure 2a-2b). It was built using concrete blocks and binder mortar as the building material. No steel element was used in its construction. There is a core body staircase inside the minaret. The average height of the stairs is 20 cm. The total height of the minaret is 33.20 m. The pedestal dimensions of the minaret are 2.27 x 2.27 m². Its geometric properties are given in Figure 2c.

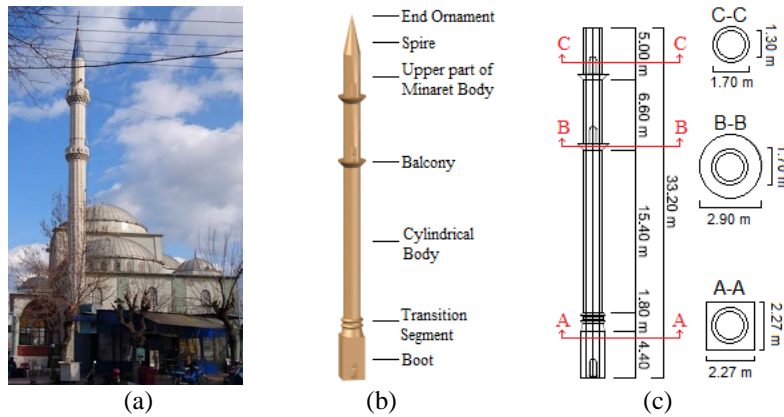


Figure 2. The parts and geometric features of the minaret. (a) Industry mosque and minaret, (b) Parts and (c) Geometrical properties

3.2. Damage Survey

Many buildings got damaged due to the windstorm that occurred in Manisa on January 27, 2021. The most striking of these damages was the failure of Industry Mosque's minaret. According to the information obtained by the Provincial Meteorology Directorate, the wind's maximum speed was 25.8 m/s (92.9 km/h). It was observed that there was a double row concrete block in the transition segment of the minaret. At the same time, the minaret had 2 balconies and a tall body. It was foreseen that the minaret collapsed by the influence of the stresses accumulated in the transition segment. The photographs of the minaret before and after the collapse are presented in Figure 3.



Figure 3. Before and after the collapse of the minaret of Industry Mosque

3.3. Materials

Following the collapse of the minaret due to wind, various tests were conducted on samples extracted from its concrete blocks and mortar material. Compression tests were administered, yielding an average compressive strength (f_b) of 6.30 MPa for the concrete blocks and 3.36 MPa for the mortar sample. According to the Turkish Building Earthquake Code-2018 (TBEC-2018) [64], the compressive strength (f_k) of the masonry wall is determined as 3.34 MPa. Based on TBEC-2018, the modulus of elasticity of the masonry wall (E_{div}) can be determined as 750 times f_k . Consequently, the modulus of elasticity is calculated as 2504.3 MPa.

4. Wind Analyses

In this study, CFD analyzes of a minaret that collapsed due to the wind were carried out using wind profiles calculated according to TS 498 and Eurocode-1 regulations. Other structures around the minaret were also included in the modeling. Pressure and suction values on the minaret surface under the influence of the wind were obtained and applied to the relevant surfaces of the minaret modeled in ABAQUS. The obtained results are presented comparatively and the collapse mechanism of the minaret is simulated. The flow chart of the study is given in Figure 4.

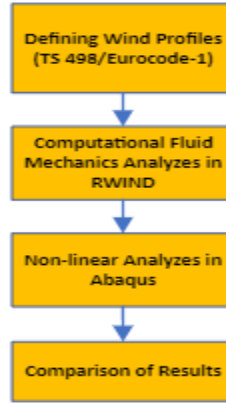


Figure 4. The flow chart of the study

4.1. Wind Loads According to Eurocode-1 and TS 498

Due to the speed and mass of the moving air, if an object with a fixed position comes in front of the air with kinetic energy, its flow will either stop or its direction will be deflected. The magnitude of wind pressure exerted on any surface of an object is subject to variation based on several factors, including the object's geometry, wind direction, wind speed, and air density. Obstacles present on the ground surface diminish wind velocity, with speed escalating proportionally with height. Wind velocity attains its peak value at an elevation known as the gradient height (Table 1).

Table 1. Wind speed and suction stresses (TS 498)

Height (h) (m)	Wind speed (n)		Suction (q) (kN/m ²)
	m/s	km/h	
0-8	28	100	0.5
9-20	36	130	0.8
21-100	42	150	1.1
> 100	46	165	1.3

The minaret's wind profiles were obtained according to Eurocode-1 and TS 498 standards in this study. TS 498 and Eurocode-1 are among the most common standards used for wind load designing in Turkey. TS 498 is generally used for load bearing systems and facade elements. Some international standards and regulations provide more detail. TS 498 can be used regardless of the structural carrier system (RC, steel, masonry, wood). In TS 498, the wind pressure (w), which does not directly affect the building carrier system, but directly affects the unit area on the upper surface of the building, is calculated with equation 1. (q) is the wind pressure acting perpendicular to the surface, and C_p is the suction coefficient determined for the surface, depending on the various blowing directions.

$$w = C_p \times q \quad (1)$$

In Eurocode-1, some formulations express the wind speed variation and turbulence intensities depending on the height. $V_m(z)$ represents the wind speed at height z and is calculated as shown in equation 2.

$$V_m(z) = c_r(z) \times c_0(z) \times V_b \quad (2)$$

V_b is the basic wind velocity and is calculated as in equation 3.

$$V_b = c_{dir} \times c_{season} \times V_{b,0} \quad (3)$$

Equation 3 introduces the directional factor, c_{dir} , where $V_{b,0}$ represents the fundamental value of the basic wind velocity, and c_{season} denotes the seasonal factor. According to the Eurocode-1, both the direction (c_{dir}) and season (c_{season}) factors can be assumed as 1.00.

In equation 2, $c_r(z)$ is the roughness factor and $c_o(z)$ is the orography factor. It started in the Eurocode-1 that it is appropriate to take the Orography factor ($c_o(z)$) as 1. The roughness factor ($c_r(z)$) is calculated as in equation 4.

$$c_r(z) = k_r \times \ln\left(\frac{z}{z_0}\right) \quad z_{min} \leq z \leq z_{max} \quad (4)$$

$$c_r(z) = c_r(z_{min}) \quad z \leq z_{min}$$

In equation 3, k_r is the terrain factor and can be calculated using equation 5.

$$k_r = 0.19 \left(\frac{z_0}{z_{0.11}}\right)^{0.07} \quad (5)$$

z_{min} is the lowest height, z_0 is the roughness length and z_{max} is the highest height depending on the terrain category. z_{min} , z_0 and z_{max} values are determined as 5 m, 0.3 m and 200 m, respectively. The obtained results are presented in Table 2.

Table 2. Roughness factor, orography factor, basic wind velocity and wind velocity values depending on height

No	Height from ground	$c_r(z)$	$c_o(z)$	V_b	$V_m(z)$
1	0-4.4	0.59092	1	19.76	11.6765792
2	4.4-6.2	0.66638	1	22.28	14.8469464
3	6.2-21.6	0.94094	1	31.47	29.6113818
4	21.6-27.6	0.99484	1	33.27	33.0983268
5	27.6-33.2	1.03554	1	34.63	35.8607502

According to Eurocode-1, the wind turbulence intensity (l_v) can be calculated using equation 6. The obtained values are given in Table 3.

$$l_v(z) = \frac{k_l}{c_o(z) \times \ln\left(\frac{z}{z_0}\right)} \quad z_{min} \leq z \leq z_{max} \quad (6)$$

$$l_v(z) = l_v(z_{min}) \quad z \leq z_{min}$$

In equation 6, specifies the turbulence coefficient, denoted as k_l , with a recommended value of 1.0. As for the orography coefficient $c_o(z)$, a value of 1.0 is suggested when there is no discernible increase in velocity induced by turbulence on the terrain (Table 3).

Table 3. Wind turbulence intensities depending on height

No	Height from ground	$l_v(z)$
1	0-4.4	0.372
2	4.4-6.2	0.33
3	6.2-21.6	0.234
4	21.6-27.6	0.221
5	27.6-33.2	0.212

4.2. Numerical Simulation of the Minaret's Wind Flow

For the structures, determining the wind effect is quite complex. In such cases, one possible solution is to test the relevant buildings in a wind tunnel. This method is both expensive and time consuming. Another method is to use the programs that can perform CFD simulations. RWIND software, which can perform CFD simulations, is used in the wind analysis of the minaret. RWIND Simulation is a software application designed for conducting numerical simulations of wind flow, akin to a digital wind tunnel, particularly around buildings or other structures. Its primary function encompasses generating wind loads, representing the forces exerted on these objects due to wind effects. The wind speed profiles and turbulence intensities, which are the main parameters in the analyses, are determined according to TS 498 and Eurocode-1. The structure and surrounding conditions (structures, vehicles, trees, mountains, seas, etc.) are crucial to realistically determining the wind's effect on the structure. So, numerical models are created by considering the structures that can change the wind effect around the minaret. Satellite views of the minaret and its surrounding structures are presented in Figure 5, and a 3D model of the minaret and its surrounding structures are presented in Figure 6a. After the minaret collapsed, the effective wind direction is determined with on-site investigations. The wind angle is considered as 45° in all analyses. Besides, the dimensions of the wind tunnel, and the mesh sizes of the minaret and surrounding structures are all taken equally. In CFD modelling, mesh type and size greatly affect the accuracy of the results. The grid has been modified and improved according to the wind area. The mesh element size was gradually increased in a smooth manner to effectively resolve sections exhibiting high gradient mesh, thereby enhancing the accuracy of the velocity field results. Grid sensitivity analysis was employed to validate both the programming and computational functionality of the computational model. The grid, number of nodes, and elements were calibrated until the posterior prediction error between the calculation iterations and the posterior error indicator became negligible. The applied boundary conditions were kept constant throughout the simulation to ensure a precise comparison of the posterior error estimation. As a result of the studies, the mesh size was determined as 0.997 m (mesh density 40%). Accordingly, the minaret and its surroundings have 666703 meshes and 780184 nodes. The main input parameters of the simulation are kinematic viscosity $15 \times 10^{-6} \text{ m}^2/\text{s}$ and air density 1.25 kg/m^3 (Eurocode-1). Figure 6b is used to clearly determine the pressure and suction effects on the minaret. The wind flow chart that occurred during the analysis is presented in Figure 6c.

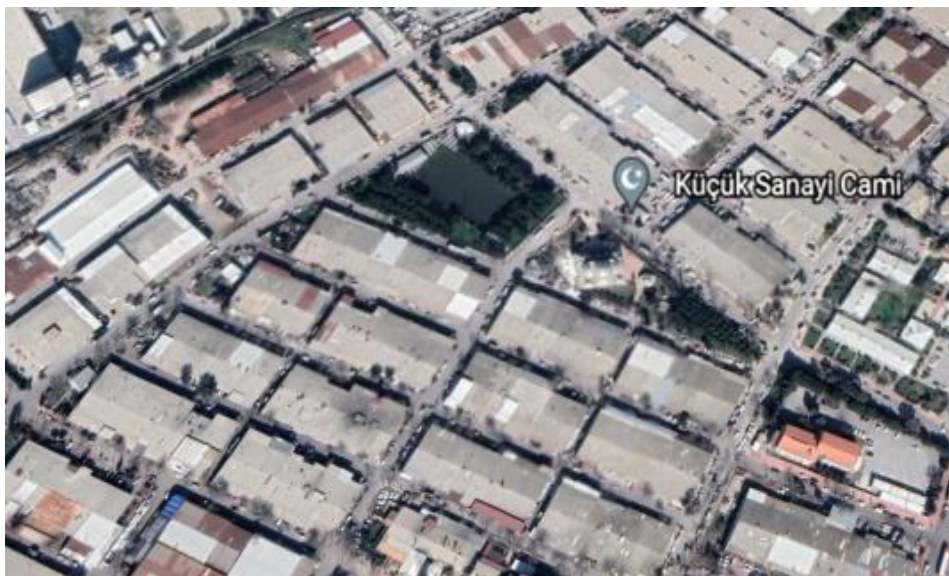


Figure 5. Satellite view of the minaret and its surrounding

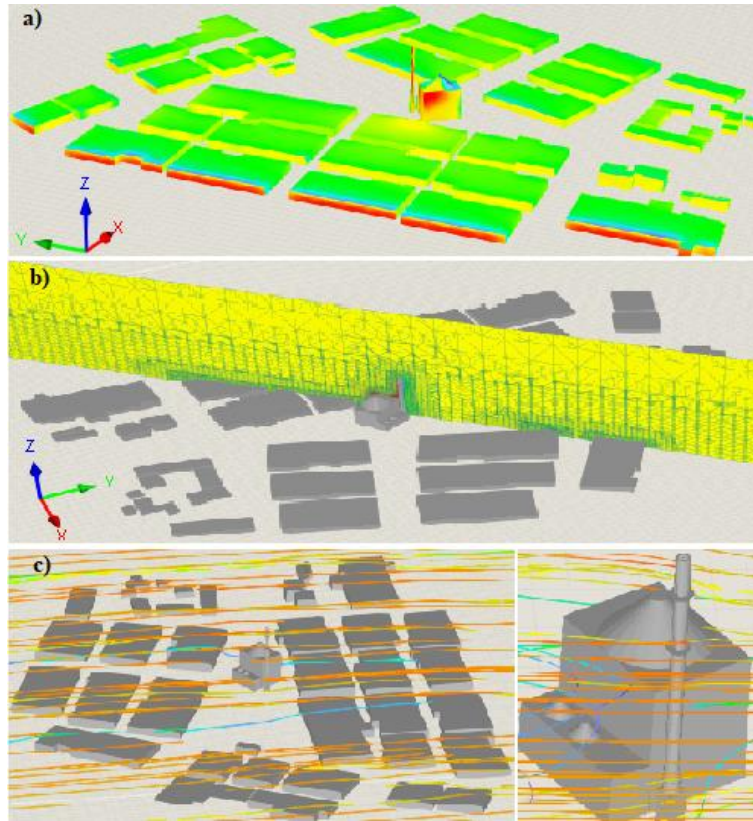


Figure 6. General view of wind flow and wind pressure effect on the surface of structures

4.3. Wind's Pressure and Suction Values

The wind profiles made with TS 498 and Eurocode-1 are shown in Figure 7. The pressure and suction values obtained in Figures 6b and 6c are presented in Figure 8. In all analyses, the suction effect occurs on the front surface, and the pressure effect occurs on the back surface of the minaret. Positive pressure is defined as the force directed towards the surface, while negative pressure, or suction, denotes the force moving away from the surface. According to the results, it is determined that the TS 498 has a more compelling effect than the Eurocode-1. The maximum pressure on the back surface of the minaret is 862.9 Pa and 777 Pa in TS 498 and Eurocode-1, respectively. The maximum suction on the front surface of the minaret is 1477.5 Pa in TS 498 and 951.3 Pa in Eurocode-1. Although the pressure and suction values are constant in the straight parts, those in varying cross-sections suddenly change. Obtained with the wind analyses, the pressure and suction values are presented in Figure 9. It is determined that the pressure and suction values increase with the height. According to the results, the wind effect reaches the highest value in the upper part of the minaret. This effect considerably increases the overturning moment. When considering the pressure and suction values calculated with TS 498 and Eurocode-1, close results are obtained.

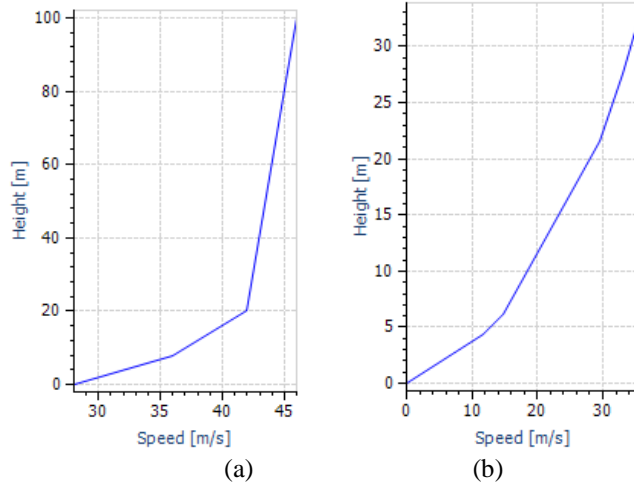


Figure 7. Wind profiles. (a) TS 498, (b) Eurocode-1

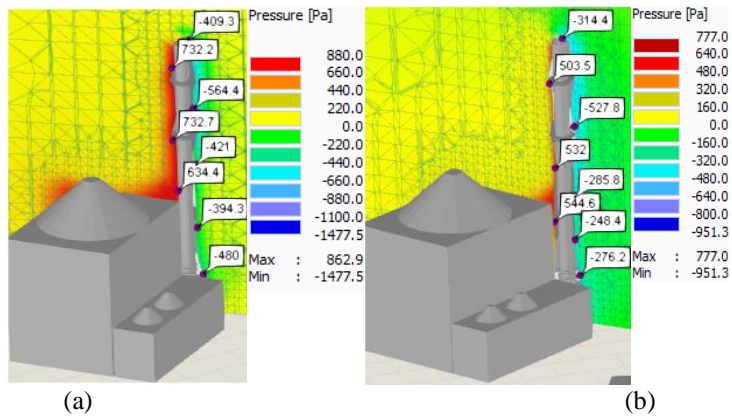


Figure 8. Pressure and suction formed on the minaret surface. (a) TS 498, (b) Eurocode-1

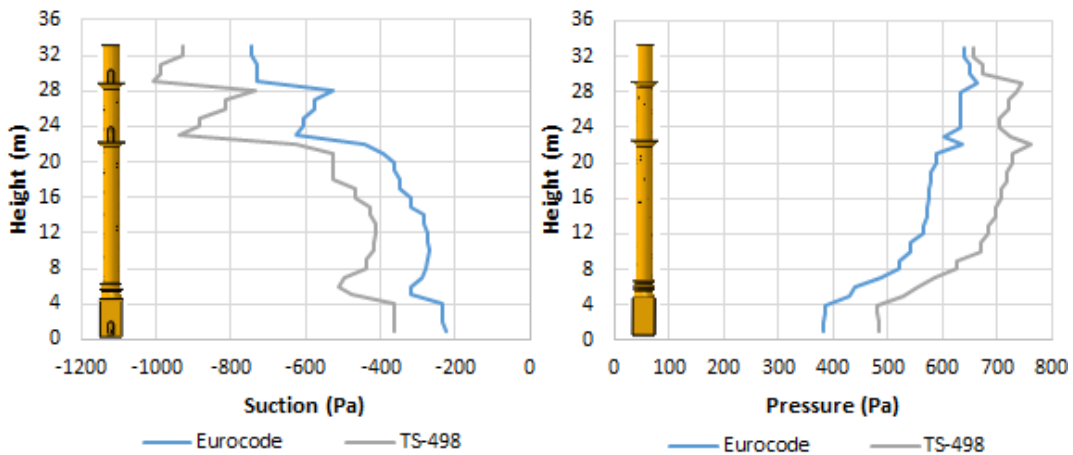


Figure 9. Pressure and suction values occurred on minaret's surfaces

5. Nonlinear FE Analyses

As a result of the wind analyses performed with RWIND software, the pressure and suction values on the minaret surface are determined. The pressure and suction values obtained with the wind analyses are applied on the relevant surface of the minaret FE model in the Abaqus program. The large geometric dimensions of the minaret and the high number of mesh elements obtained in convergence analyses increase the analysis

time. A composite material model representing the common material properties of the masonry units and mortar is selected for macro modelling. This method is frequently preferred for modeling large systems due to its significant reduction in computational time. In this study, the relevant minaret is modeled using the macro modeling technique. For this purpose, load surfaces are created on each of the minaret's back and front surfaces, with one-meter intervals on the right and left surfaces. Pressure and suction stresses are applied on these load surfaces and nonlinear Static/General analyses are performed (Figure 10b). The minaret is not adjacent to the mosque. All degrees of freedom on the foundation surface of the minaret were accepted as fixed support under initial boundary conditions (Figure 10a). The convergence analyses are performed to create a more realistic and consistent FE model (as shown in Figure 11). The Convergence graph means approaching a point, a limit, with the gap in between getting smaller, but without intersecting. The mesh size, which directly affects the analysis time and results, is determined by the analyzes made to obtain this graph. In the analyses, the optimum mesh size is determined as 0.35 m. In total, the FE model has 29412 quadratic tetrahedral (C3D10) mesh elements. Mesh properties are kept the same in all analyses.

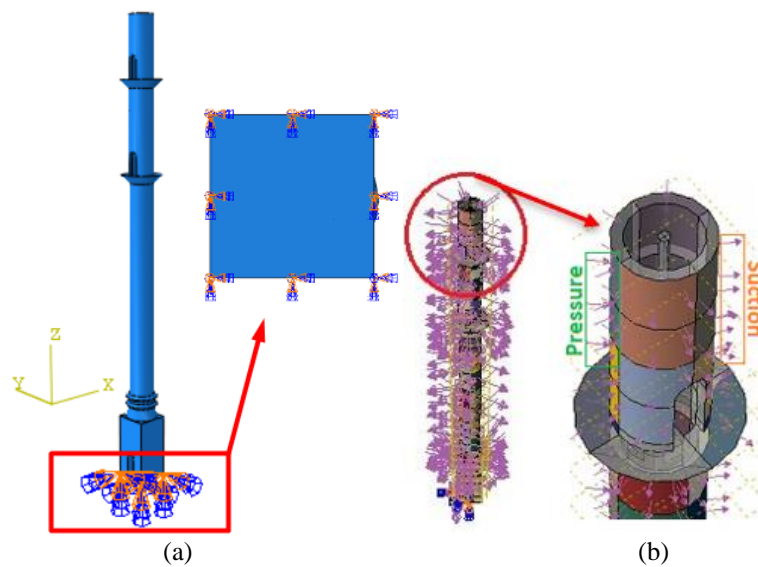


Figure 10. (a) Boundary conditions, (b) Applying pressure and suction stresses to relevant surfaces in Abaqus

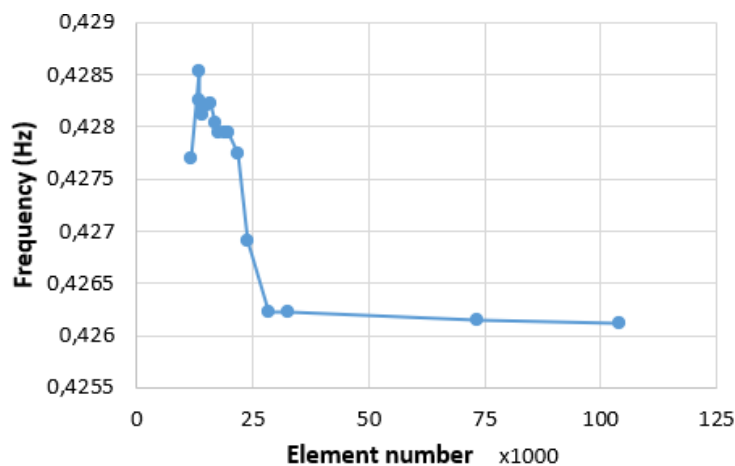


Figure 11. Convergence analysis of the minaret

The natural frequencies corresponding to the first three modes and their corresponding mode shapes obtained through finite element analysis under the initial mechanical parameters and boundary conditions of the minaret are presented in Figure 12. The first two modes represent bending modes in both the x and y directions, while the third mode represents a torsional mode.

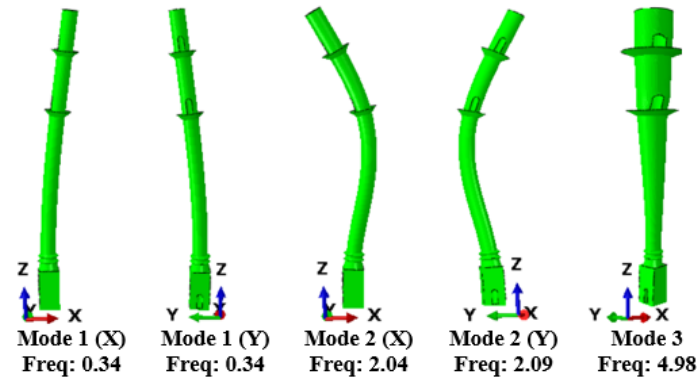


Figure 12. Mode shapes and natural frequencies of the minaret

5.1. Concrete Damage Plasticity Model

In this study, Concrete Damage Plasticity Model (CDP) was chosen to characterize the inelastic response of concrete in Abaqus. Even though the CDP material model was initially designed to capture the plastic behavior of concrete [65-66], the CDP model has also demonstrated its applicability to masonry structures [67-69]. In existing literature, there is a widespread use of the CDP material model to describe the plastic behavior of masonry structures [32-33], [68-71]. The CDP model integrated into Abaqus encompasses the plastic, compressive, and tensile behaviors exhibited by concrete. In this investigation, the plastic behavior of the concrete minaret was determined based on the values outlined in Table 4.

Table 4. Material parameters

Dilation angle	Eccentricity	f_{bo}/f_{co}	K	Viscosity
35°	0.1	1.16	0.667	0.0058

With the initial modulus of elasticity denoted as E_0 , the stress-strain relationship under axial compressive and tensile loads is obtained as in equations 7-8.

$$\sigma_c = (1 - d_c)E_0(\varepsilon_c - \varepsilon_c^{-pl}) \quad (7)$$

$$\sigma_t = (1 - d_t)E_0(\varepsilon_t - \varepsilon_t^{-pl}) \quad (8)$$

Here, E_0 represents the initial modulus of elasticity. σ_c (σ_t) denotes the uniaxial compressive (tensile) stress, while ε_c (ε_t) stands for the total strain experienced under compressive and tensile conditions, respectively. ε_c^{-pl} (ε_t^{-pl}) represents the equivalent plastic strain under such conditions. Additionally, d_c and d_t are the damage parameters associated with compressive and tensile stresses, respectively.

The materials constituting masonry structures typically exhibit low tensile strengths but high compressive strengths. It is widely acknowledged in the literature that the primary cause of collapse in such structures is attributed to tensile stresses [32, 33, 72]. Various models for tensile stiffness have been proposed [73]. In this study, the tensile stiffness model proposed by Nayal and Rasheed [73], subsequently modified by Wahalathantri et al. [74], was employed (Figure 13). This model bears resemblance to the tensile stiffness model utilized in the CDP model in Abaqus [54]. Its foundation lies in the homogenized stress-strain diagram formulated by Gilbert and Warner [75], which accurately captures the response induced by primary and secondary cracking phenomena through two descending segments of the tensile stress-strain curve [75]. In this adapted model, the sole alteration was the adjustment of the sudden decline in the tensile stress-strain curve at a critical strain ε_{cr} , from the ultimate stress σ_0 to $0.77\sigma_0$, as opposed to the previously utilized $0.80\sigma_0$. The ultimate tensile strength of concrete can be estimated using equation 9 proposed by Genikomsu and Polak [76]. The values specified in Table 5 were employed in the static/general analyses of the minaret under pressure loading.

$$f'_t = 0.33\sqrt{f'_c}(\text{MPa})$$

(9)

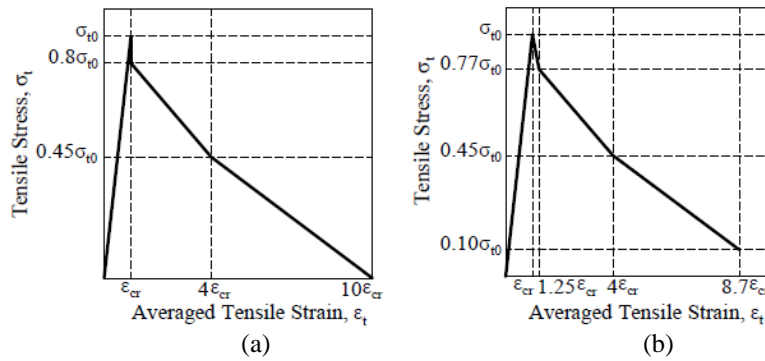


Figure 13. Tensile stiffness models: (a) Averaged tensile strain [73] (b) modified averaged tensile strain [74]

Table 5. The stress-strain curve values and scalar damage parameters for tensile behavior in masonry units

Tensile behavior			
Yield stress (MPa)	Cracking strain	Damage	Cracking strain
0.334	0	0	0
0.236531	0.000982	0.291824	0.000982
0.053322	0.007856	0.893603	0.000516
0.035554	0.010803	0.938922	0.013749

6. Results and Discussion

The pressure and suction stresses obtained with the wind analyses are applied on the minaret surfaces in Abaqus/Cae. To apply the stresses on the minaret surface, the FE model is divided into 2 parts horizontally and vertically at intervals of 1 m. The stresses are applied to the minaret surface in the horizontal direction. The pressure values on the minaret surface do not follow a uniform distribution. In nonlinear FE analyses, the mesh elements subjected to plastic deformation and tensile stresses, and displacements are determined. The top displacements of the minaret are presented in Figure 14. In the Italian Building Code [77] and Eurocode 8-Part-3 [78], if top displacement exceeds 0.4% of the masonry structure's height, the structure can get damaged or collapse. Since the minaret is 33.2 m high, the collapse limit displacement is 0.132 m according to the Italian Building Code and Eurocode 8-Part-3. This value is shown with a dashed red line in Figure 14. According to the results, the minaret's top displacement exceeds the limit value according to TS 498 and Eurocode-1. Figure 15 shows the displacement behaviour of the minaret.

Tension damages concentrate in the minaret's transition segment as shown in Figure 16. Many meshes get damaged more than 90%. It is understood that the minaret may collapse with the damages in the transition segment. The number of damaged and plastic elements according to both codes is quite similar (Figure 17). When the collapse mechanisms of masonry structures and especially tall and thin structures such as minarets are investigated, one of the most important reasons for their collapse is tensile stresses in the transition segment [72, 79, 80]. As a result of the damage analyses, the ratio of the elements damaged due to tensile stress to all elements is 0.85 in TS 498 and 0.84 in Eurocode-1. In addition, when the proportion of the number of plastic elements to all elements' number is investigated, it is 0.87 in both TS 498 and Eurocode-1.

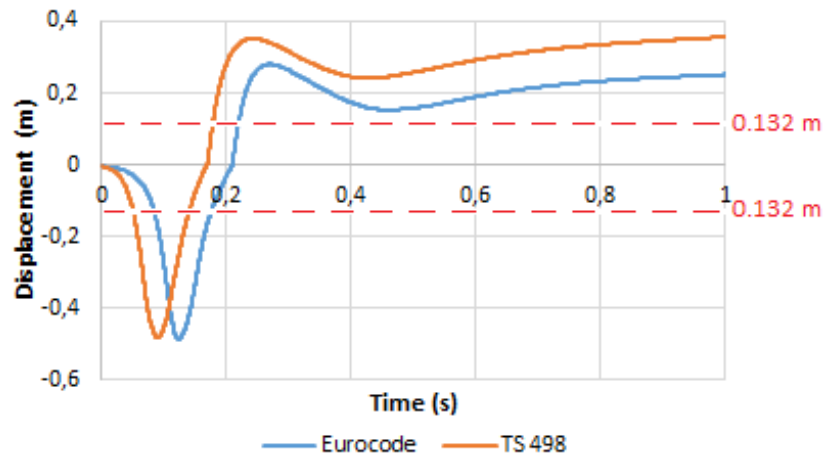


Figure 14. The displacements of the minaret's top

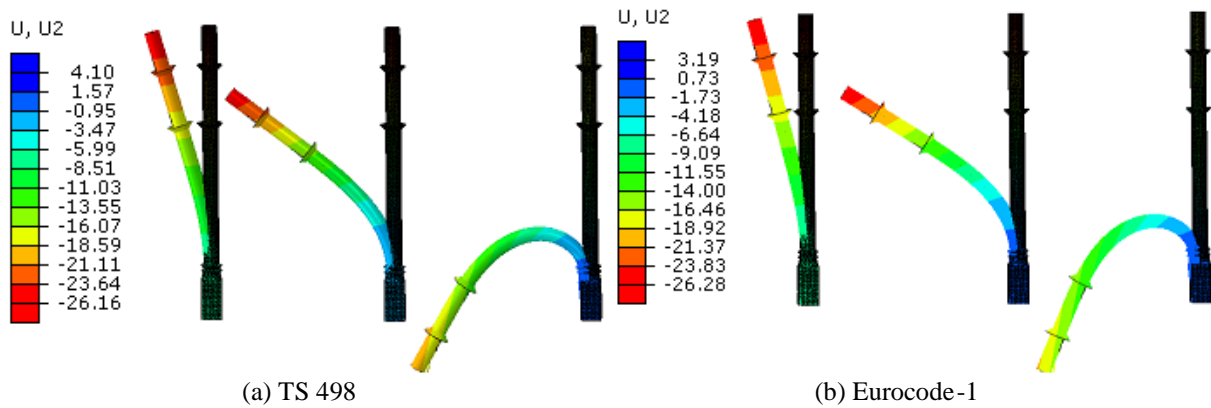


Figure 15. The minaret's displacement behavior

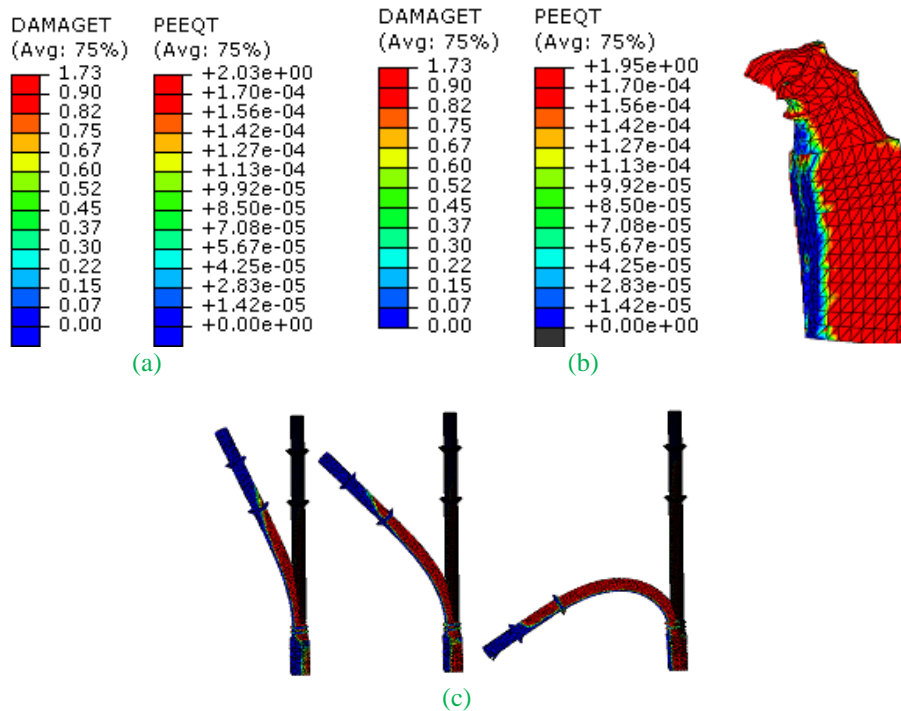


Figure 16. Damaget and PEEQT values and damage distribution. (a) TS 498, (b) Eurocode-1, (c) Development of tensile damage and deformation of the minaret under the influence of stresses

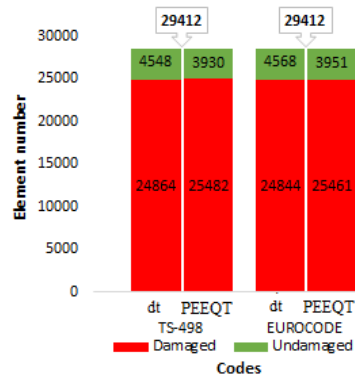


Figure 17. Number of damaged and undamaged elements

7. Conclusion

On January 27, 2021, a masonry minaret located in the western region of Turkey collapsed due to wind exposure with an average speed of 25.8 m/s. This study aims to conduct numerical analyses on the collapsed minaret and estimate its failure mechanism in accordance with TS 498 and Eurocode-1 standards, contributing to the literature in structural engineering. The numerical analyses entail two main stages. Firstly, Computational Fluid Dynamics (CFD) analyses are conducted using RWIND software to assess the wind flow around the minaret and its adjacent structures. The shape of the minaret and its surroundings significantly influence the wind flow patterns, hence necessitating the modeling of surrounding structures for comprehensive wind flow analyses with RWIND software. Subsequently, nonlinear analyses are carried out in Abaqus, incorporating pressure and suction effects obtained from the wind flow analyses to assess displacement and damage.

Evaluation of maximum pressure stresses on the minaret's rear surface reveals that TS 498 exceeds Eurocode-1 by 10%. Similarly, investigation into the maximum suction effects on the minaret's front surface indicates a 35.6% discrepancy between TS 498 and Eurocode-1. The observed top displacements surpass the limit values specified in the Italian Building Code and Eurocode 8-Part-3. Damage analysis demonstrates a close correlation between TS 498 and Eurocode-1, with an average consistency of 86% across both standards.

The simulation successfully identifies the failure mechanism of the minaret, attributing the collapse to accumulated tensile stresses in the transition segment. This underscores the importance of considering wind effects in conjunction with seismic loads for tall and slender structures. Furthermore, it is recommended to avoid geometric designs driven solely by architectural aesthetics, as such designs may compromise structural integrity.

8. Author Contribution Statement

In the conducted study, Author 1 contributed to the performance of finite element analyses, literature review, and obtaining results; while Author 2 contributed to the formation of ideas, examination of results, proofreading, and checking the article in terms of writing and content.

9. Ethics Committee Approval and Conflict of Interest

There is no need for an ethics committee approval in the prepared article. There is no conflict of interest with any person/institution in the prepared article.

10. References

- [1] K. R. C. Reddy, O. R. Jaiswal, and P. N. Godbole, "Wind and earthquake analysis of tall RC chimneys," *Int. J. Earth Sci. Eng.*, vol. 4, no. 6, pp. 508–511, 2011.
- [2] Z. Karaca and E. Türkeli, "Determination and comparison of wind loads for industrial reinforced concrete chimneys," *Struct. Des. Tall Spec. Build.*, vol. 21, no. 2, pp. 133–154, 2012.
- [3] Eurocode-1, "Actions on Structures/General Actions, Part 1-4: Wind Actions," CEN/TC 250, Management Centre, Brussels, 2005.
- [4] S. M. Spence and M. Gioffrè, "Large scale reliability-based design optimization of wind excited tall buildings," *Probabilistic Eng. Mech.*, vol. 28, pp. 206–215, 2012.
- [5] E. Bernardini, S. M. Spence, and A. Kareem, "A probabilistic approach for the full response estimation of tall buildings with 3D modes using the HFFB," *Struct. Saf.*, vol. 44, pp. 91–101, 2013.
- [6] D. T. Resio, J. L. Irish, J. J. Westerink, and N. J. Powell, "The effect of uncertainty on estimates of hurricane surge hazards," *Nat. Hazards*, vol. 66, no. 3, pp. 1443–1459, 2013.
- [7] L. Caracoglia, "A stochastic model for examining along-wind loading uncertainty and intervention costs due to wind-induced damage on tall buildings," *Eng. Struct.*, vol. 78, pp. 121–132, 2014.
- [8] A. Suryawanshi and D. Ghosh, "Wind speed prediction using spatio-temporal covariance," *Nat. Hazards*, vol. 75, no. 2, pp. 1435–1449, 2015.
- [9] Q. S. Li, Y. Q. Xiao, J. Y. Fu, and Z. N. Li, "Full-scale measurements of wind effects on the Jin Mao building," *J. Wind Eng. Ind. Aerodyn.*, vol. 95, no. 6, pp. 445–466, 2007.
- [10] R. Merrick and G. Bitsuamlak, "Shape effects on the wind-induced response of high-rise buildings," *J. Wind Eng.*, vol. 6, no. 2, pp. 1–18, 2009.
- [11] A. M. Aly, A. Zasso, and F. Resta, "Tall buildings under multidirectional winds: response prediction and reduction," *Wind Tunn. Exp. Fluid Dyn. Res.*, p. 301, 2011.
- [12] Z. Yang, P. Sarkar, and H. Hu, "An experimental study of a high-rise building model in tornado-like winds," *J. Fluids Struct.*, vol. 27, no. 4, pp. 471–486, 2011.
- [13] K. M. Heiza and M. A. Tayel, "Comparative study of the effects of wind and earthquake loads on high-rise buildings," *Concr. Res. Lett.*, vol. 3, no. 1, pp. 386–405, 2012.
- [14] D. K. Kwon and A. Kareem, "Comparative study of major international wind codes and standards for wind effects on tall buildings," *Eng. Struct.*, vol. 51, pp. 23–35, 2013.
- [15] Z. Ouyang and S. M. Spence, "Performance-based wind-induced structural and envelope damage assessment of engineered buildings through nonlinear dynamic analysis," *J. Wind Eng. Ind. Aerodyn.*, vol. 208, p. 104452, 2021.
- [16] H. Nohutcu, A. Demir, E. Ercan, E. Hokelekli, and G. Altintas, "Investigation of a historic masonry structure by numerical and operational modal analyses," *Struct. Des. Tall Spec. Build.*, vol. 24, no. 13, pp. 821–834, 2015.
- [17] A. Demir, H. Nohutcu, E. Ercan, E. Hokelekli, and G. Altintas, "Effect of model calibration on seismic behaviour of a historical mosque," *Struct. Eng. Mech.*, vol. 60, no. 5, pp. 749–760, 2016.
- [18] H. Sezen, R. Acar, A. Dogangun, and R. Livaoglu, "Dynamic analysis and seismic performance of reinforced concrete minarets," *Eng. Struct.*, vol. 30, no. 8, pp. 2253–2264, 2008.
- [19] A. Doğangün, R. Acar, R. Livaoglu, and Ö. İ. Tuluk, "Performance of masonry minarets against earthquakes and winds in Turkey," in *Proceedings of the 1st International Conference on Restoration of Heritage Masonry Structures*, , pp. 24–27, April 2006.
- [20] E. M. Higazy, "Vulnerability of historical minarets; investigation of their seismic assessment & retrofitting," *Emir. J. Eng. Res.*, vol. 9, no. 2, pp. 59–64, 2004.
- [21] A. G. El-Attar, A. M. Saleh, and A. H. Zaghw, "Conservation of a slender historical Mamluk-style minaret by passive control techniques," *Struct. Control Health Monit. Off. J. Int. Assoc. Struct. Control Monit. Eur. Assoc. Control Struct.*, vol. 12, no. 2, pp. 157–177, 2005.
- [22] A. Dogangun, R. Acar, H. Sezen, and R. Livaoglu, "Investigation of dynamic response of masonry minaret structures," *Bull. Earthq. Eng.*, vol. 6, no. 3, pp. 505–517, 2008.
- [23] A. Bayraktar, A. C. Altunişik, B. Sevim, and T. Türker, "Seismic response of a historical masonry minaret using a finite element model updated with operational modal testing," *J. Vib. Control*, vol. 17, no. 1, pp. 129–149, 2011.
- [24] F. Portioli et al., "Seismic retrofitting of Mustafa Pasha Mosque in Skopje: finite element analysis," *J. Earthq. Eng.*, vol. 15, no. 4, pp. 620–639, 2011.

- [25] Y. Calayır, E. Sayın, and B. Yön, "Performance of structures in the rural area during the March 8, 2010 Elazığ-Kovancılar earthquake," *Nat. Hazards*, vol. 61, no. 2, pp. 703–717, 2012.
- [26] A. Bayraktar, A. C. Altunişik, and M. Muvafik, "Damages of minarets during Erciş and Edremit earthquakes, 2011 in Turkey," 2014.
- [27] M. Muvafik, "Field investigation and seismic analysis of a historical brick masonry minaret damaged during the Van Earthquakes in 2011," *Earthq. Struct.*, vol. 6, no. 5, pp. 457–472, 2014.
- [28] H. Nohutcu, E. Hökelekli, E. Ercan, A. Demir, and G. Altintas, "Collapse mechanism estimation of a historical slender minaret," *Struct. Eng. Mech.*, vol. 64, no. 5, pp. 653–660, 2017.
- [29] H. Nohutcu, "Seismic Failure Pattern Prediction in a Historical Masonry Minaret under Different Earthquakes," *Adv. Civ. Eng.*, vol. 2019, 2019.
- [30] A. Bayraktar and E. Hökelekli, "Influences of earthquake input models on nonlinear seismic performances of minaret-foundation-soil interaction systems," *Soil Dyn. Earthq. Eng.*, vol. 139, p. 106368, 2020.
- [31] T. Y. Altiok and A. Demir, "Collapse mechanism estimation of a historical masonry minaret considered soil-structure interaction," *Earthq. Struct.*, vol. 21, no. 2, pp. 161–172, 2021.
- [32] A. Demir and T. Y. Altiok, "Numerical assessment of a slender structure damaged during October 30, 2020, İzmir earthquake in Turkey," *Bull. Earthq. Eng.*, pp. 1–26, 2021.
- [33] T. Y. Altiok and A. Demir, "Seismic damage assessment of a historical masonry minaret considering soil-structure interaction," *J. Struct. Eng. Appl. Mech.*, vol. 4, no. 3, pp. 196–212, Sep. 2021.
- [34] E. Ercan, B. Arisoy, E. Hökelekli, and A. Nuhuğlu, "Estimation of seismic damage propagation in a historical masonry minaret," *Sigma J. Eng. Nat. Sci. Ve Fen Bilim. Derg.*, vol. 35, no. 4, 2017.
- [35] A. Bayraktar and E. Hökelekli, "Influences of earthquake input models on nonlinear seismic performances of minaret-foundation-soil interaction systems," *Soil Dyn. Earthq. Eng.*, vol. 139, p. 106368, 2020.
- [36] B. R. Hughes and S. A. A. Abdul Ghani, "A numerical investigation into the effect of windvent dampers on operating conditions," *Build. Environ.*, vol. 44, no. 2, pp. 237–248, Feb. 2009.
- [37] S. Liu, C. M. Mak, and J. Niu, "Numerical evaluation of louver configuration and ventilation strategies for the windcatcher system," *Build. Environ.*, vol. 46, no. 8, pp. 1600–1616, Aug. 2011.
- [38] H. Montazeri, "Experimental and numerical study on natural ventilation performance of various multi-opening wind catchers," *Build. Environ.*, vol. 46, no. 2, pp. 370–378, Feb. 2011.
- [39] B. R. Hughes, J. K. Calautit, and S. A. Ghani, "The development of commercial wind towers for natural ventilation: A review," *Appl. Energy*, vol. 92, pp. 606–627, Apr. 2012.
- [40] O. Saadatian, L. C. Haw, K. Sopian, and M. Y. Sulaiman, "Review of windcatcher technologies," *Renew. Sustain. Energy Rev.*, vol. 16, no. 3, pp. 1477–1495, Apr. 2012.
- [41] B. M. Jones and R. Kirby, "Quantifying the performance of a top-down natural ventilation Windcatcher," *Build. Environ.*, vol. 44, no. 9, pp. 1925–1934, Sep. 2009.
- [42] A. A. Elmualim, "Effect of damper and heat source on wind catcher natural ventilation performance," *Energy Build.*, vol. 38, no. 8, pp. 939–948, Aug. 2006.
- [43] Y. Su, S. B. Riffat, Y.-L. Lin, and N. Khan, "Experimental and CFD study of ventilation flow rate of a Monodraught™ windcatcher," *Energy Build.*, vol. 40, no. 6, pp. 1110–1116, Jan. 2008.
- [44] A. Ural, A. Dogangun, and S. Meraki, "Response evaluation of historical crooked minaret under wind and earthquake loadings," *Wind Struct.*, vol. 17, no. 3, pp. 345–359, 2013.
- [45] A. Ural and F. K. Firat, "Evaluation of masonry minarets collapsed by a strong wind under uncertainty," *Nat. Hazards*, vol. 76, no. 2, pp. 999–1018, Mar. 2015.
- [46] R. Reşatoğlu, T. Mirata, and L. Karaker, "Earthquake and wind load effects on existing RC minarets in north Cyprus," *Int. J. Eng. Technol.*, vol. 7, no. 4, pp. 3074–3085, 2018.
- [47] M. A. Adam, T. S. El-Salakawy, M. A. Salama, and A. A. Mohamed, "Assessment of structural condition of a historic masonry minaret in Egypt," *Case Stud. Constr. Mater.*, vol. 13, p. e00409, Dec. 2020.
- [48] E. Türkeli, "Dynamic Seismic and Wind Response of Masonry Minarets," *Period. Polytech. Civ. Eng.*, vol. 64, no. 2, pp. 353–369, 2020.
- [49] M. Pouraminian, "Multi-hazard reliability assessment of historical brick minarets," *J. Build. Pathol. Rehabil.*, vol. 7, no. 1, p. 10, Dec. 2021.

- [50] A. H. Al-Zuhairi, A. R. Ahmed, and S. R. Al-Zaidee, "Numerical Analysis of Historical Masonry Minaret Subjected to Wind Load," in *Geotechnical Engineering and Sustainable Construction*, M. O. Karkush and D. Choudhury, Eds., Singapore: Springer, pp. 545–555, 2022.
- [51] H. H. Awad and M. Desouki, "Integrating physical experiments with computational fluid dynamics to transform mosque minarets into efficient solar chimneys," *Sci. Rep.*, vol. 14, no. 1, p. 9721, Apr. 2024.
- [52] Turkish Standard Institute, *Turkish Standard, TS498: The Calculation Values of Loads used in Designing Structural Elements*, Ankara, Turkey, 1997.
- [53] Dlubal Software, *RWIND-Simulation Generation of WindInduced Loads on General Models: User Manual*, October 2020. Available at: <https://www.dlubal.com/en/downloads-and-information/documents/online-manuals/rwindsimulation-1/01/01>.
- [54] Dassault Systemes Simulia Corp., *Abaqus v10*, Providence, Rhode Island, USA, 2010.
- [55] NTV Haber, <http://arsiv.ntv.com.tr/news/120847.asp> (accessed 29/10/2021).
- [56] Hürriyet, <http://www.hurriyetim.com.tr/haber/> (accessed 27/02/2002).
- [57] Milliyet, "<http://www.milliyet.com.tr/2003/02/09/guncel/gun15.html>" (accessed 09/02/2003).
- [58] Hürriyet, "<http://www.hurriyetim.com.tr/haber/0>" (accessed 24/07/2005).
- [59] Haberler.com, "<https://www.haberler.com/22-yillik-caminin-minaresi-yikildi-haberi/>" (accessed 22/09/2019).
- [60] Cumhuriyet, "<http://www.cumhuriyet.com.tr>" (accessed 10/04/2015).
- [61] Haberler.com, "<https://www.haberler.com/ordu-da-57-metrelik-minare-siddetli-ruzgarda-8074105-haberi/>" (accessed 22/09/2019).
- [62] Ajans Niğde, (2021). "http://www.ajansnigde.com/nigdede-cami-minaresi-yikildi_d89720.html" (erişim tarihi: 29/11/2021).
- [63] Ankara Masası, (2021). "<https://www.ankaramasasi.com/haber/1053206/aydinda-siddetli-ruzgar-minareyi-yikti-o-anlar-kamerada>" (erişim tarihi: 29/11/2021).
- [64] Türkiye Building Seismic Code-2018, Ankara, Türkiye.
- [65] J. Lubliner, J. Oliver, S. Oller, and Ejj. Onate, 'A plastic-damage model for concrete', *Int. J. Solids Struct.*, vol. 25, no. 3, pp. 299–326, 1989.
- [66] J. Lee and G. L. Fenves, 'Plastic-damage model for cyclic loading of concrete structures', *J. Eng. Mech.*, vol. 124, no. 8, pp. 892–900, 1998.
- [67] M. Resta, A. Fiore, and P. Monaco, 'Non-linear finite element analysis of masonry towers by adopting the damage plasticity constitutive model', *Adv. Struct. Eng.*, vol. 16, no. 5, pp. 791–803, 2013.
- [68] M. Valente and G. Milani, 'Non-linear dynamic and static analyses on eight historical masonry towers in the North-East of Italy', *Eng. Struct.*, vol. 114, pp. 241–270, 2016.
- [69] M. Valente and G. Milani, 'Damage assessment and collapse investigation of three historical masonry palaces under seismic actions', *Eng. Fail. Anal.*, vol. 98, pp. 10–37, 2019.
- [70] E. Hökelekli and A. Al-Helwani, 'Effect of soil properties on the seismic damage assessment of historical masonry minaret–soil interaction systems', *Struct. Des. Tall Spec. Build.*, vol. 29, no. 2, p. e1694, 2020.
- [71] E. Hökelekli, A. Demir, E. Ercan, H. Nohuçu, and A. Karabulut, 'Seismic Assessment in a Historical Masonry Minaret by Linear and Non-linear Seismic Analyses', *Period. Polytech. Civ. Eng.*, vol. 64, no. 2, pp. 438–448, 2020.
- [72] T. Y. Altıok and A. Demir, 'Collapse mechanism estimation of a historical masonry minaret considered soil-structure interaction', *Earthq. Struct.*, vol. 21, no. 2, pp. 161–172, 2021.
- [73] R. Nayal and H. A. Rasheed, 'Tension stiffening model for concrete beams reinforced with steel and FRP bars', *J. Mater. Civ. Eng.*, vol. 18, no. 6, pp. 831–841, 2006.
- [74] B. Wahalathantri, D. Thambiratnam, T. Chan, and S. Fawzia, 'A material model for flexural crack simulation in reinforced concrete elements using ABAQUS', in *Proceedings of the first international conference on engineering, designing and developing the built environment for sustainable wellbeing*, Queensland University of Technology, pp. 260–264, 2011.
- [75] R. I. Gilbert and R. F. Warner, 'Tension stiffening in reinforced concrete slabs', *J. Struct. Div.*, vol. 104, no. 12, pp. 1885–1900, 1978.
- [76] A. S. Genikomsou and M. A. Polak, 'FINITE element analysis of punching shear of concrete slabs using damaged plasticity model in ABAQUS', *Eng. Struct.*, vol. 98, pp. 38–48, 2015.

- [77] Italian Public Works Council. (2019). “Guidelines for Application of Italian Building Code; Istituto Poligrafico e Zecca dello Stato”, Roma, Italy.
- [78] Eurocode 8. (2005). “Design of Structures for Earthquake Resistance—Part 3: Assessment and Retrofitting of Buildings”. CEN: Brussels, Belgium.
- [79] A. Demir and T. Y. Altıok, ‘Numerical assessment of a slender structure damaged during October 30, 2020, İzmir earthquake in Turkey’, *Bull. Earthq. Eng.*, vol. 19, no. 14, pp. 5871–5896, 2021.
- [80] T. Y. Altıok and A. Demir, ‘Seismic damage assessment of a historical masonry minaret considering soil-structure interaction’, *J. Struct. Eng. Appl. Mech.*, vol. 4, no. 3, pp. 196–212, Sep. 2021.



Çinko Ekstraksiyon Atığı Kullanılarak Sulu Çözeltilerden Fosfat Gideriminin Araştırılması

Feride Naime TÜRK^{1*}

¹Merkezi Araştırma Laboratuvarı Uygulama ve Araştırma Merkezi, Çankırı Karatekin Üniversitesi, Çankırı, Türkiye.

¹feridenaimeturk@karatekin.edu.tr

Geliş Tarihi: 05.02.2024
Kabul Tarihi: 07.06.2024

Düzeltilme Tarihi: 24.04.2024

doi: 10.62520/fujece.1432277
Araştırma Makalesi

Alıntı: F.N. Türk, "Çinko ekstraksiyon atığı kullanılarak sulu çözeltilerden fosfat gideriminin araştırılması", Fırat Üni. Deny. ve Hes. Müh. Derg., vol. 3, no 3, pp. 313-325, Ekim 2024.

Öz


Çinko üretim tesislerinde açığa çıkan ve içerdikleri metaller nedeniyle tehlikeli atık olarak sınıflandırılan katı liç artıklarının çevre ve insan sağlığına zarar vermeden ekonomik olarak değerlendirilmesi atık yönetimi açısından önemlidir. Bu kalıntıların bertarafı çoğu zaman özel teknolojiler gerektirse de, bu teknolojilerin pahalı olması ve bazı durumlarda yasal yaptırımların yetersiz kalması nedeniyle tehlikeli atıklar çevreye veya çöp depolama alanlarına bırakılmaktadır. Bu nedenle bu kalıntıların değerlendirilerek sanayiye kazandırılması ekonomik ve çevresel açıdan önemlidir. Bu çalışmada, Kayseri Çinkur işletmesinden getirilen çinko ekstraksiyonu üretimi sırasında oluşan kurşun keki kullanılmıştır. Bu atık, çinko ve demirin yanı sıra yüksek miktarda kurşun da içerdiğinden, sulu çözeltilerden fosfatın uzaklaştırılması koşulları araştırıldı. Elde edilen toplu test sonuçları kullanılarak fosfat giderme adsorpsiyon izotermi elde edildi. Ayrıca fosfat giderimine ilişkin bazı termodinamik büyüklükler de hesaplanmıştır. Deney sonucunda sulu çözeltilerden P giderim veriminin önemli ölçüde çözelti pH'ına ve atık kurşun keki dozuna bağlı olduğu belirlendi. Ayrıca sulu çözeltilerden fosfat gideriminin Langmuir ve Freundlich izotermine uyduğu belirlendi. Ayrıca 120 dakikalık bir süre sonunda fosfat adsorpsiyon dengesinin kurulduğu gözlemlendi. pH'ı 7.69 olan 100 mg/L fosfat çözeltisinin herhangi bir ilave olmaksızın 20 g/L kurşun keki ile karıştırılması ve 120 dakika süreyle temas ettirilmesiyle fosfatın yaklaşık %74'ü adsorpsiyonla etkili bir şekilde giderilebilir.

Anahtar kelimeler: Ekstraksiyon kalıntısı, Liç, Kurşun, Fosfat adsorpsiyonu, Atık

*Yazılan yazar



Investigation of Phosphate Removal from Aqueous Solutions Using Zinc Extraction Waste

Feride Naime TÜRK^{1*} 

¹Central Research Laboratory Application and Research Center, Çankırı Karatekin University, Çankırı, Türkiye.

¹feridenaimeturk@karatekin.edu.tr

Received: 05.02.2024

Accepted: 07.06.2024

Revision: 24.04.2024

doi: 10.62520/fujece.1432277

Research Article

Citation: F.N. Türk, "Investigation of phosphate removal from aqueous solutions using zinc extraction waste", Firat Univ. Jour. of Exper. and Comp. Eng., vol. 3, no 3, pp. 313-325, October 2024.

Abstract

It is important for waste management to economically evaluate the solid leach residues released in zinc production facilities and classified as hazardous waste due to the metals they contain, without harming the environment and human health. Although the disposal of these residues often requires special technologies, hazardous wastes are left to the environment or landfills due to the expense of these technologies and the inadequacy of legal sanctions in some cases. For this reason, it is important from an economic and environmental perspective to evaluate these residues and bring them into the industry. In this study, lead cake formed during zinc extraction production, brought from Kayseri Çinkur enterprises, was used. Since this waste contains high amounts of lead as well as zinc and iron, the conditions for removing phosphate from aqueous solutions were investigated. Phosphate removal adsorption isotherms were obtained using the obtained batch test results. Additionally, some thermodynamic quantities regarding phosphate removal were calculated. As a result of the experiment, it was determined that the P removal efficiency from aqueous solutions significantly depends on the solution pH and the dose of waste lead cake. It was also determined that phosphate removal from aqueous solutions obeyed the Langmuir and Freundlich isotherm. Additionally, it was observed that phosphate adsorption equilibrium was established after a period of 120 min. By mixing 100 mg/L phosphate solution with pH 7.69 with 20 g/L lead cake without any addition and contacting for 120 minutes, approximately 74% of the phosphate can be effectively removed by adsorption.

Keywords: Extraction residue, Leaching, Lead, Phosphate adsorption, Waste

*Corresponding author

Plagiarism Checks: Yes – Turnitin

Complaints: fujece@firat.edu.tr

Copyright & License: Authors publishing with the journal retain the copyright to their work licensed under the CC BY-NC 4.0

1. Introduction

Eutrophication can be defined as the deterioration of water quality as a result of the enrichment of water with nutrients and the active development of plant life, adversely affecting the ecological balance of water. The limiting nutrient in most freshwater lake and river reservoirs is phosphorus, and the migration of these elements from anthropogenic sources into waters accelerates the eutrophication process, which proceeds very slowly during the natural aging of lakes. As a result of this event occurring in the lake environment, the dissolved oxygen present is consumed significantly by the algae formed. Depletion of dissolved oxygen can lead to fish mortality, and some blue-green algae can cause poisoning of fish and sometimes livestock [1-6].

Considering these bad effects of phosphates in waters, it becomes necessary to prevent their passage into waters as much as possible. For this, first of all, phosphate sources for waters must be determined well and phosphates must be removed to a significant extent before being discharged from these sources into surface waters [7-9].

Important sources of phosphorus transfer to surface waters are runoff from agricultural areas and farm areas, domestic and industrial wastewater, and urban drainage seepage. A significant portion of phosphates pass through point sources such as domestic and industrial flows. These sources can be controlled more easily than non-point sources [10-12].

Research has shown that the phosphorus concentration in domestic wastewater is around 5-30 mg-P/L. Currently used treatment techniques are suitable for the treatment of wastewater with these concentration limits. However, the treatment of water containing high phosphate, such as boiler water and some food industry wastewater, requires special techniques. Much research has been done on the treatment of wastewater containing normal levels of phosphate. Economical treatment processes are needed for special wastewaters with high phosphate content. In existing phosphate treatment technologies, manufactured chemicals are generally used. However, using waste from another industry with low economic value in the treatment may make the process attractive in terms of cost [13-17].

At the end of the production process in zinc production facilities, a mixture containing precious metals is formed. For the production of metallic zinc, these mixtures are leached with dilute sulfuric acid solution, and then the solid residue, which is insoluble in acid and rich in other components, especially lead, is filtered through filters. Depending on the composition of the raw material used, the content of the zinc extraction waste may consist of approximately 16% lead, 5% zinc, as well as precious metals such as manganese, cadmium, silver and gold.

The high amount of zinc production and the limited storage areas cause facility waste problems. As a result of production in the zinc zinc production facility, there is an excessive amount of zinc in it and the inability to use this solid residue in the system creates problems in terms of economy and environment. The failure to develop a sustainable waste utilization approach to waste negatively affects the competitiveness of the zinc production facility.

In this study, the removal of phosphate from waters with high orthophosphate concentration was investigated by using filtration residue cakes containing significant amounts of lead compounds, which are released during the production of zinc from carbonate ores by the leaching-electrolysis method. Preliminary tests have shown that a significant amount of phosphorus can be removed by treating solutions with high concentrations of phosphate (100-200 mg-P/L) with these wastes.

A large amount of residue called rotary filter cake is formed in ÇİNKÜR facilities in Kayseri. In this study, the possibilities of using this residue in the treatment of waters containing high levels of phosphate were investigated. In the experimental section, the results of the experiments on the effects of factors such as pH, time, concentration and temperature on the adsorption of phosphate from water using this cake were given and discussed. Additionally, some thermodynamic parameters were determined by applying the obtained results to adsorption isotherms.

2. Materials and Methods

2.1. Supply and Preparation of Lead Cake

In the experiments, zinc production residue lead cake obtained from Kayseri Zinc-Lead Enterprise Inc. was used. This cake, which formed after the leaching process, was first washed with distilled water 5 times to remove metal sulfates that could dissolve and pass into the environment. It was partially dried at room temperature and then dried in an oven at 105°C, passed through a -200 mesh sieve and stored in capped plastic bottles. The XRD and SEM-EDX results are given in Figure 1, Figure 2 and Figure 3. Chemical analysis of the zinc extraction residue was carried out by the LiBO₂ dissolution-HNO₃ solubilization method [8, 9].

2.2. Preparation of Phosphate Solution

Phosphate solutions used in the experimental study were prepared from Na₂HPO₄ salt. For this purpose, 14.314 g of 80% pure Na₂HPO₄ salt was weighed, dissolved in some water, and then its volume was made up to 500 mL. The standard stock solution at a concentration of 5000 mg-P/L prepared in this way was diluted appropriately and used in the experiments. Dilutions were made with distilled water.

2.3. Experimental Study

In the study, first the effects of adsorbent amount and time on the efficiency of phosphate removal were examined. For this, phosphate solutions were prepared at a concentration of 100 mg-P/L from the standard stock solution. 100 mL of these solutions were placed in 150 mL conical flasks, varying amounts of lead cake were added to them, varying between 0.5-5 g, and they were sealed and placed in a shaking incubator (ZCHENG 200D) at 25°C. The samples were shaken at 400 oscillations/minute for periods ranging from 10 to 240 min. After shaking, the mixtures were filtered through blue band filter paper. pH measurement, phosphorus, zinc, lead, manganese, iron, cadmium and cobalt analyzes were performed on the filtrates. Removal percentages were calculated taking into account the phosphorus concentration.

To determine the effect of phosphate concentrations, phosphate removal experiments were performed for varying periods of time with phosphate solutions with initial concentrations of 100, 125, 150 mg-P/L. Then, in order to examine the effect of initial pH on phosphate removal, experiments were carried out with phosphate solutions at a concentration of 100 mg-P/L, pH varying between 3-12. Finally, an isotherm study was conducted with phosphate solutions with concentrations varying between 25-125 mg-P/L, at the appropriate pH and equilibration time determined by previous experiments. All experiments were carried out on two parallel samples, and results within ± 5% agreement were considered correct and averaged.

2.4. Phosphate Analyzes

Phosphorus analyzes in the filtrates obtained during the experiments were carried out spectrophotometrically according to the Ascorbic Acid method [18].

2.5. Metal Analysis

All metal analyzes were carried out with an atomic absorption spectrophotometer (Perkin elmer analyst 400). As a result of the analyzes performed using appropriate standards and diluting to the determination range, the leaching percentages of metals from the zinc extraction residue were calculated by backcalculating from the determined metal concentrations.

3. Results and Discussions

The composition of lead cake used as an adsorbent in phosphate adsorption is given in Table 1. As seen in the table, the sample used contains 15.8% Pb, 8.5% Zn and 5.3% Fe as the main components. The idea that certain materials can remove anionic complex ions from wastewater due to the presence of polyvalent metal ions is supported by multiple research findings. Polyvalent metal ions can indeed interact with anionic species, facilitating their removal through various mechanisms, such as adsorption, electrochemical processes, and the formation of inner-sphere complexes. In this study, the removal of phosphate from aqueous media using lead cake was investigated.

In some preliminary studies, it was found that lead cake effectively removed low concentrations of phosphate from aqueous environments. For this reason, it was thought that it would be more advantageous to remove the high concentration of phosphate in the aqueous environment with lead cake. In line with this idea, the first experiments were carried out with phosphate solutions at a concentration of 100 mg-P/L in order to reveal the effect of the amount of lead cake on phosphorus removal depending on time. 100 mL of phosphate solution was mixed with lead cake in amounts ranging from 0.5 to 5 g and shaken for periods ranging from 10 to 240 minutes. The phosphorus removal percentage calculated from analyzes and measurements and the metal ion concentrations that dissolve from the cake and pass into solution are given in Figure 4.

Table 1. Chemical composition of the lead cake used in the experiments.

Component	Composition
Pb	% 15.80
Zn	% 8.50
Fe	% 5.30
Ca	% 1.30
Mn	2155 mg/kg
Cd	318 mg/kg
Cu	2280 mg/kg
Ni	475 mg/kg
Cr	249 mg/kg

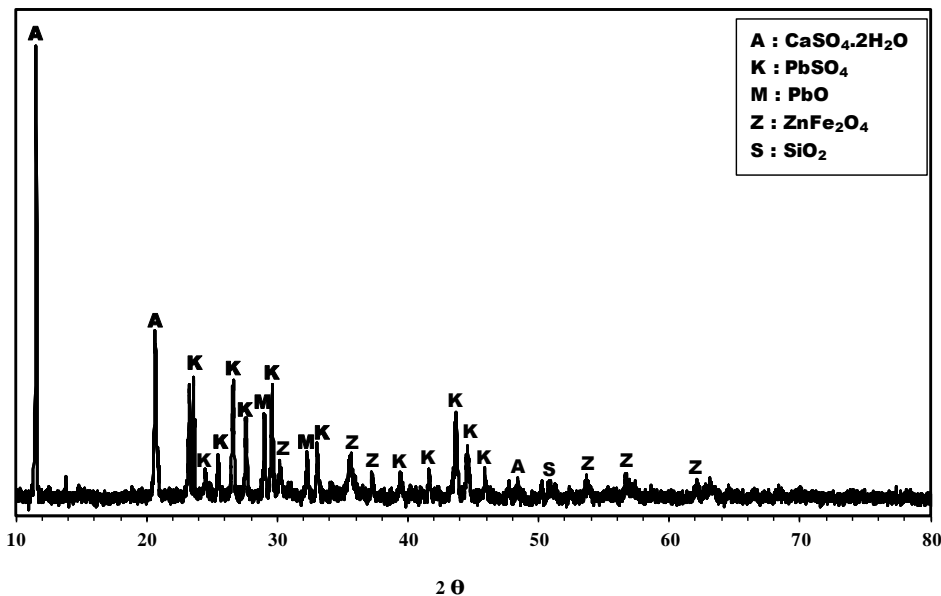


Figure 1. XRD diagram of the lead cake used in the experiments.

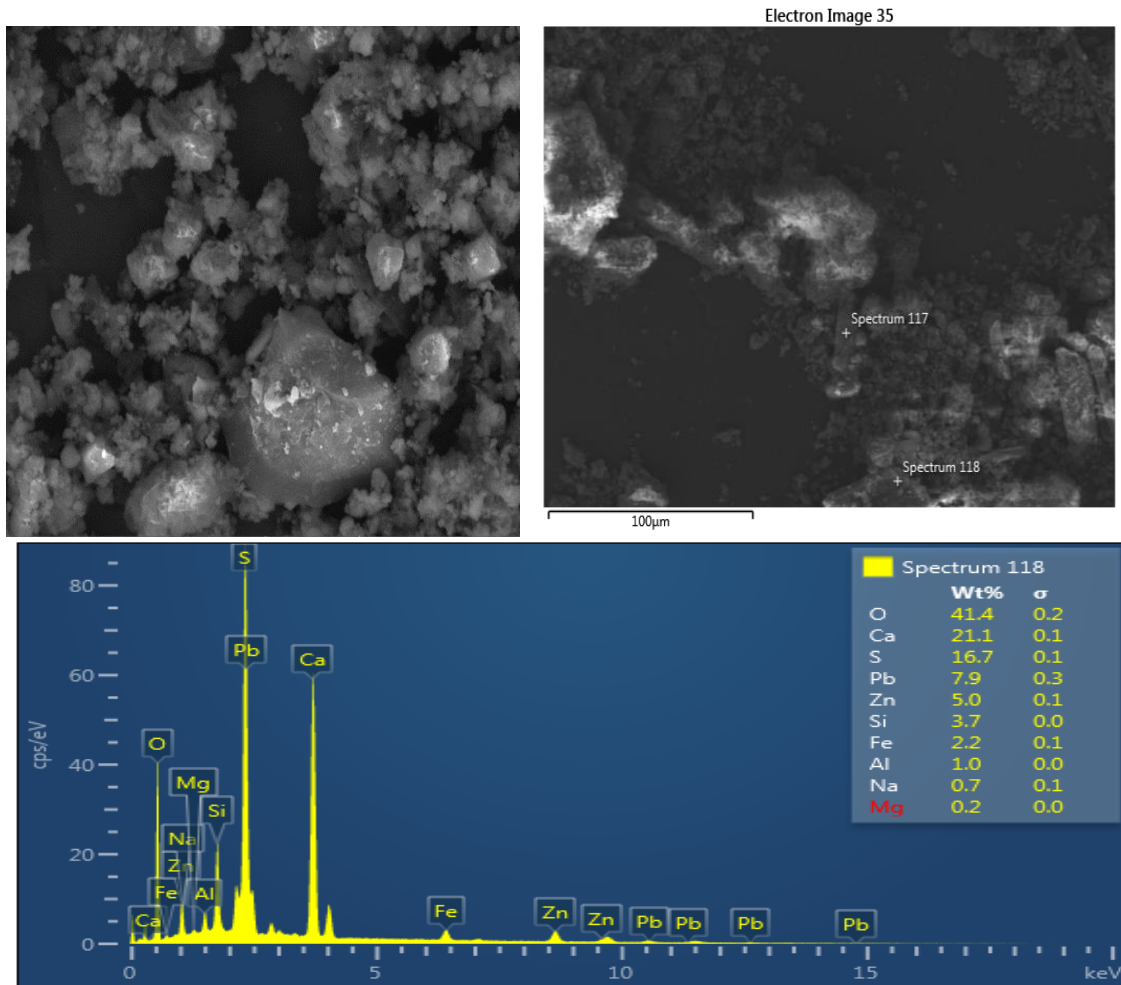


Figure 2. SEM image and EDX evaluation of the lead cake used in the experiments

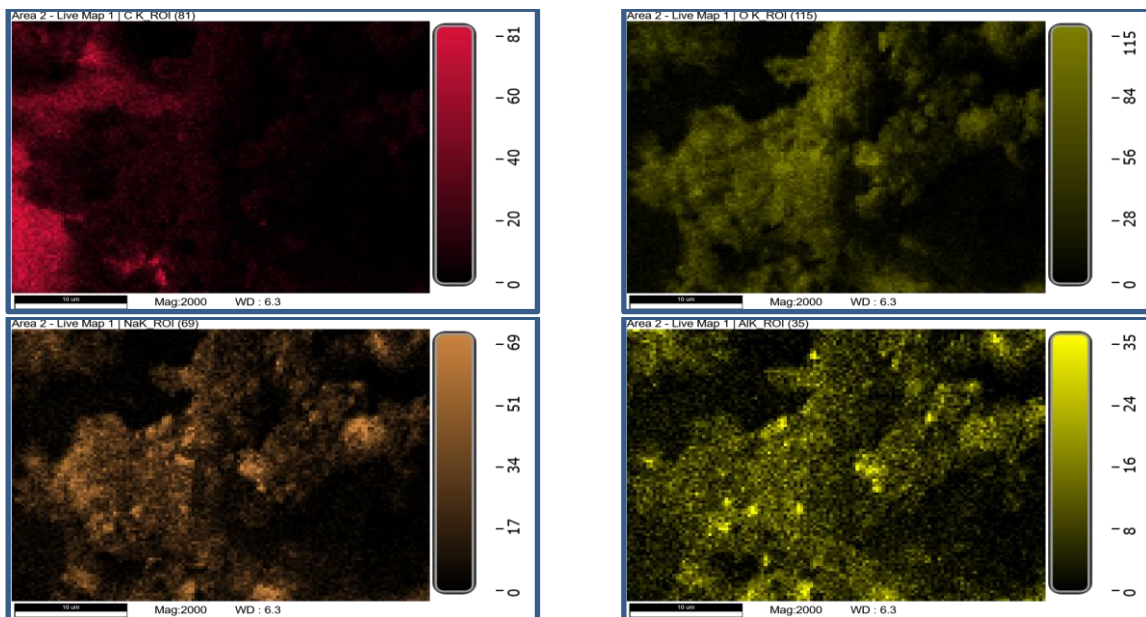


Figure 3. SEM image and EDX evaluation of the lead cake used in the experiments

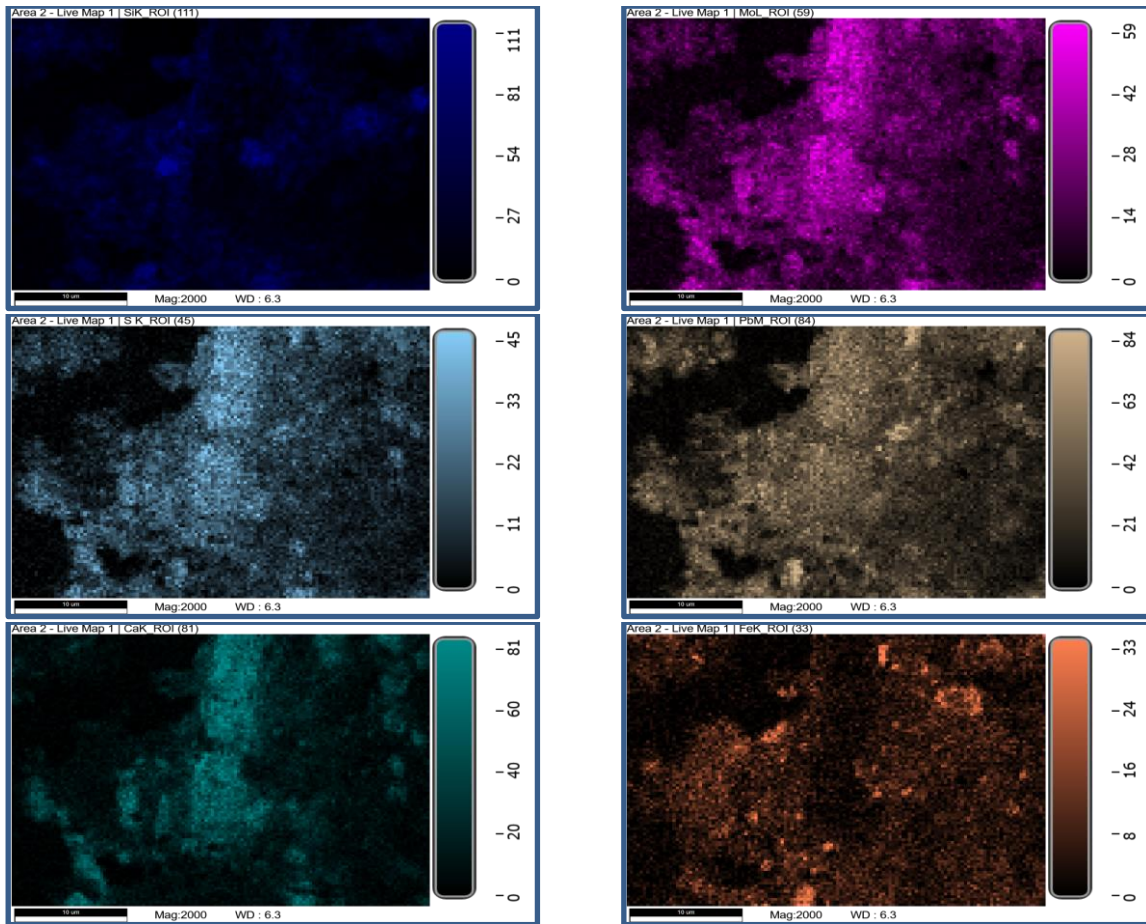


Figure 3. SEM image and EDX evaluation of the lead cake used in the experiments (Continue)

It can be said that with increasing lead cake amount and time, the phosphorus removal efficiency generally increases and an equilibration time is reached at the end of a reaction time of approximately 120 min for all cake amounts. Figure 4 shows that the concentration of metal ions that dissolve from the lead cake into the solution environment increases depending on the amount of cake. Considering the phosphorus removal percentage, it can be said that a dose of 50 g/L lead cake is suitable to remove phosphorus at a concentration of 100 mg/L. However, in order for a treatment process to be applicable, it is required that the treatment in question be carried out in the most effective way and that no other pollution occurs in the process. This is why the concentrations of metal ions in the lead cake that pass into solution must be taken into account. Figure indicates that much higher amounts of Zn and Pb pass into the solution when the 50 g/L lead cake dose is used. For example, in the experiment conducted with a 30 g/L lead cake dose, where the phosphorus removal percentage is relatively high at the end of the equilibration period, 0.82 mg/L lead and 1.02 mg/L zinc pass into the solution, while with a 50 g/L dosage, 0.94 mg/L lead and 18.20 mg/L zinc passes. In order not to cause any further pollution, it can be said that it would be more appropriate to use cake at a dosage of 30 g/L to remove phosphorus at a concentration of 100 mg/L.

In the second stage, the effect of ambient pH on phosphate removal was examined. For this, phosphate solutions at a concentration of 100 mg/L, the initial pH of which was adjusted between 3-12 using NaOH and H₂SO₄, were shaken for 120 min using cake at a dosage of 30 g/L. The results obtained are seen in figure 4.

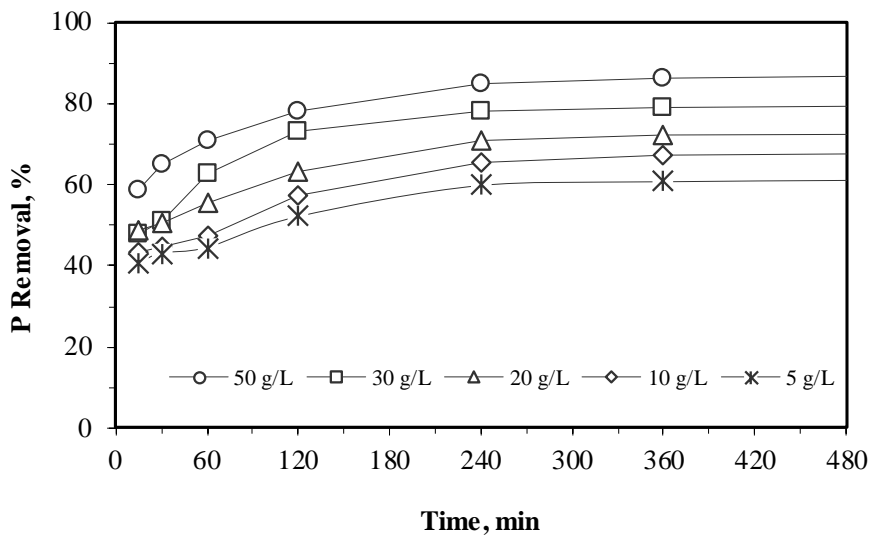


Figure 4. Results of experiments conducted with different doses of lead cake for different periods of time. [25°C; 100mg-P/L; 100 mL; pH: 7.69]

The percentage of phosphate removal increased significantly due to the increase in initial pH. While 2-20% of the total phosphorus can be removed in the pH<6 region, more than 80% of the total phosphorus can be removed at pH>9. It can be seen that at the original pH of the solution, 7.69, approximately 75% of the phosphorus is removed. On the other hand, it is seen that the concentration of Pb ion, which dissolves from the cake and passes into the solution, increases with increasing pH. Zinc passes into solution more at low pH.

Very low and high pH values have no practical applicability due to both acid and base consumption and deterioration of the neutral properties of water. It can be seen from Figure 5 that the most effective phosphorus removal is at pH>10. However, in this case, it is seen that Pb and Zn pass into the solution well above their concentration limits. It can be said that it is more suitable in terms of process economy and applicability to carry out the process at its own pH in order to prevent such secondary pollution and eliminate alkali consumption. For this reason, experiments examining the effects of other parameters on phosphate adsorption were carried out at the original pH of the solution.

Figure 6 shows the effect of initial phosphate concentration on phosphate adsorption. As the phosphate concentration increases, the removal percentage decreases, but the amount of phosphate removed per unit adsorbent (lead cake) increases. Additionally, after approximately 100-120 minutes, an equilibration period is reached for all concentrations. For example, in phosphate solutions at a P concentration of 100 mg/L, an adsorption of approximately 74.98% occurs after 120 minutes of equilibration, while this value becomes 66.17% and 48.98% for concentrations of 125 and 150 mg-P/L, respectively.

The data obtained as a result of contacting phosphate solutions with different initial concentrations with cake at a dosage of 30 g/L, at optimum pH and for 120 min, were applied to Langmuir and Freundlich isotherms (equations 1 and 2).

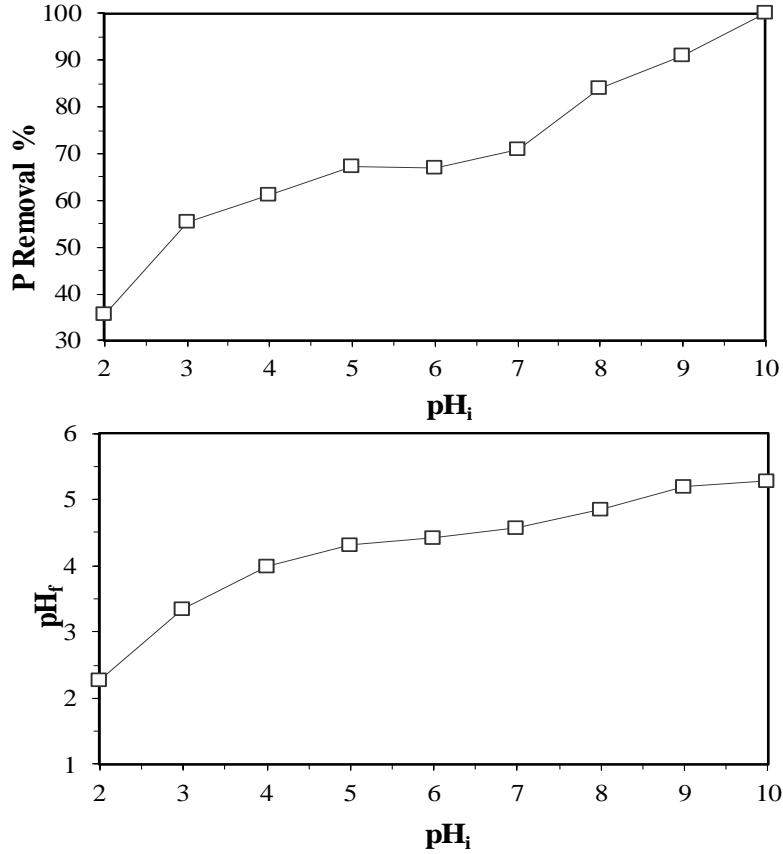


Figure 5. Experimental results examining the effect of initial pH on phosphate adsorption with lead cake. [25°C; 100 mL; 30 g/L lead cake; 100mg-P/L; 120 minutes contact time]

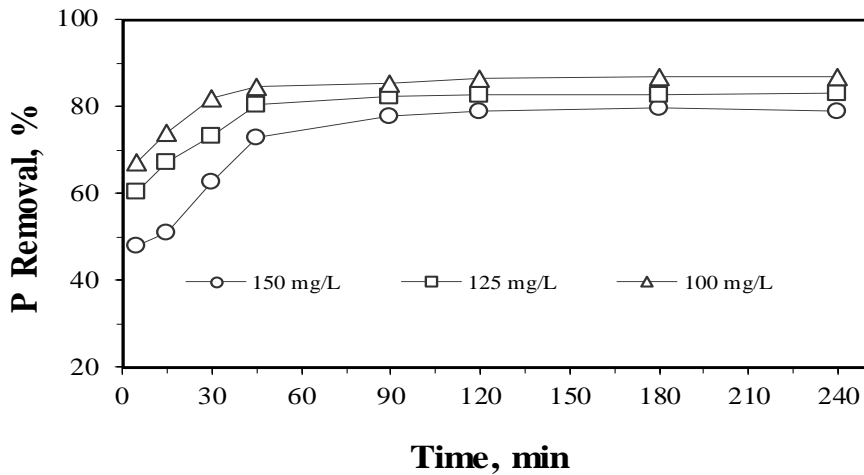


Figure 6. Effect of initial phosphorus concentration on phosphate adsorption by lead cake. [25°C; 30 g/L lead cake; 100 mL; pH: 7.69].

Langmuir isotherms obtained after phosphate adsorption at different temperatures are given in Figure 7. b and Q_0 values were calculated from the slope and shift of the isotherms using linear regression. By plotting $\ln b$ values against $1/T$ values according to Equation 3, the adsorption enthalpy was found to be -11.5941 kJ/mol. Adsorption free enthalpy and entropy changes at different temperatures were calculated using Equations 4 and 5. The results are seen in table 2.

$$\frac{C_e}{q_e} = \frac{1}{q_{\max} b} + \frac{C_e}{q_{\max}} \quad (1)$$

$$\ln\left(\frac{x/m}{C_e}\right) = \ln K_f + \frac{1}{n} \ln C_e \quad (2)$$

$$\ln b = \ln b' - \Delta H/RT \quad (3)$$

$$\ln(1/b) = \Delta G/RT \quad (4)$$

$$\Delta G = \Delta H^\circ - T \Delta S \quad (5)$$

In the equations, x: The amount of adsorbed substance (mg), m: The amount of adsorbent (g), C_e : The equilibrium concentration of the adsorbed substance in the solution (mg/L). K_f (mg/g) is the Freundlich constant, which is a measure of adsorption capacity. The other Freundlich constant n is dimensionless. q_{\max} : Maximum adsorption capacity, (mg/g), b: A constant related to adsorption energy, (l/mg). T is the absolute temperature (K) and R is the universal gas constant ($8.314 \text{ Jmol}^{-1}\text{K}^{-1}$). Thermodynamic parameters of the adsorption process, such as free energy (ΔG°), enthalpy (ΔH°) and entropy (ΔS°) change, can be calculated with the above equations.

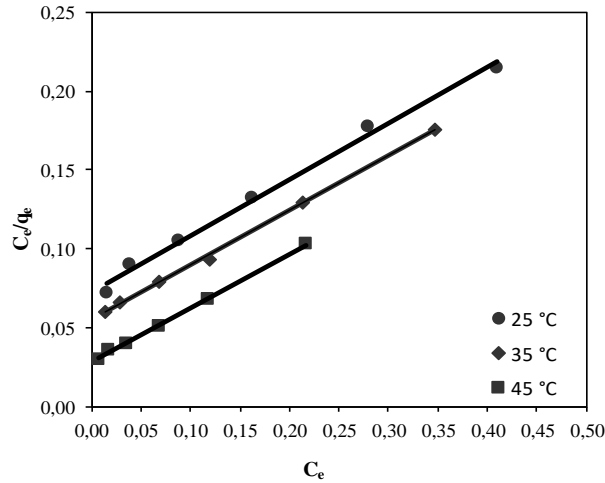


Figure 7. Langmuir isotherm for phosphate adsorption with lead cake. [pH: 7.69; 100 mL; 25-125 mg-P/L; 120 min contact time; 30 g/L lead cake].

The negative sign of the adsorption enthalpy calculated for phosphate adsorption indicates that the adsorption event is exothermic. In addition, in the temperature studies carried out while obtaining the isotherms, the decrease in the percentage of phosphate removal with increasing temperature proves that the phenomenon is exothermic. Table 2 shows that the free enthalpy change of phosphorus adsorption with lead cake is negative. This shows that the adsorption of phosphate to the cake is a spontaneous event.

Table 2. Langmuir constants and Thermodynamic constants.

Temperature, °C	Langmuir		ΔG (kJ/mol)	ΔS (kJ/mol)
	b	q_{\max}		
25	0.3371	2.6441	5.479	
35	0.2312	2.3463	5.433	0.02
45	0.1049	2.2104	5.109	

The isotherm data obtained for each temperature were applied to the Freundlich equation. The lines obtained by plotting $\ln(x/m)$ values against $\ln C_e$ values show that the results are applicable to the Freundlich isotherm (Figure 8). Freundlich constants obtained depending on temperature are given in Table 3. As can be seen from the table, Freundlich constant K_f , which is a measure of adsorption capacity, decreases with increasing temperature.

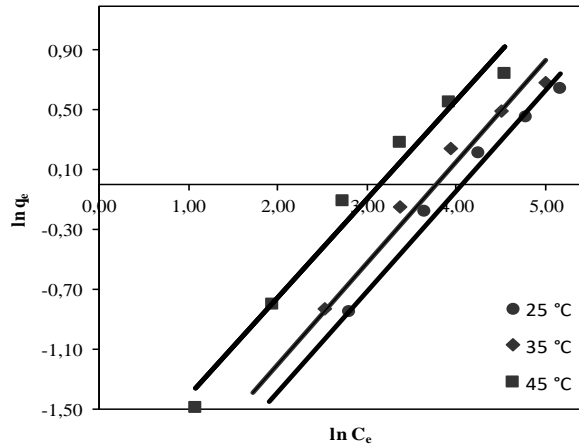


Figure 8. Freundlich isotherm for phosphate adsorption with lead cake. [pH: 7.69; 100 mL; 25-125 mg-P/L; 120 min contact time; 30 g/L lead cake].

Table 3. Freundlich constants.

Temperature, °C	n	1/n	K_f
25	2.41	0.42	0.66
35	3.18	0.32	0.69
45	2.64	0.37	0.44

The maximum monolayer capacity obtained from Langmuir isotherms is 2.644 mg/g at 25°C with an initial concentration range of 25-125 mg-P/L and a dose of 30 g/L. As the temperature increases, the adsorption capacity decreases and the phosphate adsorption capacity at 45°C is 2.210 mg/g.

4. Conclusions

The study investigating the phosphate adsorption properties of lead cakes, which are the residual materials after zinc extraction from carbonate ores, yielded significant insights into their potential application for wastewater treatment. This analysis draws from multiple research articles to provide a comprehensive understanding of the mechanisms and factors influencing phosphate adsorption by such lead cakes. In the equilibration time study conducted with solutions prepared from orthophosphate at a concentration of 100 mg-P/L, at a dose of 30 g/L lead cake and at 25°C, it was found that equilibrium was achieved after 120 minutes. Under these conditions, approximately 75% of the phosphate in the environment is removed. As a result of experiments conducted at different pH values, it was found that lead cake removes more phosphate as pH increases. Phosphate removal efficiency is higher in strongly alkaline environments (pH 10-12). However, this has no practical significance. As a result of experiments conducted with solutions at different temperatures and different initial phosphate concentrations, phosphate removal complies with the Langmuir and Freundlich isotherms in the concentration range of 25-125 mg-P/L. In the calculations made regarding this; Langmuir monolayer adsorption capacity was found to be 2.6441 mg/g adsorbent at 25°C. Adsorption efficiency decreases depending on temperature. The fact that the adsorption enthalpy is negative indicates that the event is exothermic. The fact that the

free enthalpy changes are negative indicates that the adsorption of orthophosphate onto the lead cake is a spontaneous event.

As a final result, it can be said that orthophosphate effectively adsorbs lead cake. However, even though soluble zinc and lead residues have been removed by prior washing, zinc and lead ions may pass from the lead cake into the solution medium. As a matter of fact, the results show this. Therefore, this material cannot be used to remove phosphate from wastewater. Because this time, there is a need to remove these secondary pollutants. In cases where the presence of lead and zinc ions in the environment does not pose a problem, it can be taken into consideration in phosphate removal.

5. Acknowledgments

I would like to thank Çankırı Karatekin University for their contribution to the experimental studies in this research.

6. Author Contribution Statement

Feride N. Turk: Investigation, Conceptualization, Data curation, Validation, Formal analysis, Methodology, Visualization, Writing - review & editing, Writing – original draft.

6. Ethics Committee Approval and Conflict of Interest

There is no need for an ethics committee approval in the prepared article. There is no conflict of interest with any person/institution in the prepared article.

7. References

- [1] V. Kuroki, G. E. Bosco, P. S. Fadini, A. A. Mozeto, A. R. Cestari, and W. A. Carvalho, "Use of a La (III)-modified bentonite for effective phosphate removal from aqueous media," *Jour. of Hazar. Mater.*, vol. 274, pp. 124-131, 2014.
- [2] J. Diao, L. Shao, D. Liu, Y. Qiao, W. Tan, L. Wu, and B. Xie, "Removal of phosphorus from leach liquor of steel slag: Adsorption dephosphorization with activated alumina," *JOM*, vol. 70, pp. 2027-2032, 2018.
- [3] J. Xiong, Z. He, Q. Mahmood, D. Liu, X. Yang, and E. Islam, "Phosphate removal from solution using steel slag through magnetic separation," *Jour. of Hazar. Mater.*, vol. 152, no. 1, pp. 211-215, 2008.
- [4] M. Kondalkar, U. Fegade, S. Attarde, and S. Ingle, "Phosphate removal, mechanism, and adsorption properties of Fe-Mn-Zn oxide trimetal alloy nanocomposite fabricated via co-precipitation method," *Separ. Sci. and Tech.*, vol. 54, no. 16, pp. 2682-2694, 2019.
- [5] R. Fan, C. Chen, J. Lin, J. Tzeng, C. Huang, C. Dong, and C. Huang, "Adsorption characteristics of ammonium ion onto hydrous biochars in dilute aqueous solutions," *Bior. Tech.*, vol. 272, pp. 465-472, 2019.
- [6] J. Jang and D. S. Lee, "Effective phosphorus removal using chitosan/Ca-organically modified montmorillonite beads in batch and fixed-bed column studies," *Jour. of Hazar. Mater.*, vol. 375, pp. 9-18, 2019.
- [7] H. Yoshida and W. A. Galinada, "Equilibria for adsorption of phosphates on OH-type strongly basic ion exchanger," *AIChE Jour.*, vol. 48, no. 10, pp. 2193-2202, 2002.
- [8] H. S. Altundoğan and F. Tümen, "Removal of phosphates from aqueous solutions by using bauxite. I: Effect of pH on the adsorption of various phosphates," *Jour. of Chem. Tech. & Biotec.*, vol. 77, no. 1, pp. 77-85, 2002.
- [9] H. S. Altundoğan and F. Tümen, "Removal of phosphates from aqueous solutions by using bauxite II: The activation study," *Jour. of Chem. Tech. & Biotec.*, vol. 78, no. 7, pp. 824-833, 2003.
- [10] Y. Li, C. Liu, Z. Luan, X. Peng, C. Zhu, Z. Chen, Z. Zhang, J. Fan, and Z. Jia, "Phosphate removal from aqueous solutions using raw and activated red mud and fly ash," *Jour. of Hazar. Mater.*, vol. 137, no. 1, pp. 374-383, 2006.

- [11] Y. Liu, X. Sheng, Y. Dong, and Y. Ma, "Removal of high-concentration phosphate by calcite: Effect of sulfate and pH," *Desal.*, vol. 289, pp. 66-71, 2012.
- [12] K. Karageorgiou, M. Paschalis, and G. N. Anastassakis, "Removal of phosphate species from solution by adsorption onto calcite used as natural adsorbent," *Jour. of Hazar. Mater.*, vol. 139, no. 3, pp. 447-452, 2007.
- [13] M. Li, J. Liu, Y. Xu, and G. Qian, "Phosphate adsorption on metal oxides and metal hydroxides: A comparative review," *Environ. Rev.*, vol. 24, no. 3, pp. 319-332, 2016.
- [14] H. Liu, X. Sun, C. Yin, and C. Hu, "Removal of phosphate by mesoporous ZrO₂," *Jour. of Hazar. Mater.*, vol. 151, nos. 2-3, pp. 616-622, 2008.
- [15] W. Huang, S. Wang, Z. Zhu, L. Li, X. Yao, V. Rudolph, and F. Haghseresht, "Phosphate removal from wastewater using red mud," *Jour. of Hazar. Mater.*, vol. 158, no. 1, pp. 35-42, 2008.
- [16] H. Yin, Y. Yun, Y. Zhang, and C. Fan, "Phosphate removal from wastewaters by a naturally occurring, calcium-rich sepiolite," *Jour. of Hazar. Mater.*, vol. 198, pp. 362-369, 2011.
- [17] T. Nguyen, H. Ngo, W. Guo, J. Zhang, S. Liang, D. J. Lee, P. Nguyen, and X. Bui, "Modification of agricultural waste/by-products for enhanced phosphate removal and recovery: Potential and obstacles," *Biores. Techn.*, vol. 169, pp. 750-762, 2014.
- [18] *APHA-AWWA/WEF, Standard Methods for the Examination of Water and Wastewater*, 20th Edition, Washington DC, USA: American Public Health Association, 1998.



Hidrotermal Karbonizasyon Yöntemiyle Biyokütle Bazlı Aktif Karbon Üretim Prosesinin Geliştirilmesi

Nida KATI¹ , Ferhat UÇAR^{2*} 

¹Metalurji ve Malzeme Mühendisliği, Teknoloji Fakültesi, Fırat Üniversitesi, Elazığ, Türkiye.

²Yazılım Mühendisliği, Teknoloji Fakültesi, Fırat Üniversitesi, Elazığ, Türkiye.

¹nkati@firat.edu.tr, ²fucar@firat.edu.tr

Geliş Tarihi: 26.04.2024
Kabul Tarihi: 07.06.2024

Düzelme Tarihi: 21.05.2024

doi: 10.62520/fujece.1473852
Araştırma Makalesi

Alıntı: N. Katı ve F. Uçar, "Hidrotermal karbonizasyon yöntemiyle biyokütle bazlı aktif karbon üretim prosesinin geliştirilmesi", Fırat Üni. Deny. ve Hes. Müh. Derg., vol. 3, no 3, pp. 326-336, Ekim 2024.

Öz

Bu çalışma, kayısı çekirdeği kabukları (KÇK) kullanılarak hidrotermal karbonizasyon ve kimyasal aktivasyon yöntemleriyle üretilen hidrokömürlerin ve aktif karbonların ayrıntılı karakterizasyonunu içeren bir süreç geliştirmeyi sunmaktadır. İlk olarak, KÇK öğütülerek işlenmiş, ardından 24, 36 ve 48 saat boyunca 240°C'de hidrotermal karbonizasyona tabi tutularak üç farklı hidrokömür elde edilmiştir. Daha sonra, bu hidrokömürler 3 saat boyunca KOH ile karıştırılmış ve aktif karbonlar elde etmek için 700°C'de 1 saat boyunca karbonizasyon işlemine tabi tutulmuştur. Aktif karbonların yapısal özelliklerini belirlemek için Brunauer-Emmett-Teller (BET) yüzey alanı analizi, Taramalı Elektron Mikroskopu (SEM) ve Enerji Dağılım Spektroskopisi (EDS), X-Işını Kırınımı (XRD) analizi ve Fourier-Transform Kızılötesi spektroskopisi (FTIR) ölçümleri gibi çeşitli karakterizasyon yöntemleri kullanılmıştır. Elde edilen sonuçlar, hidrotermal reaksiyon süresinin karbon içeriğini artırdığını ve gözenekli yapıların oluşumuna yol açtığını göstermektedir. Özellikle, SEM görüntülerinden de anlaşılacağı üzere, kimyasal aktivasyon sürecinin gözenek oluşumunda etkili olduğu görülmüştür. Sonuç olarak, bu çalışma hidrokömürlerin ve KÇK'den elde edilen aktif karbonların karakteristik özelliklerinin ayrıntılı bir tanımını sunmaktadır.

Anahtar kelimeler: Hidrotermal karbonizasyon, Aktif karbon, Kayısı çekirdeği kabuğu

*Yazılan Yazar

İntihal Kontrol: Evet – Turnitin

Şikayet: fujece@firat.edu.tr

Telif Hakkı ve Lisans: Dergide yayın yapan yazarlar, CC BY-NC 4.0 kapsamında lisanslanan çalışmalarının telif hakkını saklı tutar.



Development of a Production Process for Biomass-Based Activated Carbon via Hydrothermal Carbonization Method

Nida KATI¹ , Ferhat UÇAR^{2*} 

¹Metalurgical and Materials Engineering, Faculty of Technology, Firat University, Elazığ, Türkiye.

²Software Engineering, Faculty of Technology, Firat University, Elazığ, Türkiye.

¹nkati@firat.edu.tr, ²fucar@firat.edu.tr

Received: 26.04.2024

Accepted: 07.06.2024

Revision: 21.05.2024

doi: 10.62520/fujece.1473852

Research Article

Citation: N. Katı and F. Uçar, "Development of a Production Process for Biomass-Based Activated Carbon via Hydrothermal Carbonization Method", *Firat Univ. Jour. of Exper. and Comp. Eng.*, vol. 3, no 3, pp. 326-336, October 2024.

Abstract

This study presents a process development including detailed characterization of hydrochars and activated carbons produced by hydrothermal carbonization and chemical activation methods using apricot kernel shells (AKS). Initially, the AKS were processed by grinding, followed by subjecting them to hydrothermal carbonization at 240°C for 24, 36, and 48 hours, resulting in three distinct hydrochars. Subsequently, these hydrochars were mixed with KOH for 3 hours and subjected to a carbonization process at 700°C for 1 hour to obtain activated carbons. Various characterization methods such as Brunauer-Emmett-Teller (BET) surface area analysis, Scanning Electron Microscopy (SEM) and Energy Dispersive Spectroscopy (EDS), X-Ray Diffraction (XRD) analysis, and Fourier-Transform Infrared spectroscopy (FTIR) measurements were employed to determine the properties of the activated carbons. The results obtained indicate that the duration of the hydrothermal reaction increases the carbon content and leads to the formation of porous structures. Particularly, the chemical activation process was found to be effective in pore formation, as evident in SEM images. In conclusion, this study provides a detailed description of the characteristic properties of hydrochars, and activated carbons derived from AKS.

Keywords: Hydrothermal carbonization, Activated carbon, Apricot kernel shell

*Corresponding Author

Plagiarism Checks: Yes – Turnitin

Complaints: fujece@firat.edu.tr

Copyright & License: Authors publishing with the journal retain the copyright to their work licensed under the CC BY-NC 4.0

1. Introduction

Türkiye is the largest producer of fresh and dried apricots in the world. Consequently, a substantial amount of cheap apricot kernel shells (AKS), obtained as waste in apricot production, is available. Approximately 25,000 tons of AKS are generated annually in Türkiye as industrial waste. Through the utilization of activation techniques, around 4,000 tons of high value activated carbon can be produced from this biomass [1]. In 2021, Malatya accounted for 48.7% of the total apricot production in Türkiye with 389,000 tons of fresh apricots. Following Malatya, Mersin contributed 20.3%, Iğdir .4%, Elazığ 3.9%, and Isparta 2.8% to the overall production [2]. Analysis of the AKS data used in our study indicates an annual yield of approximately 20,000 tons in the Malatya region [3]. Biomass structures can be converted into high-value components containing solid, liquid, and gaseous products using the hydrothermal method. The variation in specific properties depending on the temperature and pressure of water brings significant advantages to the processing of biomass with the hydrothermal method. During hydrothermal conversion, hot water, acting both as a solvent and as a reactive or catalytic agent, plays a crucial role. For instance, many cellulose-based biomasses are insoluble in water, but they can become soluble in supercritical water during the hydrothermal process. Additionally, another advantage of the hydrothermal method is its suitability as a thermochemical conversion method for biomass with high moisture content [4]. There are several studies in the literature regarding biomass waste, particularly AKS. L. Wang et al. synthesized activated carbon from apricot shell extract using chemical methods with the support of H_3PO_4 in a process, investigating the relationship between pore structure and electrochemical performance for supercapacitor applications [5]. In another proposed study by the same research group, activated carbon was produced from apricot shells using a one-step chemical synthesis method, and its supercapacitor performance was evaluated. The positive attributes contributed by the hierarchical pore structure in this study were presented in detail. The morphological structure of the activated carbon synthesized from AKS was demonstrated to provide a broad adsorption area, with micro-pores addressing the flow of electrolyte ions and storage capacity, and meso-pores and macro-pores serving as transport channels and buffer reservoirs for electrolyte ions, respectively [6]. Temirgaliyeva et al. prepared an active carbon and carbon nanotube-based composite material from three different biomass types, including AKS, proposing an electrode structure for use in hybrid supercapacitor [7]. Eom et al. analyzed the use of activated porous carbon obtained from spent black tea residues as long-lasting supercapacitor electrodes, emphasizing the suitability of its recyclable use [8]. Canbaz obtained active carbon electrodes through hydrothermal carbonization from hazelnut shell-derived biomass material and investigated their potential use for sodium-ion batteries [9].

This study pioneers a novel approach to the sustainable valorization of industrial biomass waste, specifically AKS, by utilizing the hydrothermal method to produce high value activated carbon especially for supercapacitor applications. **Our research stands out for its innovative contributions, which include:**

1. Innovative hydrothermal conversion process: We developed and optimized a unique hydrothermal conversion technique specifically designed for AKS. This method not only enhances the efficiency of biomass conversion but also improves the quality and functionality of the resulting activated carbon. Our process is distinguished by its ability to handle the high moisture content of biomass, which typically complicates biomass conversion efforts.

2. Detailed characterization and application of activated carbon: Our research provides an exhaustive characterization of the activated carbon produced, detailing its morphological properties. This contribution is significant as it bridges the gap between theoretical research and practical, commercial applications of activated carbons in supercapacitor technology.

These contributions not only advance the field of biomass waste management but also highlight the potential of agricultural waste to be transformed into economically valuable products, aligning with global sustainability goals and advancing green technology initiatives.

2. Material and Method

The AKS used as raw material in our study were obtained from the Elazığ. The shells were ground to 60 mesh sizes using a laboratory-type blender (Waring blender), and the resulting powdered shells were stored in a glass jar. The Potassium Hydroxide (KOH) with CAS number 1310-58-3 used in the activation process and Hydrochloric Acid (HCl) from the Biorad brand used in the washing process were commercially obtained. The raw material, AKS powder (N-Raw), utilized as biomass for the preparation of hydrochars through hydrothermal carbonization, was mixed with 40 mL of distilled water to achieve a ratio of 4 grams in a stainless-steel reactor (Fytronix FYHT-8000 model) equipped with a Teflon vessel. The hydrothermal apparatus, manufactured by Fytronix Electronics, comprises a temperature and time-controlled control panel and a hydrothermal reactor. The inner part of the stainless-steel reactor is designed to accommodate a 100 ml Teflon vessel. The reactor's lid features two valves and a digital pressure gauge to facilitate gas inlet and outlet. After placing the mixture in the Teflon vessel, hydrochars were produced under hydrothermal carbonization conditions at 240°C for 24, 36, and 48 hours, resulting in hydrochars produced under three different parameters. The obtained hydrochars were filtered using membrane filter paper, washed with distilled water, and dried in an oven at 100°C for 24 hours. One-third of the dried products were separated, stored in a glass sample dish, and labeled as N-H1, N-H2, and N-H3. The remaining products were impregnated with commercially obtained KOH in a 1:3 ratio at a temperature between 60-70°C for 3 hours for chemical activation. The KOH-loaded hydrochars were filtered, dried in an oven at 100°C for 24 hours, transferred to a ceramic crucible, and subjected to carbonization in a tube furnace at 700°C for 1 hour with a nitrogen flow rate of 300 cm³/min. The resulting activated carbons were then washed with HCl acid until reaching a pH of 6-7, followed by washing with distilled water and filtration. The filtered products were dried at 100°C for 24 hours. The obtained activated carbons were named N-A1, N-A2, and N-A3. Table 1 provides information on the samples and production parameters, while Figure 1 illustrates the production stages of the activated carbons.

Table 1. Samples and production parameters.

Sample Name	Hydrothermal Reaction Temperature (°C)	Hydrothermal Reaction Pressure (MPa)	Hydrothermal Reaction Time (hr)	Chemical Activation
N-H1	240	5-6	24	No Chemical Activation
N-H2	240	5-6	36	
N-H3	240	5-6	48	
N-A1	240	5-6	24	KOH
N-A2	240	5-6	36	
N-A3	240	5-6	48	

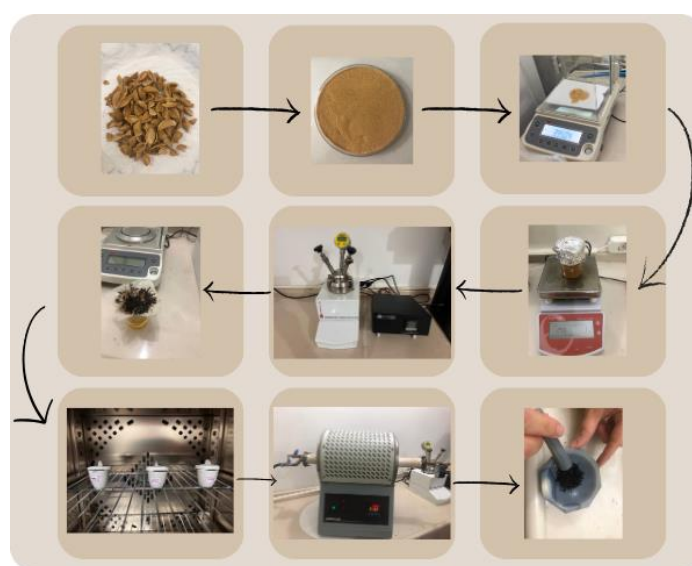


Figure 1. Activated carbon production stages.

To determine the surface area and pore size distribution of hydrochars and activated carbons, nitrogen adsorption was performed at -196°C using the Micromeritics ASAP 2020 instrument in the Department of Chemical Engineering at Firat University. The hydrochars and activated carbons were subjected to vacuum treatment at 150°C for 12 hours, and nitrogen adsorption/desorption isotherms were obtained in the relative pressure (P/P_0) range of 0-1. The surface area (SBET) of the adsorbents was determined using the Brunauer-Emmett-Teller (BET) method based on nitrogen adsorption/desorption isotherm data. For the structural characterization of untreated AKS, hydrochars, and activated carbons, Scanning Electron Microscopy (SEM) and Energy Dispersive Spectroscopy (EDS) analysis was conducted using the JEOL JSM-7001F model SEM instrument available at the KITAM Laboratory of Ondokuz Mayıs University. X-Ray Diffraction (XRD) analyses of the samples were carried out using the SmartLab X-RAY Diffractometer XRD instrument at the KITAM Laboratory of Ondokuz Mayıs University. XRD measurements were performed in the $2\theta = 20^{\circ}$ - 80° angle range with values of 45 kV and 40 mA. To identify the functional bonds in the molecular structure of the samples, Fourier-Transform Infrared spectroscopy (FTIR) measurements were conducted using the Thermo SCIENTIFIC Nicolet iS5 Spectrophotometer apparatus in the Central Laboratory of Firat University (spectrum range $4000\text{-}400\text{ cm}^{-1}$).

3. Results and Discussion

BET surface area values of hydrochar and activated carbons produced by the hydrothermal carbonization method are given in Table 2. When examining the BET surface area values of hydrochars produced through hydrothermal reaction, it can be stated that the reaction duration has an impact on the surface area. Comparing the raw AKS sample (N-Raw) with the processed samples N-H1 to N-H3, the hydrothermal process increased the bet surface area. As the particle size of the material decreases, an increase in surface area occurs. The presence of a porous structure, as evident in the SEM images in Figure 2, supports this increase. The lower porosity of samples obtained through the hydrothermal carbonization of biomass explains their lower surface areas [10]. The BET surface areas of samples obtained from lignocellulosic biomass generally show similarities with the literature. The application of KOH activation to hydrochars results in an increase in surface areas [11], [12], [13]. The highest surface area value, $976.650\text{ m}^2/\text{g}$, was found in the N-A3 sample subjected to a 48-hour hydrothermal reaction and KOH activation. The activating agent plays a significant role in the development of the porous structure. In another study in the literature, samples obtained through hydrothermal carbonization at 280°C for 1 hour, 3 hours, and 6 hours showed an increase in BET surface area values from $46\text{ m}^2/\text{g}$ to $92\text{ m}^2/\text{g}$ with increasing reaction time. It was indicated that the trend of increased surface areas with extended reaction time is related to the surface roughness resulting from the transformation of cellulose, hemicellulose, and lignin present in lignocellulosic biomass [14], [15].

Table 2. BET surface area results of the samples

Sample Name	BET surface area (m^2/g)
N-Raw	4.2756
N-H1	5.8682
N-H2	20.7856
N-H3	80.6333
N-A1	637.970
N-A2	842.310
N-A3	976.650

SEM analysis was performed to evaluate the surface structures of AKS powder (N-Raw) without hydrothermal carbonization, hydrochar obtained by hydrothermal carbonization, and activated carbon samples with the activation process. SEM images provide important information about the physical morphology of the surface. The changes occurring on the surface and the micro and mesopores formed before and after the hydrothermal carbonization process applied to the raw apricot seed shell and after the carbonization process can be seen in the SEM images.

The SEM images of raw apricot kernel shell (N-Raw), samples subjected to hydrothermal reactions at 240°C for 24 hours, 36 hours, and 48 hours (N-H1, N-H2, and N-H3), and activated carbons named N-A1, N-A2, and N-A3 after carbonization are presented in Figure 2.

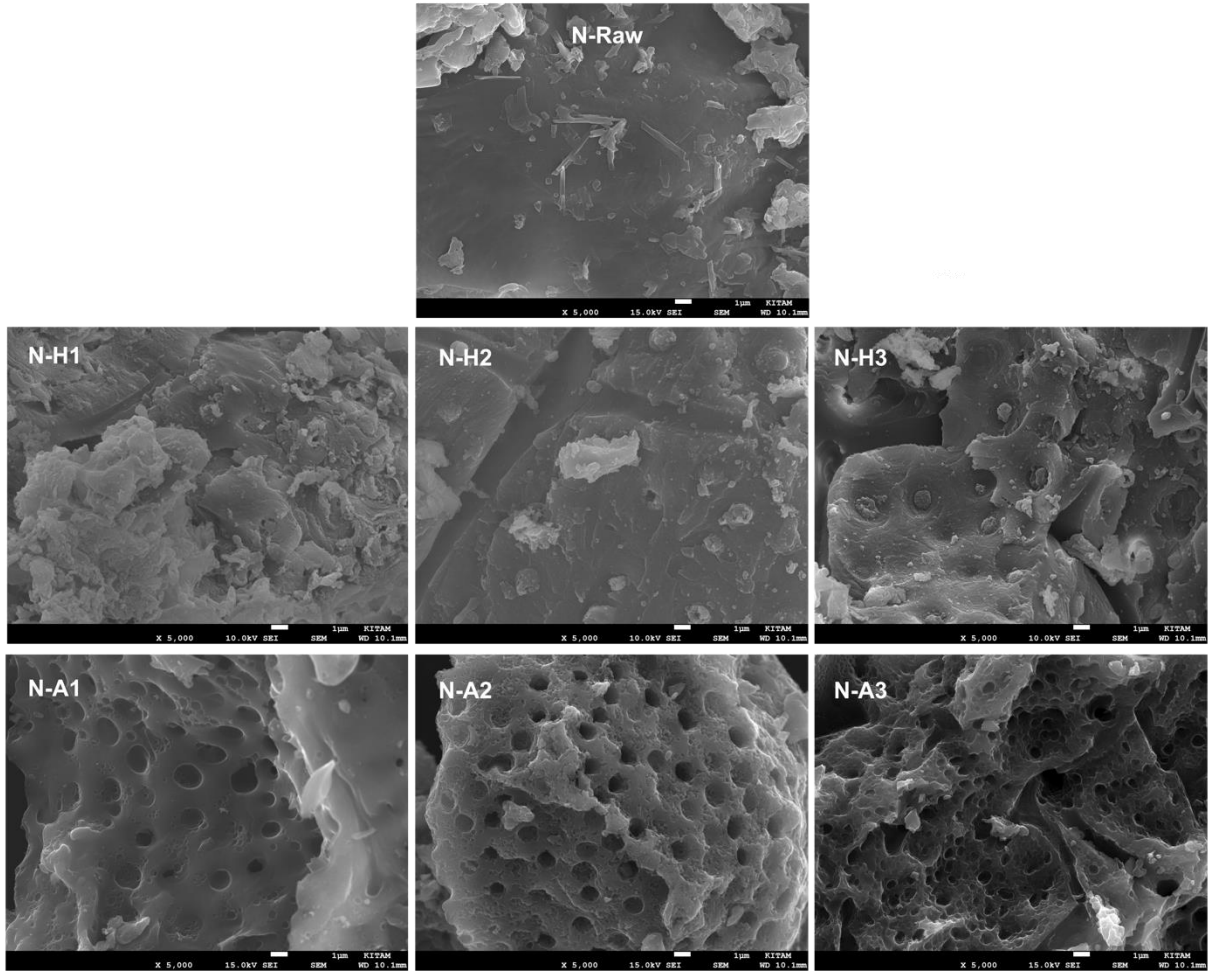


Figure 2. SEM images (5000x) of N-Raw, N-H1, N-H2, N-H3, N-A1, N-A2 and N-A3 samples

Upon examination of the SEM images of the N-Raw sample and the samples obtained after hydrothermal reaction, it is observed that N-H1 and N-H2 samples do not exhibit a porous structure, and the surface is smooth. However, a porous structure is observed in the N-H3 sample. When SEM images of activated carbons subjected to carbonization (N-A1, N-A2, and N-A3) are examined, porous structures are observed. In all samples, the pore structures are irregular and form a block-like void structure. The surfaces are uneven with protrusions and recesses. SEM images indicate that the chemical activation process applied after the hydrothermal reaction is effective in pore formation. KOH, as an activation agent, facilitated the faster degradation of the raw material structure during the carbonization process. During carbonization, the product's structure was significantly degraded through thermal decomposition, and many functional groups were removed from the structure.

As volatile substances were largely removed, a porous structure was obtained. Consistent with the literature findings, SEM images suggest that the activation method applied with KOH is effective in pore formation [16]. In another study in the literature, AKS, after chemical activation, exhibited pores mostly in the interparticle areas, and the surface was disrupted with strong $ZnCl_2$ activation, resulting in the formation of pores and cell configuration [17]. From the SEM images, it is evident that the hydrothermal carbonization method significantly affected the surface of the N-Raw sample. The obtained activated carbons clearly show pores formed on the surface in SEM images. The breaking of bonds in the raw material's structure and the separation of volatile compounds from the structure due to the influence of temperature and pressure result in the formation of pores, cracks, and cavities on the surface. The decomposition of hemicellulose, which is more easily broken down compared to cellulose, and the formation of a rough and even porous surface may

lead to increased surface roughness depending on the reaction temperature in reactions taking place in aqueous environments [18].

Conducting the EDS analyses, EDS maps of the N-H3 sample subjected to 240 °C for 48 hours of hydrothermal reaction to observe the effect of reaction time on the structure and the N-A3 sample subjected to activation with KOH are presented in Figures 3 and 4, respectively.

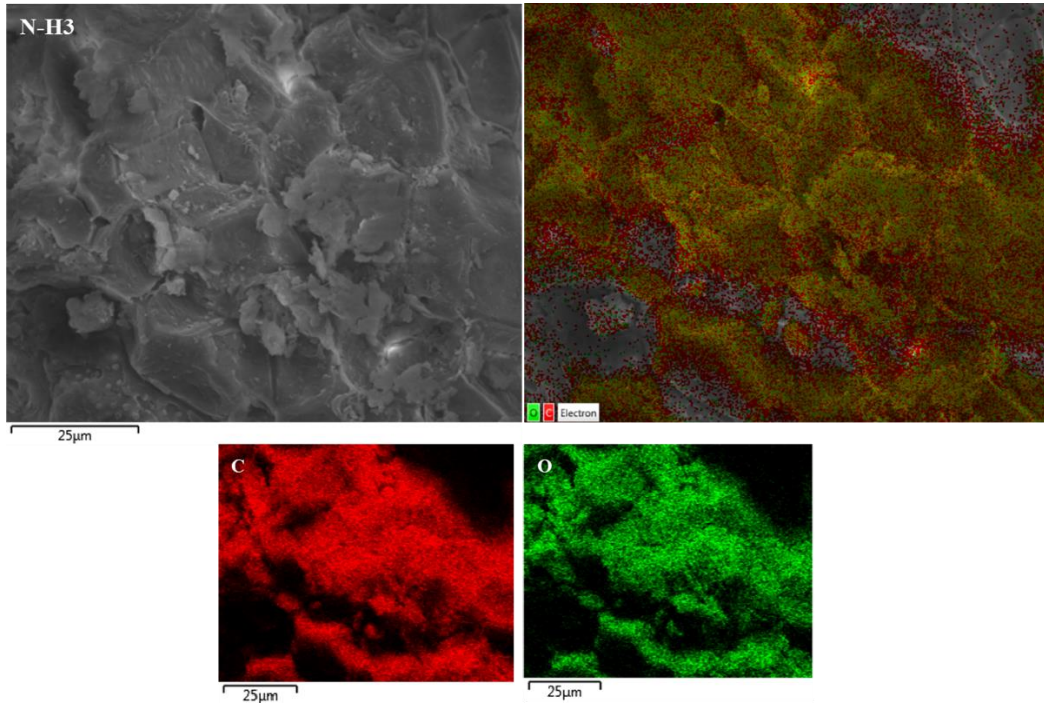


Figure 3. Elemental map of the N-H3 sample

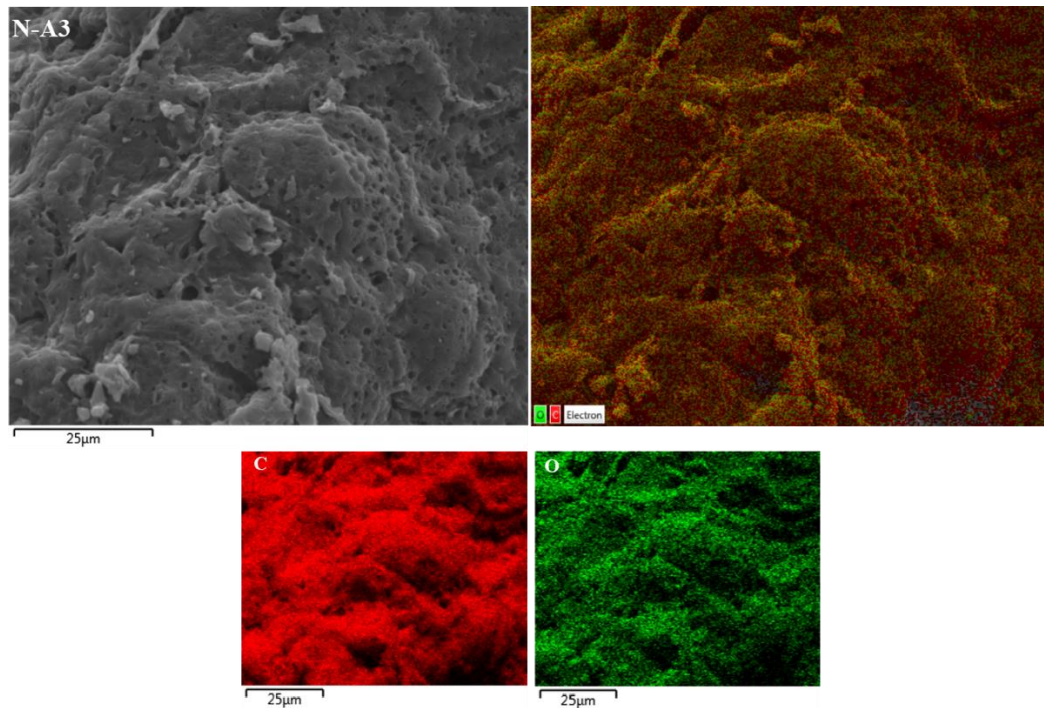


Figure 4. Elemental map of the N-A3 sample

Elemental analysis results for all samples are provided in Table 3. It is observed that as the hydrothermal reaction time increases, the carbon content increases and the oxygen content decreases in all samples obtained as a result of the hydrothermal reaction and carbonization process. During hydrothermal carbonization, organic materials transform into carbon, a process known as carbonization. This carbonization process can lead to an increase in carbon ratios as organic components turn into carbon. The increase in carbon content after the activation process is a result of the conversion of organic compounds into carbon. Under high temperature and pressure, hydrothermal conditions cause oxygen to react with water. In this case, oxygen molecules can combine with water to form volatile gases or other forms that can exit the system. This can result in a decrease in oxygen ratios. Additionally, chemical transformations of organic materials during hydrothermal carbonization can break the bonds between oxygen and organic components, leading to a decrease in oxygen ratios in these chemical transformations. Hydrothermal carbonization processes carried out at different durations can yield different results depending on the process duration. Longer processes result in increased carbonization and the removal of oxygen from the system.

Table 3. The weight-based elemental ratios of the samples

Sample	Weight Ratios of Elements (%)					
	C	O	Mg	K	Ca	S
N-Raw	59.83	36.66	0.18	1.55	0.69	1.09
N-H1	68.98	31.02	-	-	-	-
N-H2	69.13	30.87	-	-	-	-
N-H3	69.31	30.69	-	-	-	-
N-A1	83.44	16.01	0.31	-	0.24	-
N-A2	84.02	15.63	0.10	-	-	-
N-A3	88.14	11.86	-	-	-	-

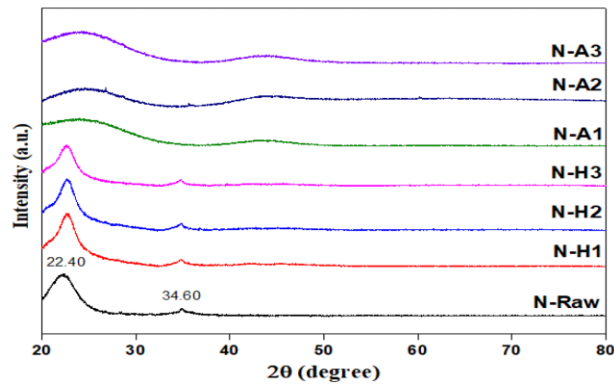


Figure 5. The XRD spectra of the samples

X-ray diffraction analyses were conducted to determine the changes in the crystal structure of AKS, hydrochars, and activated carbons. In Figure 5, X-ray diffraction patterns for these samples are presented. In the raw AKS biomass, two peaks are observed at $2\theta=22.40^\circ$ and $2\theta=34.60^\circ$. The XRD peak at $2\theta=22.40^\circ$ is characteristic of amorphous carbon, while the second, smaller peak around $2\theta=34.60^\circ$ can be attributed to the typical cellulose I structure, specifically to the (004) lattice plane. The presence of free hydroxyl groups, allowing for a regular crystal arrangement in cellulose, leads to intra- and intermolecular hydrogen bonding [19]. The structure of hydrochars obtained through hydrothermal reaction was found to be similar to the AKS sample, with the only difference being a slight broadening of the sharp peak. This broadening observed in the peaks after hydrothermal reaction at different durations indicates the initiation of structural degradation. Despite the carbon-based nature of our raw material, these broadened peaks suggest the onset of amorphous carbon formation. However, it is noted that the conditions of 240°C temperature and reaction durations of 24, 36, and 48 hours are insufficient for the complete elimination of cellulose's crystal structure. In samples activated with KOH at 700°C under an N_2 gas atmosphere, the peaks related to cellulose gradually broaden, indicating the formation of an amorphous structure. It is observed that the hydrothermal carbonization process induces chemical changes in the AKS powder, leading to the formation of an entirely different product.

The comparative FTIR spectra of raw AKS, hydrochars, and activated carbons are shown in Figure 6. The spectrum of the raw apricot kernel shell exhibits a broad band at 3722 cm^{-1} , attributed to the absorption of hydroxyl groups in polysaccharides [20], [21]. This result indicates that polysaccharides, including cellulose, hemicellulose, and lignin, are the main components of the apricot kernel shell. The bands at $3000\text{--}3600\text{ cm}^{-1}$ in raw AKS and hydrochar samples correspond to the O-H stretching vibrations of hydroxyl or carboxyl groups [22].

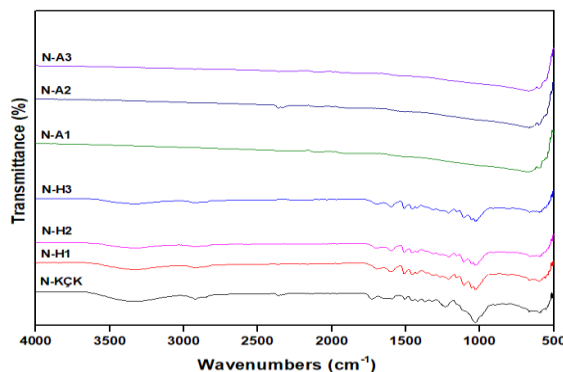


Figure 6. FTIR spectra of the samples

The two bands at 2923 and 2851 cm^{-1} in the raw AKS and hydrochar samples correspond to the asymmetric and symmetric stretching vibrations of methyl and methylene groups in cellulose, hemicellulose, and lignin [23]. The peak at 1734 cm^{-1} is attributed to the $\text{C}=\text{O}$ stretching vibration of ester groups in hemicellulose and lignin [24]. The peak at 1026 cm^{-1} in the spectrum of raw AKS and hydrochar samples is related to the β -glycosidic bond in cellulose and hemicellulose [25, 26]. The strong $\text{C}-\text{O}$ band at around 1100 cm^{-1} indicates the $\text{C}-\text{H}$ aromatic plane bending from the $-\text{OCH}_3$ in the lignin structure, while the bending of the aromatic plane at approximately 833 cm^{-1} is observed. In hydrochar samples, a weak peak at 3455 cm^{-1} indicates $-\text{OH}$ groups, possibly a result of phenolic-hydroxyl cleavage [19, 27]. After activation with KOH , some vibrations disappear, and some peaks shift. In the N-A2 sample, a $\text{C}=\text{C}$ stretching vibration of alkyne groups is observed at 2300 cm^{-1} , which is not present in other activated samples [28]. The peak at 1230 cm^{-1} , indicating the G (guaiacyl) unit in lignin, disappears after activation, suggesting the degradation of the lignin structure. The ester carbonyl groups at 1734 cm^{-1} in the spectrum of the raw sample are completely lost in the activated carbon samples due to decomposition at high operating temperatures [29]. The aromatic skeleton vibrations at 1585 and 1505 cm^{-1} observed in the spectrum of the raw sample, attributed to lignin, are completely absent in the activated carbon samples due to the transformation of phenyl chains [30, 31]. Additionally, the peak around 1026 cm^{-1} is almost absent in activated carbon samples, indicating the decomposition of hemicellulose and cellulose. The absence of a band at 1102 cm^{-1} in activated carbon samples also suggests the loss of $-\text{OCH}_3$ due to deoxygenation reactions [32, 33].

4. Conclusion

This study provides a detailed characterization of hydrochars and activated carbons produced through hydrothermal carbonization and chemical activation methods using AKS. Initially, AKS were ground and subjected to hydrothermal carbonization at 240°C for 24, 36, and 48 hours, resulting in three different hydrochars. Subsequently, these hydrochars were chemically activated with KOH , mixed for 3 hours, and carbonized at 700°C for 1 hour to obtain activated carbons. Various characterization methods, including BET surface area, SEM analysis, XRD analysis, and FTIR measurements, were employed to determine the properties of the activated carbons. The results indicated that the hydrothermal reaction duration increased carbon content and led to the formation of porous structures. Chemical activation with KOH further enhanced the surface area, particularly evident in SEM images. The study highlighted the effectiveness of the activation process in pore formation, as indicated by irregular pore structures observed in all activated carbon samples. SEM analysis was instrumental in evaluating the surface morphologies of raw AKS powder (N-Raw), hydrochars obtained through hydrothermal carbonization (N-H1, N-H2, and N-H3), and activated carbons (N-A1, N-A2, and N-A3). The images revealed a lack of porous structure in N-H1 and N-H2 samples, while a porous structure was observed in N-H3. Activated carbons displayed consistent irregular pore structures

with protrusions and recesses, emphasizing the effectiveness of the KOH activation process in pore formation. Elemental analysis results showed an increase in carbon content and a decrease in oxygen content with extended hydrothermal reaction time, indicating the transformation of organic materials into carbon. X-ray diffraction analyses revealed changes in the crystal structure, with hydrochars exhibiting amorphous carbon formation. Comparative FTIR spectra of raw AKS, hydrochars, and activated carbons demonstrated shifts and disappearances of peaks, reflecting chemical transformations during the hydrothermal carbonization and activation processes. The study concluded that hydrothermal carbonization and chemical activation significantly influenced the physical, surface, and chemical properties of hydrochars and activated carbons obtained from apricot kernel shells, showcasing their potential for diverse applications.

5. Acknowledgement

We gratefully acknowledge the support of The Scientific and Technological Research Council of Türkiye (TÜBİTAK), which has generously funded our research under Project Number 122M793. Also, some analyzes of the study have been conducted with the support of Fırat University Scientific Research Projects Coordination Unit (FÜBAP) under the Project Number ADEP 23.19.

6. Author Credit Statement

All authors contributed equally to this work in the conception of the idea, the design of the study, and conducting the literature review along with the acquisition of data, performing the analysis, and critically revising the manuscript for important intellectual content. Both authors collaborated closely in sourcing materials and resources needed for the study. Each author contributed significantly to the writing and editing of the manuscript, ensuring that the final version submitted for publication met all necessary criteria for accuracy and integrity.

7. Ethics Committee Approval and Conflict of Interest

“There is no conflict of interest with any person/institution in the prepared article”

8. References

- [1] G. Hekimoğlu, A. Sarı, Y. Önal, O. Gencel, V. V. Tyagi, and E. Aslan, “Utilization of waste apricot kernel shell derived-activated carbon as carrier framework for effective shape-stabilization and thermal conductivity enhancement of organic phase change materials used for thermal energy storage,” *Powder Technol.*, vol. 401, p. 117291, Mar. 2022.
- [2] T. Ekonomi and P. Geliştirme Enstitüsü, “Hazırlayan Mine Hasdemir.”
- [3] E. Haberleri, “Kabuk diye sakın çöpe atmayın! Bu ilimize yıllık 12 milyon kazandırıyor - Ekonomi Haberleri.” Accessed: Nov. 09, 2023. [Online]. Available: <https://www.sabah.com.tr/ekonomi/2019/01/01/kabuk-diye-sakin-cope-atmayin-bu-ilimize-yillik-12-milyon-kazandiriyor>
- [4] M. Ahtik, “Antep Fıstığı Kabuğundan Hidrotermal Karbon Üretimi ve Karakterizasyonu,” *Karabük Üniv.*, 2022, (In Turkish).
- [5] L. Wang et al., “H₃PO₄-assisted synthesis of apricot shell lignin-based activated carbon for capacitors: Understanding the pore structure/electrochemical performance relationship,” *Ener. and Fuels*, vol. 35, no. 9, pp. 8303–8312, May 2021.
- [6] L. Wang, L. Xie, H. Wang, H. Ma, and J. Zhou, “Sustainable synthesis of apricot shell-derived hierarchical porous carbon for supercapacitors: A novel mild one-step synthesis process,” *Coll. and Surf. A: Physic.and Eng. Aspects*, 637, 128257, 2022.
- [7] T. S. Temirgaliyeva et al., “Self-supporting hybrid supercapacitor electrodes based on carbon nanotube and activated carbons,” *Eur. Chem. Techn. Jour.*, vol. 20, no. 3, pp. 169–175, 2018.
- [8] H. Eom, J. Kim, I. Nam, and S. Bae, “Recycling black tea waste biomass as activated porous carbon for long life cycle supercapacitor electrodes,” *Mater.*, vol. 14, no. 21, 2021.
- [9] E. Canbaz, “Fındık Kabuklarından Hidrotermal Karbonizasyon Yöntemi ile Karbon Malzemelerinin Eldesi Ve Sodyum-Iyon Bataryalar İçin Kullanım Potansiyelinin İncelenmesi,” *Gebze Teknik Üni.*, 2020, (In Turkish).
- [10] A. B. Fuertes et al., “Chemical and structural properties of carbonaceous products obtained by pyrolysis and hydrothermal carbonisation of corn stover,” *Soil Res.*, vol. 48, no. 7, pp. 618–626, Sep. 2010.

- [11] K. Aydınçak, "Hidrotermal karbonizasyon yöntemiyle gerçek ve model biyokütllerden karbon nanoküre sentezi ve karakterizasyonu," Ankara Üniversitesi, 2012, (In Turkish).
- [12] S. Román, J. M. Valente Nabais, B. Ledesma, J. F. González, C. Laginhas, and M. M. Titirici, "Production of low-cost adsorbents with tunable surface chemistry by conjunction of hydrothermal carbonization and activation processes," *Microp. and Mesop. Mater.*, vol. 165, pp. 127–133, Jan. 2013.
- [13] K. Q. Tran, A. J. Klemsdal, W. Zhang, J. Sandquist, L. Wang, and Ø. Skreiberg, "Fast Hydrothermal Liquefaction of Native and Torrefied Wood," *Ener. Proc.*, vol. 105, pp. 218–223, May 2017.
- [14] B. K. Kızılduman, "Pirinç Kabuğundan Hidrotermal Karbonizasyon Yöntemi ile Karbon Küre Üretilmesi ve Enerji ve İlaç Salimi Alanında Kullanılabilirliğinin Araştırılması," Balıkesir Üniversitesi, 2020, (In Turkish).
- [15] E. Unur, S. Brutti, S. Panero, and B. Scrosati, "Nanoporous carbons from hydrothermally treated biomass as anode materials for lithium ion batteries," *Microp. and Mesop. Mater.*, vol. 174, pp. 25–33, Jul. 2013.
- [16] M. Süner, "Hidrotermal Karbonizasyon Yöntemi ile Çay Tesis Atıkları ve Badem Kabuklarından Aktif Karbon Üretimi," *Fırat Üniversitesi*, 2022, (In Turkish).
- [17] M. I. Satayev, R. S. Alibekov, L. M. Satayeva, O. P. Baiysbay, and B. Z. Mutaliyeva, "Characteristics of activated carbons prepared from apricot kernel shells by mechanical, chemical and thermal activations," *Mod Appl Sci*, vol. 9, no. 6, pp. 104–119, 2015.
- [18] T. Wang, Y. Zhai, Y. Zhu, C. Li, and G. Zeng, "A review of the hydrothermal carbonization of biomass waste for hydrochar formation: Process conditions, fundamentals, and physicochemical properties," *Renew. and Sustain. Ener. Rev.*, vol. 90, pp. 223–247, Jul. 2018.
- [19] B. Janković et al., "Physico-chemical characterization of carbonized apricot kernel shell as precursor for activated carbon preparation in clean technology utilization," *J Clean Prod*, vol. 236, p. 117614, Nov. 2019.
- [20] K. Aljoumaa, H. Tabeikh, and M. Abboudi, "Characterization of apricot kernel shells (*Prunus armeniaca*) by FTIR spectroscopy, DSC and TGA," *Jour. of the Indian Acad. of Wood Sci.*, vol. 14, no. 2, pp. 127–132, Dec. 2017.
- [21] J. Krumins, M. Klavins, and V. Seglins, "Comparative Study of Peat Composition by using FT-IR Spectroscopy," *Mater. Sci. and Appl. Chem.*, vol. 26, p. 106, 2012.
- [22] Y. Lin, X. Ma, X. Peng, and Z. Yu, "A mechanism study on hydrothermal carbonization of waste textile," *Ener. and Fuels*, vol. 30, no. 9, pp. 7746–7754, Sep. 2016.
- [23] B. K. Via, O. Fasina, and H. Pan, "Assessment of pine biomass density through mid-infrared spectroscopy and multivariate modeling," *Biores.*, vol. 6, no. 1, pp. 807–822, Apr. 2013.
- [24] J. Jayaramudu, S. C. Agwuncha, S. S. Ray, E. R. Sadiku, and A. Varada Rajulu, "Studies on the chemical resistance and mechanical properties of natural polyalthia cerasoides woven fabric/glass hybridized epoxy composites," *Adv Mater Lett*, vol. 6, no. 2, pp. 114–119, Feb. 2015.
- [25] S. Fong Sim, M. Mohamed, N. Aida Lu Mohd Irwan Lu, N. P. Safitri Sarman, and S. Nor Sihariddh Samsudin, "Computer-assisted analysis of Fourier Transform Infrared (FTIR) spectra for characterization of various treated and untreated agriculture biomass," *Bioresour.*, vol. 7, no. 4, pp. 5367–5380, 2012.
- [26] N. A. Nikonenko, D. K. Buslov, N. I. Sushko, R. G. Zhibankov, and B. I. Stepanov, "Investigation of stretching vibrations of glycosidic linkages in disaccharides and polysaccharides with use of IR spectra deconvolution," *Wiley Online LibraryNA Original Res. on Biomol.*, pp. 257–262, 2000.
- [27] J. Cao, G. Xiao, X. Xu, D. Shen, and B. Jin, "Study on carbonization of lignin by TG-FTIR and high-temperature carbonization reactor," *Fuel Proce. Techn.* vol. 106, pp. 41–47, Feb. 2013.
- [28] M. A. Islam, M. J. Ahmed, W. A. Khanday, M. Asif, and B. H. Hameed, "Mesoporous activated coconut shell-derived hydrochar prepared via hydrothermal carbonization-NaOH activation for methylene blue adsorption," *J Env. Manage*, vol. 203, pp. 237–244, Dec. 2017.
- [29] G. Sivasankarapillai and A. G. McDonald, "Synthesis and properties of lignin-highly branched poly (ester-amine) polymeric systems," *Bio. Bioen.*, vol. 35, no. 2, pp. 919–931, Feb. 2011.
- [30] B. E. Obinaju and F. L. Martin, "ATR-FTIR spectroscopy reveals polycyclic aromatic hydrocarbon contamination despite relatively pristine site characteristics: Results of a field study in the Niger Delta," *Environ Int*, vol. 89–90, pp. 93–101, Apr. 2016.
- [31] X. Zhao et al., "Efficient solid-phase synthesis of acetylated lignin and a comparison of the properties of different modified lignins," *J Appl Polym Sci*, vol. 134, no. 1, p. 44276, Jan. 2017.
- [32] S. Başakçılardan Kabakçı and S. S. Baran, "Hydrothermal carbonization of various lignocellulosics: Fuel characteristics of hydrochars and surface characteristics of activated hydrochars," *Waste Manag.*, vol. 100, pp. 259–268, Dec. 2019.
- [33] Z. Liu, A. Quek, S. Kent Hoekman, and R. Balasubramanian, "Production of solid biochar fuel from waste biomass by hydrothermal carbonization," *Fuel*, vol. 103, pp. 943–949, Jan. 2013.



Hareketli Kayma Yüzeyle DC Motor Modelli Klasik Kayan Kipli Kontrolün Dönel Ters Sarkaç Sistemine Uygulanması

Muhammet AYDIN^{1*} , Oğuz YAKUT² 

^{1, 2}Mechatronics Engineering, Faculty of Engineering, Fırat University, Elazığ, Türkiye.
¹muhammeta@firat.edu.tr, ²oyakut@firat.edu.tr

Geliş Tarihi: 01.03.2024
Kabul Tarihi: 11.07. 2024

Düzeltilme Tarihi: 22.05.2024

doi: 10.62520/fujece.1445734
Araştırma Makalesi

Alıntı: M. Aydın ve O. Yakut, "Hareketli kayma yüzeyle dc motor modelli klasik kayan kipli kontrolün dönel ters sarkaç sistemine uygulanması", Fırat Üni. Deny. ve Hes. Müh. Derg., vol. 3, no 3, pp. 337-349, Ekim 2024.

Öz

Bu çalışmada kontrol uygulamalarında çok tercih edilen dönel ters sarkaç sistemi (DTS) ele alınmıştır. DTS elemanlarının ağırlıklı merkezi koordinatları bulunarak sistemin toplam kinetik ve potansiyel enerjileri elde edilmiştir. Kinetik ve potansiyel enerji ifadeleri kullanılarak Lagrange fonksiyonu oluşturulmuştur. Lagrange yöntemi dikkate alınarak sistemin hareket denklemlerini veren ifadeler bulunmuştur. Ayrıca sistemi harekete geçirecek olan motorun denklemleri dikkate alınmıştır. Durum değişkenleri kullanılarak Matlab da yazılan program yardımıyla sistemin sarkaç açısı, kayma yüzeyi hareketli klasik kayan kipli kontrol yöntemiyle kontrol edilmiştir. Kayma yüzeyinin eğimi sistemin dinamiklerine bağlı olarak hesaplatılmıştır. Kontrol yapısında kullanılan katsayıların optimum değerleri genetik algoritma yardımıyla bulunmuştur. Sonuçlardan sarkaç açısının istenilen referans değere yaklaşık 1.5 sn civarında ulaştığı ve hatanın yaklaşık sıfır olduğu görülmüştür. Ayrıca motor tork değerinin 12 Nm seviyelerinde ve motor akım değerinin 2.5 amper seviyelerinde olduğu gözlemlenmiştir. Motor değerlerinin pratik uygulamalardaki değerlere yakın makul seviyelerde olduğu sonuçlardan elde edilmiştir. Elde edilen bu değerlere göre motor seçimi yapıldığında gerçek zamanlı uygulamalarda kontrol için sorun yaşanmayacaktır.

Anahtar kelimeler: Dönel ters sarkaç, Hareketli kayan kipli kontrol, Kayma yüzeyi, Motor model

*Yazışılan yazar



An Application of DC Motor Modelled Classical Sliding Mode Control with Moving Sliding Surface to Rotary Inverted Pendulum System

Muhammet AYDIN^{1*} , Oğuz YAKUT² 

^{1,2}Mechatronics Engineering, Faculty of Engineering, Firat University, Elazığ, Türkiye.

¹muhammeta@firat.edu.tr, ²oyakut@firat.edu.tr

Received: 01.03.2024
Accepted: 11.07. 2024

Revision: 22.05.2024

doi: 10.62520/fujece.1445734
Research Article

Citation: M. Aydın ve O. Yakut, "A comparative study of segmentation algorithms for intracerebral hemorrhage detection", Firat Univ. Jour.of Exper. and Comp. Eng., vol. 3, no 2, pp. 337-349, October 2024.

Abstract

The rotary inverted pendulum system (RIP), which is highly favored in control applications, is examined in this work. By determining the coordinates of the Rip elements' centers of gravity, the system's total kinetic and potential energies were determined. The kinetic and potential energy expressions were used to generate the Lagrangian function. Expressions providing the system's equations of motion were discovered by taking the Lagrangian approach into consideration. The motor's equations, which will initiate the system, have also been considered. Through the use of state variables and a Matlab program, the system's pendulum angle was managed by using a moving sliding surface and the traditional sliding mode control technique. Based on the dynamics, the slip surface's slope was computed. The sliding surface's slope was computed based on the system's dynamics. The genetic algorithm was utilized to determine the ideal values for the coefficients employed in the control structure. The findings showed that the inaccuracy was roughly zero and that the pendulum angle took around 1.5 seconds to reach the intended reference value. Furthermore, it noted that the motor torque and current values are 12 Nm and 2.5 amps, respectively. The findings show that the motor values are reasonably similar to the values seen in real-world applications. Control in real-time applications won't be an issue if the motor is chosen based on these values.

Keywords: Rotary inverted pendulum, Moving sliding mode control, Sliding surface, Motor model

*Corresponding author

1. Introduction

One of the most popular approaches for applying control techniques is the inverted pendulum system because of their challenging controllability. Among the inverted pendulum systems created to date are single rod trolley and rotary inverted pendulum systems, double rod trolley and rotary inverted pendulum systems [1-4].

The rotary inverted pendulum (rip) system is among the inverted pendulum systems that are used most frequently. A valuable test system for investigating the control of nonlinear unstable systems is the inverted pendulum system driven indirectly, often referred to as the "rip system." In recent years, the rip has become standard for applications in control due to its lower cost and easier construction than the trolley inverted pendulum system. The pendulum of the rip system rotates vertically, while the rotary arm moves horizontally. The rotating arm is propelled by the DC motor. It is tried to stabilize the rotary arm-mounted pendulum at the higher equilibrium point, or the point of instability, subsequent to the rotary arm's movement by the DC motor [5, 6].

There are studies published in the literature so far on the angle control of the rotary inverted pendulum system shown in Figure 1. The prominent ones among these are the studies using classical control methods such as PID, PI, PD, sliding mode controlled adaptive control methods, fuzzy control method, sliding mode control method, particle swarm optimization based PID control and artificial neural network sliding mode control methods [7-22].

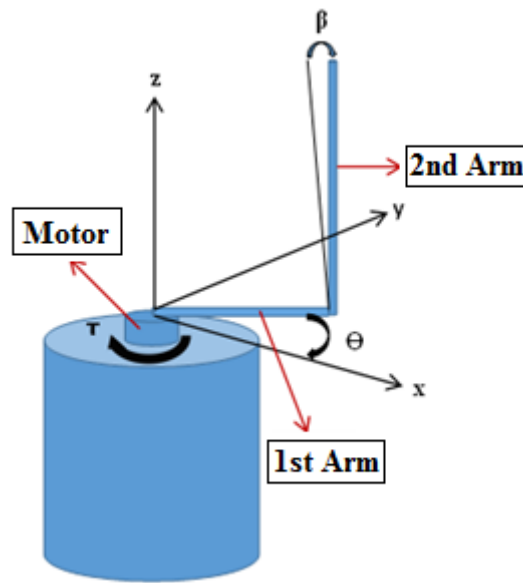


Figure 1. Rotational inverted pendulum system

In this paper, a nonlinear mathematical system of the rip is obtained and the sliding mode control method with moving sliding surface is used to control the pendulum. The dynamics of the system are employed to derive the slope of the sliding surface. The optimization method using genetic algorithms is then applied to calculate the required coefficients for the control system.

2. Modelling of Rotational Inverted Pendulum System

A single motor powers the two-degree-of-freedom system shown in Figure 1. The system's changeable parameters are Θ and β . Figure 1 displays the system's coordinate axis layout. If this coordinate axis set is used to determine the system's total kinetic energy;

$$T = \frac{1}{2}m_1(\dot{x}_1^2 + \dot{y}_1^2) + \frac{1}{2}I_1\dot{\theta}^2 + \frac{1}{2}m_2(\dot{x}_2^2 + \dot{y}_2^2 + \dot{z}_2^2) + \frac{1}{2}I_2\dot{\beta}^2 \quad (1)$$

In the equations x_1 , y_1 are the centre of gravity coordinates of the first arm. x_2 , y_2 and z_2 represent the the second arm's coordinates for center of gravity. m_1 and m_2 are the masses of each arm. I_1 and I_2 are the mass moments of inertia of the arms. L_1 and L_2 , respectively, are the limb dimensions of arms. The coefficients of friction at the joint joints are b_1 and b_2 . τ is the control torque applied by the motor.

Equations (1) yields the following equations for the unknown expressions.

$$x_1 = L_1 \cos\theta \quad (2)$$

$$y_1 = L_1 \sin\theta \quad (3)$$

$$x_2 = x_1 - L_2 \sin\beta \sin\theta \quad (4)$$

$$y_2 = y_1 + L_2 \sin\beta \cos\theta \quad (5)$$

$$z_2 = L_2 \cos\beta \quad (6)$$

If the aforementioned equations are changed to determine the system's total kinetic energy;

$$T = \frac{1}{2}m_1L_1^2\dot{\theta}^2 + \frac{1}{2}I_1\dot{\theta}^2 + \frac{1}{2}m_2(L_1\dot{\theta}^2 + 2L_1L_2\cos\beta\dot{\theta}\dot{\beta} + L_2^2\dot{\beta}^2 + L_2^2\sin^2\beta\dot{\theta}^2) + \frac{1}{2}I_2\dot{\beta}^2 \quad (7)$$

Potential energy of the system:

$$V = m_2gz_2 \quad (8)$$

$$V = m_2gL_2\cos\beta \quad (9)$$

This gives rise to the following construction of the Lagrange function.

$$L = T - V \quad (10)$$

$$L = \frac{1}{2}(m_1L_1^2 + I_1)\dot{\theta}^2 + \frac{1}{2}m_2[(L_1 + L_2^2\sin^2\beta)\dot{\theta}^2 + 2L_1L_2\cos\beta\dot{\theta}\dot{\beta} + L_2^2\dot{\beta}^2] + \frac{1}{2}I_2\dot{\beta}^2 - m_2gL_2\cos\beta \quad (11)$$

Equation of motion for θ :

$$\frac{d}{dt}\left(\frac{\partial L}{\partial \dot{\theta}}\right) - \frac{\partial L}{\partial \theta} = Q_\theta \quad (12)$$

The equation of motion for θ can be found by substituting and calculating the expressions in the equation.

$$(m_1L_1^2 + I_1 + m_2L_1 + m_2L_2^2\sin^2\beta)\ddot{\theta} + m_2L_1L_2\cos\beta\ddot{\beta} - m_2L_1L_2\sin\beta\dot{\beta}^2 + 2m_2L_2^2\sin\beta\cos\beta\dot{\beta}\dot{\theta} = \tau - b_1\dot{\theta} \quad (13)$$

Equation of motion for β :

$$\frac{d}{dt}\left(\frac{\partial L}{\partial \dot{\beta}}\right) - \frac{\partial L}{\partial \beta} = Q_\beta \quad (14)$$

Here is the equation of motion for β after performing the appropriate operations in the preceding equation.

$$m_2L_1L_2\cos\beta\ddot{\theta} + (m_2L_2^2 + I_2)\ddot{\beta} - m_2L_2^2\sin\beta\cos\beta\dot{\theta}^2 - m_2gL_2\sin\beta = -b_2\dot{\beta} \quad (15)$$

After extracting $\ddot{\beta}$ and $\ddot{\theta}$ expressions from the equations of motion, the following equations are produced.

$$\ddot{\theta} = \frac{(m_2 L_2^2 + I_2)(b_1 \dot{\theta} - \tau - m_2 L_1 L_2 \sin \beta \dot{\beta}^2 + 2 m_2 L_2^2 \sin \beta \cos \beta \dot{\beta} \dot{\theta})}{(m_2 L_1 L_2 \cos \beta)^2 - (m_2 L_2^2 + I_2)(m_1 L_1^2 + I_1 + m_2 L_1 + m_2 L_2^2 \sin^2 \beta)}$$

$$- \frac{m_2 L_1 L_2 \cos \beta (b_2 \dot{\beta} - m_2 L_2^2 \sin \beta \cos \beta \dot{\theta}^2 - m_2 g L_2 \sin \beta)}{(m_2 L_1 L_2 \cos \beta)^2 - (m_2 L_2^2 + I_2)(m_1 L_1^2 + I_1 + m_2 L_1 + m_2 L_2^2 \sin^2 \beta)} \quad (16)$$

$$\ddot{\beta} = \frac{(m_1 L_1^2 + I_1 + m_2 L_1 + m_2 L_2^2 \sin^2 \beta)(b_2 \dot{\beta} - m_2 L_2^2 \sin \beta \cos \beta \dot{\theta}^2 - m_2 g L_2 \sin \beta)}{(m_2 L_1 L_2 \cos \beta)^2 - (m_2 L_2^2 + I_2)(m_1 L_1^2 + I_1 + m_2 L_1 + m_2 L_2^2 \sin^2 \beta)}$$

$$- \frac{m_2 L_1 L_2 \cos \beta (b_1 \dot{\theta} - \tau - m_2 L_1 L_2 \sin \beta \dot{\beta}^2 + 2 m_2 L_2^2 \sin \beta \cos \beta \dot{\beta} \dot{\theta})}{(m_2 L_1 L_2 \cos \beta)^2 - (m_2 L_2^2 + I_2)(m_1 L_1^2 + I_1 + m_2 L_1 + m_2 L_2^2 \sin^2 \beta)} \quad (17)$$

The DC motor responsible for the first arm's rotational movement has the following equation of motion. Where L is the motor inductance coefficient, N is the gear ratio, I is the electrical current flowing through the motor windings, R is the motor winding ohmic resistance, and V_a is the motor supply voltage and control signal. The opposite electromotive voltage coefficient is denoted by K_b .

$$\frac{di}{dt} = \frac{V_a - Ri}{L} - \frac{K_b \dot{\theta}}{LN} \quad (18)$$

Should we change the equations' expressions into state variables;

$$\theta = x(1) \quad (19)$$

$$\dot{\theta} = x(2) \quad (20)$$

$$\beta = x(3) \quad (21)$$

$$\dot{\beta} = x(4) \quad (22)$$

$$i = x(5) \quad (23)$$

is acquired as. If the torque used for motor control is;

$$\tau = \frac{K_t i}{N} \quad (24)$$

is computed using the format. The motor torque coefficient in this case is K_t .

A Matlab programme is used to apply a approach to movable sliding mode control for the rip system by using these variables of state. It is guaranteed that β will reach the intended zero reference point when using moving sliding mode control approach. Table 1 provides the numerical values for the system parameters.

Table 1. Values for rip system parameters

Parameter	Value	Unit
m_1	0.15	kg
m_2	0.1	kg
L_1	0.4	m
L_2	0.4	m
b_1	0.01	Ns/m
b_2	0.01	Ns/m
I_1	0.0248	kgm ²
I_2	0.00386	kgm ²
L	0.1	Henry
R	1.4	Ohm
K_t	0.25	---
K_b	0.05	---
N	1/20	---

3. Classical Sliding Mode Control Design with Moving Sliding Surface

A reliable and nonlinear control technique is sliding mode control. Unlike other control systems, it is unaffected by outside disruptions. It can rapidly and accurately approach the desired reference because of the vibrations on the sliding surface [23]. When the system's boundary values are known, sliding mode control offers long-term controllability in situations when the system's parameters are dynamic or uncertain as well as when external disturbances affect the system.

Before implementing sliding mode control, it is imperative to determine the location of the sliding surface and establish a control rule that ensures reaching this identified surface. The reaching time denotes the duration required to reach the sliding surface, and the phase trajectory section during this process is referred to as the reaching mode. During the reaching mode, the plant is susceptible to external noise and uncertainties in parameters [24]. Upon achieving the sliding surface, the system transitions into the sliding mode. In this mode, the system's trajectory remains unaffected by external variables and unpredictable parameters. The application of sliding mode control unveils previously unrepresented high-frequency dynamics of the system, manifesting as crackling. This phenomenon arises from oscillations near the equilibrium point that the system is endeavoring to reach.

Control expression in sliding mode using sign function;

$$U = -k \operatorname{sign}(S) \quad (25)$$

is able to communicate as slip surface function (S) in this case is represented by equation (26) and is dependent on the error (e) and its time variation (de) with respect to the system's response.

$$S = C e + de \quad (26)$$

Figure 2 shows a sliding surface example for the sliding mode control. The sliding surface's precise slope is depicted in the illustration. In equation (26), the coefficient C provides this slope.

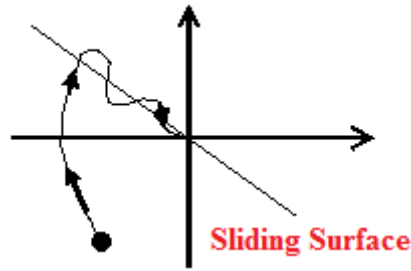


Figure 2. Sliding surface

The ideal slope value must be found in order to guarantee the controller's success. These sliding surface slope coefficients of the sliding mode controller are assumed to be shifting in this study. Expression (27) is used to get the slope coefficient C instantly. Here, the evolutionary algorithm was used to determine the constant coefficients C_1 and C_2 's optimal values. As a result, the slope of sliding surface coefficient for the sliding mode control was instantly determined.

$$C = C_1 - C_2 \frac{de}{e} \quad (27)$$

The main applications of genetic algorithms are in machine learning and problem optimization, among many other areas. The process of making something better than it was before is called optimization. In optimization, a set of inputs is given, and the outcome is determined by the inputs. In order for optimization to produce the "best" result, we must provide an insert. The precision of "best" depends on the different types of the problem [25]. The parameters preferred as FitnessLimit 1e-10, Generations 100, and PopulationSize 20 in the genetic algorithm structure. The block design for the genetic algorithm technique used to optimize the controller's coefficients is displayed in Figure 3.

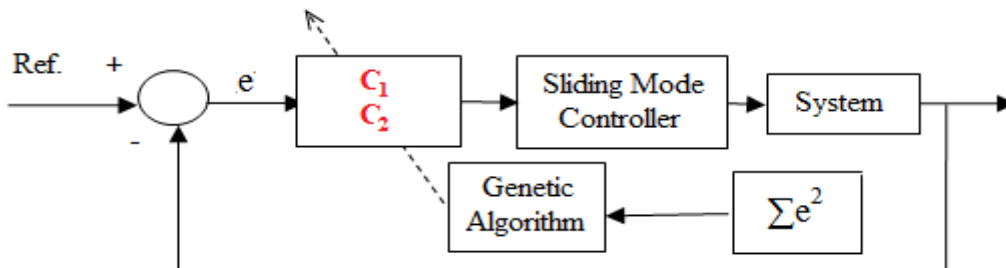


Figure 3. Controller block diagram

There is a shifting sliding surface in our control approach since the obtained coefficient C will change every time. Figure 4 displays the C coefficient's mobility.

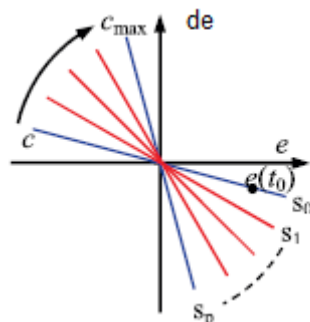


Figure 4. C coefficient variation

For the fitness function, the mean squared error criterion—which is also known as the system performance index—is favored in order to determine the ideal controller parameter values.

$$E(k) = \frac{1}{2}e^2(k) \quad (28)$$

The sliding mode control expression's signalling function results in a crackling control signal. Various functions are employed in place of the sign function in order to solve this issue. In this study, the sign function is replaced with the commonly utilized saturation function. As a result, it is computed to obtain the expression for the regulation of the sliding mode with saturation function. Here, genetic algorithm determines epsilon value to be 37.77.

$$U = -k \cdot \text{sat}\left(\frac{s}{\text{Epsilon}}\right) \quad (29)$$

4. Results and Discussion

The results obtained as a result of the study were examined respectively. Figure 5 illustrates the temporal evolution of the angular position of the first arm, connected to the motor, over time. The motion commences from the zero-point and undergoes a change in direction within the initial seconds. This observed change corresponds with the anticipated outcome when elevating the pendulum.

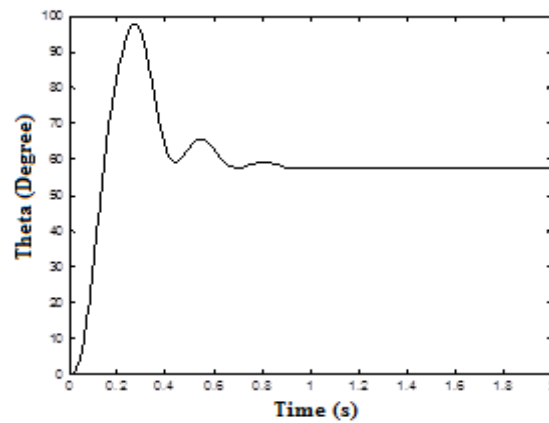


Figure 5. Theta angle variation in relation to time

The graphical representation of the angular velocity of the first arm is depicted in Figure 6 over time. The graph showcases oscillations in angular velocity, reaching a maximum of 11 rad/s before eventually stabilizing at 0 rad/s.

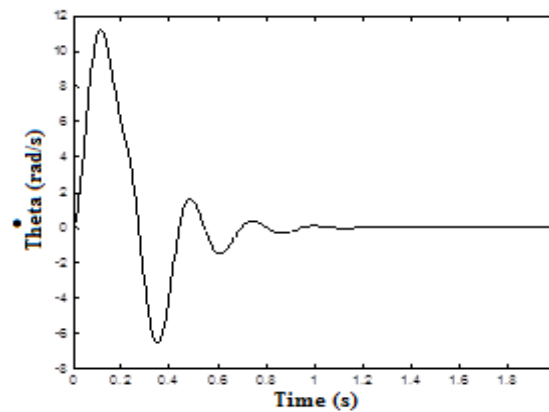


Figure 6. Change in the first arm's angular velocity to time

In Figure 7, the graph illustrates the variation in the pendulum angle over time. The unstable upper equilibrium point is where the pendulum is expected to cease movement. Therefore, the pendulum angle should approach the intended zero reference point. According to the visual data, it takes approximately 1.5 seconds for the pendulum to reach the target reference value.

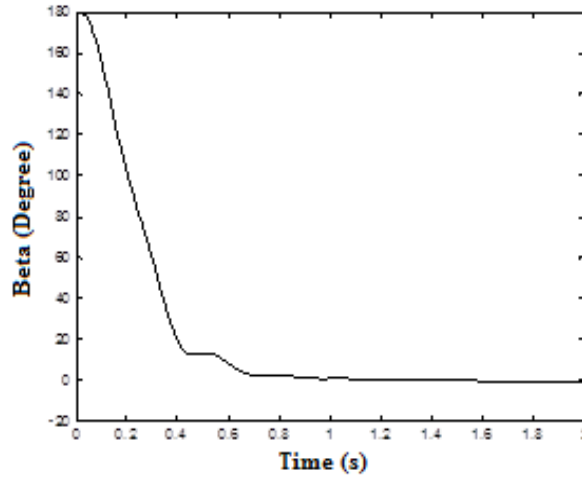


Figure 7. Beta angle (pendulum angle) variation to time

The pendulum's angular velocity fluctuates with regard to time, as seen in Figure 8. The graph indicates that, in 1.5 seconds, the pendulum's angular velocity goes to zero.

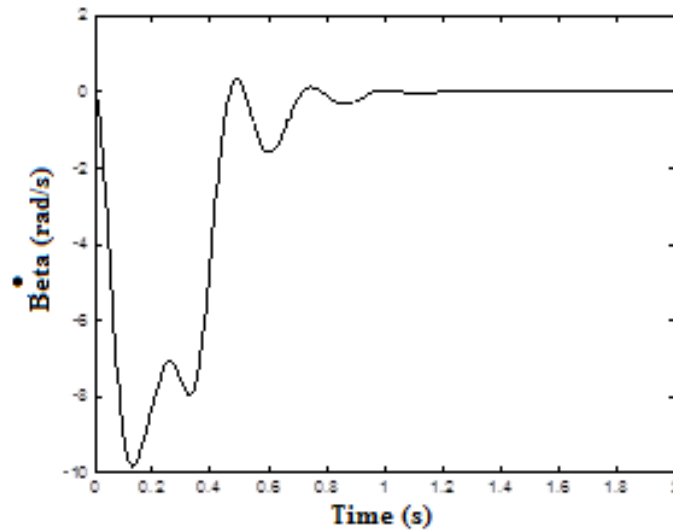


Figure 8. Beta angle (pendulum angle) variation to time

Figure 9 portrays the torque values that the DC motor should apply to the first arm and the slope values of the sliding surface, respectively. It is clear from examining the DC motor torque curve in Figure 9 shows that the pendulum may be raised to the required reference value with a motor torque of roughly 12 Nm. In light of realistic applications, it can be said that this torque value makes sense. Approximately 1.5 seconds pass before the motor torque drops to zero.

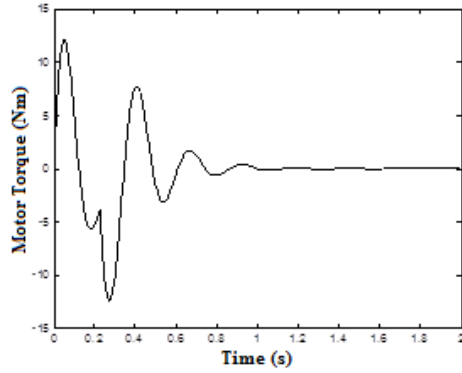


Figure 9. Changes in DC motor torque over time

Figure 10 shows the data from the slope graph of the sliding surface.

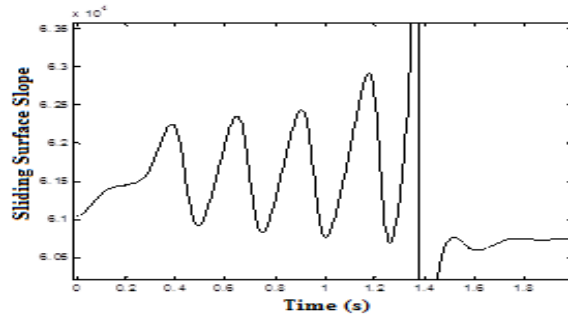


Figure 10. Sliding surface slope graph

The supply voltage variation over time that will be used as a control signal for the DC motor is depicted in Figure 11. The graph indicates that the maximum voltage source for the DC motor supply is 12 volts.

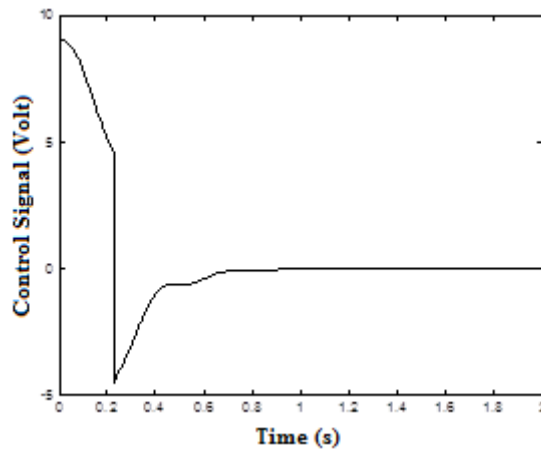


Figure 11. DC motor control signal change graph over time

Figure 12 illustrates the temporal variation of the current flowing through the DC motor windings. It is apparent that, after approximately 1.5 seconds, the motor ceases to draw any current. The graph clearly indicates that the motor is limited to drawing a maximum of 2.5 amps of electricity.

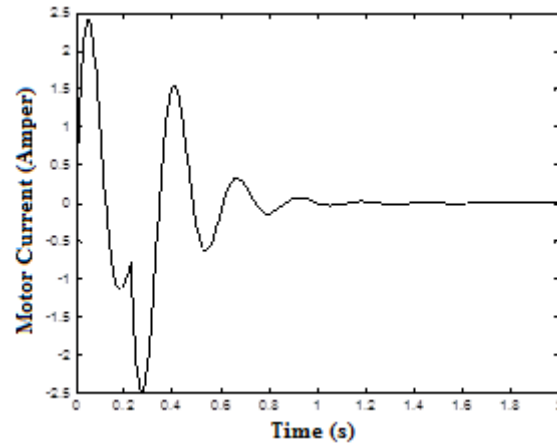


Figure 12. Graph of DC motor current change with time

In Table 2, the results of the study conducted in this research article and a publication in the literature are compared [26]. As can be seen in the table, the pendulum angle of the system achieved a better settling time of 0.9 s in the current study.

Table 2. Comparison of between the literature and the present work

	Method	Settling Time (s)
Rotary inverted pendulum arm angle	SMC	0.89
	MSMC (Present Work)	0.85
Pendulum angle	SMC	1.2
	MSMC (Present Work)	0.90

5. Conclusion

The initial phase of this study involves the application of the Lagrange technique to formulate the nonlinear model for a single-degree-of-freedom spinning inverted pendulum system. The control of the pendulum angle is conducted through Matlab software, utilizing state variables within the final model. This control is achieved by implementing the moving sliding mode technique. The dynamics of the system were computed, revealing variations in the slope of the sliding surface. To determine the coefficients in the structure of the sliding modal control, a genetic algorithm was employed. As a result, the identified error was rectified, leading to a control signal reduction to zero. According to the investigation, the pendulum took approximately 1.5 seconds to reach the specified reference value. Notably, the motor's characteristics, including a maximum torque of 12 Nm and a maximum power consumption of 2.5 amps, were documented. These findings underscore the successful application of moving sliding mode control to the system, provided that motor selection is performed by considering real-time motor values during the selection process.

In future studies, moving sliding mode control method is considered to be applied to many robotic systems. Since the moving sliding mode control method gives better results than the classical sliding mode control, it will be a robust and better control method in other systems where it will be applied.

6. Author Contribution Declaration

Author 1 developed the concept for the study, derived the system's dynamic equations, obtained the state space equations, evaluated the results, reviewed the literature, checked for spelling errors, and ensured the article's content was correct. Author 2 developed the system's software program, obtained the program's result graphics, evaluated the results, checked for spelling errors, and ensured the article's content was correct.

7. Ethics Committee Approval and Conflict of Interest Declaration

Ethics committee permission is not required for the prepared article. There is no conflict of interest with any person/institution in the prepared article.

8. References

- [1] M. Bugeja, "Non-linear swing-up and stabilizing control of an inverted pendulum system," The IEEE Region 8 EUROCON 2003. Computer as a Tool., Ljubljana, Slovenia, pp. 437-441, vol. 2, 2003.
- [2] W. Zhong and H. Rock, "Energy and passivity based control of the double inverted pendulum on a cart," in Proceedings of the 2001 IEEE International Conference on Control Applications (CCA'01), Mexico City, Mexico, pp. 896-901, 2001.
- [3] J. Krishen and V. M. Becerra, "Efficient fuzzy control of a rotary inverted pendulum based on LQR mapping," in Proceedings of the 2006 IEEE Conference on Computer Aided Control System Design, 2006 IEEE International Conference on Control Applications, 2006 IEEE International Symposium on Intelligent Control, Munich, Germany, pp. 2701-2706, 2006.
- [4] S. Awtar, N. King, T. Allen, I. Bang, M. Hagan, D. Skidmore, K. Craig, "Inverted pendulum systems: rotary and arm-driven - a mechatronic system design case study," *Mechat.*, vol. 12, no. 2, pp. 357-370, 2002.
- [5] Q. Yan, "Output tracking of underactuated rotary inverted pendulum by nonlinear controller," in Proceedings of the 42nd IEEE International Conference on Decision and Control (IEEE Cat. No.03CH37475), Maui, HI, USA, vol. 3, pp. 2395-2400, 2003.
- [6] T. C. Kuo, Y. J. Huang, and B. W. Hong, "Adaptive PID with sliding mode control for the rotary inverted pendulum system," in Proceedings of the 2009 IEEE/ASME International Conference on Advanced Intelligent Mechatronics, Singapore, pp. 1804-1809, 2009.
- [7] J. Nuo and H. Wang, "Nonlinear Control of an Inverted Pendulum System based on Sliding mode method," *ACTA Analy. Funct. Appl.*, vol. 9, no. 3, pp. 234-237, 2008.
- [8] J. Krishen and V. M. Becerra, "Efficient fuzzy control of a rotary inverted pendulum based on LQR mapping," in Proceedings of the 2006 IEEE Conference on Computer Aided Control System Design, 2006 IEEE International Conference on Control Applications, 2006 IEEE International Symposium on Intelligent Control, Munich, Germany, pp. 2701-2706, 2006.
- [9] O. Altinoz, A. Tolga, E. Yilmaz, and G. W. Weber, "Chaos particle swarm optimized PID controller for the inverted pendulum system," in Proceedings of the 2nd international conference on engineering optimization, 2010.
- [10] S. Toshiharu and K. Fujimoto, "Controller design for an inverted pendulum based on approximate linearization," *International Journal of Robust and Nonlinear Control: IFAC-Affiliated Journal*, vol. 8, no. 7, pp. 585-597, 1998.
- [11] M. A. Khanesar, M. Teshnehlab, and M. A. Shoorehdeli, "Fuzzy Sliding Mode Control of Rotary Inverted Pendulum," in Proceedings of the 2007 IEEE International Conference on Computational Cybernetics, Gammarrh, Tunisia, pp. 57-62, 2007.
- [12] W. Wang, "Adaptive fuzzy sliding mode control for inverted pendulum," in Proceedings of the 2009 International Symposium on Computer Science and Computational Technology (ISCSCI 2009), Academy Publisher, pp. 231, 2009.
- [13] A. Bogdanov, "Optimal control of a double inverted pendulum on a cart," Oregon Health and Science University, Tech. Rep. CSE-04-006, OGI School of Science and Engineering, Beaverton, OR, 2004.
- [14] I. Hassanzadeh and S. Mobayen, "PSO-based controller design for rotary inverted pendulum system," *Jour. of Appl. Sci.*, vol. 8, no. 16, pp. 2907-2912, 2008.
- [15] V. Sukontanakarn and M. Parnichkun, "Real-time optimal control for rotary inverted pendulum," *American Journal of Applied Sciences*, vol. 6, no. 6, pp. 1106, 2009.
- [16] M. Aydın, O. Yakut, and H. Tutumlu, "Implementation of the network-based moving sliding mode control algorithm to the rotary inverted pendulum system," *Jour. of Eng. and Techn.*, vol. 3, no. 1, pp. 31-40, 2009.

- [17] S. Horikawa, T. Furuhashi, and Y. Uchikawa, "Fuzzy control for inverted pendulum using fuzzy neural networks," *J. Rob. and Mechat.*, vol. 7, no. 1, pp. 36-44, 1995.
- [18] I. H. Zadeh and S. Mobayen, "PSO-based controller for balancing rotary inverted pendulum," *J. Appl. Sci.*, vol. 16, pp. 2907-2912, 2008.
- [19] S. D. Sanjeeva and M. Parnichkun, "Control of rotary double inverted pendulum system using LQR sliding surface based sliding mode controller," *Jour. of Con. and Dec.*, vol. 9, no. 1, pp. 89-101, 2022.
- [20] A. Ma'arif, M. A. M. Vera, M. S. Mahmoud, S. Ladaci, A. Çakan, and J. N. Parada, "Backstepping sliding mode control for inverted pendulum system with disturbance and parameter uncertainty," *Jour. of Robotics and Con. (JRC)*, vol. 3, no. 1, pp. 86-92, 2022.
- [21] R. Hernández and F. Jurado, "Adaptive Neural Sliding Mode Control of an Inverted Pendulum Mounted on a Ball System," in *Proceedings of the 2018 15th International Conference on Electrical Engineering, Computing Science and Automatic Control (CCE)*, Mexico City, Mexico, pp. 1-6, 2018.
- [22] S. Irfan, A. Mehmood, M. T. Razzaq, and J. Iqbal, "Advanced sliding mode control techniques for inverted pendulum: Modelling and simulation," *Eng. Sci. and Techn., an Inter. Jour.*, vol. 21, no. 4, pp. 753-759, 2018.
- [23] K. D. Young, V. I. Utkin, and U. A. Ozguner, "Control engineer's guide to sliding mode control," *IEEE Transactions on Control Systems Technology*, vol. 7, no. 3, pp. 328-342, 1999.
- [24] C. Edwards and S. K. Spurgeon, *Sliding Mode Control: Theory and Applications*, New York: Taylor and Francis, 1998.
- [25] Chuan-Kang Ting, "On the Mean Convergence Time of Multi-parent Genetic Algorithms without Selection," in *Advances in Artificial Life*, Springer, Berlin, Heidelberg, pp. 403-412, 2005.
- [26] K. Nath and L. Dewan, "A comparative analysis of linear quadratic regulator and sliding mode control for a rotary inverted pendulum," in *Proceedings of the 2018 International Conference on Recent Trends in Electrical, Control and Communication*, pp. 302-307, 2018.



Öğütülmüş Diyatomitin Kendiliğinden Yerleşen Harçların Erken Dayanımına Etkisi

Büşra KARABULUT¹ , Merve ŞAHİN YÖN^{2*} , Mehmet KARATAŞ³ 

¹İnşaat Mühendisliği Bölümü, Mühendislik Fakültesi, Fırat Üniversitesi, Elazığ, Türkiye.

^{2,3}İnşaat Mühendisliği Bölümü, Mühendislik Fakültesi, Munzur Üniversitesi, Tunceli, Türkiye.

¹221115102@firat.edu.tr, ²mervesahinyon@munzur.edu.tr, ³mehmetkaratas@munzur.edu.tr

Geliş Tarihi: 14.05.2024
Kabul Tarihi: 20.08.2024

Düzeltilme Tarihi: 01.08.2024

doi: 10.62520/fujece.1484058
Araştırma Makalesi

Alıntı: B. Karabulut, M. Ş. Yön ve M. Karataş, “Öğütülmüş diyatomitin kendiliğinden yerleşen harçların erken dayanımına etkisi”, Fırat Üni. Deny. ve Hes. Müh. Derg., vol. 3, no 3, pp. 350-361, Ekim 2024.

Öz

Çimento üretimi doğaya salınan karbondioksit miktarını arttıran önemli bir etkidir. Bu nedenle çimento yerine puzolanik özellik gösteren doğal ve atık malzemelerin kullanımı oldukça önemlidir. Bu makalede, çimento ile ikame edilebilecek doğal puzolanik bir malzeme olan diyatomit kayacının kendiliğinden yerleşen harç üretiminde kullanılabilirliği araştırılmıştır. Deneysel çalışmada, öğütülmüş diyatomitin kendiliğinden yerleşen harçlarda erken yaşta mekanik özelliklerine olan etkisini incelemek için 40×40×160 mm boyutlarında olan prizmatik numuneler; sırasıyla %0, %5, %10, %15, %20 oranında diyatomitin çimento ile değiştirilmesiyle üretilmiştir. kendiliğinden yerleşen harç elde etmek için çökme-akış testi, Avrupa Uzman Yapı Kimyasalları ve Beton Sistemleri Federasyonu kılavuzuna göre yürütülmüştür. %0, %5, %10, %15 ve %20 diyatomit kullanılarak hazırlanan numuneler 3 gün boyunca 23±2 °C sıcaklıktaki suda kürlenmeye tabi tutulmuştur. Kür süresi tamamlanan numunelerin 3 günlük (erken yaş) eğilme ve basınç dayanım değerleri elde edilmiştir. Bu deneysel çalışmanın sonucunda en yüksek dayanımların referans numuneleri de aşarak, %5 diyatomit içeren serilerde olduğu belirlenmiştir. Ayrıca karışımlardaki diyatomit oranının %5 ten fazla olmasıyla mekanik dayanımların azaldığı tespit edilmiştir.

Anahtar kelimeler: Öğütülmüş diyatomit, Kendiliğinden yerleşen harç, Mekanik özellikler, Erken dayanım

*Yazışılan Yazar

İntihal Kontrol: Evet – Turnitin

Şikayet: fujece@firat.edu.tr

Telif Hakkı ve Lisans: Dergide yayın yapan yazarlar, CC BY-NC 4.0 kapsamında lisanslanan çalışmalarının telif hakkını saklı tutar



Effect of Ground Diatomite on Early Strength of Self-Compacting Mortars

Büşra KARABULUT¹ , Merve ŞAHİN YÖN^{2*} , Mehmet KARATAŞ³ 

¹Department of Civil Engineering, Engineering Faculty, Firat University, Elazığ, Türkiye.

^{2,3}Department of Civil Engineering, Engineering Faculty, Munzur University, Tunceli, Türkiye.

¹221115102@firat.edu.tr, ²mervesahinyon@munzur.edu.tr, ³mehmetkaratas@munzur.edu.tr

Received: 14.05.2024
Accepted: 20.08.2024

Revision: 01.08.2024

doi: 10.62520/fujece.1484058
Research Article

Citation: B. Karabulut, M. Ş. Yön and M. Karataş, "Effect of ground diatomite on early strength of self-compacting mortars", *Firat Univ. Jour. of Exper. and Comp. Eng.*, vol. 3, no 3, pp. 351-360, October 2024.

Abstract

Portland cement fabrication is a significant factor that increases the amount of carbon dioxide released into nature. For this reason, it is very important to use natural and waste materials with pozzolanic properties instead of portland cement. In this article, the usability of diatomite rock, a natural pozzolanic material that can be substituted with portland cement, in the manufacture of self-compacting mortar was studied. In the experimental study, prismatic specimens with dimensions of 40 × 40 × 160 mm were used to examine the impact of ground diatomite on the early age mechanical properties of self-compacting mortar; it was produced by replacing 0%, 5%, 10%, 15%, 20% of diatomite with portland cement, respectively. The slump-flow test to obtain self-compacting mortar was conducted according to the European Federation of Specialized Construction Chemicals and Concrete Systems guidance. Specimens prepared using 0%, 5%, 10%, 15% and 20% diatomite were cured in water at 23±2 °C temperature for 3 days. 3-day (early age) flexural and compressive strength worths were gained for the samples whose curing period was completed. As a result of this experimental study, it was specified that the highest strengths were in the series containing 5% diatomite, exceeding the reference samples. Additionally, it has been determined that mechanical strength decreases when the diatomite ratio in mixtures is more than 5%.

Keywords: Ground diatomite, Self-compacting mortar, Mechanical properties, Early strength

*Corresponding author

1. Introduction

Portland cement (PC) production, an important building material, is increasing day by day [1]. PC consumption is approximately 1 ton per person per year in the world. PC, one of the basic components of concrete, constitutes 10-12% of concrete [2]. PC has a significant share in the construction cost. High temperatures occur during PC production and a significant amount of CO₂ is released in this process. While there is no need for manufacturing to obtain sand, it requires research and operation of quarries [3]. As the world population increases, the need for infrastructure has increased. In parallel with this, the need for natural aggregates is also increasing. For instance, while sand fabrication in China was 2500 million metric tons (2014), it reached 39.9 million cubic meters in Algeria [3]. Therefore, sand pits need to be protected by using alternative materials. Researchers have produced normal concrete or SCC using marble waste instead of PC or aggregate [4-6]. Also, the use of natural resources with pozzolanic properties that can replace PC is of great importance [7]. Pozzolanic materials that can be used instead of PC, in addition to offering both economic and environmental advantages, can also increase the properties of concrete such as preventing alkaline aggregate reactions and resistance to chemical environments [1].

Diatomite (D), which is among the different pozzolanic materials, is an abundant and cheap material with good quality reserves in Turkey [8]. The impact of D, which is used as an additive in concrete, on concrete/mortar has been the subject of research in recent years. Concrete samples were produced by substituting diatomite and WMP (waste marble powder) with cement by Ergun. As a result of the work, they obtained the best compressive and flexural strength in concrete samples containing 10% diatomite, 5% WPM and 5% WPM + 10% diatomite by weight. He also stated that the use of cement with different proportions of diatomite and WMP, separately and together with superplasticizer, gave positive results [9]. In their study, Zhang et al. investigated the usability of diatomite in recycled aggregate concrete (RAC). They found that the wide capillary pores in the specimens were diminished by using diatomite. They stated that there was an increase in both split tensile and compressive strengths by partially replacing up to 20% by weight OPC with diatomite [10]. Santos and Cordeiro examined the impact of grinding on developing the pozzolanic activity of small-porosity diatomite. They stated that the increase in the specific surface area (SSA) of diatomite increases the silica solubility and pozzolanic activity of diatomite [11]. Sarıdemir et al. In their study, they investigated the mechanical and microstructural characteristics of high-strength mortars (HSMs) produced with calcined diatomite powder (CDP) at ambient and high temperatures. The highest mechanical strength at ambient and high temperatures was obtained in HSM modified with 15% CDP (15CDP-HSM) [12]. Degirmenci and Yılmaz used diatomite as a partial substitute for cement. They conducted mechanical strength, sulfate resistance and freeze-thaw, dry unit weight and water absorption tests. According to the test results, they found a decrease in compressive and flexural strength as the diatomite ratio increased [13]. Xu et al. to produce hydraulic mortars, they used natural hydraulic lime (NHL2) (NHL) as aggregate and diatomite as a partial substitute for masonry waste powder (MWP). For NHL2, they used 0-20% diatomite with a 10% increase in weight. Specimens were produced with diverse water binder ratios (w/b). Diatomite substitution increased the mechanical strength of the hydraulic mortars produced. The change in diatomite ratio affected the compactness, porosity and strength of the mortars. Additionally, adding diatomite to the mortar improved the acid and sulfate resistance of the mortars [14]. Sun et al. used diatomite in their experimental studies to increase frost resistance. In the experimental results, they stated that the use of diatomite instead of silica fume significantly increased the freezing resistance of the mortar [15]. Koçak and Pınarcı conducted research on the hydration systems, compressive strength, physical and microstructural properties of cement pastes and mortars substituted with diatomite in different proportions. In the results, they found that portlandite content decreased with increasing age and diatomite addition. They stated that diatomite added cements had a higher degree of hydration and a higher amount of hydration products were formed in 28 and 90 days. This structure had a positive impact on the compressive strength of the mortars at later ages [16].

Self-compacting (consolidation) concrete (SCC) is a kind of concrete that can reach places where reinforcement placement is frequent and collapse under its own weight. SCC, which has high fluidity, maintains its stable structure without decomposition until it gains strength. It was developed by Okamura in Japan in 1986 to reduce workmanship errors in the compaction of concrete. SCCs have many positive features such as filling ability, good workmanship, construction time, occupational safety, noise reduction, design and

energy efficiency [17]. To produce fresh SCC with good mechanical properties and excellent processability without using vibration, basic parameters such as high passing ability and filling capacity need to be met. To ensure the solidity and combination of the mixture, a mixture that can produce a significant amount of powder material and/or change in viscosity is needed. Pozzolans are siliceous or siliceous aluminous materials that have little or no stringent properties when used alone, but can get stringent properties by reacting with calcium hydroxide $\text{Ca}(\text{OH})_2$ when finely ground [18]. About the use of diverse pozzolanic materials such as silica fume [19, 20], slag [21, 22], metakaolin [23], [24], fly ash [25], marble powder [26], [27], pumice powder [28, 29] in self-compacting mortars (SCMs) important studies have been carried out. In this way, it will minimize cement cost and CO_2 emissions and provide the advantage of achieving high strength.

There are some studies to determine the early age strength of concrete or mortar [30], [31]. In their study, Shah et al. investigated the fresh and early age strength properties of fly ash/slag-based alkali-activated mortar. The curing temperature contributed to the improvement of the early age strength of the single-component AAM (Alkali-activated mortar). Through microstructural tests, they stated that this effect increased the geopolymerization reaction [22] and thus provided a significant increase in early strength [32]. Ren et al. blended calcium formate and methacrylic acid with PC paste powder and examined the effects on the setting time, fluidity and mechanical properties of the mortar. According to experimental results, 0.5, 1, 3 and 28 days compressive strength increased [33].

The purpose of this experimental work is to investigate the effect of replacing fine particle D (0%, 5%, 10%, 15% and 20%) with PC, which has not been used together before, on fresh and hardened self-compacting mortars. In this article, the fresh properties (mini-slump flow and viscosity experiments) of SCMs made from (D) and (PC) were evaluated. Also, early age strengths of SCMs produced with these substitution rates were determined. The results show that SCM in its fresh state achieved good workability and flow time when 5%-20% D was substituted with PC at a 5% increase in weight.

2. Materials

For this laboratory study, CEM I 42.5 R type PC complying with TS-EN 197-1 was used. PC has specific gravity of 3.09. Locally available river sand with a specific gravity of 2.63, a water absorption rate of 1.91%, a maximum size of 4 mm and a fineness modulus of 2.87 was used. D, as a fine filler pozzolanic binder, was included in the mixture with the PC to increase the viscosity. In addition, D, which is a sedimentary rock, was obtained from NB Global Mining and Chemical Industry and Trade Company. Polycarboxylate based Sika Viscocrete SF 18 super plasticizer (SP) was used as water reducer. Its density is 1.1 g/cm^3 and pH value is 3-7. The aggregate and binder materials used for the experimental study are shown in Figure 1.



Figure 1. Dry ingredients used in mixes a) sand, b) PC, c) D

Characteristic properties and some mineralogical compositions of D and PC are presented in Table 1. Figure 2 was given the granulometry curve of river sand.

Table 1. Characteristics of PC and diatomite

Component (%)	PC	D
SiO ₂	18.36	60.98
Al ₂ O ₃	4.72	9.35
Fe ₂ O ₃	3.63	3.86
MgO	1.58	2.52
CaO	63.06	2.34
SO ₃	3.29	0.38
Na ₂ O	0.18	-
K ₂ O	0.82	-
Loss on ignition (LOI)	4.13	20.31
Specific gravity	3.09	2.41

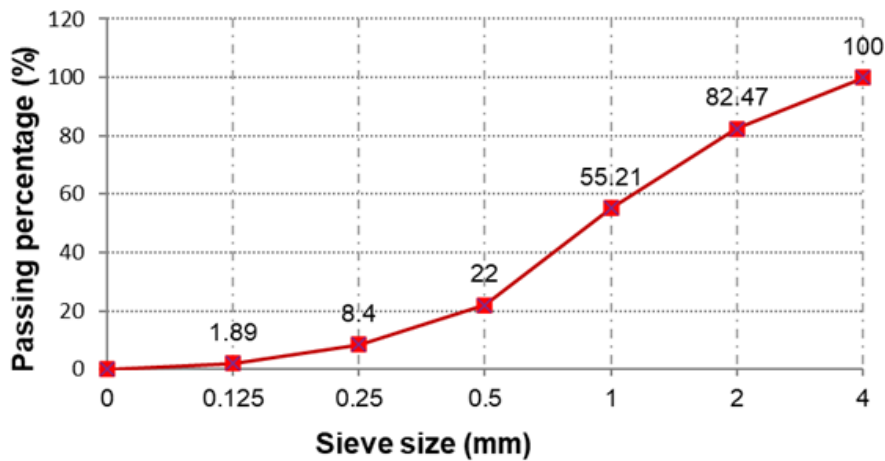


Figure 2. Granulometry curve of river sand

2.1. SCMs Mix Proportions

A control and five mixtures were prepared to determine the fresh and hardened properties of SCMs produced by substituting D with different proportions of cement. The content compositions of SCM are shown in Table 2. Substitution rates by weight were used at 0%, 5%, 10%, 15% and 20%, respectively. After repeated trial mixtures, water/powder (w/p) volume ratios were calculated as 0.36, 0.38, 0.45, 0.57 and 0.69 for control, D5, D10, D15 and D20, respectively. In all prepared mixtures, the binder amount was 630 kg/m³ and the SP amount was chosen as 8 kg/m³. In order provide the EFNARC (European Federation of Specialized Construction Chemicals and Concrete Systems guidance standards) [34] of the spreading diameters of SCMs, the water content was changed depending on the increase in D. Table 2 shows the water/binder (=C + D) (w/b) and water/powder (=C + 0.9D + 0.0191 sand) (w/p) ratios.

Table 2. Mixture proportions for SCM (kg/m³)

Mix name	C	D	Sand	Water	SP	Water/binder	Water/powder
Control	630	0	1367.5	260	8	0.41	0.36
D5	598.5	31.5	1333.4	270	8	0.43	0.38
D10	567	63	1227.0	315	8	0.50	0.45
D15	535.5	94.5	1028.7	380	8	0.60	0.57
D20	504	126	836.8	450	8	0.71	0.69

3. Experimental Method

3.1. Casting and curing

A mixer was used to create SCMs. To create mortar samples, first dry binding materials and river sand were taken into the mixing bowl. Firstly, the dry components (fine aggregate, binders) were mixed until homogeneous. Then, water was added to the SP and poured into the dry mixture and mixed. The prepared mixtures were poured in three stages, taking care to keep the $40 \times 40 \times 160$ mm sized prismatic molds stable. SCMs, which hardened after 24 hours, were removed from the mold. The specimens removed from the mold were left to cure in water at around 23°C until the test day. The fresh mortars poured into molds are given in Figure 3.



Figure 3. Fresh SCM

3.2. Tests

3.2.1. Fresh properties

Mini-slump flow testing and viscosity experiments were conducted to determine the workability and flowability properties of fresh mortars (Figure 4.). Before the strength tests, mini-slump flow test was conducted according to EFNARC criteria to examine the workability properties of SCM to achieve filling and passing ability. Mini slump flow tests were carried out to ensure that the fluidity and spreading diameter of the fresh mortar were compatible with the limit values in accordance with the EFNARC regulation.



Figure 4. a) mini-slump spreading diameter, b) viscometer test machine

Viscometer test is a method used to determine the fluidity of concrete/mortar. It is important to evaluate the workability and plastic properties of concrete/mortar [35]. In the measurement made using the Brookfield DVE brand viscosity device, the mixed mortar was poured into a beaker. The torsional moment response of the mortar in the container to the rotation of the shaft at the end of the device was measured. To determine the rheological properties, the rotational speed of the shaft was measured between 1.0-100 rpm (legs with increasing shear rate-shear stress) and 100-1.0 rpm (legs with decreasing shear rate-shear stress) [28]. The

values obtained for different angular velocities were evaluated by drawing the viscosity-angular velocity graph. The fresh property values used for the prepared SCMs are shown in Table 3.

Table 3. Fresh properties for SCMs

Mix name	Mini-slump flow (mm)
Control	242
D5	243
D10	245
D15	243
D20	250

3.2.2. Hardened properties

Mechanical tests were conducted to decide the early strength of the mixtures whose fresh properties were determined. To measure the flexural strength values of SCMs, three prismatic samples with dimensions of 40 x 40 x 160 mm were cast for a test age of 3 days. After cleaning the surface of the SCM prismatic samples, a three-point flexural test (Figure 5.) was performed at a loading rate of 0.2 kN/s. The 3-day flexural strength test of the mortars was conducted in accordance with ASTM C348 [36]

After the flexural test, the compressive strength of each piece divided into two under a loading speed of 2.4 kN/s was determined according to the ASTM C349 [37] standard.



Figure 5. Three-point flexural test

4. Results and Discussions

This study focused on the usability of grounded D with PC in various proportions (0%, 5%, 10%, 15% and 20%). D and cementitious compositions were conducted fresh mortar tests, and their early strengths were evaluated in experimental study.

4.1. Characteristics of fresh SCMs

The workability and fluidity of SCMs containing diatomite were determined by mini-slump test, considering the EFNARC regulation. The results obtained are given in the Figure 6. As seen in the figure, mini-slump results provide limit values between 240-260 mm. These ranges were maintained by changing the amount of water. Accordingly, it has been observed that as the D ratio increases, the water needs increases. Due to the

increase in the D ratio, the increase in the w/b ratio can be associated with the increase in the spreading diameters [38], [39]. As seen in Figure 6, the lower fluidity of the fresh SCMs produced results in a parallel flow time delay [40].

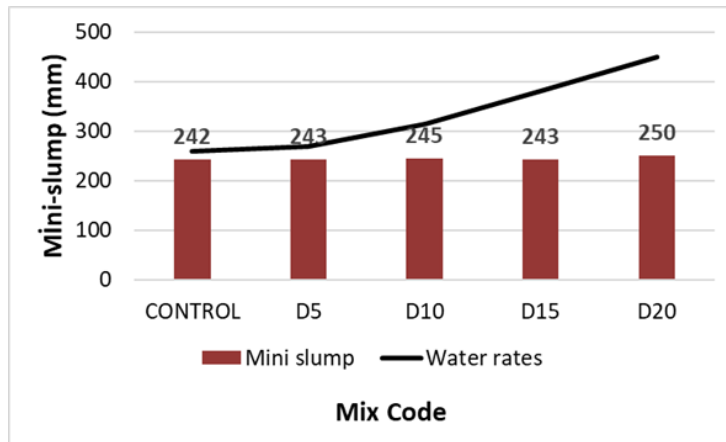


Figure 6. Mini-slump values and the amounts of water

The most important feature of SCMs is sufficient fluidity and resistance to segregation [41]. In order for these parameters to be realized in SCMs, there must be appropriate viscosity, low shear stress and cohesion. For this reason, the viscosity test of mortars containing D was performed to determine their consistency and workability features. Figure 7 shows the viscosity results of the produced samples. This graph shows that as the angular speed of the spindle increased, the viscosity values of the samples decreased asymptotically [18]. As seen in Figure 7, the viscosity value of the samples containing D5 remained above the viscosity value of the control and other mixtures at the first 2 rotation speeds. With increasing speed after 5 rpm, the viscosity of all series decreased and the inclusion of D at this speed reduced the viscosity, resulting in lower results than the control mixture. The lowest viscosity was measured at 100 Rpm for the D15 mixture, while the highest viscosity was measured at low rpm for the D5 mixture.

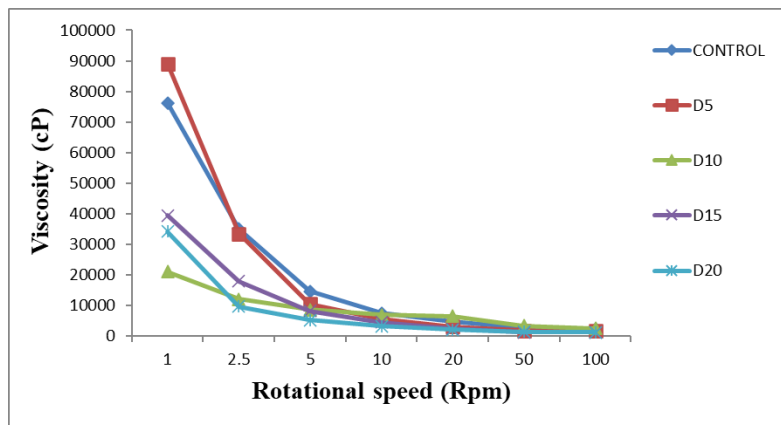


Figure 7. Viscosity values of SCMs

4.2. Characteristics of hardened SCMs

Failure loads for three-point flexural test was given in Table 4. The Figure 8 presents the effect of D on the flexural strength of prismatic samples prepared for 3- days. It was observed that the addition of 5% D increased the flexural strength on compared to the reference samples. When the 3-day flexural strengths of the control sample were compared with the combinations containing 5% D, 10% D, 15% D and 20% D, a 14.6% increase, 13.55%, 44% and 61.6% decrease were detected, respectively. While this shows that the 3-

day strength of the 5% D series was better than the control sample, this situation was reversed due to the increase in the D rate.

Table 4. Failure loads for flexural tests

Mix name	Failure loads (N)
Control	2181.55
D5	2501.12
D10	1885.87
D15	1221.55
D20	836.70

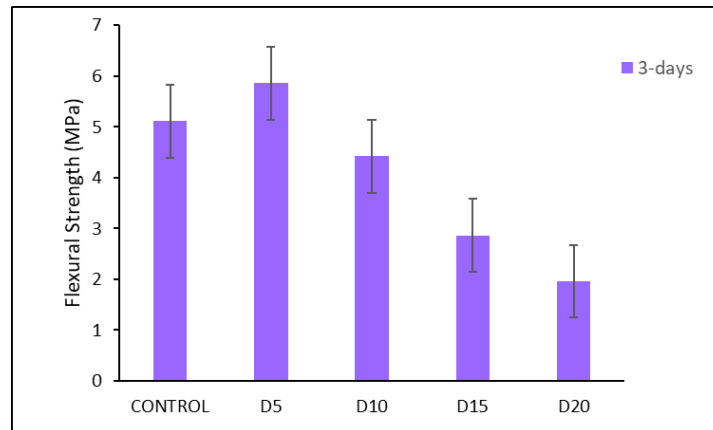


Figure 8. Flexural strength of 3-days SCMs

3-days compressive strengths of SCMs are shown in Figure 9. According to this figure, 3-day strength value of the all the sample, a decrease in compressive strength was observed as the D ratio increased. When the compressive strengths of the D5, D10, D15 and D20 series were compared with the control sample, there was an increase of 11.65%, a decrease of 19.96%, 52.13% and 71.3%, respectively. This situation is similar to the results of the researchers [22].

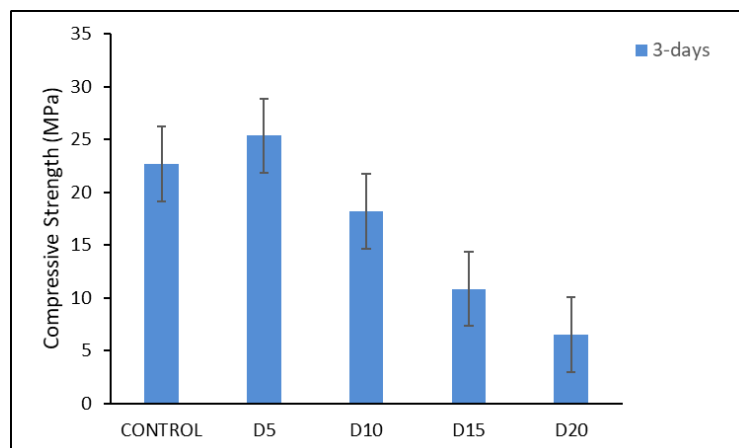


Figure 9. Compressive strength of 3-days SCMs

5. Conclusion

In this study, the fresh and hardened situations of five self-compacting mortars with different replacement rates of diatomite, a sedimentary rock, were examined. For this, rheological and fresh properties were determined by mini-slump flow and viscometer tests on the produced SCMs. Then, flexural and compressive

strength experiments were performed on SCM mixtures containing diatomite. The findings obtained from this experimental research are explained below.

- In order to ensure the self-compacting of mortars containing diatomite, mini-slump values in the range of 240-260 mm were determined in accordance with EFNARC. It has been determined that to achieve this, different amounts of water are required depending on the substitution rates of the binders.
- As the D content increased, the slump flow value increased due to the increase in water need.
- The viscosity readings of the reference sample are higher than all other samples for rotation speeds of 2.5, 5 and 10.
- While the highest flexural strength among all series is measured in the series with 5% D additive, the lowest strength is in the series with 20% D content. This decrease is approximately 67%.
- When the compressive strengths were examined, the highest strength occurred in the mixture with 5% D content, similar to the flexural strength. As the D content increased, the strength gradually decreased. The largest decrease occurred in the D20 series, with a rate of 74% compared to the D5 series.

As a result, it was determined by early strength tests that D could be replaced with PC at a rate of 5%-10%. However, for more detailed examination, 28- and 90-days mechanical strengths should be determined in future studies. In addition, freeze-thaw, sulfate resistance, abrasion, high temperature, etc. tests should be carried out to determine durability properties.

6. Author Contribution Statement

In this study, Author 1 covers the topics of conducting experiments, literature review, and obtaining the materials used; Author 2 under the headings of literature review, preparation of the article and evaluation of the results obtained; Author 3 contributed to the formation of the idea, design, spelling and checking the article for content.

7. Ethics Committee Approval and Conflict of Interest Declaration

There is no need to obtain ethics committee permission for the article prepared. There is no conflict of interest with any person/institution in the prepared article.

8. References

- [1] B. Yilmaz and N. Ediz, "The use of raw and calcined diatomite in cement production," *Cement and Concrete Composites*, vol. 30, no. 3, pp. 202–211, 2008.
- [2] G. Kaplan et al., "Physico-mechanical, thermal insulation and resistance characteristics of diatomite and attapulgitic based geopolymer foam concrete: Effect of different curing regimes," *Construction and Building Materials*, vol. 373, no. March, p. 130850, 2023.
- [3] N. Bentlemsan, W. Yahiaoui, and S. Kenai, "Strength and durability of self-compacting mortar with waste marble as sand substitution," *Case Studies in Construction Materials*, vol. 19, no. June, p. e02331, 2023.
- [4] K. Vardhan, R. Siddique, and S. Goyal, "Strength, permeation and micro-structural characteristics of concrete incorporating waste marble," *Construction and Building Materials*, vol. 203, pp. 45–55, 2019.
- [5] I. B. Topçu, T. Bilir, and T. Uygunoğlu, "Effect of waste marble dust content as filler on properties of self-compacting concrete," *Construction and Building Materials*, vol. 23, no. 5, pp. 1947–1953, 2009.
- [6] M. J. Munir, S. M. S. Kazmi, and Y. F. Wu, "Efficiency of waste marble powder in controlling alkali-silica reaction of concrete: A sustainable approach," *Construction and Building Materials*, vol. 154, pp. 590–599, 2017.

- [7] A. C. Aydın and R. Gül, "Influence of volcanic originated natural materials as additives on the setting time and some mechanical properties of concrete," *Construction and Building Materials*, vol. 21, no. 6, pp. 1277–1281, 2007.
- [8] Z. Lv, A. Jiang, and J. Jin, "Influence of ultrafine diatomite on cracking behavior of concrete: an acoustic emission analysis," *Construction and Building Materials*, vol. 308, no. July, p. 124993, 2021.
- [9] A. Ergün, "Effects of the usage of diatomite and waste marble powder as partial replacement of cement on the mechanical properties of concrete," *Construction and Building Materials*, vol. 25, no. 2, pp. 806–812, 2011.
- [10] H. Zhang, B. He, B. Zhao, and P. JM Monteiro, "Using diatomite as a partial replacement of cement for improving the performance of recycled aggregate concrete (RAC)-Effects and mechanism," *Construction and Building Materials*, vol. 385, no. April, p. 131518, 2023.
- [11] A. A. Mota dos Santos and G. C. Cordeiro, "Investigation of particle characteristics and enhancing the pozzolanic activity of diatomite by grinding," *Materials Chemistry and Physics*, vol. 270, no. May, 2021.
- [12] M. Sarıdemir, S. Çelikten, and A. Yıldırım, "Mechanical and microstructural properties of calcined diatomite powder modified high strength mortars at ambient and high temperatures," *Advanced Powder Technology*, vol. 31, no. 7, pp. 3004–3017, 2020.
- [13] N. Degirmenci and A. Yılmaz, "Use of diatomite as partial replacement for Portland cement in cement mortars," *Construction and Building Materials*, vol. 23, no. 1, pp. 284–288, 2009.
- [14] S. Xu, J. Wang, Q. Ma, X. Zhao, and T. Zhang, "Study on the lightweight hydraulic mortars designed by the use of diatomite as partial replacement of natural hydraulic lime and masonry waste as aggregate," *Construction and Building Materials*, vol. 73, pp. 33–40, 2014.
- [15] M. Sun, C. Zou, and D. Xin, "Pore structure evolution mechanism of cement mortar containing diatomite subjected to freeze-thaw cycles by multifractal analysis," *Cement and Concrete Composites*, vol. 114, no. June, p. 103731, 2020.
- [16] Y. Kocak and İ. Pınarcı, "Effects of hydration mechanism on mechanical properties of diatomite-cement composites," *European Journal of Environmental and Civil Engineering*, vol. 27, no. 12, pp. 3707–3721, 2023.
- [17] P. Ramanathan, I. Baskar, P. Muthupriya, and R. Venkatasubramani, "Performance of self-compacting concrete containing different mineral admixtures," *KSCE Journal of Civil Engineering*, vol. 17, no. 2, pp. 465–472, 2013.
- [18] M. Ş. Yön, F. Arslan, M. Karatas, and A. Benli, "High-temperature and abrasion resistance of self-compacting mortars incorporating binary and ternary blends of silica fume and slag," *Construction and Building Materials*, vol. 355, no. September, 2022.
- [19] E. Türk, M. Karataş, and M. Dener, "Rheological, mechanical and durability properties of self-compacting mortars containing basalt powder and silica fume," *Construction and Building Materials*, vol. 356, no. September, 2022.
- [20] A. Benli, M. Karataş, and E. Gurses, "Effect of sea water and MgSO₄ solution on the mechanical properties and durability of self-compacting mortars with fly ash/silica fume," *Construction and Building Materials*, vol. 146, pp. 464–474, 2017.
- [21] M. Karatas, M. Dener, A. Benli, and M. Mohabbi, "High temperature effect on the mechanical behavior of steel fiber reinforced self-compacting concrete containing ground pumice powder," *Structural Concrete*, vol. 20, no. 5, pp. 1734–1749, 2019.
- [22] M. Ş. Yön and M. Karataş, "Evaluation of the mechanical properties and durability of self-compacting alkali-activated mortar made from boron waste and granulated blast furnace slag," *Journal of Building Engineering*, vol. 61, no. September, p. 105263, 2022.
- [23] M. K. Sharbatdar, M. Abbasi, and P. Fakharian, "Improving the properties of self-compacted concrete with using combined silica fume and metakaolin," *Periodica Polytechnica Civil Engineering*, vol. 64, no. 2, pp. 535–544, 2020.
- [24] F. Arslan, A. Benli, and M. Karatas, "Effect of high temperature on the performance of self-compacting mortars produced with calcined kaolin and metakaolin," *Construction and Building Materials*, vol. 256, p. 119497, 2020.

- [25] S. Dadsetan and J. Bai, "Mechanical and microstructural properties of self-compacting concrete blended with metakaolin, ground granulated blast-furnace slag and fly ash," *Construction and Building Materials*, vol. 146, pp. 658–667, 2017.
- [26] N. Gülmez, "Performance of marble powder on cementitious composites including waste steel chips as an additive," *Construction and Building Materials*, vol. 312, no. October, p. 125369, 2021.
- [27] N. Gülmez, "Performance of marble powder on cementitious composites including waste steel chips as an additive," *Construction and Building Materials*, vol. 312, no. March, p. 125369, 2021.
- [28] M. Sarıdemir and S. Çelikten, "Investigation of fire and chemical effects on the properties of alkali-activated lightweight concretes produced with basaltic pumice aggregate," *Construction and Building Materials*, vol. 260, 2020.
- [29] F. Ameri, P. Shoaie, M. Zahedi, M. Karimzadeh, H. R. Musaei, and C. B. Cheah, "Physico-mechanical properties and micromorphology of AAS mortars containing copper slag as fine aggregate at elevated temperature," *Journal of Building Engineering*, vol. 39, no. September 2020, p. 102289, 2021.
- [30] H. Y. Aruntaş, E. Yildiz, and G. Kaplan, "the Engineering Performance of Eco-Friendly Concretes Containing Diatomite Fly Ash and Ground Granulated Blast Furnace Slag," *Acta Polytechnica*, vol. 62, no. 5, pp. 505–521, 2022.
- [31] E. Bozkurt, S. Türkel, and B. Feleko, "Effect of aging on the mechanical properties of woven fabric-reinforced calcined diatomite substituted cement-based composites," 2024.
- [32] S. F. A. Shah, B. Chen, S. Y. Oderji, M. A. Haque, and M. R. Ahmad, "Improvement of early strength of fly ash-slag based one-part alkali activated mortar," *Construction and Building Materials*, vol. 246, p. 118533, 2020.
- [33] G. Ren, Z. Tian, J. Wu, and X. Gao, "Effects of combined accelerating admixtures on mechanical strength and microstructure of cement mortar," *Construction and Building Materials*, vol. 304, no. March, p. 124642, 2021.
- [34] EFNARC, "EFNARC, (European Federation of Specialist Construction Chemicals and Concrete Systems), The European guidelines for selfcompacting concrete: Specification, production and use, U.K, 2002," *Magazine of Concrete Research*, vol. 64, no. 5, pp. 401–409, 2002.
- [35] K. Turk and S. Demirhan, "Effect of limestone powder on the rheological, mechanical and durability properties of ECC," *European Journal of Environmental and Civil Engineering*, vol. 21, no. 9, pp. 1151–1170, 2017.
- [36] A. ASTM C348, "Flexural strength of hydraulic-cement mortars," *American Society for Testing and Material*, vol. 04, pp. 1–6, 2002.
- [37] ASTM C349, "Standard test method for compressive strength of hydraulic-cement mortars (Using portions of prisms broken in flexure)," *ASTM International*, pp. 1–6, 2002.
- [38] Z. Ahmadi, J. Esmacili, J. Kasaei, and R. Hajialioghli, "Properties of sustainable cement mortars containing high volume of raw diatomite," *Sustainable Materials and Technologies*, vol. 16, pp. 47–53, 2018.
- [39] S. Xu, J. Wang, Q. Ma, X. Zhao, and T. Zhang, "Study on the lightweight hydraulic mortars designed by the use of diatomite as partial replacement of natural hydraulic lime and masonry waste as aggregate," *Construction and Building Materials*, vol. 73, pp. 33–40, 2014.
- [40] N. Roussel and R. Le Roy, "The Marsh cone: A test or a rheological apparatus?," *Cement and Concrete Research*, vol. 35, no. 5, pp. 823–830, 2005.
- [41] S. Saraç, M. Karatas, and A. Benli, "The effect of dunite powder and silica fume on the viscosity, physico-mechanical properties and sulphate resistance of self-compacting mortars," *Construction and Building Materials*, vol. 375, no. March, p. 130970, 2023.



Geniş Frekans Bantlı Anten Sistemleriyle Gömülü Nesnelerin Türünün Tespitinde Yapay Zeka Tabanlı Hibrit Bir Yaklaşım

Ebru EFEOĞLU^{1*}

^{1,*} Yazılım Mühendisliği, Mühendislik Fakültesi, Kütahya Dumlupınar Üniversitesi, Kütahya, Türkiye.
¹ebru.efeglu@dpu.edu.tr

Geliş Tarihi: 01.05.2024
Kabul Tarihi: 18.07.2024

Düzeltilme Tarihi: 26.06.2024

doi: 10.62520/fujece.1476716
Araştırma Makalesi

Alıntı: E. Efeoğlu, "Geniş frekans bantlı anten sistemleriyle gömülü nesnelerin türünün tespitinde yapay zeka tabanlı hibrit bir yaklaşım", Fırat Üni. Deny. ve Hes. Müh. Derg., vol. 3, no 3, pp. 362-376, Ekim 2024.

Öz

Kazı öncesinde gömülü nesnenin cinsinin bilinmesi gereksiz kazı yapılmasını önler. Üstelik zamandan ve paradan tasarruf sağlar. Bu çalışmada gömülü nesnelerin tespiti için bir deney seti hazırlandı. Deney seti, geniş frekans bandında elektromanyetik dalgalar gönderip alan bir anten, yansımaları kaydeden ve işleyen bir yazılımdan ve kum havuzundan oluşturuldu. Çalışmada bu kum havuzuna farklı derinlik, boyut ve şekillerde metalik ve metalik olmayan nesneler gömülerek bir profil boyunca ölçümler alındı. Yapılan ölçümlerden 2 boyutlu görüntüler oluşturuldu ve bu görüntülere görüntü işleme teknikleri uygulandı. İşlenmiş görüntülerden nesnenin türünü tespit etmek için sınıflandırma algoritmaları kullanıldı. Algoritmaların başarısını artırmak için, nitelik seçme teknikleri olarak korelasyona dayalı öznelik seçimi (CFS) ve Temel Bileşen Analizi (PCA) kullanılmıştır. CFS ile öznelik seçiminde arama yöntemleri olarak metasezgisel optimizasyon algoritmalarından genetik algoritma (GA), Parçacık Sürü Optimizasyonu (PSO), Harmony arama (HA) ve Evrimsel arama (EA) tercih edildi. Algoritmaların performansı 10 kat çapraz doğrulama yöntemi kullanılarak analiz edildi. Sonuç olarak PCA algoritmasının öznelik seçiminde kullanımının metasezgisel algoritmalara göre sınıflandırma başarısını daha fazla arttırdığı anlaşıldı. Kullanılan sınıflandırma algoritmaları arasında en başarılı olanı Rastgele ağaç algoritması oldu. PCA sonrasında bu algoritmanın doğruluk değeri %95,8'e ulaşıldı. Bu nedenle ölçüm sistemine gömülü yazılımda PCA ve Rastgele ağaç algoritmalarının kullanıldığı hibrit bir yaklaşım önerilmektedir.

Anahtar kelimeler: Yapay Zeka, Gömülü nesne, Metasezgisel optimizasyon algoritmaları, PCA, Görüntü işleme.


*Yazılan yazar

İntihal Kontrol: Evet – Turnitin
Şikayet: fujece@firat.edu.tr

Telif Hakkı ve Lisans: Dergide yayın yapan yazarlar, CC BY-NC 4.0 kapsamında lisanslanan çalışmalarının telif hakkını saklı tutar.



An Artificial Intelligence-Based Hybrid Approach to Detect the Type of Buried Objects with Broad Frequency Band Antenna Systems

Ebru Efeoğlu ^{1*} 

^{1,*} Software Engineering, Faculty of Engineering, Kütahya Dumlupınar University, Kütahya, Türkiye.
eburu.efeoglu@dpu.edu.tr

Received: 01.05.2024
Accepted: 18.07.2024

Revision: 26.06.2024

doi: 10.62520/fujece.1476716
Research Article

Citation: E. Efeoğlu "An artificial intelligence-based hybrid approach to detect the type of buried objects with broad frequency band antenna systems", *Firat Univ. Jour. of Exper. and Comp. Eng.*, vol. 3, no 3, pp. 362-376, October 2024.

Abstract

Knowing the type of buried object before excavation prevents unnecessary excavation. Moreover, it saves time and money. In this study, an experiment set was prepared for the detection of buried objects. The experimental set was composed of an antenna that sends and receives electromagnetic waves in a wide frequency band, software that records and processes reflections, and a sandbox. In the study, metallic and non-metallic objects with different depths, sizes and shapes were buried in this sand pool and measurements were taken along a profile. 2D images were created from the measurements and image processing techniques were applied to these images. Classification algorithms were used to detect the type of buried object from processed images. To increase the success of the algorithms, correlation-based attribute selection (CFS) and Principal Component Analysis (PCA) were used as attribute selection techniques. Genetic algorithm (GA), Particle Swarm Optimization (PSO), Harmony search (HA), and Evolutionary search (EA), which are among the metaheuristic optimization algorithms, were preferred as search methods in attribute selection with CFS. The performance of the algorithms was analyzed using the 10-fold cross-validation method. As a result, it was understood that the use of the PCA algorithm in attribute selection increases the classification success more than metaheuristic algorithms. The most successful among the classification algorithms used is the Random tree algorithm. After PCA, the accuracy value of this algorithm was 95.8. Therefore, a hybrid approach is proposed in which PCA and Random tree algorithms are used in the software embedded in the measurement system.

Keywords: Artificial Intelligence, Buried object, Metaheuristic optimization algorithms, PCA, Image processing

*Corresponding author

1. Introduction

There are many Geophysical prospecting methods. Seismic [1], Electrical Resistivity Tomography [2] etc. for detection of buried objects underground. However, the GroundPenetrating Radar (GPR) method is often used in near-surface applications. Buried objects can be metallic or non-metallic. Detection of buried non-metallic objects is more difficult than detection of metallic objects. Although metallic objects are detected using Electromagnetic Induction (EMI) sensors, Magnetic induction spectroscopy [3], non-metallic objects cannot be detected by EMI sensors [4]. For this reason, the GPR method is preferred especially for the detection of non-metallic objects [5]. This method is very popular in military and engineering fields due to its fast data collection [5,6]. It was often used to detect mines and buried explosives [7,8], objects buried at different depths [9], archaeological remains [10,11], underground pipeline [12].

GPR systems are divided into pulse-modulated systems and non-pulse-modulated systems. Pulseless modulation systems operate in the time domain and use a pulse signal [13]. Pulse modulation systems emit a Gaussian electromagnetic wave signal. This system uses a signal over a wide frequency band. Detecting buried objects from such systems requires expertise and time [12]. Therefore, approaches that automatically detect objects have been researched and proposed. Wavelet transform [14], Hough transform [15] and radon transform [13], image processing techniques [16], Ellipse inversion model [17] are some of these approaches. In recent years, studies on automatic detection of buried objects with machine learning techniques have been examined [18]. Automatic detection of consecutive lines from sonar images was done using machine learning methods [19]. Machine learning methods were used to detect underwater mines with synthetic aperture sonar images [20], to detect voids in underground pipelines, and to analyze GPR radargrams [21]. In addition, an automatic flaw detection system for sewer pipes has been developed from CCTV images [22]. It is difficult and costly to produce real data in studies for the detection of buried objects. For this reason, many researchers preferred to use synthetic data in their studies [23]. For example, synthetic images were created for the detection of buried pipes and hyperbolas in these images were detected by machine learning techniques [24]. Synthetic data were used for automatic recognition of tunnel lining elements from GPR images [25].

Synthetic data were not used in this study. An experimental setup was created. Metallic and non-metallic objects (Brick, tile, marble ceramic) of different shapes were buried in the sandbox at different depths. Measurements were taken. Then, classification algorithms were used with the data obtained from the measurement system. To date, many studies have been carried out for the detection of metallic and non-metallic buried objects. The buried objects were detected, but the buried objects were not classified as metallic or non-metallic. In this study, a measurement system and software based on artificial intelligence techniques are proposed to classify buried objects as metallic and non-metallic objects. The difference of the proposed system from other systems is that it determines the type of buried object regardless of its shape.

2. Experimental Setup and Data Collecting

The experimental setup consists of an antenna used as both a transmitter and a receiver, a laptop, a Vector Network Analyzer (VNA) and a sand box (Figure. 2). A signal is sent from the VNA to the sand box with a set step frequency and frequency band range (Figure. 1).

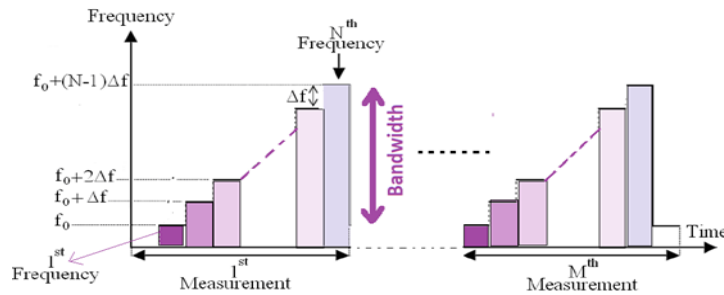


Figure 1. Implementation of measurement

The transmitted signal is a sequence of rising step frequencies. It starts from the starting frequency and the frequency is increased step by step. The frequency of the n th sample in the sequence can be calculated by Equation (1) when the starting frequency F_0 is taken as the constant rise frequency Δf .

$$F_n = F_0 + \Delta f \quad n = 0, \dots, M - 1 \quad (1)$$

The maximum penetration depth (d_{max}) of the signal is calculated using equation (2).

$$d_{max} = \frac{c}{2\Delta f} \quad (2)$$

where c is the speed of light.

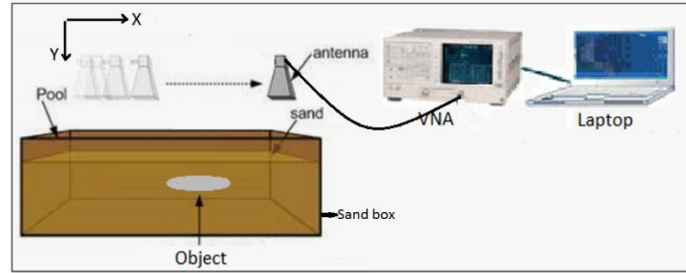


Figure 2. Experimental setup

For measurements metallic and non-metallic objects of different depths and shapes were buried in the sand box. Measurements were taken by slowly moving the antenna along the x axis from the surface of the sand box as shown in Figure. 2. The profile length is 60 cm, the number of measuring points is 61, the frequency band range is 1Ghz 6Ghz, the number of frequency steps is 64.

3. Imaging and Image Processing

1-D depth profiles were created by applying the inverse Fourier transform to the data collected at each measurement point. Then, these 1-dimensional depth profiles were aligned side by side to obtain 2-D images. Color layout filter applied to 2D images.

3.1. Color layout filter

Color is the most basic quality of the image. Colors can be used to describe and represent an image. The Color Layout Descriptor (CLD) is designed to capture the spatial distribution of dominant colors in an image. for cld computation, color are expressed in the YCbCr color space. CLD is very compact descriptor, therefore it fits perfectly for fast browsing and search applications. It is also resolution invariant.

CLD can be computed by following these steps.

1-Image Partitioning: The image is divided into $8 \times 8 (64)$ block. This makes CLD Scale invariant.

2- Representative Colour Detection: There is a representative color for each block. The average color of the block is used to select the representative color. Also the image is reduced to 64×64 so each block shrinks to 8×8 .

3-color space change: The image having average color blocks is in RGB space. Now this RGB is changed to YCbCr color space.

4- DCT transformation: Each color channel (Y,Cb,Cr) is transformed into DCT coefficients by performing 8×8 discrete Cosine Transform (DCT) of each 8×8 block. Therefore, each block carries 64 DCT coefficients.

5- *Quantization*: Zigzag scanning is used. A few low frequency coefficients are selected and quantized to form the descriptor. For Y-DCT only 6 coefficients are selected while from both Cb and Cr only three coefficients are selected and quantized.

6- *Forming CLD attribute vector*: For avarage image and its DCT it can be seen that expect DC coefficient, rest of coefficients are zero as one 8x8 block is a constant function. Therefore instead of taking 6,3 and 3 coefficients from DCT-Y, DCT-Cb and DCT-Cr respectively, it is sufficient to take only single DC coefficient from each block. The coefficients are arranged as given in Equation 1.

$$CLD = [Y_{dct1}, Y_{dct2}, \dots, Y_{dct64}, Cb_{dct1}, Cb_{dct2}, \dots, Cb_{dct64}, Cr_{dct1}, Cr_{dct2}, \dots, Cr_{dct64} \quad (1)$$

4. Attribute Selection

Using all attributes in classifications may not yield good results in some cases. In particular, the use of all attributes in noisy data and images negatively affects the success. Therefore, it is necessary to remove some unnecessary attributes. By using accurate data and relevant attributes, classification success is increased and the size of the data set is reduced. As the size of the dataset decreases, the computation speed increases and the memory requirement decreases. Attribute selection is very important to increase classification success and computational speed. There are algorithms used in the selection of attributes. In this study Correlation-based attribute selection (CFS) and PCA method will be used. The generalized version of attribute selection is given in Figure 3.

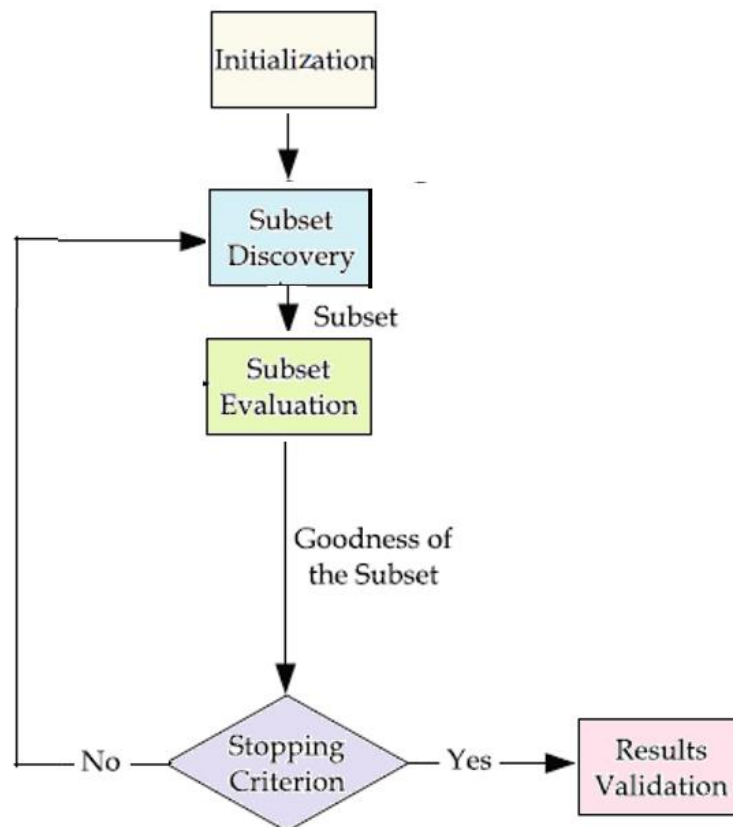


Figure 3. Generalized version of attribute selection flowchart [26].

4.1. Correlation-based attribute selection (CFS)

This method selects attributes that are low correlated to other attributes and highly correlated to class [27]. A function and different search algorithms are used to calculate the information values of the attribute subsets of the dataset. Metaheuristic optimization algorithms are preferred as search algorithms. In this study, PSO, GA, HA, EA algorithms were used in metaheuristic optimization algorithms.

4.1.1. Particle Swarm Optimization (PSO)

This algorithm was inspired by the foraging behavior of flocks and was developed by Dr. Kennedy and Dr. Eberhart. This method is a population-based metaheuristic optimization method [28]. In this method, each individual is defined as a particle. Particles in random coordinates update their position and velocity information to reach the best solution value. The experience of the particles from their neighbors is taken into account in the update.

4.1.2. Genetic Search Algorithm (GA)

This algorithm was proposed by Charles Darwin [29]. It was put forward, inspired by the theory of evolution [30]. The theory of evolution is based on the rule of survival of the fittest. The algorithm searches in accordance with this rule and tries to find a solution. Chromosomes are the variables of the problem to be solved. On these chromosomes, a random solution is first created and then the best solution is reached by making changes in the chromosomes.

4.1.3 Harmony Search Algorithm (HA)

It was suggested by Geem et al. [31]. This algorithm was inspired by the notes in the music. Notes combine to form harmony. Each harmony represents a workaround. It is aimed to reach the best melody in terms of harmonic with the notes in the music [32].

4.1.4 Evolutionary Search Algorithm (EA)

It is used to find the best solution to a problem in the search space. This algorithm uses mutation and elitist selection as search operators. Chromosomes are represented by strategy parameters and pairs of individuals. The strategy parameter is the parameter that mutates the individual it belongs to. It evolves to have optimal value in each generation.

4.2 Principal Component Analysis (PCA)

The first studies on PCA were started in 1901 by Karl Pearson [33]. PCA preserves the existing changes in the data set containing interrelated variables. It is a transformation that includes a large number of interrelated variables and reduces the size of the data set to less size by preserving the existing changes in the data as much as possible. PCA is a very effective statistical method in revealing the necessary information in the data. With this method, a new set of dimensions is found to better represent the diversity of the data. The first dimension shows the most variety. 2. The dimension is chosen to be perpendicular to the first dimension and to show as much variation as possible.

5. Clasification Algorithms

Decision trees are used in classification and regression. In decision trees, the model can be compared to an inverted tree. This model consists of root node, branches and leaves. Nodes have variables, branches have values of variables, leaves have results. The first node in the decision tree is called the root node. The root node can be split. Branching starts from the root node and new nodes are obtained. Decisions are made by following successive nodes until they reach the leaf from the root node. Two popular methods are used to select the best attribute for nodes in a Decision tree. These are the information gain and the Gini index. Knowledge Gain calculates the extent to which a attribute provides information about a class. The nodes are split using the value of the information gain. During the division, the node with high information gain is divided first. The Gini Index is a measure of purity in constructing the Decision tree. Node with low Gini index is preferred for attribute selection. Pruning is removing unnecessary nodes from the tree. It is applied to obtain an optimal decision tree. In the study, AD tree [34], BF tree [35], Randon forest [36], Random tree, Decision Stump [37], Simple Cart [38] and

Optimized forest algorithms [39]. were used. The characteristic attributes of the algorithms are given in Figure.4.

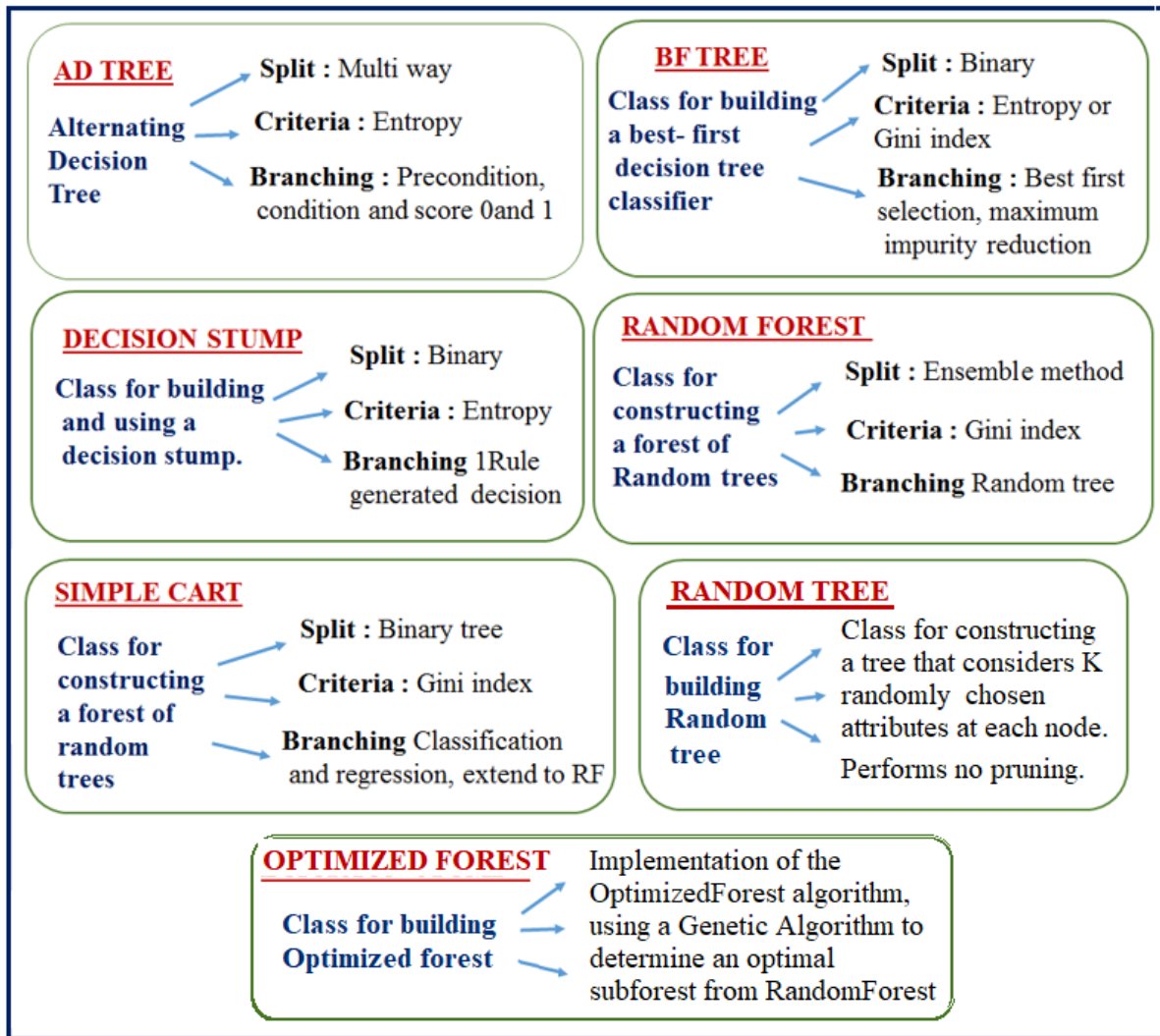


Figure 4. Decision Tree Algorithm Characteristics

6. Performance Metrics

Some metrics are used to compare the classification performance of algorithms. Thanks to these metrics, it is decided which algorithm is more successful. The formulas of the metrics are given in Figure 5. In the formula, TP and TN represent the number of samples that the algorithms predicted correctly, and FP and FN represent the number of samples that the algorithms predicted incorrectly.

PERFORMANCE METRICS

$\text{Accuracy} = \frac{TP + TN}{TP + TN + FP + FN}$	$\text{Precision} = \frac{TP}{TP + FP}$
$\text{F - Score} = \frac{2}{\frac{1}{\text{Recall}} + \frac{1}{\text{Precision}}}$	$\text{Recall} = \frac{TP}{TP + FN}$
$\text{MCC} = \frac{TP * TN - FP * FN}{\sqrt{(TP + FP) * (TP + FN) * (TN + FP) * (TN + FN)}}$	
$\text{TPR} = \frac{TP}{TP + FN}$	$\text{FPR} = \frac{FP}{FP + TN}$

Figure 5. Performance metrics

MCC value is generally preferred to evaluate the classification performance when unbalanced datasets are used. The F-measure value is used when precision and Recall are incompatible. Apart from the metrics indicated in Figure (1), there are other metrics that can be used in performance analysis. These are Area Under the ROC Curve (AUC), Precision Recall curve, Kappa and RMS. The ROC curve is plotted with TPR against the FPR where TPR is on the y-axis. The area under the ROC curve is the AUC value. PR curves are created by plotting precision (x-axis) versus recall (y-axis). Kappa refers to the agreement between the actual classes and the predicted classes. Performance metrics take a minimum of 0 and a maximum of 1. The root mean square (RMS) error value is used when the performance of the two algorithms is almost the same [40]. Indicates the error rate in classification. Unlike other metrics, a low rms value is required for successful classification.

In the study, data collected in the frequency domain were transferred to the time domain using IFFT. Zero padding has been applied to increase resolution in the IFFT application. 1D depth profiles were created for each measurement point. Then, 1D depth profiles were lined up side by side to obtain 2D color images. Color layout Filter has been applied to these images. Data was classified without and with attribute selection. To analyze the classification performances of the algorithms, various performance metrics were calculated and the results were interpreted. PCA and CFS methods were preferred in feature selection. The flow chart of the study is shown in Figure 6. When evaluating the performance of algorithms, the data set is generally divided into two: test data set and training data set. The algorithm is tested with a specific test data. In this study, the cross-validation method was used to test the entire data set. Another reason for using the cross-validation method is to test the success of the algorithms in classifying data that is not in the database.

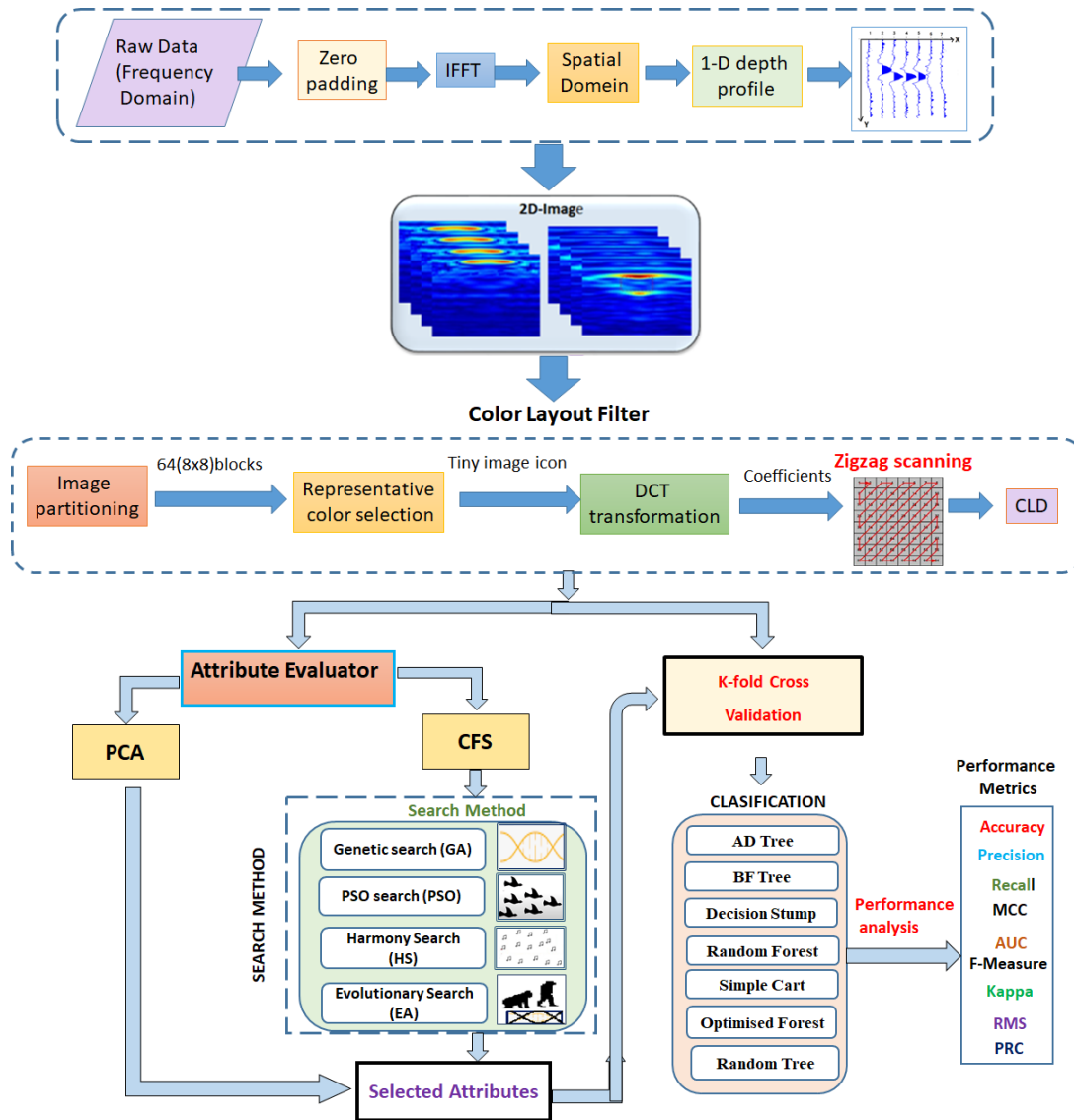


Figure 6. The flow chart of the study

7. Results

The most important metric used in performance analysis is accuracy. Without attribute selected the highest accuracy rate obtained in the classications was 85,4%. The use of the PCA algorithm increased the accuracy of all algorithms. The accuracy value of the random tree algorithm was 95.8%. As can be seen, the PCA algorithm was more effective than CFS in increasing the accuracy of the algorithms. It is unreliable to evaluate performance using just accuracy without using other performance metrics [41]. Therefore, other metric values were also calculated. Calculated metrics are given in Tables and Figures. The highest kappa and lowest rms values were obtained when the random tree and PCA method were used together.(Figure. 7b,7c).

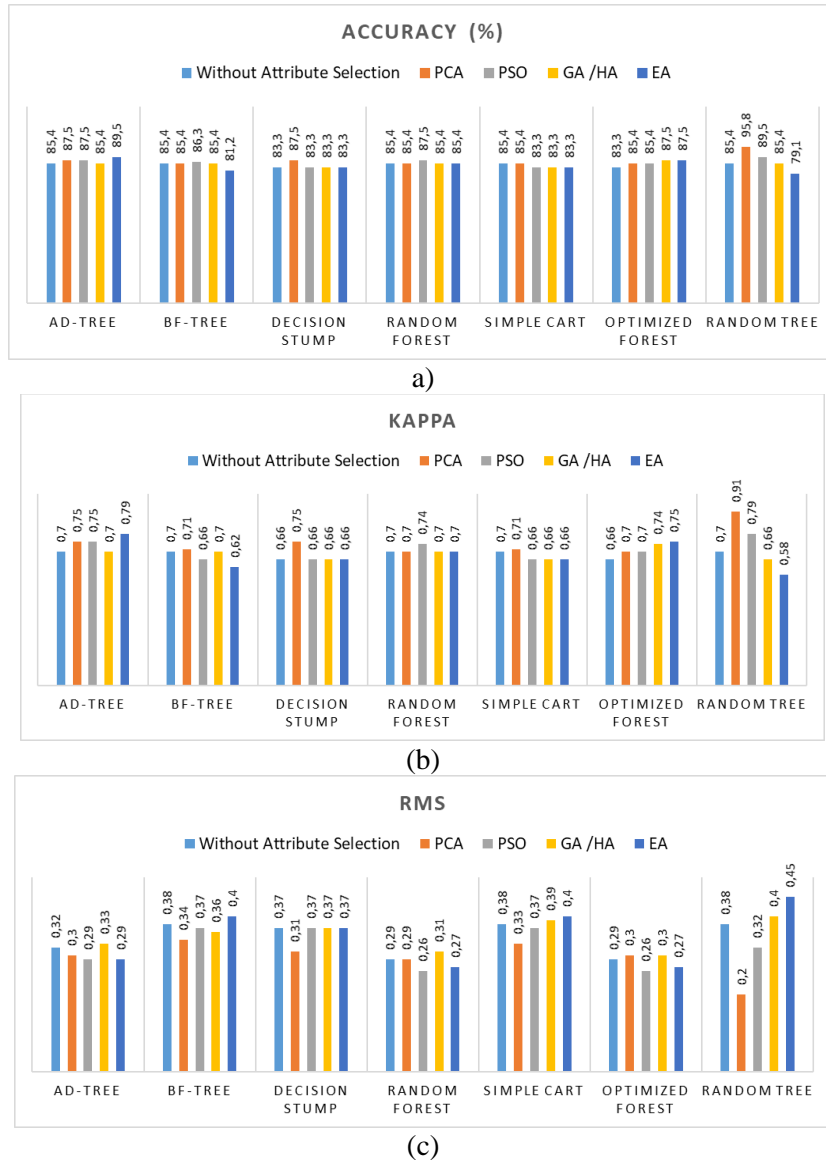


Figure 7. Performance metrics of algorithms a) Accuracy b) Kappa c) Rms

In order to understand which algorithm is more successful in detecting which type of object, the performance metrics of the two classes are calculated separately. The results are given in Table 1 and Table 2. The Recall value indicates how many of the objects that should be predicted as metallic are predicted as metallic, or how many of the objects that we should predict as non-metallic are predicted as non-metallic. In archaeological studies, predict a non-metallic object as metallic will lead to incorrect excavation and damage to the buried object. When the algorithm correctly predicts all objects of the non-metallic class, the Recall value of the non-metallic class is 1. For example, when the Random forest algorithm is applied without attribute selection, the recall value of the metallic class is lower than the recall value of the non-metallic class. This result is an indication that the algorithm is more successful in detecting non-metallic objects. On the other hand, when the Decision strump algorithm is applied without attribute selection, the recall of the non-metallic class is lower than the recall of the metallic class. This result is an indication that the algorithm is more successful in detecting metallic objects. When the metal object is searched, if the algorithm predicts the metal as non metal, there will be a loss because the metal object cannot be detected. For this reason, high precision value is an important criterion for us in model selection. According to the table, the highest Recall and Precision values were obtained with the hybridization of PCA and Random tree algorithm. Other performance metrics given in the table are also compatible with these values. The MCC metric is often used on unbalanced datasets. Since the data used in the study is not unbalanced, the MCC values of the two classes are approximately the same. It was understood from the tables that PCA increased all metrics more than CFS. In PCA and

Random tree hybridization, the calculated metric values of the non-metallic class are higher than the metrics of the metallic class. This result shows that the algorithm is more successful in detecting non-metallic objects.

Table 1. Performance metrics without attribute selection and after attribute selection for Non metallic class

Attribute Evaluator	Search Method	Classification Algorithm	Precision	Recall	F-Score	MCC	AUC	PRC
Without attribute selection		AD Tree	0,88	0,84	0,86	0,70	0,93	0,95
		BF Tree	0,88	0,84	0,86	0,70	0,84	0,83
		Decision Stump	0,90	0,76	0,83	0,67	0,82	0,88
		Randon Forest	0,85	0,88	0,86	0,70	0,70	0,94
		Simple Cart	0,85	0,88	0,86	0,70	0,83	0,81
		Optimized Forest	0,84	0,84	0,84	0,66	0,94	0,95
		Random Tree	0,85	0,88	0,86	0,70	0,85	0,81
PCA		AD Tree	0,91	0,84	0,88	0,75	0,93	0,95
		BF Tree	0,95	0,76	0,85	0,72	0,84	0,91
		Decision Stump	1	0,76	0,87	0,77	0,83	0,90
		Randon Forest	0,85	0,88	0,86	0,70	0,95	0,96
		Simple Cart	0,95	0,76	0,85	0,72	0,84	0,90
		Optimized Forest	0,85	0,88	0,86	0,70	0,94	0,96
		Random Tree	0,96	0,96	0,96	0,91	0,95	0,94
PSO		AD Tree	0,91	0,84	0,88	0,75	0,94	0,96
		BF Tree	0,84	0,84	0,84	0,66	0,89	0,88
		Decision Stump	0,90	0,76	0,83	0,67	0,82	0,88
		Randon Forest	0,88	0,88	0,88	0,74	0,96	0,97
		Simple Cart	0,87	0,80	0,84	0,66	0,86	0,85
		Optimized Forest	0,88	0,84	0,86	0,70	0,96	0,97
		Random Tree	0,95	0,84	0,89	0,79	0,90	0,89
GA /HA		AD Tree	0,88	0,84	0,86	0,70	0,95	0,96
		BF Tree	0,85	0,88	0,86	0,70	0,86	0,85
		Decision Stump	0,90	0,76	0,83	0,67	0,82	0,88
		Randon Forest	0,88	0,84	0,86	0,70	0,95	0,96
		Simple Cart	0,84	0,84	0,84	0,66	0,80	0,77
		Optimized Forest	0,88	0,88	0,88	0,74	0,95	0,96
		Random Tree	0,88	0,84	0,86	0,70	0,85	0,82
CFS		AD Tree	0,95	0,84	0,89	0,79	0,95	0,97
		BF Tree	0,87	0,76	0,81	0,63	0,85	0,87
		Decision Stump	0,90	0,76	0,83	0,67	0,82	0,88
		Randon Forest	0,88	0,84	0,86	0,70	0,96	0,96
		Simple Cart	0,87	0,80	0,84	0,66	0,78	0,79
		Optimized Forest	0,91	0,84	0,88	0,75	0,96	0,97
		Random Tree	0,83	0,76	0,80	0,58	0,79	0,76

Table 2. Performance metrics without attribute selection and after attribute selection for metallic class

Attribute Evaluator	Search Method	Clasification Algorithm	Precision	Recall	F-Score	MCC	AUC	PRC
Without attribute selection		AD Tree	0,82	0,86	0,84	0,70	0,93	0,90
		BF Tree	0,82	0,86	0,84	0,70	0,84	0,76
		Decision Stump	0,76	0,90	0,83	0,67	0,82	0,69
		Randon Forest	0,85	0,81	0,83	0,70	0,94	0,94
		Simple Cart	0,85	0,81	0,83	0,70	0,83	0,79
		Optimized Forest	0,81	0,81	0,81	0,66	0,94	0,94
		Random Tree	0,85	0,81	0,83	0,70	0,85	0,78
PCA		AD Tree	0,83	0,90	0,87	0,75	0,93	0,90
		BF Tree	0,77	0,95	0,85	0,72	0,84	0,72
		Decision Stump	0,78	1	0,88	0,77	0,83	0,71
		Randon Forest	0,85	0,81	0,83	0,70	0,95	0,94
		Simple Cart	0,77	0,95	0,85	0,72	0,84	0,72
		Optimized Forest	0,85	0,81	0,83	0,70	0,94	0,96
		Random Tree	0,95	0,95	0,95	0,91	0,95	0,93
PSO		AD Tree	0,83	0,90	0,87	0,75	0,94	0,89
		BF Tree	0,81	0,81	0,81	0,66	0,89	0,86
		Decision Stump	0,76	0,90	0,83	0,67	0,82	0,69
		Randon Forest	0,86	0,86	0,86	0,74	0,96	0,96
		Simple Cart	0,79	0,86	0,82	0,66	0,86	0,82
		Optimized Forest	0,82	0,86	0,84	0,70	0,96	0,96
		Random Tree	0,84	0,95	0,89	0,79	0,90	0,82
CFS		AD Tree	0,82	0,86	0,84	0,70	0,95	0,95
		BF Tree	0,85	0,81	0,83	0,70	0,86	0,82
		Decision Stump	0,76	0,90	0,83	0,67	0,82	0,69
		Randon Forest	0,82	0,86	0,84	0,70	0,95	0,95
		Simple Cart	0,81	0,81	0,81	0,66	0,80	0,78
		Optimized Forest	0,86	0,86	0,86	0,74	0,95	0,95
		Random Tree	0,82	0,86	0,84	0,70	0,85	0,77
GA /HA		AD Tree	0,84	0,95	0,89	0,79	0,95	0,94
		BF Tree	0,76	0,86	0,80	0,63	0,85	0,76
		Decision Stump	0,76	0,90	0,83	0,67	0,82	0,69
		Randon Forest	0,82	0,86	0,84	0,70	0,96	0,95
		Simple Cart	0,79	0,86	0,82	0,66	0,78	0,70
		Optimized Forest	0,83	0,90	0,87	0,75	0,96	0,96
		Random Tree	0,75	0,81	0,78	0,58	0,79	0,69

8. Conclusions

It is important to know the type of buried object before excavation is carried out, especially in archaeological sites. Some buried objects require precise excavation to be removed without damage. In addition, the automatic detection of the buried object in field studies directs the field study. It saves time and money. In the study, a artificial intelligence based measurement system was designed for the detection of buried metallic and non-metallic objects. With this proposed system, metal and non-metallic objects were classified quickly and automatically, regardless of the shape and depth of buried objects. Decision tree algorithms, one of the popular classification algorithms, were used to select the artificial intelligence method to be integrated into the designed system. Two different attribute selection methods and metaheuristic search algorithms were used to make fast detections with high accuracy. Then the

performances of the algorithms were evaluated. As a result of the performance evaluation, it was understood that the PCA method increased the success of all classification algorithms more than the CFS method. Therefore, it is more appropriate to use the PCA method with classification. The highest metric values were obtained in the hybridization of the random tree algorithm with PCA. The accuracy value obtained in this hybridization is 95.8%. The lowest rms value was also obtained with this hybridization. When the metric values of the classes are examined separately, the metric values of the non-metallic class are higher than the metallic class. This Hybrid is more successful in detecting non-metallic objects. The results obtained in this study using an experimental setup are promising for field studies.

9. Author Contribution Statement

Author contributions The author designed the experiments, prepared the samples and carried out the experiments. Processed the data. Interpreted the results and wrote manuscript.

10. Ethics Committee Approval and Conflict of Interest

There is no conflict of interest with any person/institution in the prepared article.

11. References

- [1] G. Grandjean and D. Leparoux, "The potential of seismic methods for detecting cavities and buried objects: experimentation at a test site," *Jour. of App. Geoph.*, vol. 56, no. 2, pp. 93-106, 2004.
- [2] J. D. Ducut et al., "A review of electrical resistivity tomography applications in underground imaging and object detection," *Disply.*, vol. 73, p. 102208, 2022.
- [3] S. Jazayeri, A. Klotzsche, and S. Kruse, "Improved resolution of pipes with full waveform inversion," 2017.
- [4] W. Van Verre, L. A. Marsh, J. L. Davidson, E. Cheadle, F. J. Podd, and A. J. Peyton, "Detection of metallic objects in mineralized soil using magnetic induction spectroscopy," *IEEE Trans. on Geosc. and Rem. Sens.*, vol. 59, no. 1, pp. 27-36, 2020.
- [5] K. Ho, P. D. Gader, and J. N. Wilson, "Improving landmine detection using frequency domain features from ground penetrating radar," in *IGARSS 2004. 2004 IEEE International Geoscience and Remote Sensing Symposium*, vol. 3, IEEE, pp. 1617-1620, 2004.
- [6] D. J. Daniels, *Ground penetrating radar*. Iet, 2004.
- [7] L. E. Besaw and P. J. Stimac, "Deep convolutional neural networks for classifying GPR B-scans," in *Detection and sensing of mines, explosive objects, and obscured targets*, vol. 9454, SPIE, pp. 385-394, 2015.
- [8] S. Lameri, F. Lombardi, P. Bestagini, M. Lualdi, and S. Tubaro, "Landmine detection from GPR data using convolutional neural networks," *25th European Signal Processing Conference (EUSIPCO)*, IEEE, pp. 508-512, 2017.
- [9] H. M. Alshamy, J. W. A. Sadah, T. R. Saeed, S. A. Mohammed, G. M. Hatem, and A. H. Gatan, "Evaluation of GPR Detection for buried objects material with different depths and scanning angles," in *IOP Conference Series: Materials Science and Engineering*, vol. 1090, no. 1, IOP Publishing, p. 012042, 2021.
- [10] H. A. Gaber, A. M. Abudeif, M. A. Mohammed, G. Z. AbdelAal, and K. K. Mansour, "Archaeological prospecting on the site of Osirion-Abydos using High Resolution Ground Penetrating Radar Technique, Sohag District, Egypt," *Sohag Jour. of Scie.*, vol. 7, no. 2, pp. 115-122, 2022.
- [11] S. Saleh, "Detection of archaeological ruins using integrated geophysical surveys at the Pyramid of Senusret II, Lahun, Fayoum, Egypt," *Pure and Appl. Geophy.*, vol. 179, no. 5, pp. 1981-1993, 2022.
- [12] X. Liang, D. Hu, Y. Li, Y. Zhang, and X. Yang, "Application of GPR underground pipeline detection technology in urban complex geological environments," *Geofl.*, 2022.

- [13] A. Dell'Acqua, A. Sarti, S. Tubaro, and L. Zanzi, "Detection of linear objects in GPR data," *Signal Proce.*, vol. 84, no. 4, pp. 785-799, 2004.
- [14] Z. Hui-lin, T. Mao, and C. Xiao-li, "Feature extraction and classification of echo signal of ground penetrating radar," **Wuhan University Jour. of Natural Scie.*, vol. 10, no. 6, pp. 1009-1012, 2005.
- [15] C. G. Windsor, L. Capineri, and P. Falorni, "The estimation of buried pipe diameters by generalized hough transform of radar data," *Piers Online*, vol. 1, pp. 345-349, 2005.
- [16] S. K. Sinha and P. W. Fieguth, "Automated detection of cracks in buried concrete pipe images," *Autom. in Constr.*, vol. 15, no. 1, pp. 58-72, 2006.
- [17] X. Zhou, Q. Chen, S. Lyu, and H. Chen, "Estimating the Direction and Radius of Pipe from GPR Image by Ellipse Inversion Model," *arXiv preprint arXiv:2201.10184*, 2022.
- [18] L. C. M. Amaral, A. Roshan, and A. Bayat, "Review of machine learning algorithms for automatic detection of underground objects in GPR images," *Journal of Pipel. Systems Eng. and Pract.*, vol. 13, no. 2, p. 04021082, 2022.
- [19] S. Li, J. Zhao, H. Zhang, and Y. Zhang, "Automatic detection of pipelines from sub-bottom profiler sonar images," *IEEE Journal of Oceanic Eng.*, vol. 47, no. 2, pp. 417-432, 2021.
- [20] T. S. Brandes, B. Ballard, S. Ramakrishnan, E. Lockhart, B. Marchand, and P. Rabenold, "Environmentally adaptive automated recognition of underwater mines with synthetic aperture sonar imagery," *The Journ. of the Acoust. Socie. of America*, vol. 150, no. 2, pp. 851-863, 2021.
- [21] A. Abhinaya, "Using Machine Learning to detect voids in an underground pipeline using in-pipe Ground Penetrating Radar," *University of Twente*, 2021.
- [22] X. Yin, Y. Chen, A. Bouferguene, H. Zaman, M. Al-Hussein, and L. Kurach, "A deep learning-based framework for an automated defect detection system for sewer pipes," *Autom. in Constr.*, vol. 109, p. 102967, 2020.
- [23] M. Salucci, L. Tenuti, L. Poli, and A. Massa, "Buried object detection and imaging through innovative processing of GPR data," in *11th European Conference on Antennas and Propagation (EUCAP): IEEE*, pp. 1703-1706, 2017.
- [24] E. Pasolli, F. Melgani, M. Donelli, R. Attoui, and M. De Vos, "Automatic detection and classification of buried objects in GPR images using genetic algorithms and support vector machines," in *IGARSS 2008-2008 IEEE International Geoscience and Remote Sensing Symposium*, vol. 2: IEEE, pp. II-525-II-528, 2008.
- [25] H. Qin, D. Zhang, Y. Tang, and Y. Wang, "Automatic recognition of tunnel lining elements from GPR images using deep convolutional networks with data augmentation," *Autom. in Constr.*, vol. 130, p. 103830, 2021.
- [26] M. Dash and H. Liu, "Feature selection for classification," *Intelligent Data Analy.*, vol. 1, no. 1-4, pp. 131-156, 1997.
- [27] M. A. Hall, "Correlation-based feature subset selection for machine learning," *Ph.D. Thesis, University of Waikato*, 1988.
- [28] R. Eberhart and J. Kennedy, "A new optimizer using particle swarm theory," in *MHS'95. Proceedings of the Sixth International Symposium on Micro Machine and Human Science: IEEE*, pp. 39-43, 1995.
- [29] D. Goldenberg, *Genetic Algorithms in Search, Optimization and Machine Learning*, Reading: Addison Wesley, 1989.
- [30] L. M. Schmitt, "Theory of genetic algorithms," *Theor. Comp. Scie.*, vol. 259, no. 1-2, pp. 1-61, 2001.
- [31] Z. W. Geem, C.-L. Tseng, and Y. Park, "Harmony search for generalized orienteering problem: best touring in China," in *International Conference on Natural Computation**, Springer, pp. 741-750, 2005.
- [32] S. Fong, R. P. Biuk-Aghai, and R. C. Millham, "Swarm search methods in weka for data mining," in *Proceedings of the 2018 10th International Conference on Machine Learning and Computing*, pp. 122-127, 2018.
- [33] L. KPFERS, "On lines and planes of closest fit to systems of points in space," in *Proceedings of the 17th ACM SIGACT-SIGMOD-SIGART Symposium on Principles of Database Systems (SIGMOD)*. 19, 1901.

- [34] G. Holmes, B. Pfahringer, R. Kirkby, E. Frank, and M. Hall, "Multiclass alternating decision trees," in *Machine Learning: ECML, 13th European Conference on Machine Learning Helsinki, Finland, August 19–23, Proceedings*, Springer, pp. 161-172, 2002.
- [35] H. Shi, "Best-first decision tree learning," University of Waikato, 2007.
- [36] B. Pfahringer, "Random model trees: an effective and scalable regression method," University of Waikato, New Zealand, 1995.
- [37] C. Tan, H. Chen, and C. Xia, "The prediction of cardiovascular disease based on trace element contents in hair and a classifier of boosting decision stumps," *Biolog. Trace Element Res.*, vol. 129, pp. 9-19, 2009.
- [38] N. Landwehr, M. Hall, and E. Frank, "Logistic model trees," *Machine Lear.*, vol. 59, pp. 161-205, 2005.
- [39] M. N. Adnan and M. Z. Islam, "Optimizing the number of trees in a decision forest to discover a subforest with high ensemble accuracy using a genetic algorithm," *Knowledge-Based Syst.*, vol. 110, pp. 86-97, 2016.
- [40] P. Pradham, N. H. Younan, and R. L. King, "Concepts of image fusion in remote sensing applications," in **Image Fusion: Algorit. and Applic.*, pp. 391-428, 2008.
- [41] R. Joshi, "Accuracy, precision, recall & f1 score: Interpretation of performance measures," Retrieved April, vol. 1, no. 2018, p. 2016, 2016.